Computational Analysis of Asymmetric Environments of Soluble Epidermal Growth Factor and Application to Single Cell Polarization and Fate Control

by

Julien Verneau

A thesis

presented to the University of Waterloo

in fulfillment of the

thesis requirement for the degree of

Doctor of Philosophy

in

Chemical Engineering

Waterloo, Ontario, Canada, 2011

© Julien Verneau 2011

Author's Declaration

I hereby declare that I am the sole author of this thesis. This is a true copy of the thesis, including any required final revisions, as accepted by my examiners.

I understand that my thesis may be made electronically available to the public.

Abstract

Stem and progenitor cells have the ability to regulate fate decisions through asymmetric cells divisions. The coordinated choice of cell division symmetry in space and time contributes to the physiological development of tissues and organs. Conversely, deregulation of these decisions can lead to the uncontrolled proliferation of cells as observed in cancer. Understanding the mechanisms of cell fate choices is necessary for the design of biomimetic culture systems and the production of therapeutic cell populations in the context of regenerative medicine.

Environmental signals can guide the fate decision process at the single level but the exact nature of these signals remains to be discovered. Gradients of factors are important during development and several methods have been developed to recreate gradients and/or pulses of factors *in vitro*. In the context of asymmetric cell division, the effect of the soluble factor environment on the polarization of cell surface receptors and intracellular proteins has not been properly investigated.

We developed a finite-element model of a single cell in culture in which epidermal growth factor (EGF) was delivered through a micropipette onto a single cell surface. A two-dimensional approach initially allowed for the development of a set of metrics to evaluate the polarization potential with respect to different delivery strategies. We further analyzed a three-dimensional model in which conditions consistent with single cell polarization were identified. The benefits of finite-element modeling were illustrated through the demonstration of complex geometry effects resulting from the culture chamber and neighboring cells.

Finally, physiological effects of *in vitro* polarization were analyzed at the single cell level in HeLa and primary cells. The potential of soluble factor signaling in the context of directed fate control was demonstrated. Long term phenotypical effects were studied using live-cell imaging which demonstrated the degree of heterogeneity of *in vitro* culture systems and future challenges for the production of therapeutic cell populations.

Acknowledgements

First and foremost, I would like to acknowledge my supervisor professor Eric Jervis. It has been a great international journey in Waterloo. I am thankful for the guidance and support provided over the years and for the long discussions about music.

I would like to thank two people without whom this work would not have been possible. Sasha Avreline, for his dedication, passion for mathematics and COMSOL, the speed at which he can take his calculator out, the help in the laboratory and for his positive attitude. Erika Murray, we yelled at each other, we laughed together, we vacationed, we had dinners and shared drinks, we argued about the air conditioning, we even worked together. It's been fun!

I would like to thank the members of my examination committee for reading and commenting on this thesis; Dr. Michael Tam, Dr. Frank Gu, Dr. Guy Guillemette, and Dr. Bruce Reed from the University of Waterloo and Dr. James Piret from the University of British Columbia.

I also would like to thank former members of this laboratory who all contributed in their own way to this work: Bredon, Duane, Darik, April, Geneviève, Melanie, Jonathan, Charlie, John, Liam and Richard.

Dedication

À ma famille, pour ces longues années de soutien. Ma mère Pascale et mes grand-parents Jacqueline et Albert.

Table of Contents

List of Figures

List of Tables

List of Abbreviations

Activator Protein 1 (AP-1)

Atypical Protein Kinase C (aPKC)

Casitas B-lineage Lymphoma (Cbl)

Cell Fate Determinants (CFD)

Centipoise (cp)

Central Nervous System (CNS)

c-Jun N-terminal Kinase (JNK)

Degrees of freedom (d_f)

Diego (Dgo)

Dishevelled (Dsh)

Embryonic Stem (ES)

Epidermal Growth Factor (EGF)

Epidermal Growth Factor Receptor (EGFR)

Extracellular Matrix (ECM)

Extracellular signal-Regulated Kinase (Erk)

Fibroblast Growth Factor 4 (Fgf4)

Frizzled (Fz)

Ganglion Mother Cell (GMC)

Green Fluorescent Protein (GFP)

Growth Factor (GF)

Growth Factor Receptor-Bound protein 2 (Grb2)

Growth Factor Receptor-Bound protein 7 (Grb7)

GTPase Activating Protein (GAP)

Guanine Exchange Factor (GEF)

Guanine Tri-Phosphate (GTP)

Human Embryonic Stem Cell (hESC)

Inner Cell Mass (ICM)

Lethal Giant Larva (Lgl)

Long-term Live Cell Imaging (LTLCI)

Mitogen-Associated Protein Kinase (MAPK)

Mouse Embryonic Stem Cells (mESC)

Mouse Neural Stem Cells (mNSC)

Nerve Growth Factor (NGF)

NeuroBlast (NBs)

Non-Catalytic region of tyrosine Kinase adptor protein (Nck)

Ordinary Differential Equation (ODE)

Partial Differential Equation (PDE)

Partitioning defective (Par)

Partner of Inscuteable (Pins)

Partner of Numb (Pon)

Percentage of receptor Occupancy (PO)

PhosphoInositide 3-Kinase (PI3K)

PhosphoLipase C γ (PLCγ)

PhosphoTyrosine Binding (PTB)

Planar Cell Polarity (PCP)

Polarization Index (PI)

Prickel (Pk)

Primitive Streak (PS)

Protein Kinase C (PKC)

Receptor Tyrosine Kinase (RTK)

Region of Interest (ROI)

Son of Sevenless (Sos)

Sarcoma (Src)

Src Homology 2 (SH2)

Src Homology 3 (SH3)

Src Homology 2 domain Containing transforming protein (Shc)

Stem Cells (SC)

Strabismus (Stbm)

Transforming Growth Factor β (TGF-β)

Tyrosine Kinase Domains (TKD)

1 Chapter 1: Introduction

The field of medicine has made considerable progress over the past decades in the treatment of degenerative diseases. While the implementation of surgical procedures to transplant organs and replace malfunctioning tissues has proven effective, the shortage of organ donors is a major drawback. Most degenerative diseases do not have a cure and only palliative care is provided to improve the patient's quality of life when transplantation is not possible. Aging of the population will contribute to the doubling of healthcare expenses by 2030, with costs representing up to 25% of the Gross Domestic Product of a country such as the United States (Committee on the Biological and Biomedical Applications of Stem Cell Research, 2002). There is an important need for new therapies in the context of degenerative diseases.

There are great expectations associated with the application of regenerative medicine. Harnessing the power of stem cells of various origins could lead to new therapies specifically tailored for patients while avoiding immune rejection. Embryonic stem cells, adult stem cells or the recently discovered induced pluripotent stem cells are candidates for cellular therapies. These cells could be used *in vivo* for *de novo* engineering techniques in which the body environment would harness the cells' regenerative potential or *in vitro* through directed production of tissues that could be used for transplant. The latter approach should be most effectively developed based on an in-depth understanding of stem cell biology and mechanisms by which cells receive and integrate signals from the environment to trigger appropriated and coordinated responses in space and time.

While significant progress has been made in understanding stem cell biology, the translation towards the clinic is slow. The first embryonic stem-cell based human clinical trial was approved in July 2010 (Geron), approximately 45 years after stem cells were first reported by Till and McCulloch (Till, McCulloch et al. 1964). Human embryonic stem cells (hESC) are used to produce a population of oligodendrocyte progenitors injected at the lesion site of patients with acute spinal cord injury. In the laboratory, cells are cultivated adherently in flasks and are submerged in liquid media containing various sources of carbon, nitrogen, but also growth factors. Drugs can be tested on different stem cell populations to evaluate their potential for self-renewal or directed commitment towards a specific lineage for the production of therapeutically relevant population of cells. While our theoretical knowledge of stem cells has been constantly supported by an increasing literature, the translation of experimental findings to *in vivo* situations is generally unsuccessful.

Stem cell populations are heterogeneous based on expression levels of known transcription factors and also analysis of self-renewal and developmental potential (Singh *et al*., 2007). This may explain the variation in susceptibility to differentiation observed within cell cultures (Smith, 2001). The population level analysis of responses to various chemicals may represent an average over several subpopulations and seriously compromise the unbiased interpretation of data. Also, the production of a pure population of cells still remains a major challenge and defined cultures are required for clinical applications. Transplantable volumes of cellular cultures represent in the order of 10^9 cells all of which should have been tested prior to implantation in a tissue. Methods have been developed to enrich cell subpopulations in a

mixture, but these techniques do not exceed 95% purity and can be to some extent destructive (Jing *et a*l., 2007; Chou *et al*., 2005; Martin-Henai *et al*., 2002).

The development of biomimetic systems can help harness stem cells' potential. The analysis of cellular behavior and response to potential therapeutics *in vitro* will allow for a better appreciation of physiological significance if experimental conditions mimic *in vivo* situations. For example, embryonic or neural stem cells can be cultured as embryoid bodies or neurospheres respectively in which cells aggregate and form complex and heterogeneous three-dimensional colonies. These configurations allow for a level of complexity not attained by conventional adherent culture systems and reproduce more accurately *in vivo* situations.

In the context of stem cells, the symmetry of division is of utmost importance for fate determination. *In vivo*, the switch between symmetric (stem cell expansion) and asymmetric divisions (production of committed cells) is finely coordinated in space and time and allows for the formation of structured three-dimensional tissues. Before a cell asymmetrically divides various signals from the direct microenvironment convey positional information. Messages are transmitted through cellular interactions with the extracellular matrix, neighboring cells or through binding with soluble factors. This results in the polarization of cytoplasmic protein complexes at the cell cortex. Conventional adherent culture systems are highly heterogeneous in terms of local microenvironments and could generate a mosaic of positional information among a cell population, which indicates control of cell division symmetry at the single cell level should be investigated. This led us to the following hypothesis:

***Hypothesis 1*: Controlling mechanisms of asymmetric cell division at the single cell level is a requirement for the scale-up of culture systems in the context of the production of homogeneous cell populations.**

While growth factors diffuse rapidly *in vitro* and are supplemented in the media in large quantities, *in vivo* growth factors experience a slow apparent diffusion in the extracellular compartment due to possible entrapment in the matrix (Dowd, Cooney et al. 1999). They can differentially affect cell populations based on their concentration (as in the case of morphogens) and have a regulated temporal expression profile in tissues. Working at the single cell level can reduce signaling complexity and limit the interpretation of environmental information to soluble factor signaling only. We decided to study how engineered microenvironments of soluble factors could affect the symmetry of cell division and made the two following hypotheses:

***Hypothesis 2*: Single cell level analysis and experiments will allow for a reduction of the complexity of cellular microenvironments and permit the analysis and prediction of soluble factor binding.**

***Hypothesis 3*: Soluble factor signaling alone can dictate the symmetry of cell division.**

Epidermal growth factor receptor (EGFR) asymmetric partitioning has been reported at the time of mitosis in cancer keratinocytes and mouse neural stem cells from the ventricular and subventricular zone (Le Roy, Zuliani et al. ; Sun, Goderie et al. 2005). The asymmetric partitioning was linked with different fate and proliferative potential which illustrated the

interplay between soluble factor signaling and cell fate. It is unclear if this mechanism is intrinsic and exclusively controlled by genetic factors, or extrinsic and resulting from heterogeneities in the soluble microenvironment of EGF. We propose that the engineering of asymmetric environments of EGF around a single cell *in vitro* could help elucidate the existence of the extrinsic mechanism, which led to the two following hypotheses:

***Hypothesis 4*: Asymmetric environments of soluble factors (EGF) can be induce the asymmetric partitioning of receptor-ligand complexes (EGF-EGFR) at the single cell level.**

***Hypothesis 5*: Asymmetric partitioning of receptor-ligand complexes at the single-cell level might allow the asymmetric partitioning of activated signaling molecules at the time of mitosis which could be a regulatory mechanism for asymmetric cell division and cell fate decisions.**

Project Summary:

Computational methods are a valuable tool for the analysis and engineering of asymmetric environments of soluble factors around single cells. In silico methods will be developed to evaluate various strategies for controlled factor release in the context of single cell polarization. Using two and three-dimensional modeling, we will further analyze the complex interplay between culture systems, neighboring cells and soluble signaling at the single cell level. Once the model significance will be established, we will evaluate the potential for polarization and cell fate control both in the short and long-term. Understanding and engineering cell fate decisions at the single cell level will

help design new culture systems and techniques that allow for optimal control of cell fate decisions. We expect these findings to help increase the purity of cell populations in vitro and contribute to the development of biomimetic culture systems. These approaches could be significant in the translational research towards the clinic and ultimately benefit human health.

The following objectives were identified:

Milestone 1: Development of a two-dimensional computational framework for the analysis of asymmetric environments of soluble factors *in silico*;

Milestone 2: Development of a three-dimensional model, analysis of chamber design and cell colony effects, demonstration of model significance;

Milestone 3: Analysis of short and long-term physiological effects of asymmetric soluble factor delivery.

2 Chapter 2: Background

The formation of tissues and organs during development is the result of coordinated responses of cell populations to environmental stimuli modulated in space and time. These signals ensure the proper balance between proliferation and differentiation throughout developmental stages and thereby coordinate the growth and specialization of tissues into functional units achieving defined tasks. *In vivo*, cells are under the constant stimulation of a variety of signals and proper integration of these messages will ensure adequate responses throughout development. Among these signals, soluble factors can be secreted by a cell, transported by the blood (endocrine signaling) or diffuse in the extracellular fluid /matrix and reach a target cell (paracrine signaling). These molecules can be soluble proteins as in the case of growth factors or steroid hormones with the ability to cross the lipid bilayer. In tissues, cells interact with each other and can also communicate through direct cell-cell contact while the extracellular matrix (ECM) also provides another mechanism for cell communication. Cells present on their cellular membrane a variety of surface receptors. These are generally transmembrane proteins with the ability to bind various ligands with different affinities. The mechanisms by which signals are transmitted from the extracellular to the cytoplasmic compartment are varied, but ultimately external signals modify the level of expression of target genes and allow for the regulation of cell metabolism. This process is referred to as signal transduction and will affect cell growth, proliferation, differentiation, migration, adhesion, senescence or apoptosis through selective expression or repression of genes resulting from the activation or repression of a transcription factor (Lodish *et al*., 2005).

Dysfunction of these communication systems can lead to serious aberrations such as abnormal proliferation as observed in cancer. Understanding mechanisms by which signals are regulated will allow for the development of new *in vitro* culture systems reproducing more accurately physiological conditions of proliferation and differentiation while increasing the understanding of physiological and pathological developmental processes. A review of fundamental biological properties of stem cells and progenitor cells is necessary to develop the key concepts required for the development of these systems.

2.1 Stem Cell Biology

2.1.1 Mammalian Embryology

The ovum and spermatozoon, the respective female and male gametes in mammals are haploid. After fertilization, meiosis II is triggered in the ovum and the sperm and ovum nucleus are unified to restore the diploid condition. The resulting fertilized egg or zygote is the first cell of the new organism. Early development occurs in the uterine tube up to day six. After the initial cell cleavage, the following dividing stages are referred to as morula. Starting at day seven, the ball of dividing cells implants itself in the uterine wall, and will be referred to as embryo up to the eighth week. At this stage, the dividing cells give rise to an organized cellular structure called the blastocyst and the developing organism is called a fetus after the eighth week.

The mammalian blastocyst has developed three different cell lineages by the time of implantation: an outer layer called trophoblast that encloses the blastocoelic cavity or blastocoele; the inner cell mass (ICM) that consists of epiblast (primitive ectoderm) covered by a monolayer of primitive endoderm. Cells isolated from the primitive ICM are referred to as

Embryonic Stem (ES) cells. Gastrulation begins shortly after implantation in the uterus and is defined as the formation of the three primary germ layers of the embryo from the ICM: ectoderm, endoderm and mesoderm. During gastrulation, only one new layer is produced (mesoderm) as both primitive endoderm and ectoderm will be replaced by their definitive counterparts. Each layer gives rise to a distinct set of tissues and organs: the digestive organs and lungs come from the endoderm; muscles, the heart and blood system come from the mesoderm; the nervous system and skin come from the ectoderm. In mammals, a transient structure called the primitive streak (PS) is formed in the region of the epiblast when gastrulation begins that will ultimately form the posterior end of the embryo (Tam and Behringer 1997). The PS is located in the middle of the disc and is responsible for the formation of the mesoderm during gastrulation. Uncommitted cells move across the PS and exit either as mesoderm or definitive endoderm. Anterior, mid and posterior regions of the PS have been defined according to gene expression profiles. The ectoderm derives from the anterior region of the epiblast that does not enter the PS.

This review of embryology highlighted some of the properties of embryonic stem cells and these will be reviewed in more details in the following section.

2.1.2 Stem Cell Properties

ES cells can be defined on a functional aspect as they can regenerate any tissue. From this definition can be deduced two properties. First, stem cells have an unlimited self-renewal potential and can produce more stem cells during each round of mitotic divisions, contrary to differentiated cells that cannot self-renew over long periods of time. This makes stem cells the only primary cell type that can in theory be cultured indefinitely *in vitro* under appropriate

conditions. Second, ES cells have a multilineage potential and can give rise to several committed and differentiated cell types which lose the self-renewal potential (i.e. developmental restriction) (Till, McCulloch et al. 1964). The properties of stem cells can be studied *in vitro* using clonogenic assays in which their self-renewal and multilineage potential can be evaluated (Friedenstein, Deriglasova et al. 1974; Friedenstein, Gorskaja et al. 1976) and the ectopic formation of carcinoteratomas is also used for the assessment of stem cell properties *in vivo* (Thomson, Itskovitz-Eldor et al. 1998; Chambers and Smith 2004). The degree of multilineage potential differs based on the origin of stem cells. ES cells come from the primitive ICM of the blastocyst stage and have the broadest biological potential. ES cells are pluripotent and can give rise to all derivatives of all three germ layers from the early embryo (ectoderm, endoderm and mesoderm) (Pera, Reubinoff et al. 2000). Totipotent cells come from the fertilized egg (zygote) and the 8 cells produced by its cleavage (morula), and can give rise to all cells coming from the ICM and the trophoblast of the early embryo. It should be noted that at the stage of 16 cells, totipotency is already lost as cells start to commit in different lineages. Conversely, multipotency refers to cells that can produce cells of a related family such as the hematopoietic system. Finally, most progenitor cells are unipotent meaning that they can only give rise to a single cell type. During development, pluripotency is lost in a process called lineage restriction. Only the embryonic germ cells coming from the gonad ridge (leading to the production of gametes) remains pluripotent (Pera, Reubinoff et al. 2000).

Stem cells are not only restricted to the early stages of development but are also present in several adult tissues. Adult-derived stem cells exhibit the same properties except that somatic stem cells are multipotent. These cells contribute to the regeneration and repair of specific tissues

(Brehm, Zeus et al. 2002). Some evidence also indicates the existence of pluripotent adult stem cells that violate the germinal restriction (Coulombel 2007). Examples of organs or tissues that contain stem cells are the liver (Alison, Golding et al. 1996), brain (Taupin 2006), lungs (Gomperts and Strieter 2007), muscles (Seale and Rudnicki 2000), skin (Watt and Hogan 2000) and blood (Muller, Medvinsky et al. 1994).

The complete development from the early embryo to a fully mature organism is a highly coordinated process in which cells alternate cycles of proliferation, migration and differentiation to produce organized tissues and organs. Central to this process is cell communication or signaling as populations must communicate to choose between coordinated cycles in space and time, thereby leading to the formation of functional mature tissues. A better understanding of the signals required along different cellular lineages has emerged over the past years and several differentiation trajectories have now been defined (Ortega-Perez, Murray et al. 2007; Orkin and Zon 2008).

A major effort has been made to define genetic markers associated with the stem-cell state. Several transcription factors have been identified including Oct4 (Niwa, Miyazaki et al. 2000), Nanog (Chambers, Colby et al. 2003) and Sox2 (Masui, Nakatake et al. 2007), found in both mouse and human stem cells. The stem cell state was further characterized by an autoregulatory loop of factors that control the switch between pluripotency and commitment. In mouse ES cells, autocrine production of Fibroblast Growth Factor 4 (Fgf4) directed by *Oct4* and *Sox2* activates the Extracellular signal-Regulated Kinases (Erk) signaling pathway. This promotes a state in which mESC are not restricted to the stem-cell fate but can commit to different lineages with the

appropriate factors, a process that can be reversed by Nanog (Kunath, Saba-El-Leil et al. 2007; Silva and Smith 2008). The fine tuning of the expression of each factor is thus the key to the stem cell state, as shown in Figure 2-1.

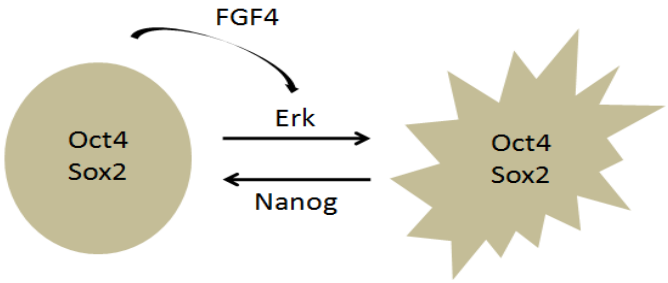

Figure 2-1: Interplay between autocrine signaling and the stem cell state. The genetic expression of markers such as Oct4, Sox2 and Nanog specifically characterizes stem cells. Autocrine induction by FGF4 activates the Erk pathway that triggers a switch to a state in which stem cells are receptive to commitment signals (right). Conversely, Nanog reverses this switch to a state where stem cells are refractory to these signals and remain stem cells (left). This state is finely regulated by expression levels of each factor (adapted from Silva and Smith, 2008).

This demonstrates how extracellular signals modulate and regulate cellular properties. Signal transduction cascades have been studied for decades and one of the most studied signaling pathways is the Epidermal Growth Factor Receptor (EGFR) system which activates the Erk pathway. It is documented in over 17000 (Pubmed) papers as of 2011 and we will review the EGFR family of receptor, their common structure, mode of action and the role EGFR can play on cell fate determination.

2.2 EGF Signaling

2.2.1 EGFR Family of Receptor

The first receptor tyrosine kinase (RTK) was discovered over 25 years ago and since then a significant number of members of this family have emerged as key regulators of cellular

processes such as growth, migration, proliferation, survival and differentiation (Ullrich and Schlessinger 1990; Blume-Jensen and Hunter 2001). Due to the ubiquitous nature of the mechanisms these receptors control, their structure and mode of action are extremely conserved from mammals to *C. elegans* and *Drosophila* (Aroian, Koga et al. 1990; Wasserman and Freeman 1997). Nonetheless, the EGFR/ErbB family has evolved in vertebrates towards higher signal diversity as it consists of four RTKs; EFGR (ErbB1/HER1), ErbB2/HER2/*Neu*, ErbB3/HER3 and ErbB4/HER4 (Yarden and Sliwkowski 2001; Schlessinger 2004). Each family exhibits a specificity of substrate as well as a specificity of downstream activated signaling pathways (Riese and Stern 1998). EGFR binds ligands such as EGF and Transforming Growth Factor β (TGF-β), ErbB2 does not have any known active ligand and relies on association with other ErbBs for activation (Cho, Mason et al. 2003; Garrett, McKern et al. 2003), ErbB3 binds neuregulins (Schaefer, Brachwitz et al. 2006) and ErbB4 binds neuregulins and EGF-like ligands. While insufficient ErbB signaling is a hallmark of neurodegenerative diseases (Bublil and Yarden 2007), overexpression and mutations of ErbB family of receptors lead to the development of a variety of cancers (Yarden and Sliwkowski 2001; Zhang, Berezov et al. 2007). Specifically, EGFR is expressed in a wide variety of cell types, including all cells from mesodermal and ectodermal origin (Yarden and Sliwkowski 2001). The significance of EGFR is illustrated by the lethal phenotype of EGFR null mutations in mice (Sibilia and Wagner 1995; Sibilia, Steinbach et al. 1998) and occurrence of tumors with mutated and/or overexpressed EGFRs as observed in glioblastomas, breast cancer and non small-cell lung cancer (Wikstrand, Reist et al. 1998; Olayioye, Neve et al. 2000; Yarden and Sliwkowski 2001; Lynch, Bell et al. 2004; Paez, Janne et al. 2004; Pao, Miller et al. 2004).

2.2.2 Structure

The EGFR and all members of the RTK family of receptors share a similar structure. The extracellular domain comprises four domains: two ligand-binding regions called domain I and III sharing approximately 40% sequence identity and domain II and IV rich in cystine. The intracellular region comprises a regulatory domain with tyrosine residues, several accessory regulatory regions and a tyrosine kinase domain. It is linked to the extracellular compartment through a single transmembrane helix. The extracellular domains I and III contain several β-helices while domain II and IV exhibit extended structures containing several disulfide bonds.

2.2.3 Mode of Action

Activation

Early studies of RTKs demonstrated a simple mechanism in which a bivalent ligand binds two monomeric receptors and triggers a ligand-based dimerization in which receptors do not interact. In the case of Nerve Growth Factor (NGF), the bivalent ligand triggers the dimerization of receptors through the Ig-C2 domain without a direct contact between receptors (Wiesmann, Ultsch et al. 1999). Other examples later demonstrated dimerization could be entirely dictated by the receptors as in the case of EGF. Before ligand binding, the dimerization "arm" or domain II is buried through intramolecular interactions with domain IV in a conformation referred to as "tethered". Interactions between regions II and IV further contribute to inhibit dimerization and maintain the tethered configuration. Binding of EGF to sites I and III triggers a conformational change exposing the dimerization domain II and thereby initiating the formation of EGFR dimers (Burgess, Cho et al. 2003). This conformational reorganization will

subsequently expose the Tyrosine Kinase Domains (TKD) of the intracellular region (Yarden and Schlessinger 1987; Ferguson, Berger et al. 2003).

The transphosphorylation of cytoplasmic tyrosine residues represents the start of the signaling cascade (Honegger, Kris et al. 1989). This mechanism varies significantly between classes of RTKs but generally, transphosphorylation of tyrosine residues in a TKD contributes to the removal of cis-autoinhibitory interactions leading to the activation of TKD activity. In the case of EGFR, the tyrosine kinase domain (TKD) of a RTK is allosterically activated by direct proximity contacts between the C-terminal region of one TKD and the N-terminal region of another TKD (Zhang, Gureasko et al. 2006; Jura, Endres et al. 2009). Recent reports indicate EGFR can dimerize before binding of any ligand and receptor activation on the cell surface and these receptors may exhibit a higher affinity for EGF than monomeric receptors (Gadella and Jovin 1995; Clayton, Tavarnesi et al. 2007).

The dimerization process can generate homo or heterodimeric receptors, as a single EGFR can be asymmetrically activated by ErbB1 (Hynes and Lane 2005), ErbB2 (Holbro and Hynes 2004), ErbB3 (Plowman, Whitney et al. 1990) or ErbB4 (Plowman, Culouscou et al. 1993; Arasada and Carpenter 2005). The relative balance of homo and heterodimers will dictate specific responses following extracellular protein binding.

Signal Transduction

Due to the variety of ErbB ligands and signaling intermediates, signals coming from these receptors are part of a very complex network of intricate signals, where the intensity, duration and frequency of signals will have a significant impact on gene expression. A detailed review of the complexity of ErbB signaling is available elsewhere (Yarden and Sliwkowski 2001) and we will focus on EGFR/ErbB1 in this section.

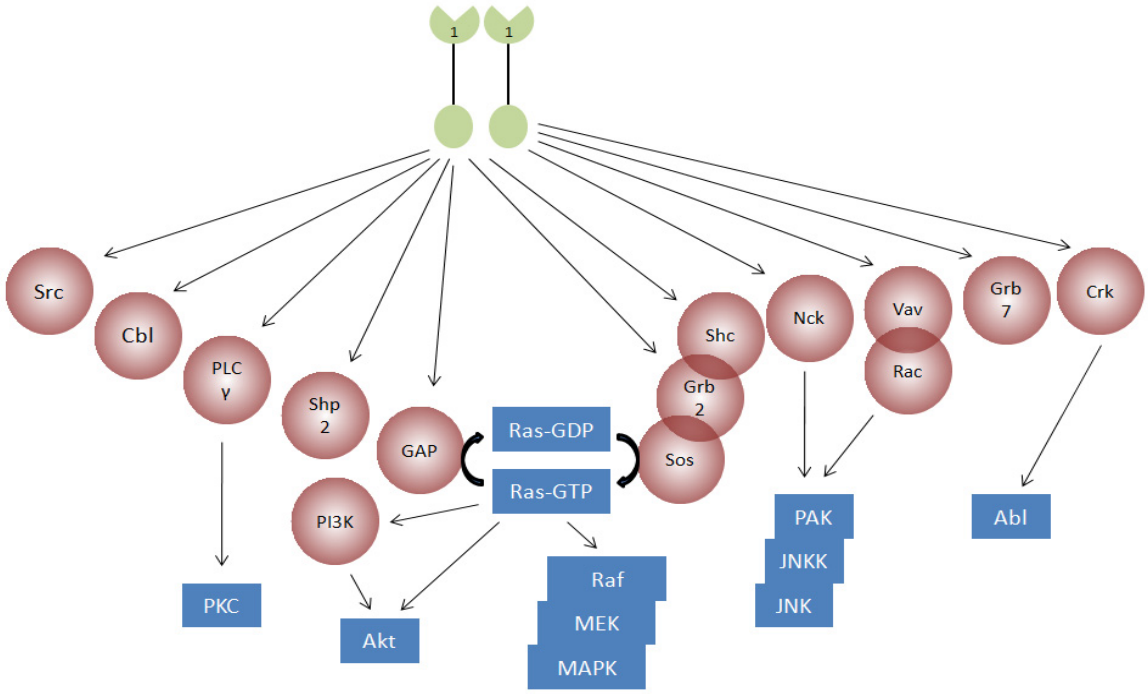

Figure 2-2: EGFR family of receptor signaling network. Homodimeric EGFRs (green) can generate over 10 different types of signals leading to the activation of five pathways (PKC, Akt, MAPK/Erk, JNK and Abl) regulating the expression of target genes (adapted from Yarden, 2001).

Following activation, EGFR signals (from homodimeric ErbB1 receptors) proceed in the intracellular compartment through several pathways such as Mitogen Associated Protein Kinase / Extracellular Regulated Kinase (MAPK/Erk), Protein Kinase C (PKC), Akt pathway and c-Jun

N-terminal kinase (JNK) as shown in Figure 2-2 (Oda, Matsuoka et al. 2005). The MAPK/Erk is the most ubiquitous of these systems and can be activated following EGF signaling in a Shc-dependent or independent manner, ultimately leading to the activation of Ras (Buday and Downward 1993; Batzer, Blaikie et al. 1995).

The first step in the signaling cascade is the recruitment of cytoplasmic adaptor proteins with Src Homology 2 (SH2), PhosphoTyrosine Binding (PTB) and Src Homology 3 (SH3) domains binding phosphotyrosine residues (Bertics and Gill 1985; Schlessinger 2000). These molecules can be recruited directly or indirectly following trans-phosphorylation of cytoplasmic tyrosine residues and the identity of these partners will dictate signal specificity (Schlessinger and Lemmon 2003; Pawson 2004). In the context of Erk, growth factor receptor-bound protein 2 (Grb2) is an adaptor protein with a SH2 domain that allows for binding to the phosphorylated EGFR. Grb2 also exhibits SH3 domains that recruit and activate Son of Sevenless (Sos) (Pawson 1995). Sos is a Guanine Exchange Factor (GEF) that allows the binding of Guanine Tri-Phosphate (GTP) to Ras and further activation (Hu and Bowtell 1996). Ras is a GTPase cycling between an inactive GDP-bound form and an active GTP-bound form (Vetter and Wittinghofer 2001). The catalytic activity of Ras is low and accelerated by GTPase Activating Protein (GAP) (Feig 1999). Ras-GTP binds the regulatory domain of Raf to activate a serine threonine kinase activity (Morrison and Cutler 1997). Hydrolysis of Ras-GTP in Ras-GDP liberates activated Raf that in turns phosphorylates and activates MAPK/Erk kinase (MAPKK or MEK). Activated MEK in turns activates and phosphorylates Erk1 and Erk2 which dimerize and are translocated towards the nucleus. Activated Erk phosphorylates and regulates several proteins and transcription factors, thereby controlling expression of target genes (Karin and Hunter 1995;

Morrison and Cutler 1997). These include proto-oncogenes such as *fos*, *jun* and *myc* as immediate-early genes (Cohen 1997; Kyriakis and Avruch 2001). Products of these genes contribute to the formation of Activator Protein 1 (AP-1, heterodimeric protein composed of fos and jun) which will ultimately act as a transcription factor and regulate the expression of late genes, thereby demonstrating the potential short and long-term metabolic effects of MAPK/Erk signaling (Hess, Angel et al. 2004).

While some receptors can activate several downstream pathways, they also present some specificity. The nature of homo or heterodimerization has significant effect on cellular responses as it has been demonstrated ErbB2 containing heterodimers are the most mitogenic (Pinkas-Kramarski, Soussan et al. 1996). Of relevance, the subcellular localization of complexes will dictate association with specific pools of adaptor proteins which contribute to the specificity of downstream signaling. For example, the Ras pathway can be activated by both surface and cytoplasmic EGFR while other adaptor molecules can be found exclusively at the membrane or cytoplasmic domains, thereby illustrating the importance of receptor trafficking on signaling (Burke, Schooler et al. 2001).

EGFR Trafficking

EGFR trafficking has been well characterized. Following EGF binding, dimerization and activation of EGFRs, dimerized receptors aggregate in clathrin coated pits through the adaptor protein adaptin (Haigler, McKanna et al. 1979; Sorkin and Carpenter 1993; Vieira, Lamaze et al. 1996; Wiley and Burke 2001). Receptor-mediated endocytosis proceeds rapidly (on the order of

five minutes) through invagination of the extracellular membrane and is dictated by motifs present on the cytoplasmic side of the receptor (Sorkin, Di Fiore et al. 1993). This process is saturable based on the availability of adaptor proteins (Wiley 1988; Lund, Opresko et al. 1990). Internalization acts as a regulator of ErbB functions as it allows for the control of receptor numbers on the cell surface and contributes to the downregulation of EGFR through lysosomal targeting. Early and late endosomal vesicles are characterized by an acidic pH and the presence of hydrolytic enzymes degrading receptor-ligand complexes. Sorting in early endosomes occurs between five and 20 minutes and is dependent upon the stability of association of homo/heterodimers at mildly acidic pH. Hence the nature of homo or heterodimers will affect sorting with ErbB1 being primarily targeted to the lysosomes (Waterman, Sabanai et al. 1998). It is now widely accepted that internalized receptors contribute to signaling (Burke, Schooler et al. 2001) and their activation state seems to dictate sorting choices, with dissociated complexes recycled towards the cell surface while activated complexes in the late endosomes (between 20 and 60 minutes post binding) will see the recruitment of c-Cbl ubiquitin ligase (Muthuswamy, Gilman et al. 1999). Signaling is stopped through ubiquitination of the receptor which initiates its degradation through targeting towards the lysosomal compartment in a time frame generally over one hour (Levkowitz, Waterman et al. 1998; Kirkin and Dikic 2007).

We have discussed numerous examples by which a soluble extracellular protein such as EGF can initiate various signals in the intracellular compartment through cascades of kinase for example. These signals will regulate the activated/repressed state of various transcription factors and genes, thereby allowing for metabolic responses following soluble signaling. In the context of EGFR, we will further discuss cell systems in which EGF directly affects cell fate.

2.2.4 **EGFR and Cell Fate**

Temple and coworkers were among the first to demonstrate a link between asymmetric EGFR partitioning and asymmetric fates in mouse neural stem cells (mNSCs) derived from the ventricular and subventricular forebrain (Sun, Goderie et al. 2005). EGFR was shown to be asymmetrically partitioned during mitosis in up to 25% of E13 cells from the mouse ventricular and subventricular zones. Dividing cells exhibited an asymmetric partitioning of EGF and Numb in 70% of cases which was indicative of different fates in the daughter cells. This was further confirmed as the daughter cell with high EGFR also exhibited radial glial/astrocytic markers which were absent in cells with low EGFR levels. Post-mitotic cells also demonstrated different proliferative potential based on BrdU analysis, consistent with prior reports of EGF as a potent mitogen in neural cells (Weiss, Reynolds et al. 1996)(Sun, Goderie et al. 2005). This analysis was the first to illustrate that the asymmetric nature of target signaling pathways at the time of division could allow for fate determination in the context of stem cells. Asymmetric partitioning of EGFR at the time of mitosis was also reported in normal human keratinocytes, squamous cell carcinoma A431 cells and primary basal cell carcinoma (Le Roy, Zuliani et al.). Because these divisions generate daughter cells with different fates, they are referred to as asymmetric cell divisions.

2.3 Symmetry of Cell Division

2.3.1 Lessons from Development

Concentration Gradients of Regulatory Factors

A single cell or cell population secreting a diffusing factor produces a concentration gradient in the extracellular compartment. Neighboring cell populations may be affected differently based on the distance from the emitting cell(s). Morphogens are important during embryonic development and allow for the creation of positional information in tissues (Wolpert 1989). Morphogens will be effective in a cellular context only if the pathway activated by the molecule exhibit different qualitative outcomes (Gurdon and Bourillot 2001). Among factors acting as morphogens, Activin, BMPs and Sonic Hedgehog (Shh) have been identified in *Xenopus* and vertebrates (Artavanis-Tsakonas, Rand et al. 1999; De Robertis, Larrain et al. 2000; Jessell 2000).

Lateral Inhibition

The cell-cell communication provides another mechanism of signal induction. The Notch signaling pathway is an example of this relay induction in which signaling from a cell to another operates through direct cell-cell contact. In the Notch system, one cell expresses the transmembrane receptor Notch on the surface while another expresses the surface ligand Delta (Wharton, Johansen et al. 1985). Following cell contact and ligand-receptor binding, the complex is cleaved and the extracellular portion of Notch remains bound with the ligand on the ligand-expressing cell while the Notch intracellular domain is internalized in the receptor-expressing cell and further regulates gene expression (Brou, Logeat et al. 2000; Nichols, Miyamoto et al. 2007). If Notch is predominant in a cell, it will activate its own synthesis in a positive feedback

loop and repress the synthesis of Delta. This contributes to the amplification of potential initial differences in Notch (N) and Delta (Dl) expression levels in two neighboring cells and produces one cell with high levels of Notch expression and one cell with high levels of Delta expression. This mechanism is called lateral inhibition and has numerous implications during development. Because two cells in contact are triggered to behave differently, this contributes to the creation of cellular frontiers or the isolation of a single-cell around a cell population as illustrated in Figure 2-3 (Artavanis-Tsakonas, Rand et al. 1999).

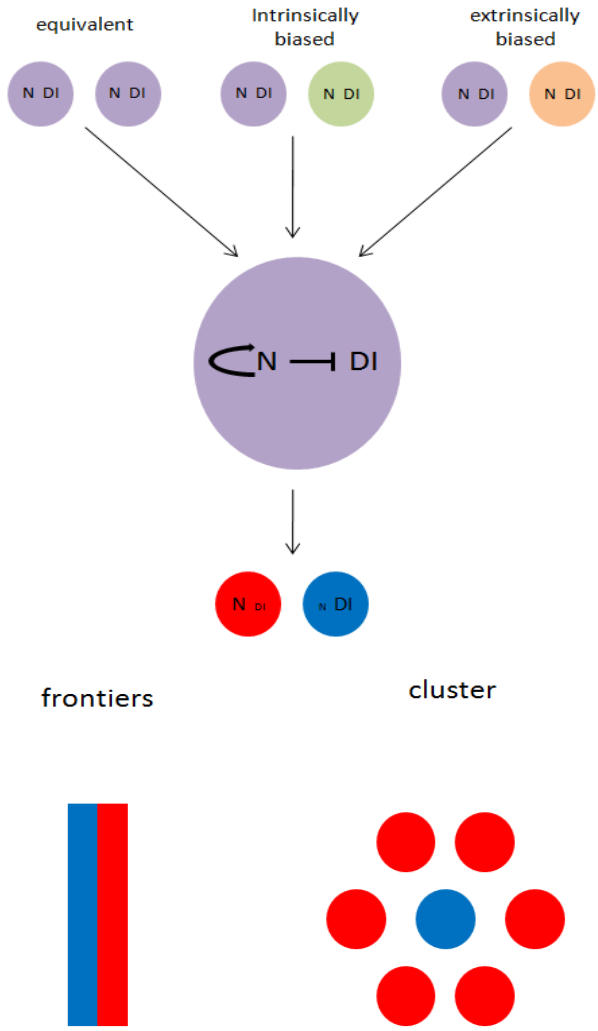

Figure 2-3: Mechanism of lateral inhibition. Notch signaling is used to amplify differences between levels of expression of Notch (N) and ligand delta (Dl) in adjacent cells. This contributes to the creation of cellular frontiers or cell cluster (adapted from Artavanis-Tsanokas *et al.*, 1999).

Planar Cell Polarity

In *Drosophila*, the receptor Frizzled has been implicated in the polarization of fields of cells leading to planar cell polarity (PCP) through the non-canonical Wnt pathway (Adler 1992). PCP mechanism can be defined as the polarization of a cell population consistent with the body plan. This leads to a common cell orientation or motility and is achieved through the polarization of members of the frizzled-PCP pathway along the apical-basal axis (Wu, Klein et al. 2004; Seifert and Mlodzik 2007).

The first complex is composed of frizzled (Fz), Dishevelled (Dsh) and Diego (Dgo) in *Drosophila* (Klingensmith, Nusse et al. 1994; Feiguin, Hannus et al. 2001). Fz recruits Dsh and Dgo to the cell membrane (Wu, Klein et al. 2004; Jenny, Reynolds-Kenneally et al. 2005); the complex promotes the activation of the signaling pathway through the appropriate set of downstream effectors. An antagonist complex composed of Strabismus (Stbm) and Prickle (Pk) (Taylor, Abramova et al. 1998; Jenny, Darken et al. 2003) is accumulating on the opposite cell side (Tree, Shulman et al. 2002). The two complexes interact, as Pk has been reported to interact with Dsh and thus prevent its recruitment on the cell surface with Fz. This also explains why this complex acts as an antagonist *in vivo*. Dgo can compete with Pk to bind Dsh and therefore antagonizes the action of Pk. A polarization is thus created in the cellular compartment based on the partitioning of the pathway components. These analyses of subcellular localization have been extended to vertebrates (Montcouquiol, Sans et al. 2006).

This example highlights the importance of cell and population polarization during development. Most importantly, we have seen that the polarization of a signaling pathway itself at the single-cell level is necessary to achieve complex developmental processes. This aspect of

polarization and asymmetry is not only restricted to PCP but is also important in the context of cell fate determination.

2.3.2 Concepts

An asymmetric division gives rise to two daughter cells with different fates. In the context of stem cells, one cell may fully retain stem cell properties while the other becomes committed to a specific lineage. Conversely, symmetric divisions give rise to two identical daughter cells whose characteristic can be identical or not to the parent cell. An asymmetric division can be generated in a great variety of ways that will be discussed conceptually.

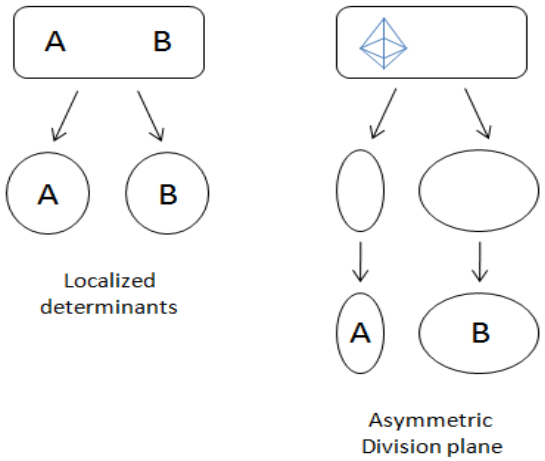

Figure 2-4: Examples of intrinsic asymmetric division. On the left side, daughter cells inherit different pool of intracellular molecules responsible for fates A and B. On the right side, the division plane at the time of mitosis is not centered, generated daughter cells with different volumes and ultimately different fates (adapted from Horvitz and Herskowitz 1992).

As pictured in Figure 2-4, molecules localized in specific regions of the cytoplasm can be asymmetrically partitioned between the two daughter cells, resulting in different cell fates (e.g. fates A and B). These molecules can be proteins, metabolites, mRNA or transcription factors

resulting in different genes activation and repression profiles in the daughter cells. One could also imagine a different epigenetic profile during chromosomal partitioning (Kim-Ha, Smith et al. 1991; Horvitz and Herskowitz 1992). Once partitioned between the daughter cells, these molecules are responsible for different fates and will be referred to as Cell Fate Determinants (CFD) (Cohen and Hyman 1994). In a second mechanism, the asymmetric localization of the mitotic spindle triggers the formation of two cells with different sizes. In conjunction with the appropriate cellular context, this could result in the acquisition of different fates. In both cases, the mechanism of asymmetric division can be referred to as intrinsic, meaning that the asymmetry is acquired during cell division. These two mechanisms are not exclusive and one could imagine a combination of the two to trigger an asymmetric division (Horvitz and Herskowitz 1992). Nevertheless, the daughter cells do not need to be different right after division in order to exhibit different fates in the long term.

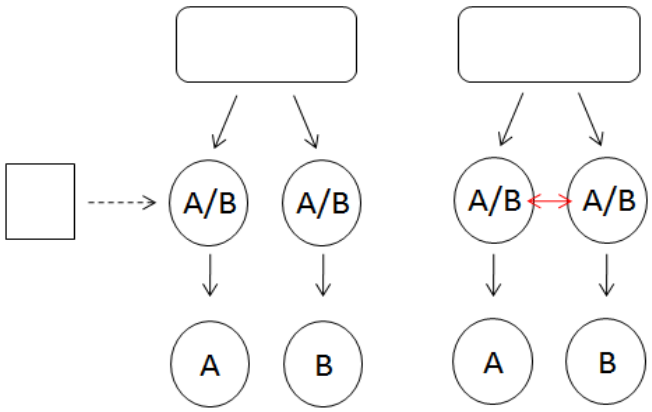

Figure 2-5: Examples of extrinsic asymmetric division. On the left side, identical daughter cells following mitosis will be subject to different environmental signals thereby inducing different fates. On the right side, identical daughter cells following division (adapted from Horvitz and Herskowitz 1992)

In Figure 2-5, the two daughter cells can follow either fate A or B after division. In the first case, signals coming from the microenvironment direct a daughter cell towards a given fate. This mechanism can be defined as passive, and the proximity or distance from the source of a signal (concentration gradient) determines which fate to express. In the second or active case, the two cells exchange signals to prevent them from entering the identical lineage restriction (Horvitz and Herskowitz 1992). We will focus on the intrinsic asymmetric division in the next section and will review mechanisms of regulation and illustrate two important requirements: first, the mother cell must be polarized; second, the mitotic spindle must be aligned with the axis of polarity to produce two daughter cells with a difference in CFD content.

2.3.3 Regulation of Asymmetric Cell Division and Cell Fate

In the intrinsic mechanism, a polarity axis is defined in the parent cell right before division and leads to the asymmetric repartitioning of polarity components. In this case, asymmetry is guided by either apical-basal or planar polarity of the surrounding cells (Knoblich 2008). Polarity complexes have two distinct roles *in vivo*: they polarize the cell domain into several distinct compartments (e.g. apical, lateral, basal) but they also direct the subsequent localization of CFDs. Because the spindle orientation is correlated *in vivo* with the polarity axis, daughter cells inherit a different CFD content after division and are thus committed to different fates, as shown in Figure 2-6.

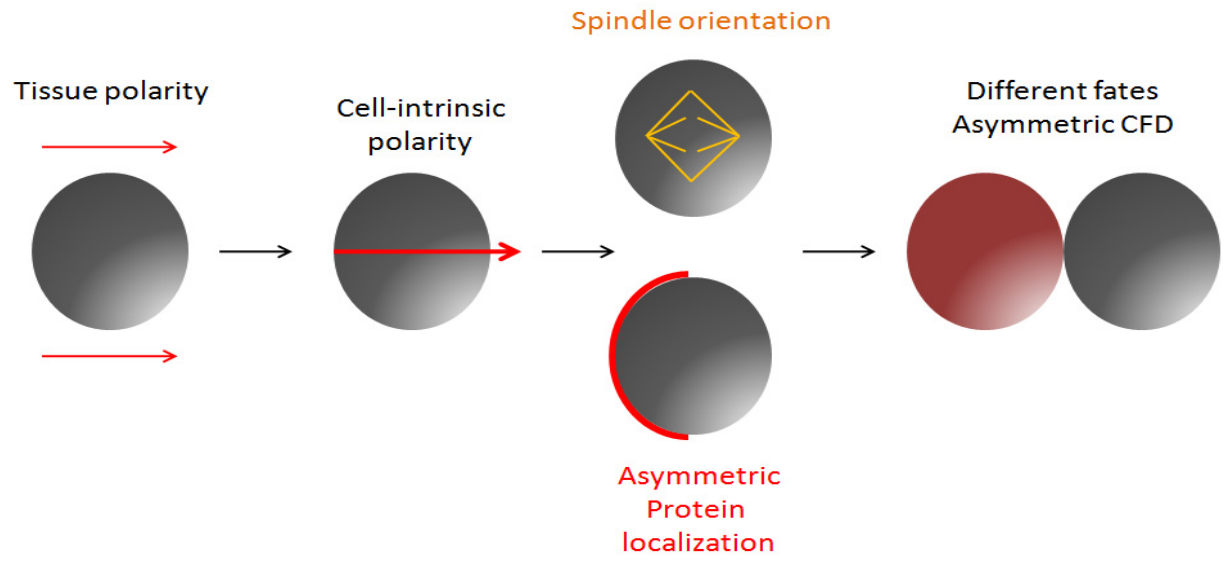

Figure 2-6: Mechanism of intrinsic asymmetric cell division as observed during embryological development (adapted from Knoblich 2008)

The *Drosophila* neuroepithelium in the central nervous system (CNS) is an example of an intrinsic pathway where Partitioning defective (Par) proteins are required for the CFDs distribution in the daughter cells. This epithelium is composed of neuroblasts (NBs) that delaminate in the embryo ventral neurogenic region. The NBs divide asymmetrically along the apical-basal axis to produce a large apical NB and a smaller basal precursor called ganglion mother cell (GMC). These GMCs will produce neurons and glia of the CNS after another round of asymmetric division (Wodarz and Huttner 2003). In this scenario, the apical-basal polarity of the epithelium is used to asymmetrically partition polarization components.

The apical cell cortex is the site of localization of several polarity complexes, including the Par complex: Par-3, Par-6 and atypical protein kinase C (aPKC) (Wodarz, Ramrath et al. 2000; Ohno 2001; Petronczki and Knoblich 2001). Following entry into mitosis, two kinases are

activated; Aurora-A is implicated in centrosome maturation and spindle formation, and Polo controls the spindle checkpoint and cytokinesis (Knoblich 2008). The correlation between the polarity axis and mitotic spindle orientation is achieved through the protein Inscuteable (Kraut, Chia et al. 1996). Inscuteable is apically localized and can bind Partner of Inscuteable (Pins) and Par-3, thereby linking the Par complex with a second apically localized protein complex composed of Pins and the α subunit of heterotrimeric G proteins $G_{\alpha i}$ (Wodarz and Huttner 2003; Betschinger and Knoblich 2004; Goldstein and Macara 2007). Par-3 binding to Inscuteable triggers the recruitment of Pins in the Par-3 / Inscuteable complex. Binding of $G_{\alpha i}$ to Pins (Nipper, Siller et al. 2007) induces a conformational change that allows for the recruitment of Mud into the cortical complex. Mud in turn recruits astral microtubules to the cell cortex and thus provides a mechanism by which cortex polarization and spindle poles orientation are correlated *in vivo* (Izumi, Ohta et al. 2006). In this case, the polarity axis intrinsically defined in interphase based on the partitioning of Par and aPKC proteins is consistent with the apical-basal polarity of the epithelium. The protein Lethal Giant Larvae (Lgl) is initially apically localized through a protein-protein interaction with Par-6 and is phosphorylated by aPKC (Betschinger, Mechtler et al. 2003). Following phosphorylation, Lgl is dissociated from the complex and becomes restricted to the opposite cell cortex. The differential localization of these complexes along the apical-basal axis creates a polarity axis inside the cell that can in turn be used to direct the localization of CFDs on the basal cortex. These include Numb, an endocytic protein acting as an inhibitor of Notch signaling (Frise, Knoblich et al. 1996) and Prospero, a homeodomain protein (Chu-Lagraff, Wright et al. 1991). Due to their asymmetric localization they asymmetrically partition during division in the GMC where Numb inhibits Notch signaling. Prospero regulates transcription of target genes and Brat function is unknown (Knoblich 2008).

The segregation of these components is mediated by two adaptor proteins Miranda and Partner of Numb (Pon) (Betschinger and Knoblich 2004). All the proteins involved in this mechanism have homologues in mammals: mPar-3 (Izaki, Kamakura et al. 2005), mPar-6 (Noda, Takeya et al. 2001), aPKC, Lgl with Hugl-1 (Grifoni, Garoia et al. 2004), Prospero with Prox-1 and Numb (Dho, French et al. 1999) and their potential role in the regulation of mammalian fate is under investigation.

Several studies have documented the interplay between asymmetric cell division and signaling. One of the most documented examples is the negative regulation of Notch by Numb in *Drosophila*. After an asymmetric cell division, the cell that receives high levels of Numb downregulates Notch signaling; the cell with low Numb levels maintain it (Frise, Knoblich et al. 1996). A relationship between Notch as a regulator of Numb has also been reported (Chapman, Liu et al. 2006). The extrinsic mechanism of asymmetric cell division is an example of how local microenvironments modulate cell fate.

2.4 Signaling Modulation by Local Microenvironments

In general, cellular growth, differentiation, migration, apoptosis and other specific cellular functions are externally regulated by the interplay of soluble factors, insoluble ECM and cell-cell interactions (Bottaro, Liebmann-Vinson et al. 2002). These factors are spatially and temporally coordinated to regulate the dynamic state of a tissue (Lutolf and Hubbell 2005). Soluble factors such as cytokines, growth factors, peptides, steroids and ions feed into complex, and often overlapping signal transduction pathways that may share common receptors and are therefore required in the appropriate combination and concentrations to be effective (Bottaro,

Liebmann-Vinson et al. 2002). A wide range of intracellular signaling pathways are activated or altered by these external factors, including those responsible for cytoskeletal turnover, cell motility, cell cycle and mitosis, and apoptosis (Howe, Aplin et al. 1998). This highlights the modulatory effects of local microenvironments.

In vitro culture thus appears as a very incomplete approach to the analysis of biological systems. Cells cultivated adherently in culture flasks grown in media containing various factors will lack important environmental cues to reproduce accurately physiological conditions and efforts have been made to improve the biological relevance of culture techniques. In this section, some of the methods developed for the control of soluble factor delivery and generation of soluble factor gradients are presented. In the context of this project, the selected method should allow for the targeting of single cells, fluorescence microscopy and should also be readily available.

Recent advances in the field of microfluidics have provided the scientific community with numerous approaches to generate radial or linear gradients of soluble factors *in vitro* (Dertinger, Jiang et al. 2002; Li Jeon, Baskaran et al. 2002; Fosser and Nuzzo 2003; Burdick, Khademhosseini et al. 2004; Chung, Flanagan et al. 2005; Gunawan, Choban et al. 2005; Lin, Nguyen et al. 2005; Abhyankar, Lokuta et al. 2006; Gunawan, Silvestre et al. 2006). Zigmond and Dunn chambers were also developed to study migratory effects under concentrations gradients (Zigmond 1977; Zicha, Dunn et al. 1997). New biomaterials allowed for the controlled release of factors from biological hydrogel carriers (Foxman, Campbell et al. 1997; Chen, He et al. 1998) or polymer scaffolds allowing dual factor delivery (Richardson *et al*., 2001).

Interestingly, all these methods mostly apply to cell populations, but some techniques have been developed that can be used to work at a single-cell level. Of particular relevance is the use of micropipettes (Zhelev, Alteraifi et al. 1996; Servant, Weiner et al. 1999; Servant, Weiner et al. 2000; Dehghani Zadeh, Seveau et al. 2003; Zadeh and Keller 2003; Zhelev, Alteraifi et al. 2004; Wong, Pertz et al. 2006). For example, delivery of chemoattractant in a single-cell microenvironment was performed to study the directional sensing in the eukaryotic mold *Dictyostelium discoideum*. The release of factor was controlled using a positive pressure in the micropipette and the authors showed that a constant gradient was created consistent with the formation of pseudopods (Zhelev, Alteraifi et al. 2004). Micropipettes can be implemented on a microscope and controlled release can be followed using fluorescence imaging. Using the proper stage, the positioning can be controlled with a submicrometer accuracy thus enabling accurate targeting of single cells. Micropipettes were therefore selected as the delivery system for this project.

3 Chapter 3: Two-dimensional Finite-Element Modeling of Controlled EGF Release to a Single Cell

3.1 Summary

In the context of engineering bioprocesses for the manufacture of cells for regenerative medicine, stem cells and progenitors can divide symmetrically or asymmetrically. Directing asymmetric division decisions during cell expansion in culture could allow for the commitment of stem/progenitor cells to a specific lineage while maintaining the stem/progenitor pool for ongoing cell expansion. Engineering asymmetric divisions using insights gained from *in vivo* systems also represents a paradigm for the development of biomimetic culture techniques. *In vivo*, local microenvironments induce complex developmental processes through different modes of extrinsic signaling (i.e. soluble factors, cell-cell interactions and cell extracellular matrix interactions). *In vitro*, the creation of local gradients of soluble factors alone might recreate environmental cues that could be interpreted at the single cell level as tissue-induced polarity signals to guide asymmetric cell division.

Herein, the primary objective is to engineer a system for the generation of asymmetric microenvironments of soluble factors *in vitro*. Controlled release from a micropipette positioned near an individual cell in culture media is simulated to analyze soluble factor gradients in the cell's microenvironment. This configuration establishes an asymmetry of receptor binding on the cell surface that we will refer to as induced cell polarization. Evaluation of the potential for directed polarization *in vitro* requires the development of quantitative metrics to examine system parameter sensitivity and more importantly allows for the formulation and evaluation of process strategies. Ligand receptor complexes involved in the binding, internalization and signaling of a

growth factor will be used to produce a partial differential equation (PDE) based model of polarization. The epidermal growth factor (EGF) and EGF receptor (EGFR), a member of the tyrosine kinase family of receptors, have been studied extensively. The EGFR is involved in a variety of stages in embryonic/post-natal and tumorigenic development (Sibilia, Steinbach et al. 1998; Kim and Muller 1999). Affected cell processes include proliferation, growth inhibition, differentiation and apoptosis (Darcy, Wohlhueter et al. 1999). The wealth of kinetic data available from a variety of sources along with its involvement in the regulation of fate determination in several cell types (Le Roy, Zuliani et al. ; Sun, Goderie et al. 2005) makes this factor a reasonable choice to develop and test the robustness of our proposed computational methodology. In this chapter, finite-element modeling is used to develop a two-dimensional simulation in which continuous diffusive transport from a point source (micropipette) delivers EGF onto a cell surface at which a model for EGF binding and trafficking is defined (i.e. reactive boundary conditions). Several metrics such as the Polarization Index (PI) and Percentage of Receptor Occupancy (PO) will be developed to evaluate system response with respect to various experimental geometries (micropipette and cell diameter, micropipette distance from the cell surface) but also to identify important kinetic parameters. The analysis of these metrics along with the concentration and velocity of formation of key members of the signaling pathway will be performed to evaluate two delivery strategies in the context of controlled EGF release in the direct cell vicinity.

3.2 Model Formulation

3.2.1 **Mass Transfer Modeling**

The first relationship that should be presented is Fick's first law of diffusion:

$$J_i = -CD\frac{\partial x_i}{\partial z} \tag{1}$$

J_i is the flux of i in the z direction (mole/length^2.time), D is the diffusion coefficient (length^2/time), xi is the mole fraction, C is the molar concentration (mole/length^3). The molar concentration of i can be defined as (mole/unit volume). This equation states that the molar flux of component i per unit of cross-sectional area perpendicular to the direction of the flux is proportional to the diffusion coefficient. The negative sign indicates that the diffusion occurs in the direction of decreasing concentration; that is to say from a highly concentrated region to one of low concentration.

The molar concentration C is the sum of the molar concentrations of all components of the mixture:

$$C = \sum_{i=1}^{n} Ci \tag{2}$$

with the molar fraction $Xi = \frac{Ci}{C}$

To describe the different flux relationships, the reference must be accurately defined. It can be a fixed reference frame and the molar flux of I can be expressed as

$$Ni = CiUi \tag{3}$$

N_i is the molar flux of i (moles/length^2.time) and U_i is the velocity of i with respect to a fixed reference frame (length/time). The total flux of i can also be written with respect to some reference other than a fixed set of coordinates:

$$ {}_0Ji = Ci\left(Ui - U^0\right) \tag{4} $$

${}_0J_i$ is the molar flux with respect to the reference velocity U^0, chosen so that:

$$ U^0 = \sum_{i=1}^{n} \chi i Ui \tag{5} $$

and $\sum_{i=1}^{n} \chi i = 1$

χi is the weighting factor relating the contribution of each species to the reference velocity. The most widely used velocities are the molar and volume average velocity:

$$ U^M \sum_{i=1}^{n} Ci = \sum_{i=1}^{n} CiUi \tag{6} $$

Or

$$ U^M = \frac{\sum_{i=1}^{n} CiUi}{\sum_{i=1}^{n} Ci} = \frac{\sum_{i=1}^{n} CiUi}{C} \tag{7} $$

The molar flux with respect to the mass average velocity can be obtained:

$$ {}_M Ji = Ci\left(Ui - U^M\right) \tag{8} $$

These flux expressions can be combined to describe a particular physical system. Using equation (4):

$$ {}_M Ji = CiUi - CiU^M \tag{9} $$

$$ Ni =_m Ji + CiU^M = -CDi\nabla xi + CiU^M \tag{10} $$

The total molar flux of i relative to a fixed reference frame is equal to the molar flux of i (due to diffusion relative to the molar average velocity) plus the bulk flow of i with respect to a fixed reference frame. Using the definition of the molar average velocity:

$$ Ni =_m Ji + \frac{Ci}{C}\sum_{i=1}^{n} CiUi =_m Ji + xi\sum_{i=1}^{n} Ni \tag{11} $$

For mixtures in which x_i is very small, the bulk flow term can be neglected.

3.2.2 **Microscopic Mass Balance**

We consider a differential volume element of fixed shape and account for the flow entering and leaving the element (Eulerian approach):

$$(N_{AX}\big|_X - N_{AX}\big|_{X+\Delta X})\Delta Y\Delta Z + (N_{AY}\big|_Y - N_{AY}\big|_{Y+\Delta Y})\Delta X\Delta Z + (N_{AZ}\big|_Z - N_{AZ}\big|_{Z+\Delta Z})\Delta X\Delta Y + r_A^v \Delta X\Delta Y\Delta Z = \Delta X\Delta Y\Delta Z \frac{\partial C_A}{\partial t} \quad (12)$$

$(N_{AX}\big|_X - N_{AX}\big|_{X+\Delta X})$ is the mole flux term (mole/area.time), $\Delta Y\Delta Z$ the surface, $(N_{AX}\big|_X - N_{AX}\big|_{X+\Delta X})\Delta Y\Delta Z$ represents the rate of transfer through the considered area along the considered axis, Ca is the mole concentration (mole/volume) r_A^v is the reaction term representing generation minus consumption (or rate of volumetric production in mole/volume.time). If the equation is divided by $\Delta X\Delta Y\Delta Z$ as the limit of the volume of the element goes to 0:

$$\frac{\partial C_A}{\partial t} + \frac{\partial N_{AX}}{\partial X} + \frac{\partial N_{AY}}{\partial Y} + \frac{\partial N_{AZ}}{\partial Z} = r_A^v \quad (13)$$

Or in vector notation:

$$\frac{\partial C_A}{\partial t} + \nabla \bullet N_A - r_A^v = 0 \quad (14)$$

Using equation (4):

$$\frac{\partial C_A}{\partial t} + \nabla \bullet C_A U_A - r_A^v = 0 \quad (15)$$

The flux can then be expressed with reference to an arbitrary reference velocity:

$${}_0J_A = C_A(U_A - U_0) \quad (16)$$

$$C_A U_A = {}_0J_A + C_A U^0 \quad (17)$$

Then the generalized conservation equation can be written:

$$\frac{\partial C_A}{\partial t} + \nabla \bullet_0 J_A + \nabla \bullet (C_A U^0) - r_A^v = 0 \tag{18}$$

$\nabla \bullet_0 J_A$ is the diffusive flux and $\nabla \bullet (C_A U^0)$ is the convective flux (from Hines and Maddox, 1985).

3.3 Finite-Element Modeling

3.3.1 Two-Dimensional Geometry

A two-dimensional mathematical model was developed using a finite-element modeling software (COMSOL 3.4, Burlington, MA) with MATLAB (Mathworks, USA) as shown in Figure 3-1 below. In the following example, a culture chamber was modeled as a square with 50 μm sides and the cell was a circle of 10 μm diameter. The delivery system was depicted as a tube with an inner diameter of 2.5 μm and a wall thickness of 0.25 μm (dimensions consistent with readily manufactured micropipettes). These types of design have previously been used to asymmetrically deliver chemoattractant molecules to human neutrophils (Zhelev, Alteraifi et al. 1996; Zhelev, Alteraifi et al. 2004). The initial distance between the micropipette and the cell surface was set to 5 μm.

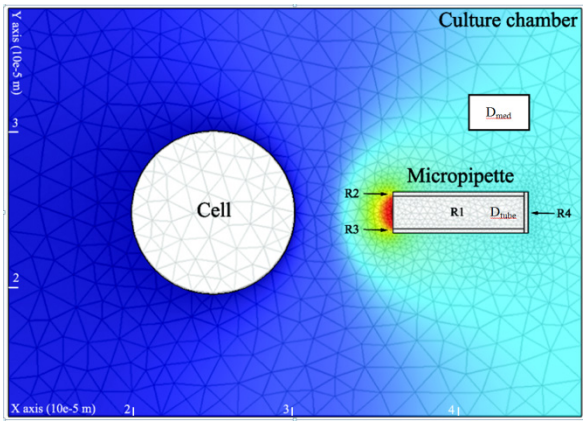

Figure 3-1: Typical two-dimensional model consisting of 21 boundaries and 6 subdomains. Because the cell division plane is considered perpendicular to the pipette axis, the front side refers to the half cell surface facing the pipette. R1 to R4 refer to the four rectangles used to design the micropipette.

Initial concentration of EGF is L_0 = 100 ng/mL inside the micropipette (R1) and movement of EGF in the pipette and in the media is diffusive only:

$$\frac{\partial \mathrm{L}}{\partial \mathrm{t}} + \nabla \cdot (-D\nabla L) = 0 \tag{19}$$

L is EGF concentration (mol/m^3), $\frac{\partial \mathrm{L}}{\partial \mathrm{t}}$ the concentration variation over time, and $\nabla \cdot (-D\nabla L)$ the diffusive flux (assumed uniform) in the x and y direction. This equation directly results from equation (18) without convective flux and in the absence of any chemical reaction in the media. The equation used in COMSOL is:

$$\frac{\partial \mathrm{L}}{\partial \mathrm{t}} + \nabla \cdot (-D\nabla L) = RT - u \cdot \nabla L \tag{20}$$

in which both the reaction term R and the convective term $u \cdot \nabla L$ are set to 0. Initial conditions for the diffusion coefficient will be discussed further as diffusion in the micropipette (D_{tube}) and in the culture media (D_{med}) will be considered as variables to evaluate potential delivery strategies.

3.3.2 EGF Binding and Trafficking

On the cell surface, boundaries are defined with the following inward flux of EGF:

$$N_0 = -k_f RL + k_r C \tag{21}$$

Equation (21) represents the binding of diffusing EGF from the media on the cell surface and also the release of EGF from complexes (C) returning to the state of free receptors (R). The kinetic model of EGF binding has been widely described and is presented below in Figure 3-2.

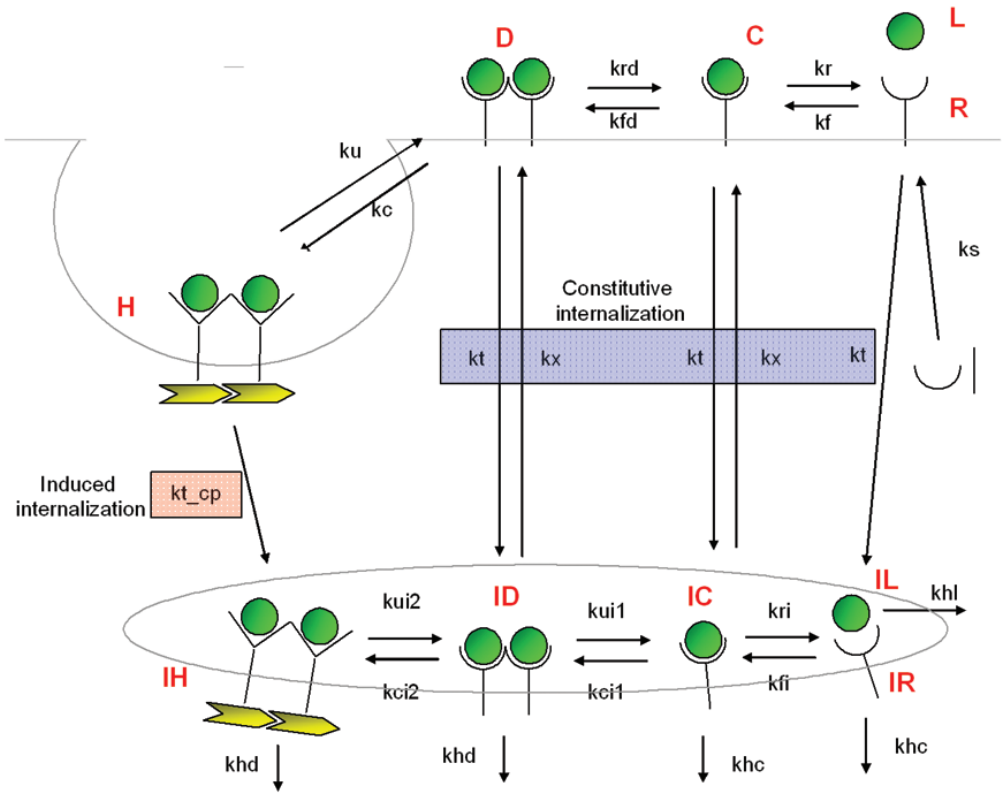

Figure 3-2: EGF binding and trafficking model. The EGFR (R) is synthesized from the Golgi (ks). Shortly after binding of EGF (L) to EGFR (kf), the complex (C) dimerises (kfd). Dimers (D) are the first potential signal transducers as dimerization is transduced into a conformational change activating the receptor. Dimers can either be internalized through a constitutive pathway (kt), non specific and non saturable (smooth pits) or through an induced pathway (kt_cp in the coated-pits). Free receptors R, complexes C and dimerized complexes D can be internalized in the endosomes (IR, IC and ID respectively with the same internalization rate kt dictated by membrane turnover). In the induced pathway, receptors reversibly gather in coated pits (H with a forward rate kc) where they are bound together through adaptor proteins. Except for the dimers coming from the coated pits (IH), IC and ID can be recycled to the cell surface (kx). All internalized members of the system can be either degraded and processed towards the lysosomes (khd and khc) or recycled to the cell surface (kx).

Following EGF binding, the newly formed complexes (*C*) rapidly dimerize (*D*). The dimerization step triggers a conformational change in the receptor structure, initiating the activation of a cytoplasmic tyrosine kinase which initiates the signal transduction cascade (Bertics and Gill 1985). Dimerized receptor-ligand complexes *D* can be internalized through a constitutive pathway (k_t), non-specific non-saturable and dictated by membrane turnover. As internalized vesicles are smooth (uncoated), it is commonly said that these dimerized receptor-ligand complexes are in the smooth pits (*D*). Membrane turnover overall allows for the non-specific internalization of *R*, *C* and *D* (*IR*, *IC* and *ID* respectively with the same internalization rate k_t).

In the induced pathway, dimerized ligand-receptor complexes *D* reversibly gather in coated pits (*H* with a forward rate k_c) in which they are bound through adaptor proteins (Mayo, Nunez et al. 1989) directly associated with the clathrin coat (Pearse and Robinson 1990). This internalization pathway is saturable depending on the amount of adaptor proteins available and non-reversible (k_{t_cp}) (van Deurs, Petersen et al. 1989) as modeled by Starbuck and Lauffenburger (Starbuck and Lauffenburger 1992). As adaptor proteins were not considered in this study, constitutive and induced internalization can be referred to as quasi first-order processes.

In the endosomal compartment, kinetic parameters differ from those on the cell surface due to the acidic environment. k_{ui2} and k_{ci2} are set equal to k_u and k_c respectively, as it is proposed that the acidic environment of the endosomes does not affect the association / dissociation constant of the cytoplasmic adaptor proteins. After internalization, *IH*, *ID*, *IC* and *IR* can be either degraded and processed towards the lysosomes (k_{hd} / k_{hc}) or recycled towards the cell surface. The internalized ligand can also be degraded (k_{hl}) but cannot be recycled to the cell

surface, as EGF is known to remain predominantly bound to EGFR in the endosomes. Various values of endosomal volume have been used in the literature, ranging from the volume of a 100 nm diameter sphere (Schoeberl, Eichler-Jonsson et al. 2002) to the approximate volume of a 30 μm diameter cell (Starbuck and Lauffenburger 1992). In the following simulations, we assumed the volume of the endosomal compartment identical to the cell volume, hence allowing for the definition of internalized members of the pathway on the cell surface. The reaction terms were defined as nine coupled, non-linear PDEs and the weak formulation was used to couple the reaction terms with surface diffusion of each member of the pathway on the cell surface as shown in Table 1:

Component	PDE	
R	$\frac{\partial R}{\partial t} = \nabla \cdot D_R \nabla R + k_s - k_t R - k_f RL + k_r C$	(22)
C	$\frac{\partial C}{\partial t} = \nabla \cdot D_C \nabla C + k_f RL - k_r C - k_t C - k_{fd} \times C \times C + k_x IC + k_{rd} D$	(23)
D	$\frac{\partial D}{\partial t} = \nabla \cdot D_D \nabla D + k_{fd} \times C \times C - k_t D + k_x ID - k_c D + k_u H - k_{rd} D$	(24)
IC	$\frac{\partial IC}{\partial t} = k_t C - k_x IC - k_{hc} IC - k_{ri} IC + k_{fi} IR.IL - k_{ci1} \times IC \times IC + k_{ui1} ID$	(25)
ID	$\frac{\partial ID}{\partial t} = k_t D - k_x ID - k_{hd} ID + k_{ci1} \times IC \times IC - k_{ui1} ID + k_{ui2} IH - k_{ci2} ID$	(26)
H	$\frac{\partial H}{\partial t} = k_c D - k_u H - k_{t\_cp} H$	(27)
IH	$\frac{\partial IH}{\partial t} = k_{t\_cp} H - k_{hd} IH - k_{ui2} IH + k_{ci2} ID$	(28)
IR	$\frac{\partial IR}{\partial t} = k_{ri} IC - k_{fi} IR.IL - k_{hc} IR$	(29)
IL	$\frac{\partial IL}{\partial t} = k_{ri} IC - k_{fi} IR.IL - k_{hl} IL$	(30)

Table 1: System of equations for the computation of surface concentrations in COMSOL.

The surface diffusion for *R*, *C* and *D* was set to $1x10^{-9}$ m^2/sec and $1x10^{-10}$ m^2/sec respectively (Kusumi, Sako et al. 1993; Shvartsman, Wiley et al. 2001) and no surface diffusion was defined for internalized members of the system. Because no cytoplasmic domain was defined in COMSOL, endosomal trafficking was not considered and internalized members were

assumed immobile. The parameters are estimates from the literature and are presented in Table 2:

constant	Litterature value	Unit	Model Value	Unit	Cell type	Reference
kf	1.06E-03	1/nM.s	1.06E+03	m^3/mole.s	B82	1
kr	0.16	1/min	2.67E-03	1/s	B82	1
ks	130	molecule/cell.min	9.17E-09	m^3/mole.s	B82	1,2
kt	5.00E-04	1/s	5.00E-04	1/s	B82	1,2
kfd	0.01	1/nM.s	10000	m^3/mole.s	HMEC / Hep	3,4
krd	0.1	1/s	0.1	1/s	HMEC / Hep	3,4
kx	5.80E-02	1/min	9.67E-04	1/s	B82	1,2
ku	0.1	1/min	1.67E-03	1/s	B82	2
kc	2.00E-05	1/min	3.33E-07	1/s	B82	2
kt_cp	1	1/min	1.67E-02	1/s	B82	2
kui1	0.413	1/s	0.413	1/s	HMEC	3
kci1	1.35E-03	1/nM.s	1.35E+03	m^3/mole.s	HMEC	3
kui2	see ku		1.67E-03	1/s	B82	2
kci2	see kc		3.33E-07	1/s	B82	2
khr	2.20E-03	1/min	3.67E-05	1/s	B82	2
khl	1.00E-02	1/min	1.67E-04	1/s	B82	2
kfi	8.46E-03	1/nM.min	1.41E+03	m^3/mole.s	B82	1
kri	0.66	1/min	0.011	1/s	B82	1
Rinit	118576	receptor/cell	6.27E-15	mole/m	B82	1
IRinit	59091	receptor/cell	3.12E-15	mole/m	B82	1

Table 2: Literature constants. 1. Tzafriri AR, Edelman ER. 2006. 2. C. Starbuck, D.A. Lauffenburger. 1992. 3. Resat H, Ewald JA, Dixon DA, Wiley SH. 2003. 4. Kholodenko BN, Demin OV, Moehren G, Hoek JB. 1999.

3.4 Results

3.4.1 **Model Validation**

The accuracy and stability of computations were evaluated based on model convergence with progressive finite-element mesh refinement. All simulations were performed on an Intel Core-i7 3.07 GHz processor with 12 gigabytes of RAM using the time dependent solver. Initial computations were performed over a time scale of 1200 seconds and a time step of one second. The chosen solver uses a time stepping algorithm with an absolute and relative tolerance (A_{tol} and R_{tol}). The error vector *(e)* is calculated such that the following equation is satisfied before the solver proceeds to the next iteration:

$$|e(i)| \leq Rtol \times |y(i)| + Atol(y(i)) \tag{31}$$

e is the error vector, *y* the vector of dependent variables and *i* is the iteration step. R_{tol} should be set at least one order of magnitude lower than the expected deviation. The convergence and accuracy of computations were studied by comparing different R_{tol} values and different mesh refinements using fixed A_{tol}. The basic mesh of the two-dimensional system consisted of 4503 degrees of freedom (d_f); three successive global refinements were performed using the mesh refine function in COMSOL with 16759, 64527 and 253087 df respectively. Model deviation decreased between refinements, with similar improvements at 30 and 60 seconds, as shown in Figure 3-3.

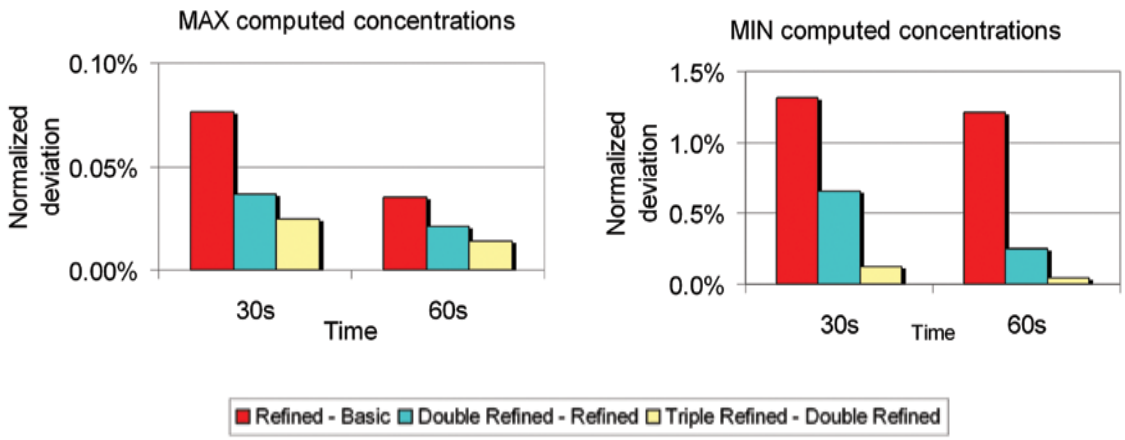

Figure 3-3: Convergence and accuracy of computations. Model deviation was measured at different mesh refinements for the highest and lowest computed surface concentrations (receptor-ligand complexes *C* and internalized dimerized ligand-receptor complexes from the coated pits *IH* respectively) and successive improvements were evaluated. Red: normalized deviation between the standard mesh and the first refinement. Green: normalized deviation between the first and second mesh refinement. Yellow: normalized deviation between the second and third mesh refinement.

The deviation between the second and third level of refinement was less than 0.5% for maximum concentrations and less than 1% for minimum concentrations at 30 seconds, with subsequent improvements at 60 seconds. The second level of refinement was preferred because of the reasonable solving time (approximately five minutes). Three values of R_{tol} (1e-6, 1e-9 and 1e-12) were compared to study the accuracy of computations. For all mesh refinements, the deviations between maximum and minimum computed *IH* concentrations were identical up to the fifth significant digit, indicating that the results had converged and the error from the numerical solver was negligible. An R_{tol} value of 1e-6 was chosen to ensure a reasonable solving time.

3.4.2 **Surface Responses of Controllable Variables**

As the system geometry is included in the finite-element model, the cell size, micropipette diameter and micropipette distance from the cell need to be carefully selected. In these simulations, the diffusion coefficient both in the media and micropipette was set to 1.84e-10 m^2/s (diffusion in water at 20ºC) which was calculated using the Stokes-Einstein equation and the viscosity of water at 20ºC μ_{water} = 1 mPa.s. This temperature was selected as subsequent experiments were performed at room temperature. To evaluate the system response for various geometries, surface plots were generated for two metrics, the Polarization Index (PI) and Percentage of receptor Occupancy (PO). PI was used to quantify the degree of asymmetry based on the ratio of computed surface concentrations between the half-front and half-back cell surfaces with respect to the point source of delivery:

$$PI(t,\overline{O}) = \frac{\int_{frontS}(D)dS}{\int_{backS}(D)dS} \tag{32}$$

$$PI(t,\overline{O}) = \frac{\int_{frontS}(H)dS}{\int_{backS}(H)dS} \tag{33}$$

$$PI(t,\overline{O}) = \frac{\int_{frontS}(D)dS + \int_{frontS}(ID)dS}{\int_{backS}(D)dS + \int_{backS}(ID)dS} \tag{34}$$

High PI values will indicate a markedly asymmetric cell, while PI = 1 will indicate a complete loss of asymmetry. Equations 32 to 34 were defined based on signaling-potent

members of the signaling pathway exclusively (dimerized ligand-receptor complexes in the smooth pits *D* and coated pits *H*). Computed PI values were identical for all equations and *D* and *H* were not included simultaneously due to the higher order of magnitude of *D* concentrations. Similar results were obtained when endosomal fractions were substituted in equations 32 and 33 and equation 32 was selected for further analysis. A generalized definition applicable to alternate and multiple signaling pathways was also defined:

$$PI(t,\overline{O}) = \begin{bmatrix} \left(\frac{\sum_{i=1}^{j} \int_{frontS} (I_i) dS}{\sum_{i=1}^{j} \int_{backS} (I_i) dS} \right)_{00} & \cdots & \left(\frac{\sum_{i=1}^{j} \int_{frontS} (I_i) dS}{\sum_{i=1}^{j} \int_{backS} (I_i) dS} \right)_{m0} \\ \cdots & \cdots & \cdots \\ \left(\frac{\sum_{i=1}^{k} \int_{frontS} (I_i) dS}{\sum_{i=1}^{k} \int_{backS} (I_i) dS} \right)_{0n} & \cdots & \left(\frac{\sum_{i=1}^{k} \int_{frontS} (I_i) dS}{\sum_{i=1}^{k} \int_{backS} (I_i) dS} \right)_{mn} \end{bmatrix} \quad (35)$$

The m elements of the matrix refer to the different possible metrics of asymmetry for a given signaling pathway, and the n elements refer to n possible signaling pathways that can be considered at a time. J possible elements are present in the first pathway but the other signaling pathways can have a different number of metrics with either k > j or k < j. For all n possible pathways, m different indicators of efficiency can be developed. In conjunction with PI, PO was used to evaluate the degree of EGF binding on the cell surface, and hence the potential for the delivery to trigger signaling responses:

$$PO(t,\overline{O}) = \left[1 - \left(\frac{\int_{frontS} (R+IR) dS + \int_{backS} (R+IR) dS}{\int_{S} (R_{init} + IR_{init}) dS} \right) \right] \quad (36)$$

Computations were performed on a time scale of 1200 seconds with a time step of one second, PI and PO were computed at 6 time points (30s, 1, 2, 5, 10 and 20 min) as previously defined and three-dimensional surface plots produced in MATLAB. Initial EGF concentration in the micropipette was 100 ng/mL. The levels selected for the controlled variables (micropipette distance from the cell, micropipette diameter and cell diameter) were 2.5, 5, 10, 20 and 40 μm. For every combination of parameters analyzed, the third parameter value was set to 10 μm. The initial number of receptors was defined based on Table 2 and was kept constant for the varying cell diameters (hence receptor density varied between different cell diameters). Prior to the analysis, finite-element model significance was evaluated using published literature values from Schoeberl and colleagues (Schoeberl, Eichler-Jonsson et al. 2002). Simulations yielded PO = 98% in 30 seconds with 50 ng/mL EGF in the culture media using R_{init} = 50000 receptors, confirming model consistency with respect to published observations (Saso, Moehren et al. 1997). This was performed to ensure

Surface response plots in terms of PI and PO will be presented in the following pages with respect to the controlled variables (micropipette distance from the cell, micropipette diameter and cell diameter: Figure 3-4 to Figure 3-9). These plots will illustrate the response of the system for various experimental conditions at different times and will allow for the selection of a working range of experimental conditions that will be used for subsequent simulations. Scaled surface responses will be presented on the left panels to best show response shape, while responses scaled to the same absolute value will be presented on the right panels. Responses scaled to the same absolute magnitude will be useful in evaluating changes in the range of computed PI and PO over time.

Response: PI
Variables: cell diameter & pipette diameter

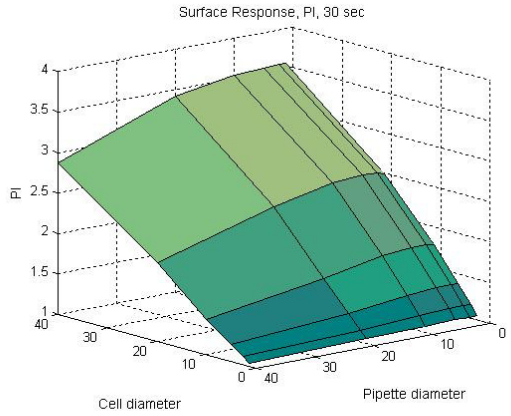

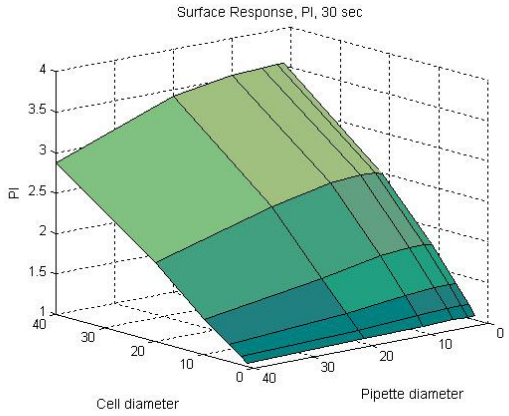

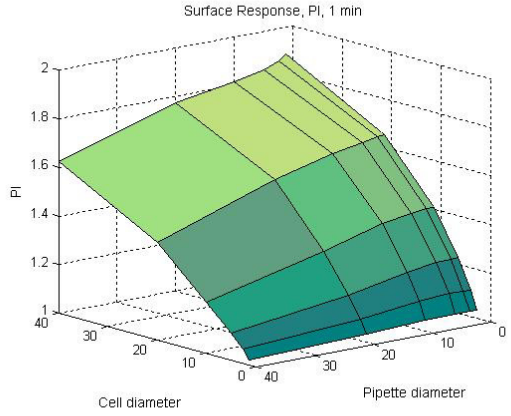

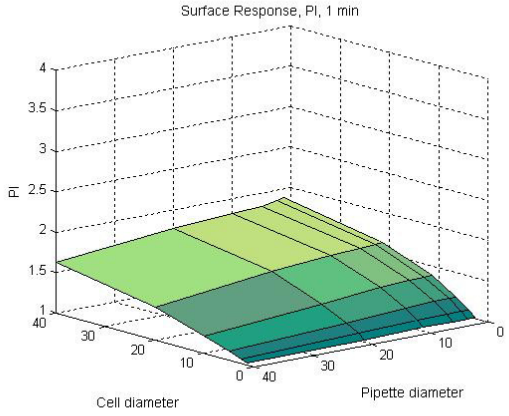

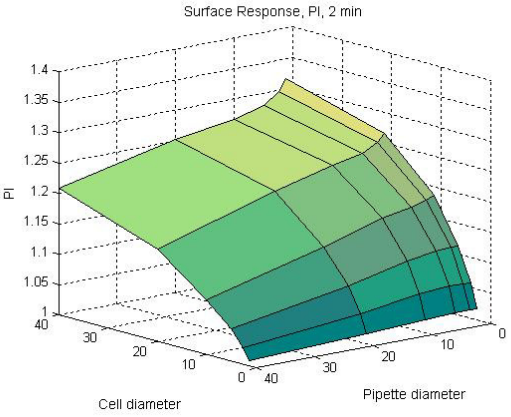

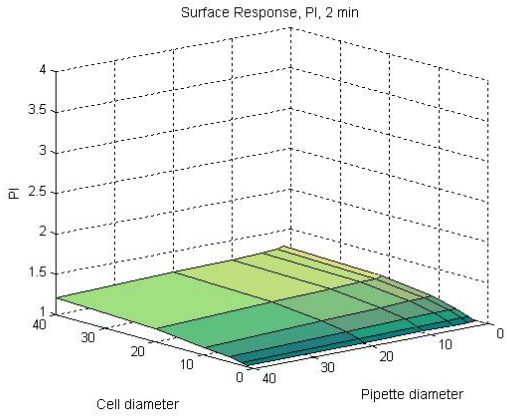

Figure continues on next page

Response: PI
Variables: cell diameter & pipette diameter

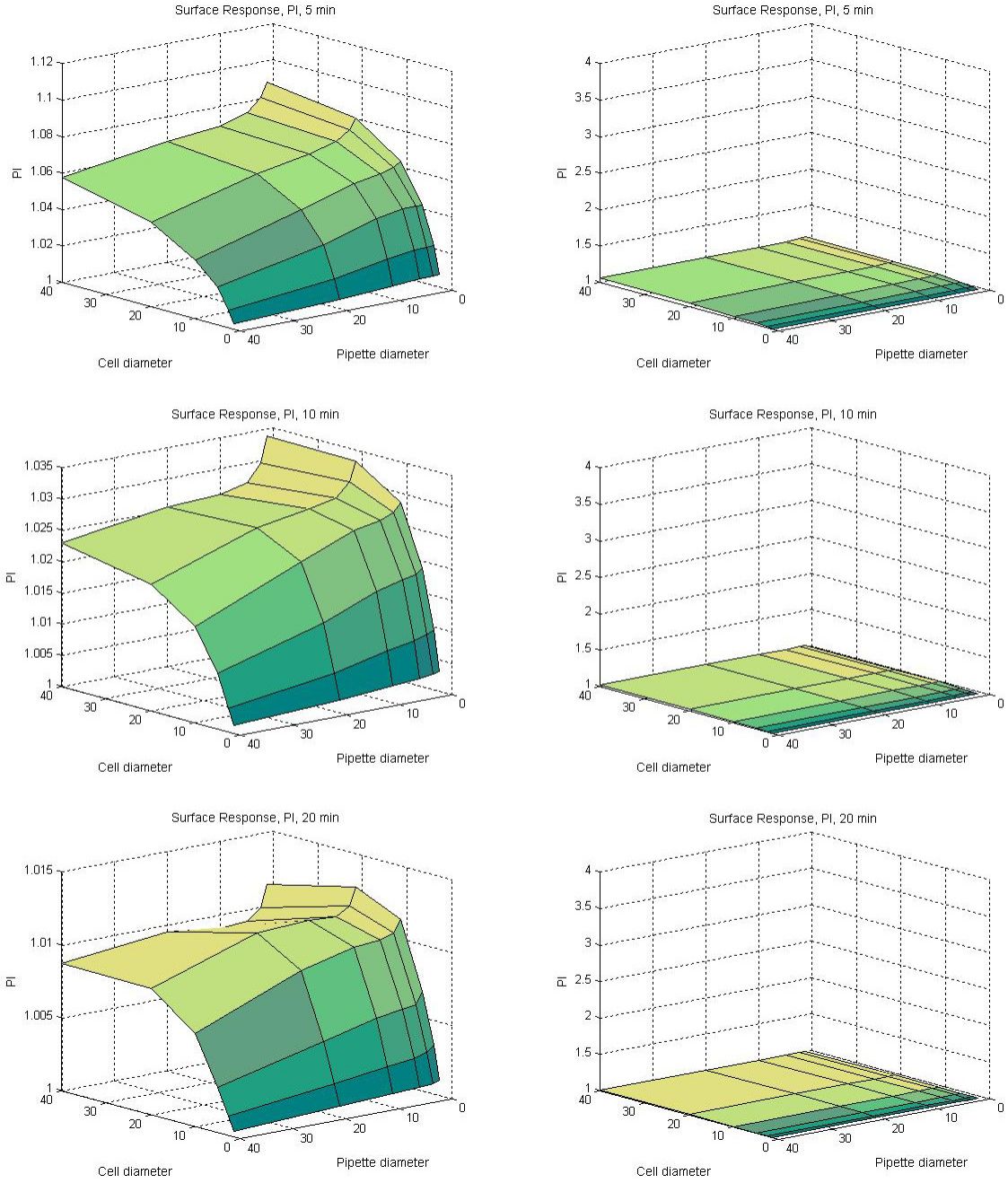

Figure 3-4: Surface responses PI plots for cell diameter versus micropipette diameter. Responses with respect to the same absolute values are presented on the right side. The micropipette distance from the cell surface was set to 10 µm.

Response: PO
Variables: cell diameter & pipette diameter

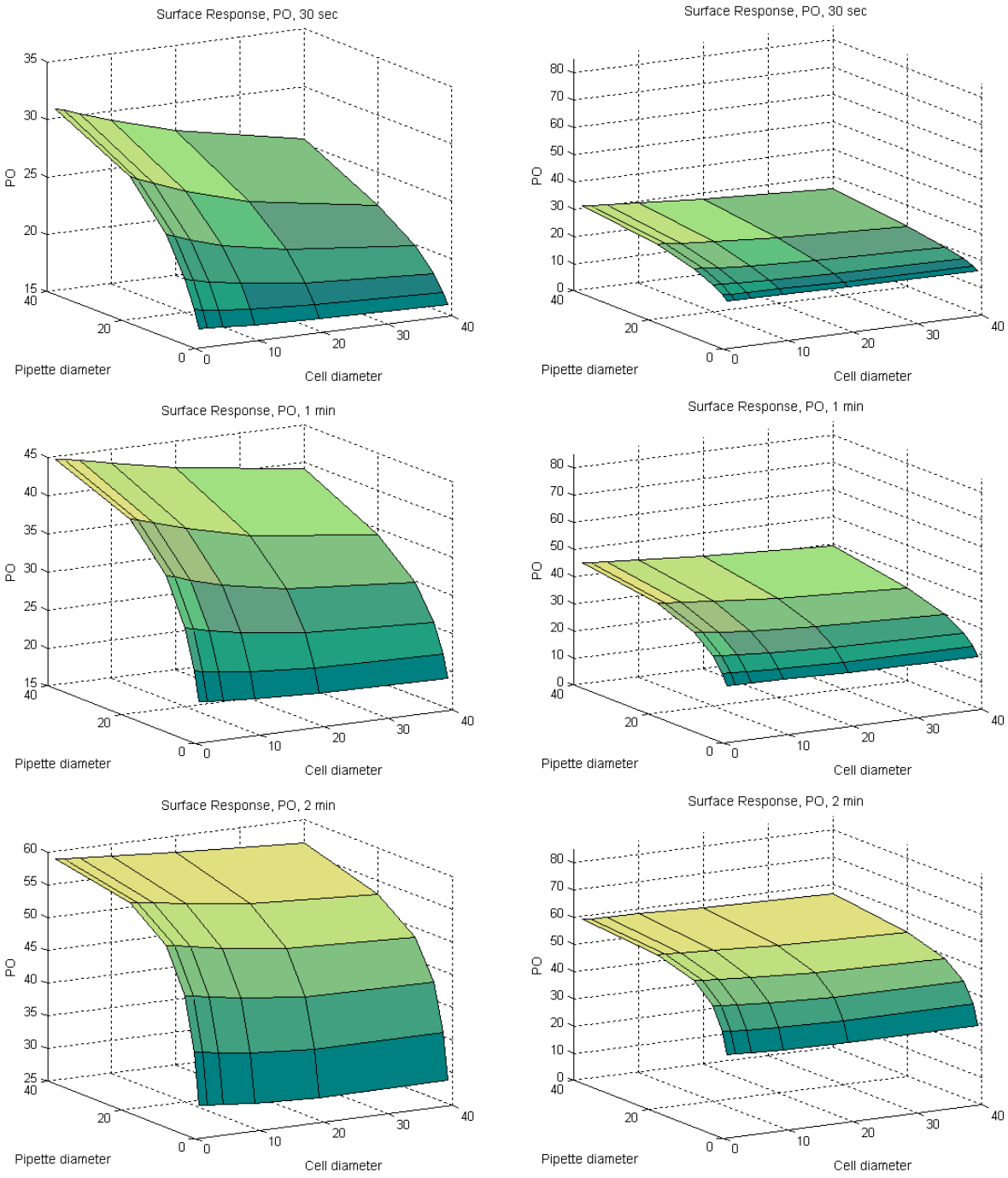

Figure continues on next page

Response: PO
Variables: cell diameter & pipette diameter

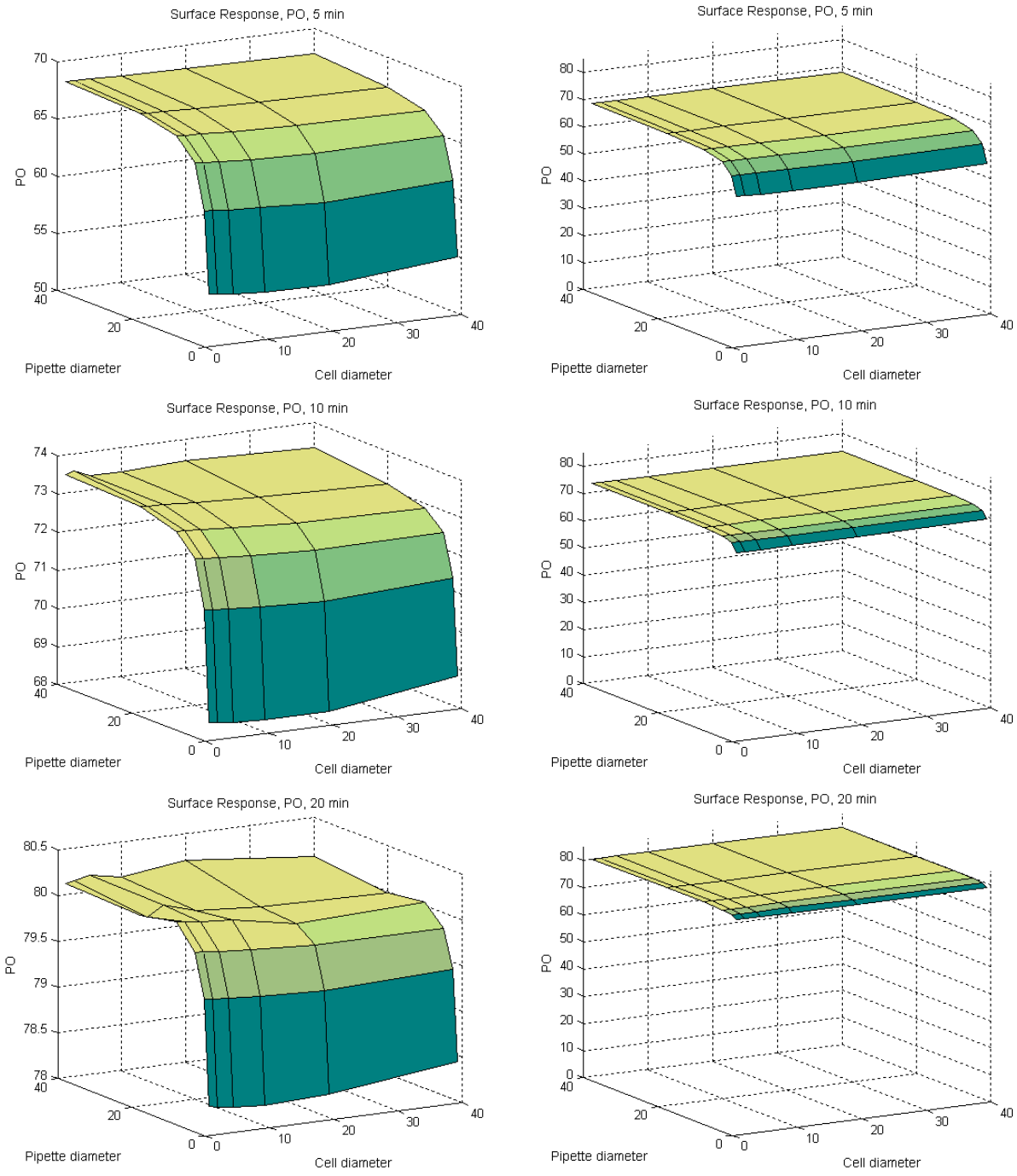

Figure 3-5: Surface responses PO plots for cell diameter versus micropipette diameter. Responses with respect to the same absolute values are presented on the right side. The micropipette distance from the cell surface was set to 10 µm.

Response: PI
Variables: pipette distance & cell diameter

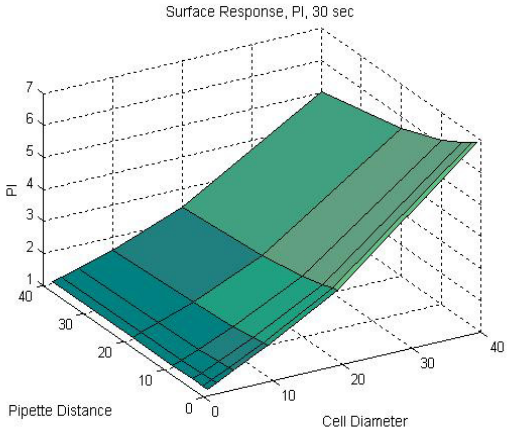

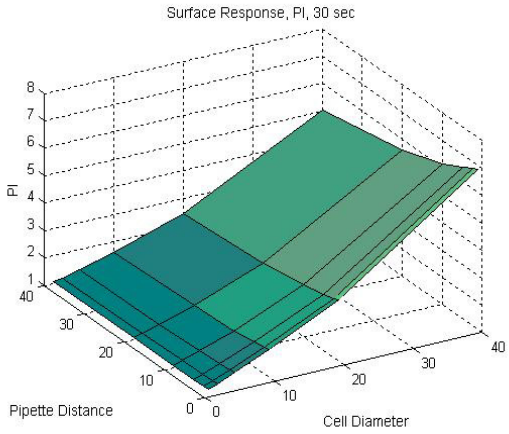

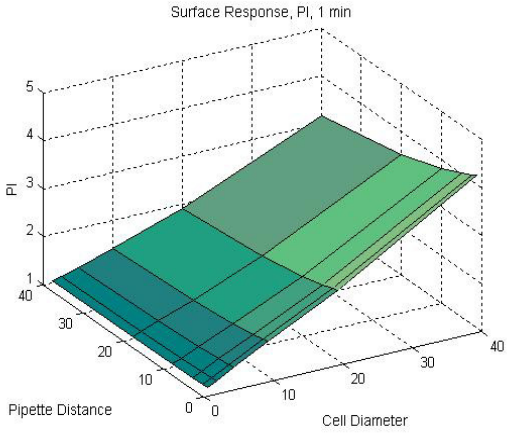

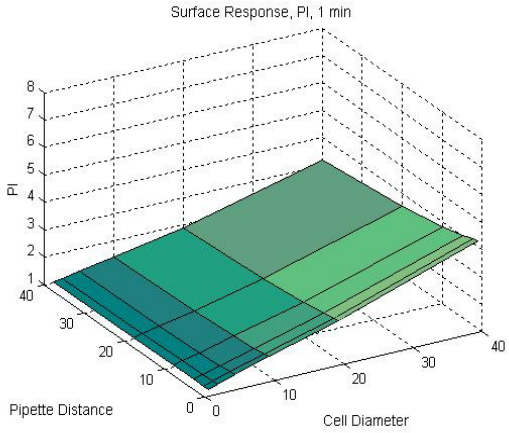

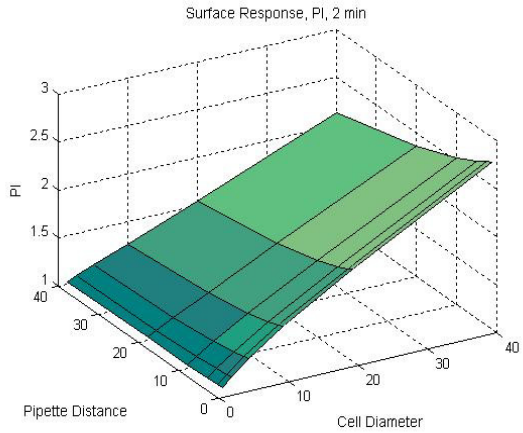

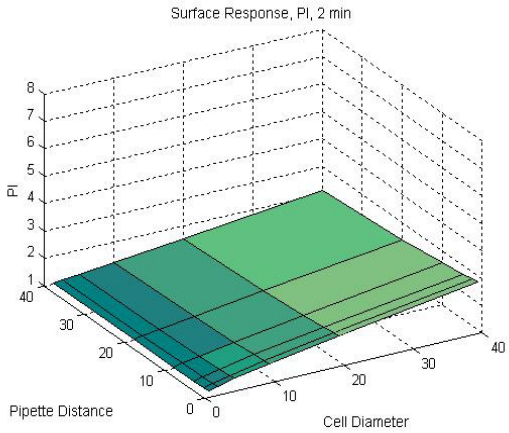

Figure continues on next page

Response: PI
Variables: pipette distance & cell diameter

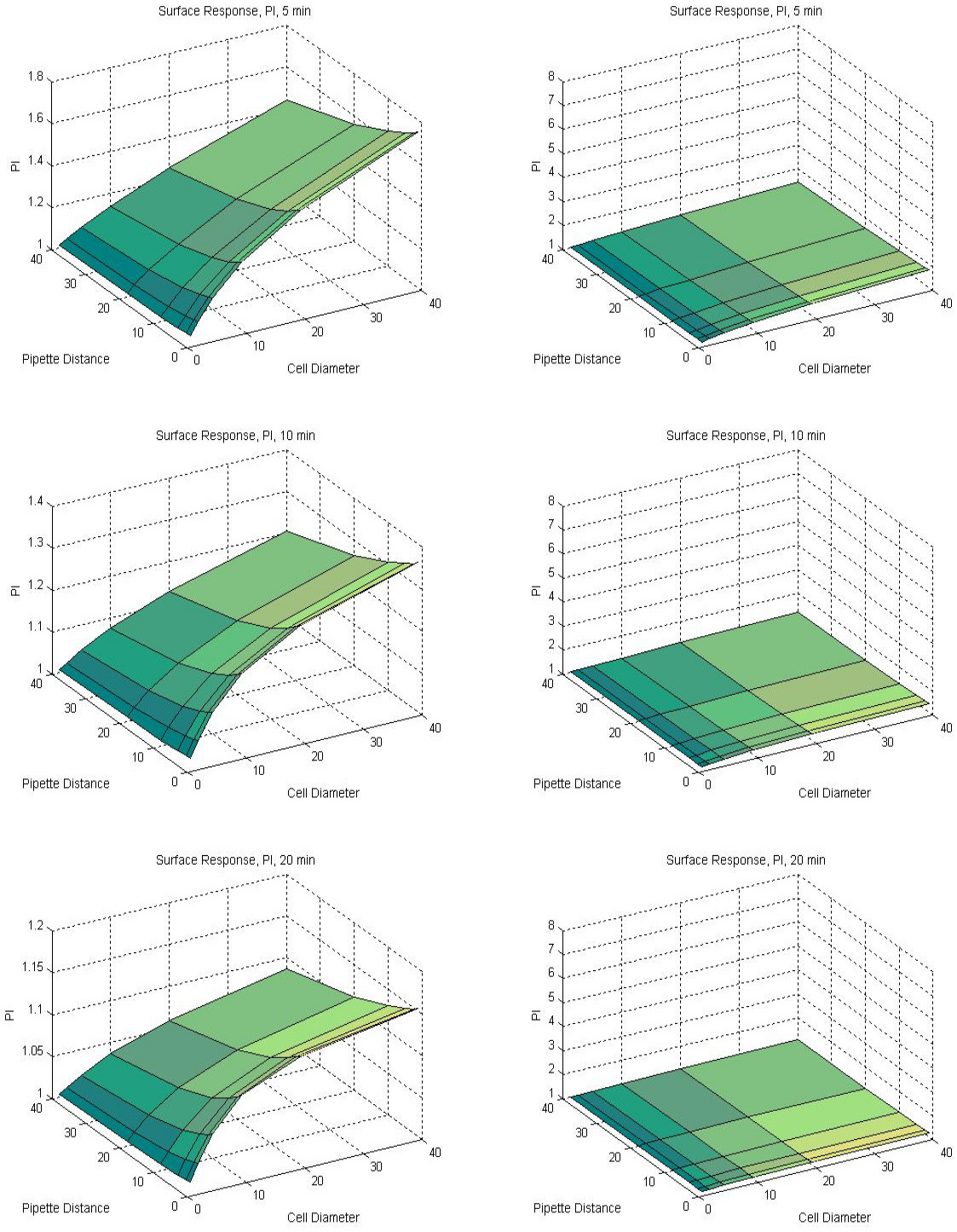

Figure 3-6: Surface response PI plots for micropipette distance versus cell diameter. Responses with respect to the same absolute values are presented on the right side. The micropipette diameter was set to 10 µm.

Response: PO
Variables: pipette distance & cell diameter

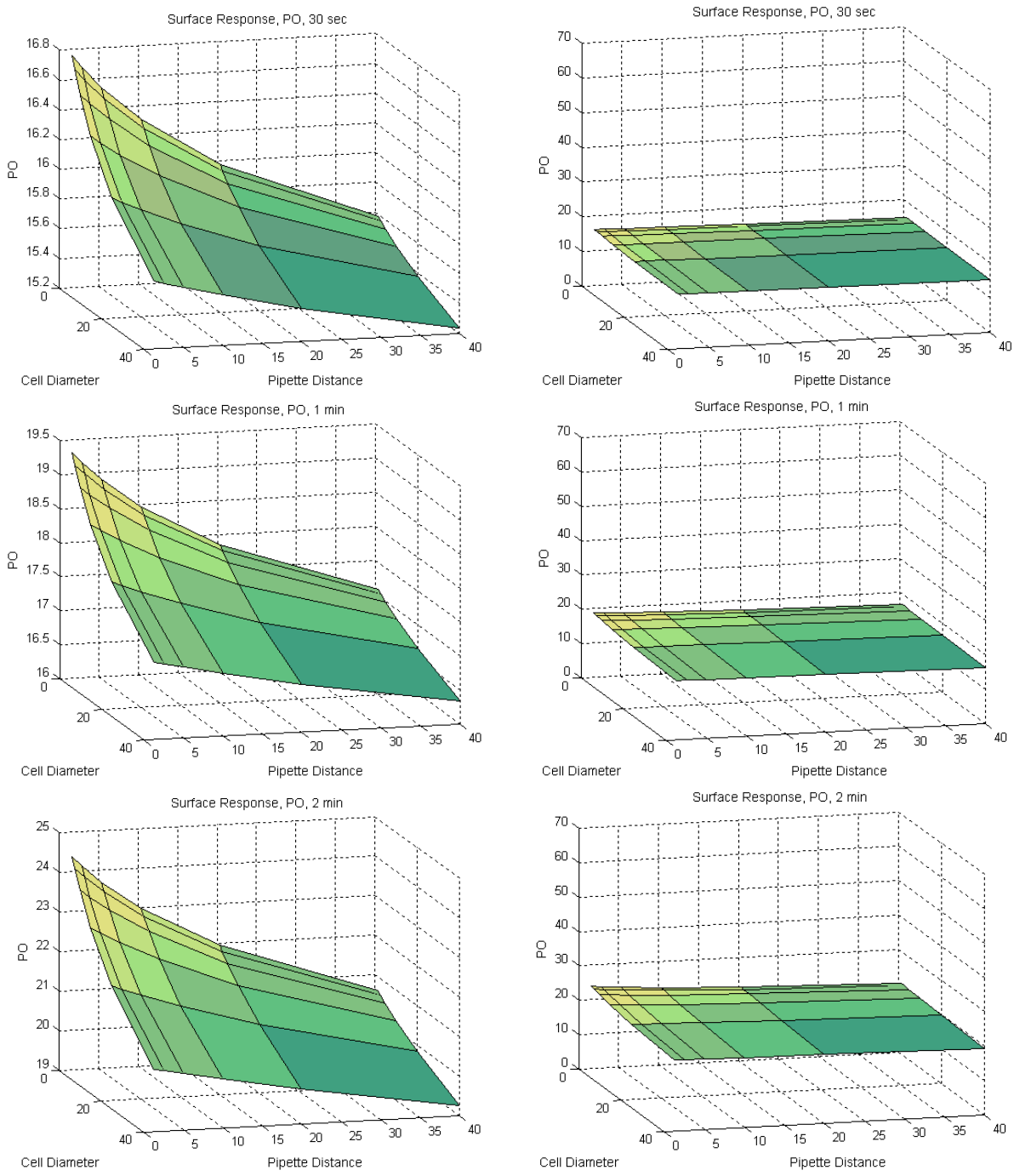

Figure continues on next page

Response: PO
Variables: pipette distance & cell diameter

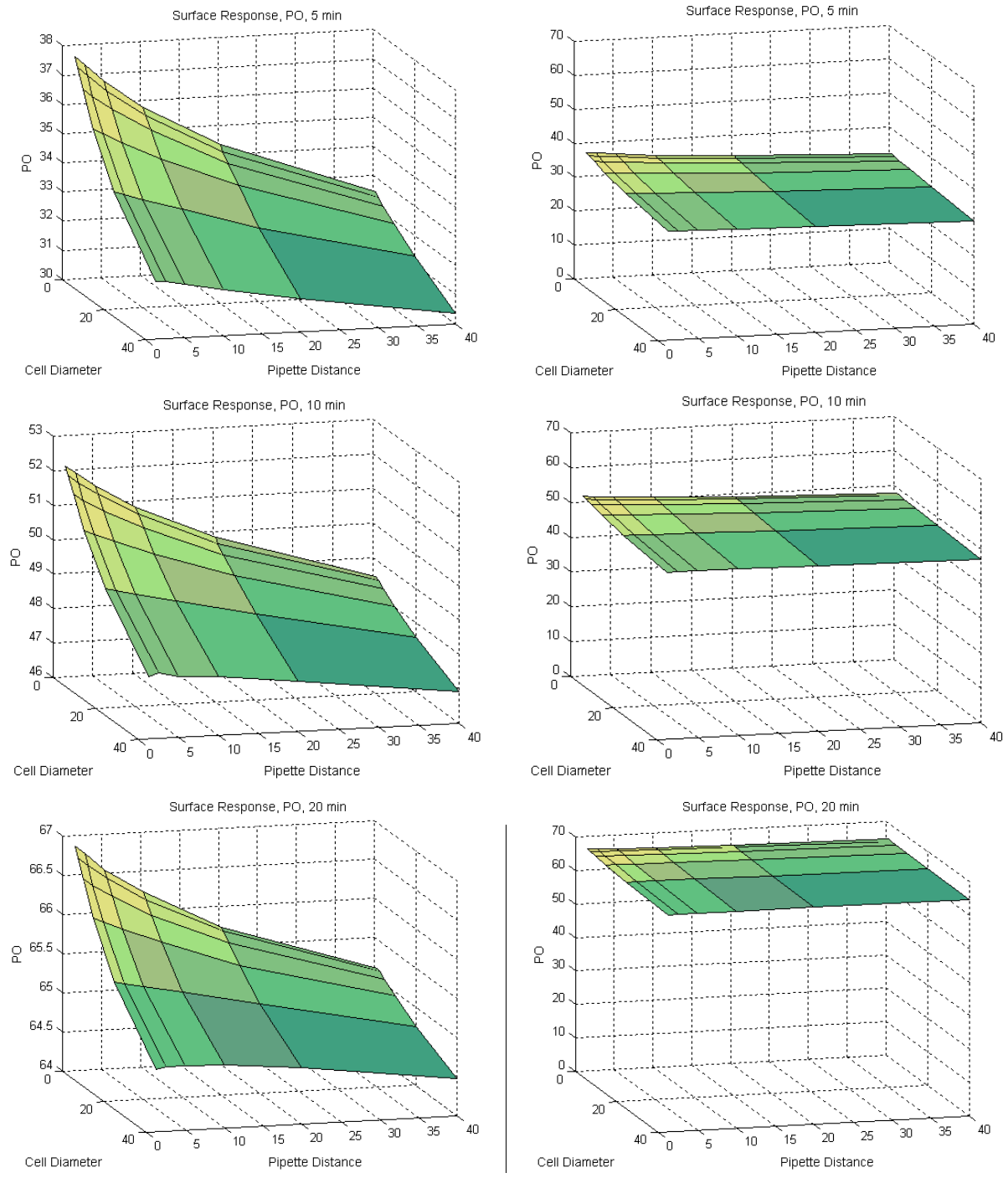

Figure 3-7: Surface response PO plots for micropipette distance versus cell diameter. Responses with respect to the same absolute values are presented on the right side. The micropipette diameter was set to 10 µm.

Response: PI
Variables: pipette diameter & pipette distance

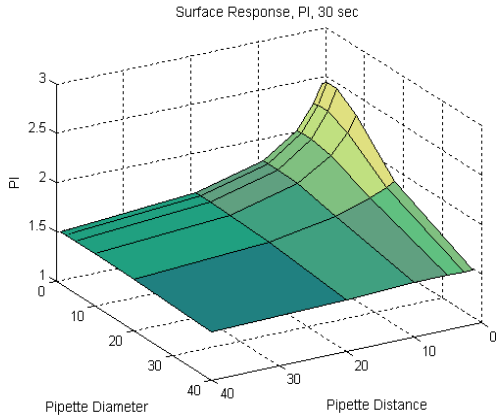

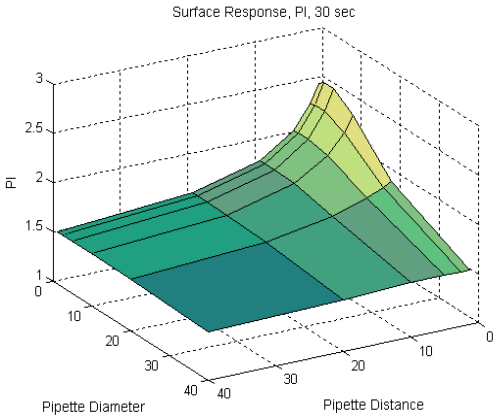

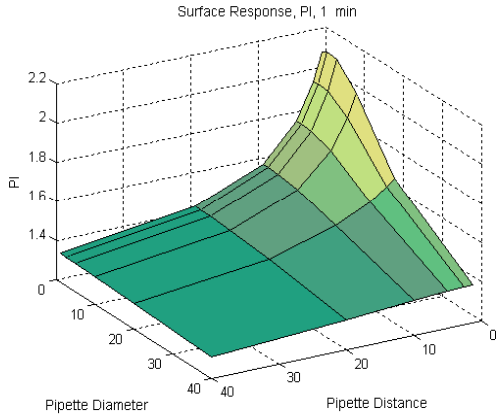

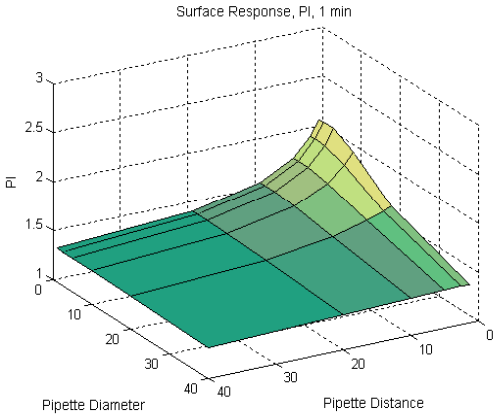

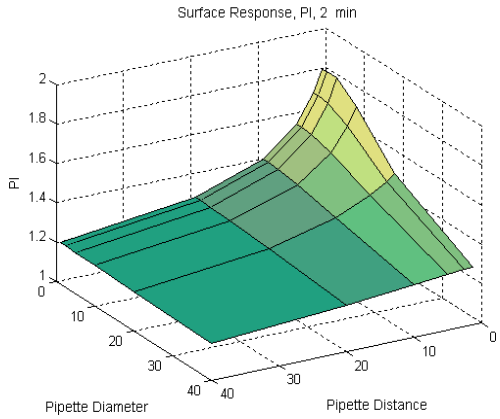

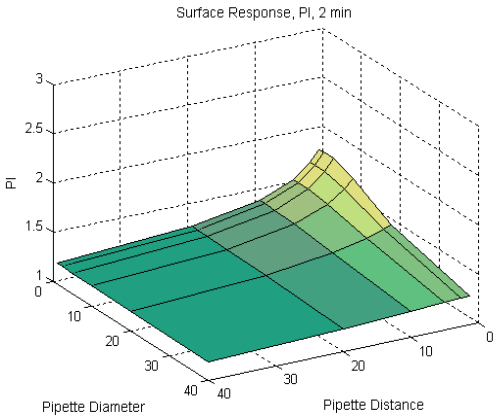

Figure continues on next page

Response: PI
Variables: pipette diameter & pipette distance

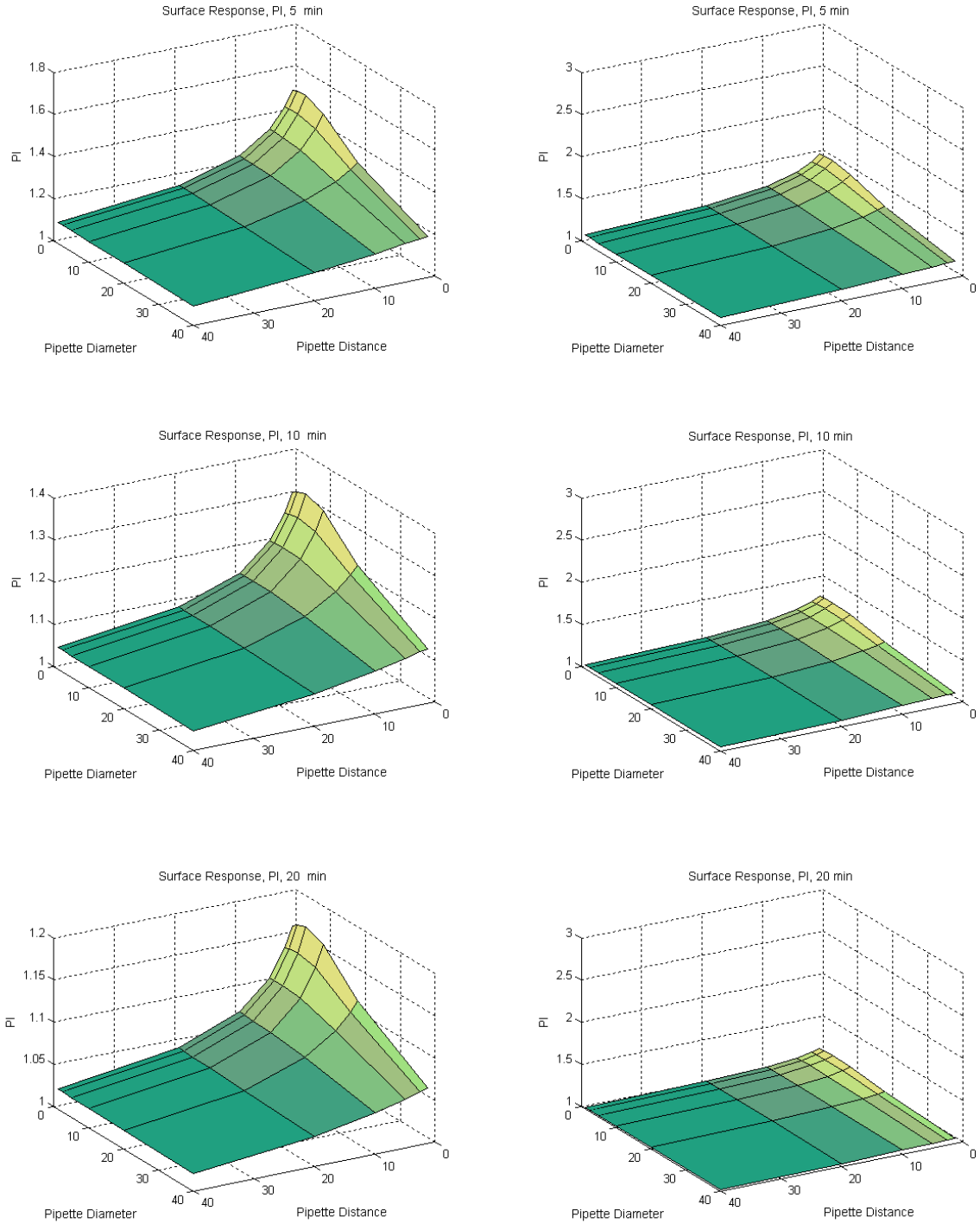

Figure 3-8: Surface response PI plots for micropipette distance versus micropipette diameter. Responses with respect to the same absolute values are presented on the right side. The cell diameter was set to 10 µm.

Response: PO
Variables: pipette diameter & pipette distance

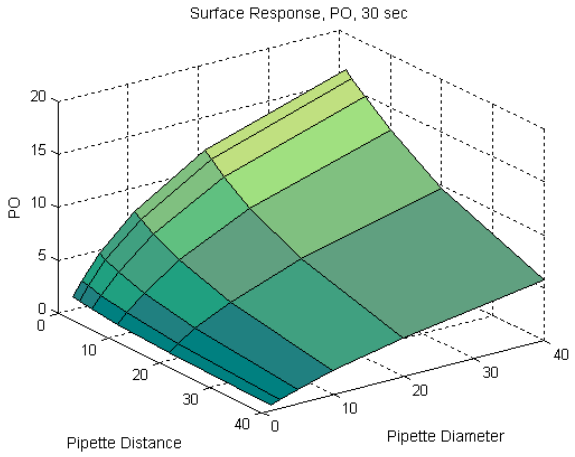

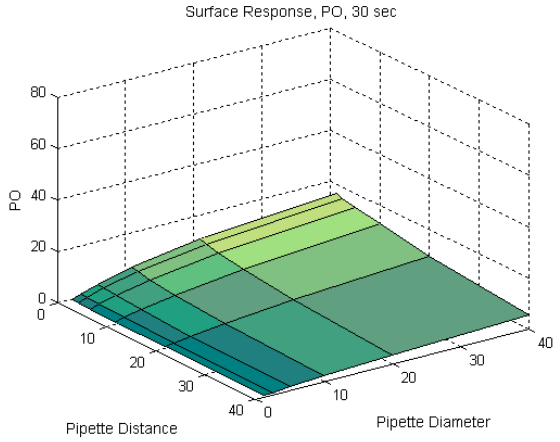

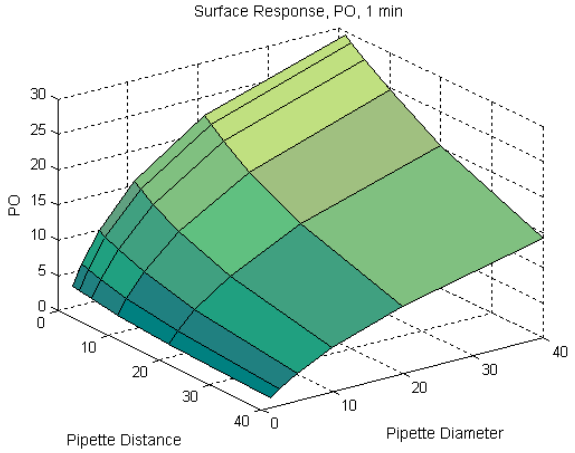

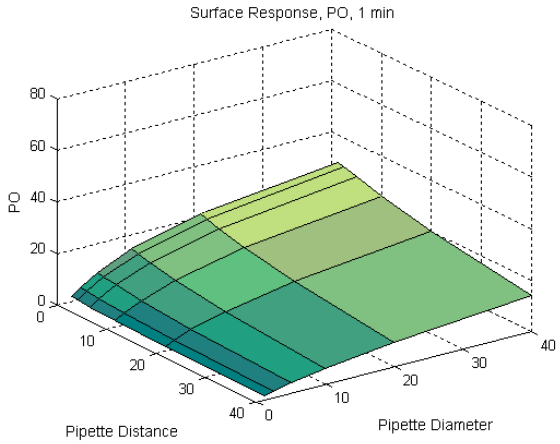

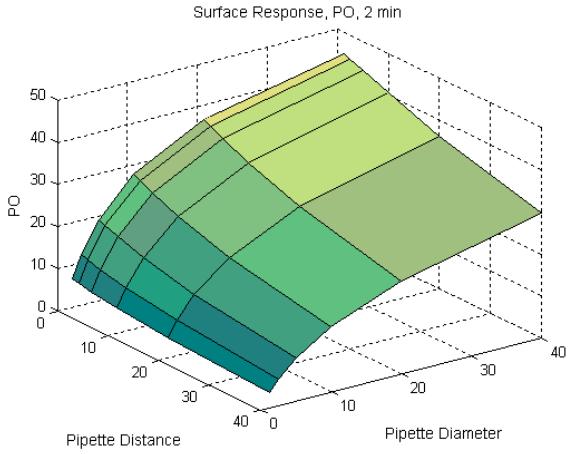

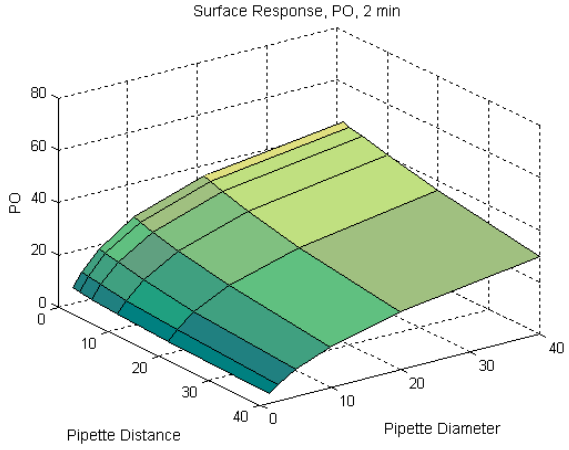

Figure continues on next page

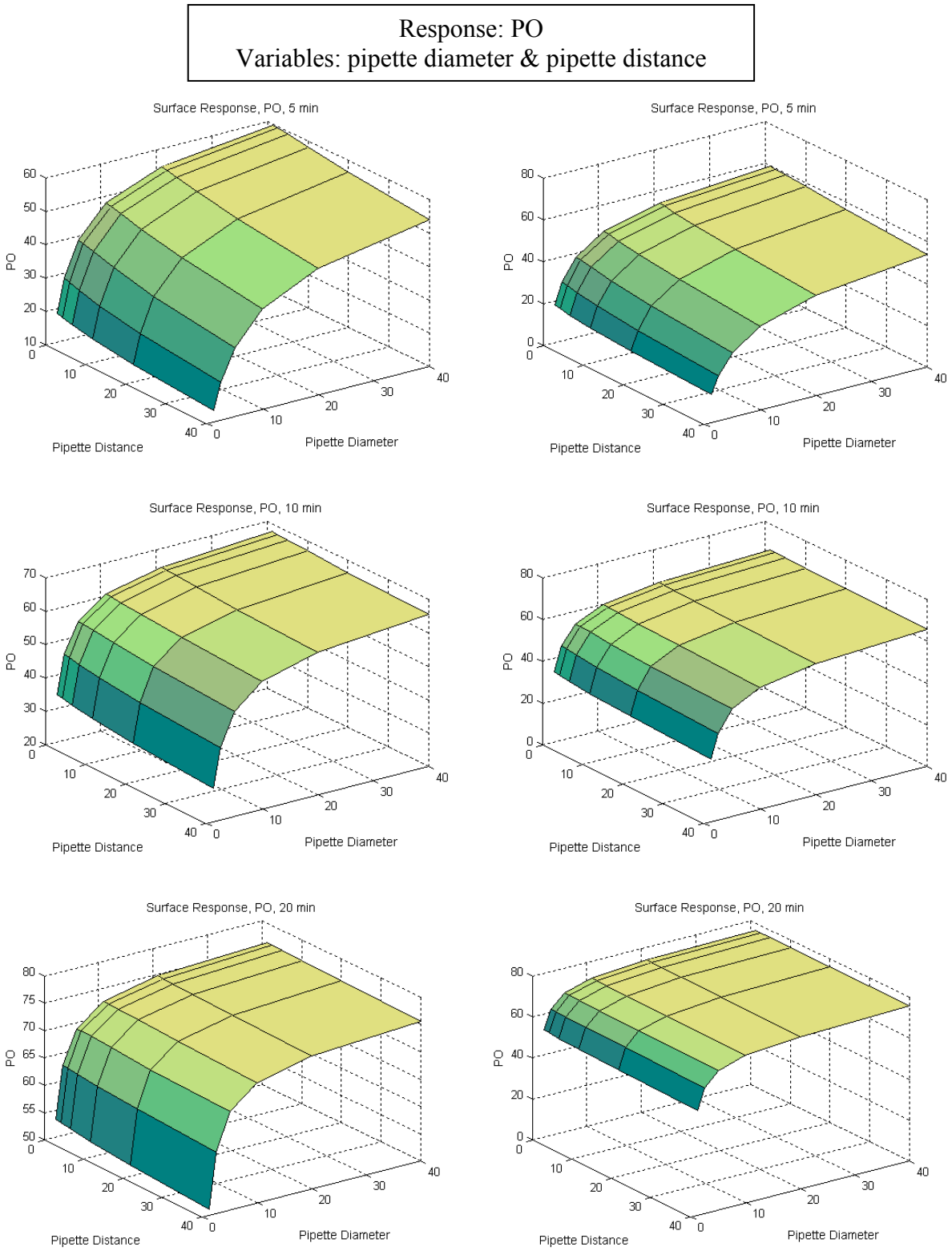

Figure 3-9: Surface response PO plots for micropipette distance versus micropipette diameter. Responses with respect to the same absolute values are presented on the right side. The cell diameter was set to 10 µm.

As shown in Figure 3-4, decreasing the diameter of the delivery system allows for higher computed PI for a cell diameter between 20 and 40 μm. Hence, a decrease in the amount of EGF molecules released in the cell vicinity allows for higher polarization when the cell diameter is significantly larger than the pipette diameter. This phenomenon is further amplified at later time points. Therefore, the design of the smallest source of EGF appears to be the optimal approach to maximize PI. Polarization is also affected by the cell diameter as shown in Figure 3-4 and 3-6; higher cell diameters allow for up to 3.5 fold increase in PI. After 10 minutes, the increase in PI with increasing cell diameter exhibited a saturable profile with no significant improvements computed for cell diameters greater than 20 μm. Regarding the micropipette distance from the cell, shorter distances allowed for slightly higher PI values as shown in Figure 3-8 thus indicating distances below 10 μm from the cell should be preferred in our analysis. As demonstrated with the non-scaled surface plots, the magnitude of responses significantly decreases over time. The selection of experimental conditions will affect PI in the early stages of delivery, as in most conditions PI converges towards 1 after 10 minutes thereby demonstrating the loss of polarized signal over time.

Results were reversed for PO as shown in Figure 3-5. Changes in cell diameter did not generate significant variations of computed PO values with a maximum computed occupancy difference of 6% between a 2.55 and 40 μm diameter cell after one minute. The initial number of receptor was kept constant in all simulations hence indicating a larger cell had a lower receptor density compared to a smaller cell. We analyzed the effect of constant receptor density between cell dimensions on computed occupancy values and demonstrated less than 3% occupancy differences between the largest and smallest cell diameter on the cell surface (data not shown).

This indicates the kinetic of binding on the cell surface dominates for a given ratio of the initial concentration compared to the availability of free receptors with the diffusion in water being the main system parameter. For the given number of receptors, the concentration of EGF reaching the surface for receptor binding will dictate responses with respect to PO, thereby indicating the controllable parameters of the delivery system (micropipette diameter and distance from the cell) should allow for the control of target occupancy values. Only an increase in the number of receptors to unrealistically high values will significantly affect the response with respect to PO. As shown in Figure 3-9, large pipette diameters allowed for increased occupancy levels; pipette diameters greater than 10 μm did not produce further improvements of computed PO after 10 minutes. Finally, the distance from the cell surface had no significant effects on PO when diffusion in water was selected, as shown in Figure 3-7 and 3-9.

Optimal system conditions for PI and PO differ. Maximal polarization is reached for large cells with a small micropipette positioned close to the cell surface. Conversely, maximum occupancy levels will be reached with a delivery system of large diameter independently of the cell size, thereby demonstrating perfectly polarized and signaling-potent states are reached under different experimental conditions. To develop an approach for polarization in the context of signaling, levels of receptor occupancy need to be analyzed in the context of downstream signaling pathways, such as the MAPK / Erk as described previously. Schoeberl and colleagues demonstrated the phosphorylation of Erk in the intracellular compartment is subject to signal amplification in HeLa cells. A similar amount of phosphorylated Erk were computed for EGF concentrations in the media ranging between 50 and 0.5 ng/mL after five minutes while 0.125 ng/mL EGF allowed for 70% of the maximum amplitude of Erk activation after 12 minutes

(Schoeberl, Eichler-Jonsson et al. 2002). Signal amplification permits activation of downstream effectors of the signaling cascade over a wide range of concentration of dimerized / activated receptors. Using kinetic parameters from Schoeberl's analysis, we analyzed occupancy levels (PO) on a single cell (10 μm diameter) cultivated in media containing 0.5 and 0.125 ng/mL EGF, as shown in Figure 3-10.

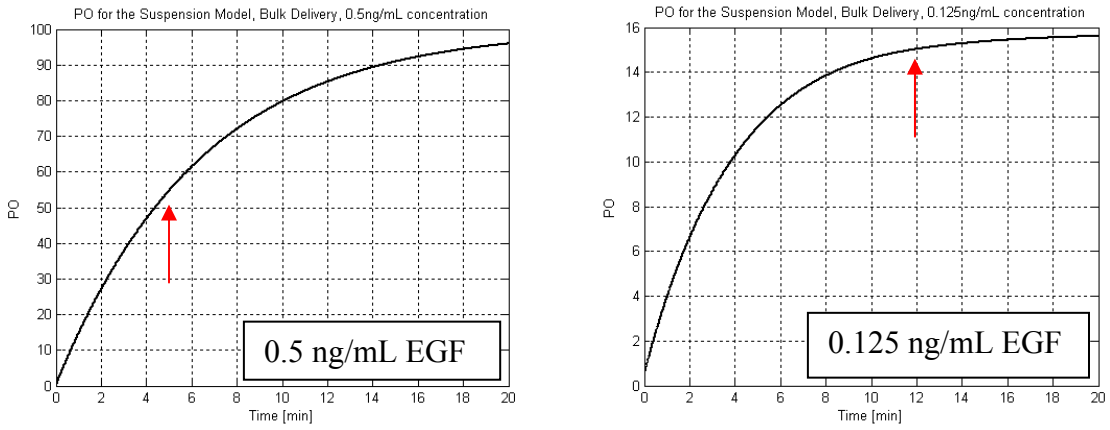

Figure 3-10: Analysis of receptor occupancy levels on a single cell cultivated in 0.5 ng/mL (left panel) and 0.125 ng/mL EGF (right panel) using kinetic parameters from Schoeberl, Eichler-Jonsson et al., 2002. The cell diameter was 10 μm. PO was computed as shown in equation (36).

0.5 ng/mL EGF in the media generated occupancy levels of ***55%*** after five minutes at which 90% of the maximum Erk activation was possible based on Schoeberl's analysis. With 0.125 ng/mL EGF, 70% of the maximal MAPK activation was observed after 12 minutes and our simulation demonstrated occupancy levels of ***15%*** at this time. Our model results are consistent with Schoeberl *et al.*'s findings which demonstrated that 32% of receptors are autophosphorylated after five minutes with 0.5 ng/mL EGF and 14% after 12 minutes with 0.125 ng/mL (Schoeberl, Eichler-Jonsson et al. 2002). This approach allows for the definition of target occupancy levels consistent with signal transduction following delivery. Therefore, 15% receptor

occupancy (PO) was selected as a lower threshold to ensure asymmetric signal significance following EGF delivery (minimum of 70% of maximal MAPK activation). The target of this approach is not to completely prevent MAPK signaling on a specific cell side, but rather generate heterogeneities in the magnitude of MAPK activation sufficiently large to enable different responses after cell division. In this context, variations between 70 to 90% of signaling could generate various pools of early gene products (jun and fos for example) leading to differential late genes profiling through proteins such as AP-1, a heterodimer of jun and fos (Hess, Angel et al. 2004).

The number of EGF receptors is subject to significant variations between cell types, ranging between R_{init} = $3x10^6$ receptors/cell in EGFR-overexpressing A431 cells and HER82 (Defize, Arndt-Jovin et al. 1988) (Benveniste, Livneh et al. 1988) to normal levels of expression between $1x10^4$ – $2x10^5$ receptors/cell as observed in HeLa (Berkers, van Bergen en Henegouwen et al. 1991), B82, COS, NIH-3T3, HER84, HER22 and human glioma cell. These variations will significantly affect PO for the same delivery strategy. The occupancy range between 15% and 55% was selected as a reference to enable comparison between different cellular systems.

Regarding system design, a micropipette diameter of 2.5 μm was selected. The analysis demonstrated that this size allowed for occupancy levels to be consistent with signaling while maximizing PI as shown in Figures 3-8 and 3-9. The chosen distance between the cell surface and the micropipette was 5 μm. This distance was preferred as it represents a more achievable target experimentally while allowing for submaximal PI values. For the cell dimensions, we

demonstrated that larger diameters allowed for higher PI values at early time points, while diameters over 20 μm exhibited no improvements at later time points. A diameter of 10 μm was selected, a size consistent with reported diameters of suspension (rounded) mammalian cells such as 13 μm for HeLa (Fujioka, Terai et al. 2006) and 14 μm for fibroblasts (Frisch and Thoumine 2002). Cell types need to be carefully selected during experimental design to ensure proper diameter range and polarization potential.

3.4.3 Sensitivity Analysis on the Parameters

All kinetic parameters identified in the literature can be considered as starting points to define the range of biologically relevant parameters. The robustness of the developed metrics (PI and PO) was studied to evaluate the impact of parameter uncertainty on these indicators. This analysis should provide insights into key regulatory steps in the process based on polarization (PI) and signaling potential metrics (PO). Only relative measures are discussed in this section as the potential effects of experimental error on the analysis were not strictly assessed with this mathematical model. A 'design of experiments' approach was used to minimize the required number of simulations and Plackett-Burman (PB) designs (resolution III) were selected. Sensitivity analysis was performed in COMSOL with MATLAB using a hadamard 24 matrix. 23 parameters were evaluated in 24 runs and all parameters were varied 10-fold for the analysis. The dependant variables selected were computed at two time points (30 seconds and 2 minutes) and computed effects were presented using Pareto charts in MATLAB. The finite element model was built as defined previously and initial EGF concentration in the micropipette was 100 ng/mL.

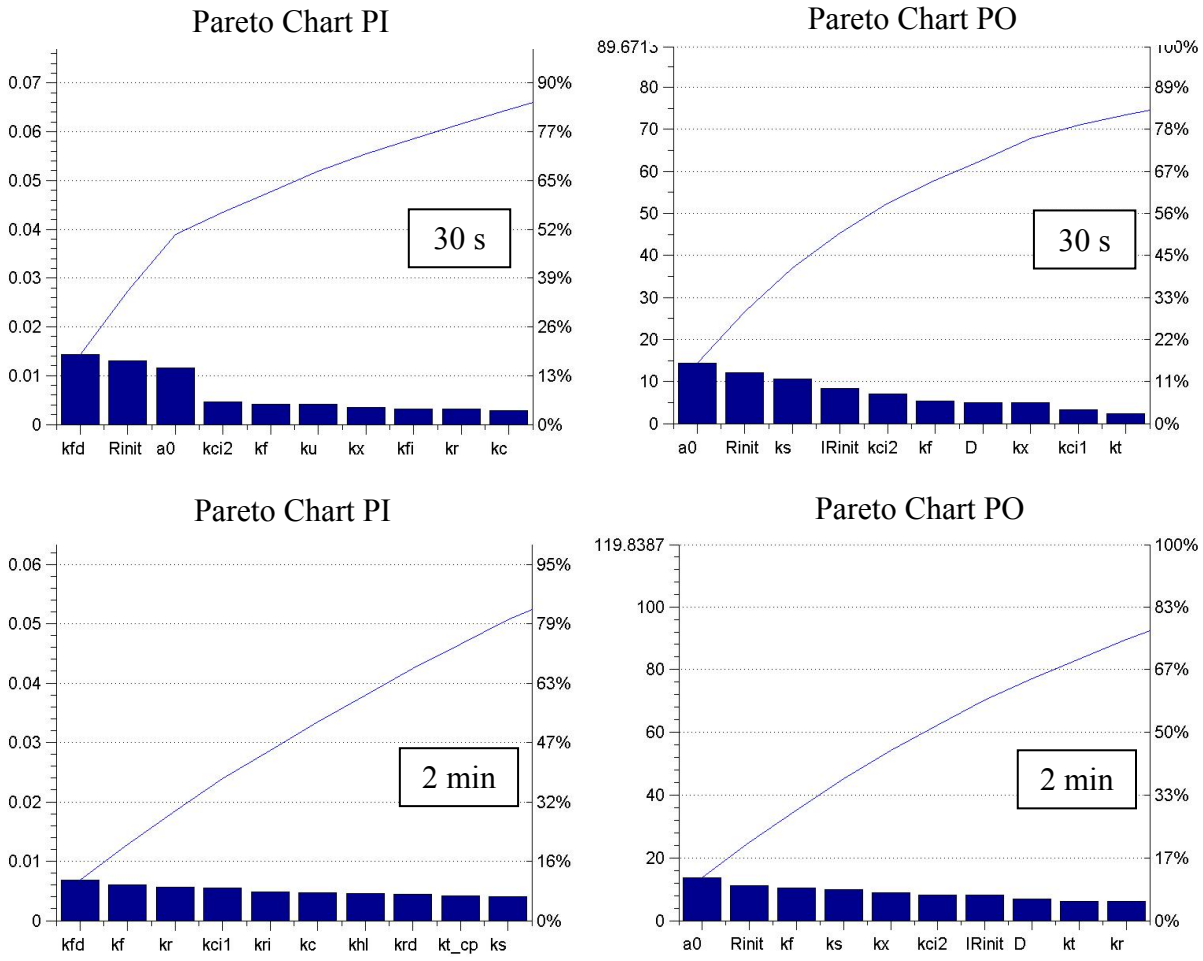

Figure 3-11: Pareto charts for PI and PO after 30 seconds and 2 minutes of delivery (D = 1.84×10^{-10} m^2/s). Top left: PI after 30 seconds. Top right: PO after 30 seconds. Bottom left: PI after 2 minutes. Bottom right: PO after 2 minutes. The blue line indicates cumulative effects presented in percentage of total computed effects (right y-axis).

The left axis of the Pareto Charts indicates the change in computed metric (PI or PO) when the independent variable value goes from upper to lower bound. On the right side, cumulative effects are presented. As shown in Figure 3-11, the pool of most important parameters for PI at 30 seconds was k_{fd} (dimerization of receptor-ligand complexes), the initial number of receptor (R_{init}) and the initial EGF concentration in the delivery system (a0). These three parameters accounted for approximately 50% of the overall measured effects. Interestingly, we found k_{ci2} (endosomal uncoupling constant) in the second category of significant parameters

along with other parameters affecting the concentration of dimerized receptor-ligand complexes in the smooth pits *D* (k_u for dimerized complexes going from the coated pits to the smooth pits and k_x for the recycling rate of internalized dimerized complexes *ID* to the cell surface in the smooth pits). After 2 minutes of delivery, PI lost sensitivity to the initial number of receptor and to the initial concentration of EGF. Therefore, the initial EGF concentration affects PI at early time points when the first wave of EGF molecules reaches the cell surface. As concentration around the cell rapidly homogenizes, EGF concentration has no effect on PI. For PO, this is notably different as a0 was the most significant parameters both at 30 seconds and 2 minutes. For PO, we identified the forward rate constant of binding k_f, R_{init} and the rate of synthesis of new receptors k_s as significant.

In the following section, we will evaluate two strategies for controlled delivery of EGF in the cell microenvironment. PI, PO and a new set of metrics such as surface concentrations and velocity of formation of dimerized receptor-ligand complexes in the smooth (*D*) and coated (*H*) pits will be used to assess the potential of each method. In a first approach, a single cell will be cultured in a collagen matrix (low diffusion coefficient) and the micropipette will be loaded with a solution containing EGF (diffusion in water). For the second strategy, a micropipette will be loaded with a gel of controlled porosity such as acrylamide (low diffusion coefficient) and EGF will diffuse in water in the culture chamber. Experimental conditions (cell diameter, micropipette diameter and distance from the cell surface) will be defined according to section 3.4.2.

3.4.4 **Diffusion in the Media as a Controlled Variable**

In this section all computations were performed on a time scale of 1200 seconds with a time step of 1 second. Initial conditions are presented in matrix $\overline{O}$ [$Q_{i=1,\ldots,J}$; $R_{k=1,\ldots,L}$; $S_{m=1,\ldots,N}$; $T_{o=1,\ldots,P}$] (37) in which Q is the set of J initial kinetic conditions including all rate constants; R is the set of L initial chemical conditions including initial concentration and diffusion values; S is the set of N initial geometrical conditions including micropipette distance and diameter, array volume/surface and boundary conditions; and T is the set of solver parameters including tolerances, type and settings of the numerical solver used. We defined a range of viscosity values for the analysis based on published viscosity measurements with up to 0.1% glutaraldehyde used for cross-linking (Ho, Lin et al. 2001):

- 50 cp = 0.050 kg m^{-1} s^{-1} (D_{50} = 3.69x10^{-12} m^2/s)
- 100 cp = 0.100 kg m^{-1} s^{-1} (D_{100} = 1.84x10^{-12} m^2/s)
- 150 cp = 0.150 kg m^{-1} s^{-1} (D_{150} = 1.23x10^{-12} m^2/s)

The diffusion coefficient D was estimated using the Stokes-Einstein equation:

$$D = \frac{kT}{6\pi\mu R} \tag{38}$$

k is the Boltzmann constant (1.38x10^{-23} m^2.kg.s^{-2}.K^{-1}), T is the temperature (298 ºK) and μ is the viscosity of the media. R is the radius of a spherical particle:

$$R = \sqrt[3]{\frac{3MW\rho}{4\pi}} \tag{39}$$

MW is the molecular weight of the protein at 6045 Da and ρ is the density at 0.69 g/cm^3. In this system, concentration of EGF was 100 ng/mL in the micropipette. The diffusion coefficient for EGF in the micropipette was estimated based on the viscosity of water at 20ºC (D_{tube}=1.84x10^{-10} m^2/s). The diffusion coefficient in the media was a controlled variable (D_{med} = D_{50}; D_{100}; D_{150}).

Concentrations

We first analyzed concentrations of various members of the kinetic system on the cell surface to identify spatial heterogeneities. Line integrals were used to estimate concentrations for the model system and results are presented in Figure 3-12. The integrals were the appropriately oriented line integrals over the cell surface facing (frontS) and away (backS) from the source(s) of free ligand. The domain of these integrals can be assigned as desired, and orthonormal projections of the cell relative to the pipette were used.

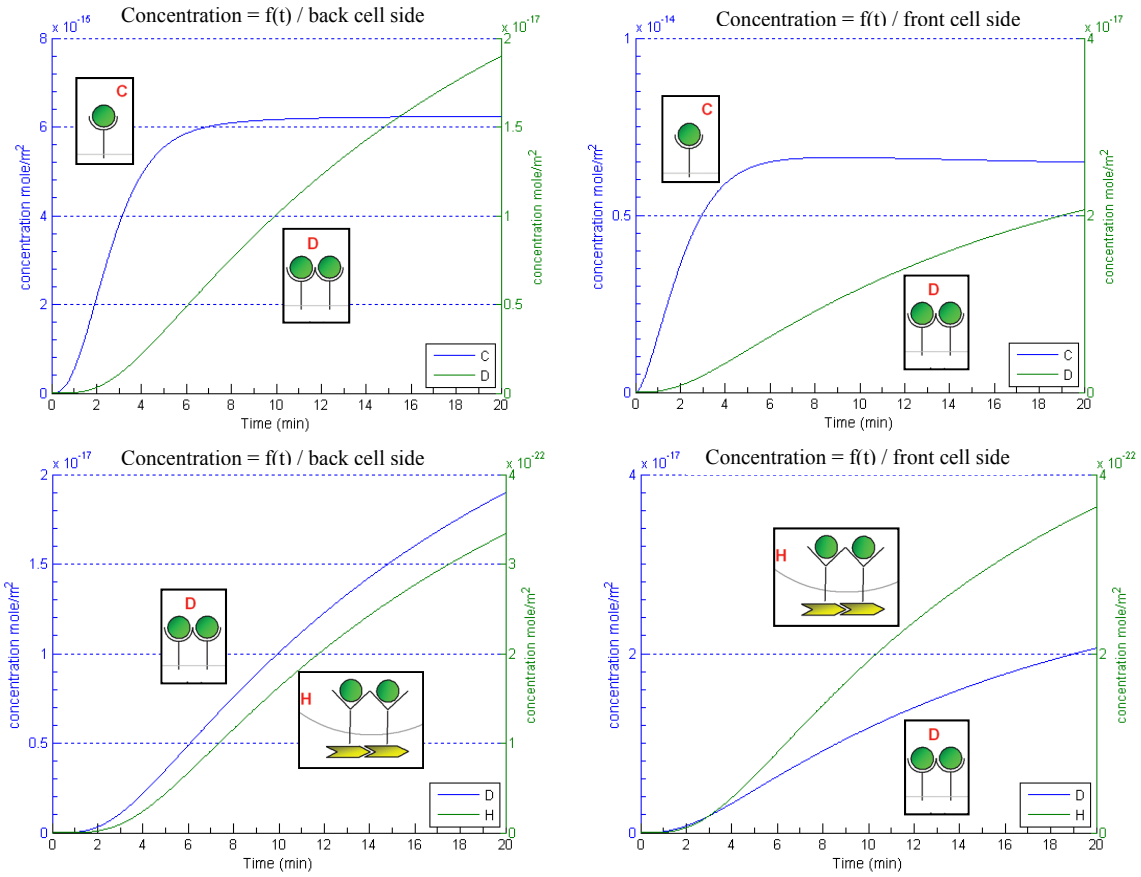

Figure 3-12: Analysis of computed concentrations of various members of the kinetic system (receptor-ligand complexes *C*, dimerized receptor-ligand complexes in the smooth pits *D*, dimerized receptor-ligand complexes in the coated pits *H*) for $D_{50} = 3.69 \times 10^{-12}$ m^2/s. Top left: Computed concentration of *C* (blue) and *D* (green) on the back cell side. Top right: Computed concentration of *C* (blue) and *D* (green) on the front cell side. Bottom left: Computed concentration of *D* (blue) and *H* (green) on the back cell side. Bottom right: Computed concentration of *D* (blue) and *H* (green) on the front cell side.

The various ranges of concentration of the different members of the system for the highest diffusion coefficient value (D_{50}) indicate the dimerization process generates a significant reduction in computed concentrations compared to ligand-receptor complexes C, with *C* values ranging around 10^{-15} mole/m^3, dimerized ligand-receptor complexes in the smooth pits *D* around 10^{-17} mole/m^3 and dimerized ligand-receptor complexes in the coated pits *H* around 10^{-22} mole/m^3. This is a result of the second order kinetics for receptor-ligand complex dimerization; potential signal transducers (*D, H*) are significantly less concentrated than non-transducers (*C*).

Interestingly, concentrations of *D* and *H* steadily increased over the course of computations, indicating no saturation was reached over the period investigated while *C* reached a plateau after 7 minutes. This is indicative of equilibrium between the formation of *C* and its subsequent involvement in dimerization and non-specific internalization. The analysis of the percentage occupancy will demonstrate that this is not a result of receptor saturation on the cell surface after 7 minutes. We next analyzed the concentration differences between the user-defined front and back cell sides with respect to the position of the point source of delivery as shown in Figure 3-13.

$$differential\ D(t,\overline{O}) = \frac{\int_{frontS}(D)dS - \int_{backS}(D)dS}{P} \tag{40}$$

$$differential\ H(t,\overline{O}) = \frac{\int_{frontS}(H)dS - \int_{backS}(H)dS}{P} \tag{41}$$

P is the cell perimeter.

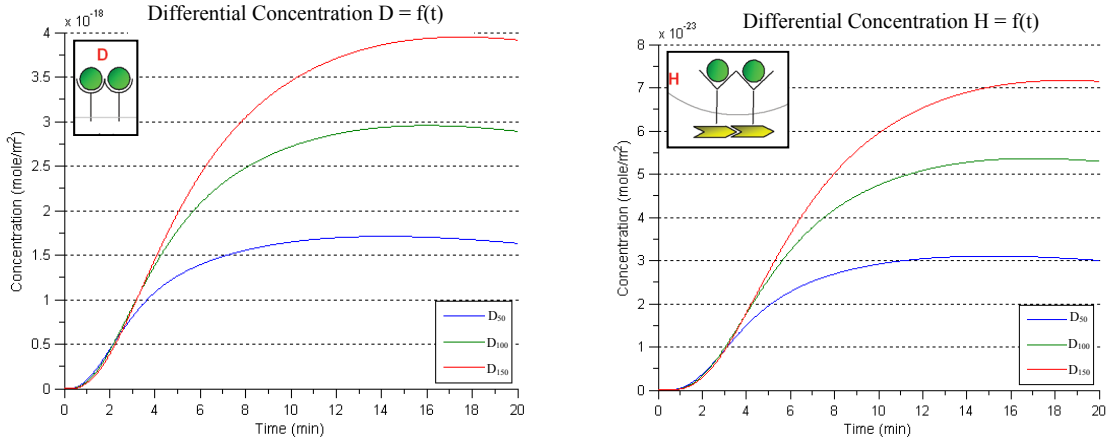

Figure 3-13: The measurement of the differential concentration between the front and back cell side for three diffusion coefficients demonstrates the effect of mass transfer limitation for the creation of spatial heterogeneity of concentrations. Left: differential of *D* concentration computed as per equation (40). Right: differential of *H* concentration computed as per equation (41). (D_{50} = 3.69x10^{-12} m^2/s, D_{100} = 1.84x10^{-12} m^2/s, D_{150} = 1.23x10^{-12} m^2/s).

These types of windows represent ways by which cellular responses could be elicited in a spatially controlled manner. A focus was given to the members with the potential to elicit intracellular signals, i.e. the dimerized receptor-ligand complexes both in the smooth and coated pits. In the case of *D*, concentration differences were measured on the cell surface as shown in Figure 3-13. A decrease of the diffusion coefficient contributed to an increase in computed spatial heterogeneities at the expense of time. The differential *D* concentration exhibited a non monotonic profile, with maximum computed differences between the front and the back cell sides shifting in time as the diffusion coefficient was decreased (14 minutes for D_{50}, 15 minutes for D_{100} and 17 minutes for D_{150}). Hence mass transfer limitation in the direct cell microenvironment could contribute to the generation of greater polarized signals in the later stages of delivery, as computed differentials were almost identical up to 4 minutes. Similar results were observed for *H*, which were adjusted in the relative range of concentration.

During signal transduction, concentration information outside the cell (EGF) is translated in kinetic information in the cytoplasmic compartment through the velocity of phosphorylation of target molecules; we further analyzed computed velocities in the system to evaluate the potential for MAPK activation.

Velocity of Formation

Prior reports of modeling of the EGF signaling cascade demonstrated the velocity of receptor activation (i.e. phosphorylation) is a rate controlling step in signal amplification for homodimeric receptors (Schoeberl, Eichler-Jonsson et al. 2002). As the present model does not include the signaling pathway itself, we considered the velocity of receptor dimerization and aggregation in the coated pits (velocity of formation of dimerized receptor-ligand complexes in the smooth pits *D* (vD) and velocity of formation of dimerized receptor-ligand complexes in the coated pits *H* formation (vH)) as potential indicators of the strength of signal transduction initiation. We expect these velocities to be correlated with the velocity of dimerized receptor phosphorylation experimentally and computational results are presented in Figure 3-14.

$$vD_{front}(t,\overline{O}) = \frac{\int_{frontS}(D)dS}{P \times t} \tag{42}$$

$$vD_{back}(t,\overline{O}) = \frac{\int_{backS}(D)dS}{P \times t} \tag{43}$$

$$vH_{front}(t,\overline{O}) = \frac{\int_{frontS}(H)dS}{P \times t} \tag{44}$$

$$vH_{back}(t,\overline{O}) = \frac{\int_{backS}(H)dS}{P \times t} \tag{45}$$

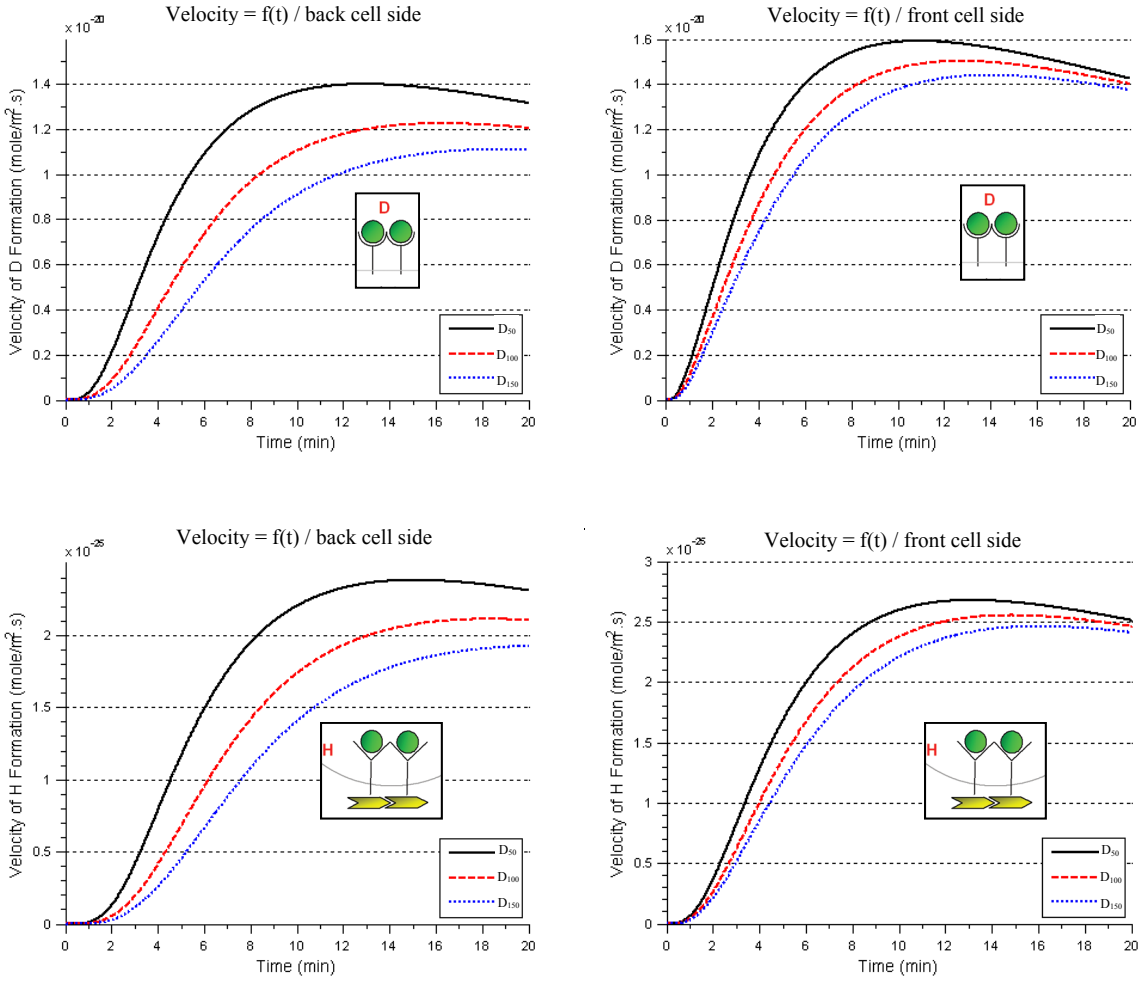

Figure 3-14: Velocity of formation of dimerized receptor-ligand complexes in the smooth pits *D* and dimerized receptor-ligand complexes in the coated pits *H* for three different diffusion coefficients and illustration of the effect of mass transport limitation on the velocity profiles. Top left: Velocity of formation of *D* on the back cell side computed as per equation (42). Top right: Velocity of formation of *D* on the front cell side computed as per equation (43). Bottom left: Velocity of formation of *H* on the back cell side computed as per equation (44). Bottom right: Velocity of formation of *H* on the front cell side computed as per equation (45) (D_{50} = 3.69x10^{-12} m^2/s, D_{100} = 1.84x10^{-12} m^2/s, D_{150} = 1.23x10^{-12} m^2/s).

The plots generated for *D* and *H* exhibited a non monotonic profile observed at the highest diffusion coefficient (D_{50}). In this case, the maximum velocity capacity is reached in approximately 10 minutes while with mass transfer limitation (D_{100} and D_{150}), maximal velocity is reached at a later time point and its amplitude is reduced. This indicates mass transfer limitations in the cell vicinity could affect the rate of receptor autophosphorylation following delivery and ultimately Erk activation. The time needed to reach this maximum amplitude with mass transfer limitation was consistent with computed times for maximal autophosphorylation levels in non-saturating EGF conditions between 15 and 20 minutes (Schoeberl, Eichler-Jonsson et al. 2002). This indicates system response, in terms of MAPK activation, can be different according to various delivery strategies. Of relevance, the effect of the diffusion coefficient on the velocity was reversed when the differential velocities of formation of *D* and *H* were analyzed.

$$differential\,vD(t,\overline{O}) = \frac{\int_{frontS}(D)dS - \int_{backS}(D)dS}{P \times t} \tag{46}$$

$$differential\,vH(t,\overline{O}) = \frac{\int_{frontS}(H)dS - \int_{backS}(H)dS}{P \times t} \tag{47}$$

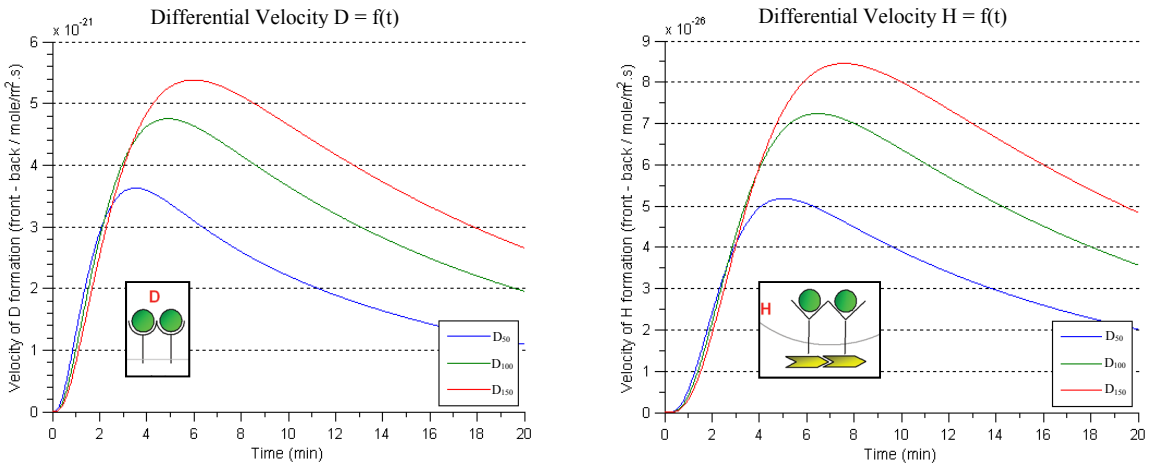

Figure 3-15: The measurement of the differential velocities between the front and back cell side for three diffusion coefficients demonstrates the effect of mass transfer limitations for the creation of spatial heterogeneity of velocities. Left: differential of *D* velocity computed as per equation (46). Right: differential of *H* velocity computed as per equation (47). (D_{50} = 3.69x10^{-12} m^2/s, D_{100} = 1.84x10^{-12} m^2/s, D_{150} = 1.23x10^{-12} m^2/s).

As shown in Figure 3-15, a small increase in the differential velocity was observed when the diffusion coefficient was decreased (smaller compared to what was observed with concentrations). In this situation, the monotonic profile exhibited a limited temporal shift compared to what was observed with the computed concentrations and maximal differential values were obtained at earlier time points (2 minutes for D_{50}, 3 minutes for D_{100} and 4 minutes for D_{150} in the case of *D*). The conclusions were similar for *H*. Two major events seem to occur during the polarization process:

- The differential rate of formation of dimerized receptor is maximal at early time points (2 – 6 minutes) and is slightly affected by the diffusion coefficient;
- The differential concentration of dimerized receptor is maximal at later time points (10 – 18 minutes) and is greatly affected by the diffusion coefficient.

This analysis provided guidelines as how to engineer systems in the context of polarized signaling. A decrease of the diffusion coefficient in the cell microenvironment slowed down the velocity profile of receptor dimerization and by inference of receptor phosphorylation / activation, while at the same time allowed for maximal computed differentials (concentration and velocity of formation) between the front and back cell sides. Internalization plays an important role in the regulation of EGF signalling. At low EGF concentrations, the phosphorylation kinetic is slowed down thereby increasing the relative importance of endosomal signals while at high EGF concentrations the rapid phosphorylation kinetic gives little importance to endosomal signals (Schoeberl, Eichler-Jonsson et al. 2002). An approach in which the diffusion coefficient is decreased in the direct cell vicinity could increase the significance of endosomal signals in the context of global cellular responses.

Receptor dimerization is also the prerequisite to the transphosphorylation step initiating the kinase activity. However, the role of kinase initiation on EGFR internalization is not clear. Some reports indicate the two processes are independent and that clathrin exclusively dictates EGFR complexes internalization (Luo, Cheng et al. 2011). Conversely, others report the dimerization of receptors controls the internalization process (Wang, Villeneuve et al. 2005). We propose the high velocity differential computed at early time points could elicit different kinetics of endocytosis in the cytoplasm between the front and back cell sides with respect to the point source of delivery.

Finally, EGF-EGFR complexes signal once in the endosomes and the subcellular diversity of protein complexes docking the Grb2-SOS system leads to different signaling

outcomes with respect to surface signals (Haugh and Lauffenburger 1998; Wang, Pennock et al. 2002). Also, a high initial velocity of heterodimer formation in E1/4 cells (which express both EGFR and Erbb4) contributes to selective binding of Grb2-SOS complexes to heterodimers versus homodimers (Nakakuki, Yumoto et al. 2008), thus demonstrating another mechanism of signal specificity directed by kinetic information.

Two successive events occur during polarization, with high velocity differentials computed initially followed by high concentration differentials at later time points. The maximum velocity of formation of dimerized receptors reached in the first ten minutes indicates maximum Erk activation would occur during this time frame. Mass transfer limitation could contribute to heterogeneous activation due to high velocity differentials computed in the first six minutes of delivery. The spatial impact on cellular processes such as internalization and signal specificity illustrate the potential effect of controlled release of growth factors around a single cell in the context of signaling. To further analyze the spatial asymmetry in the system, we evaluated the Polarization Index PI as described above.

Polarization Index

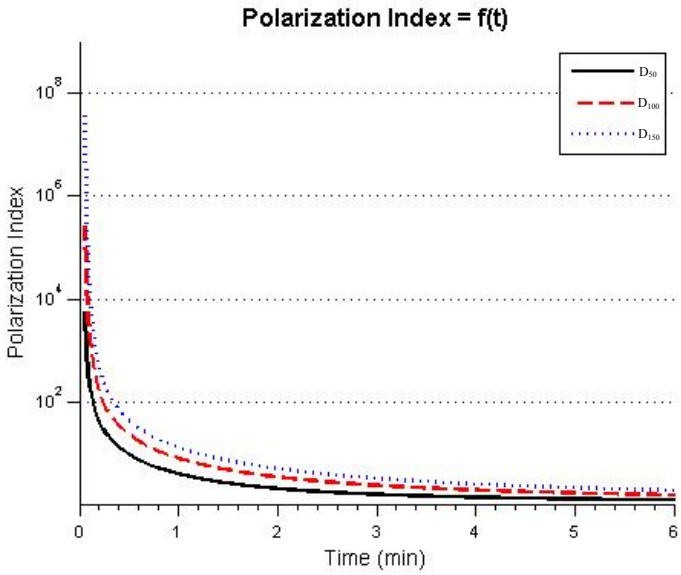

Figure 3-16: Asymmetric delivery on the scale of a single cell is a fast process. PI demonstrates the rapid decrease of dimerized receptors asymmetry on the cell surface over time. Comparison between different values of diffusion coefficient demonstrates a modification of PI during the first minutes, with increased mass transfer limitation contributing to an increase in PI (D_{50} = 3.69x10^{-12} m^2/s, D_{100} = 1.84x10^{-12} m^2/s, D_{150} = 1.23x10^{-12} m^2/s).

PI was computed as previously using equation (32). Figure 3-16 shows typical simulation results in which maximal PI was achieved at the beginning of the process followed by a rapid decrease in magnitude as the ligand subsequently diffuses to the back side of the cell. PI reached an approximate value of 1.1 in five minutes, which indicates a loss of polarized bound entities on the cell surface. The initial wave of molecules is responsible for the maximal PI value, as with mass transport limitations the time required to reach the back cell side via diffusion increases. The early polarized state is thus consistent with highly heterogeneous velocities but not concentrations, as demonstrated in the previous section. Hence, while the maximum asymmetry of surface concentrations is reached initially, the maximum differential of concentrations is reached after 10 minutes. This result is due to the considerably low range of initial computed concentrations.

The polarization strategy in the context of EGF binding and trafficking favors velocity sensitive systems and thus allows for spatially-controlled elicited MAPK signals at the single-cell level. Signal control could occur both in terms of the amount of phosphorylated downstream effectors (MEK, Erk) regulating signal intensity and in terms of signal specificity as discussed previously. While PI does not provide additional information compared to the analysis of concentrations and velocities, PI is non-dimensional and can serve as a reference for the comparison of polarization strategies and efficiencies between different delivery systems. PI can also be evaluated experimentally by measuring the ratio of fluorescence intensities on a cell surface. PI will be used for model fit with experimental data. To ensure that the computed differentials are consistent with signaling, we further studied the percentage of receptor occupancy (PO) as shown in Figure 3-17.

Percentage Occupancy

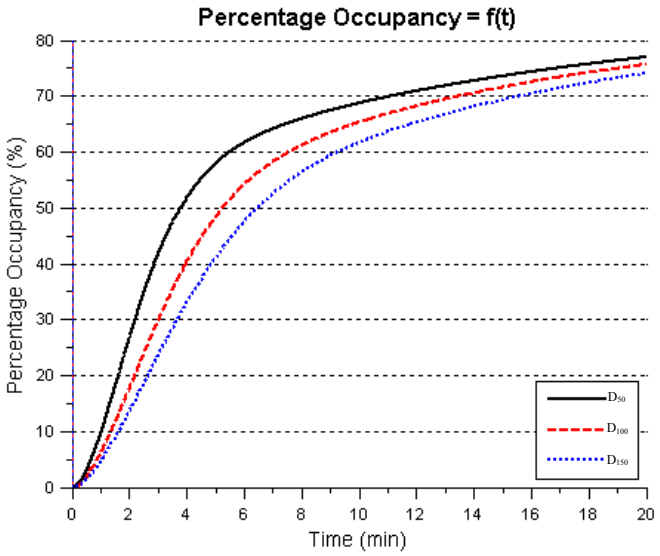

Figure 3-17: Analysis of percentage of receptor occupancy PO computed as per equation (36) for three diffusion coefficients. The computations indicate that levels of binding on the cell surface are consistent with signaling levels and a reduction in the diffusion coefficient slightly affects the profile of occupancy over time (D_{50} = 3.69x10^{-12} m^2/s, D_{100} = 1.84x10^{-12} m^2/s, D_{150} = 1.23x10^{-12} m^2/s).

Computed concentrations on the cell surface were consistent with signaling potential. PO exhibited a monotonic profile with increasing computed values over the course of the computation, indicating saturation of free receptors did not occur. With the highest diffusion coefficient (D_{50}), a PO of 25% was reached in two minutes. In the case of EGFR, we discussed previously that 70 to 90% of maximal Erk activation can be observed for occupancy ranges between 15 and 55%. Occupancy levels after one minute under diffusive mass transport limitations were thus consistent with signal activation. Furthermore, we investigated the differential occupancy levels between the front and back cell side with respect to the point source of factor delivery as shown in Figure 3-18:

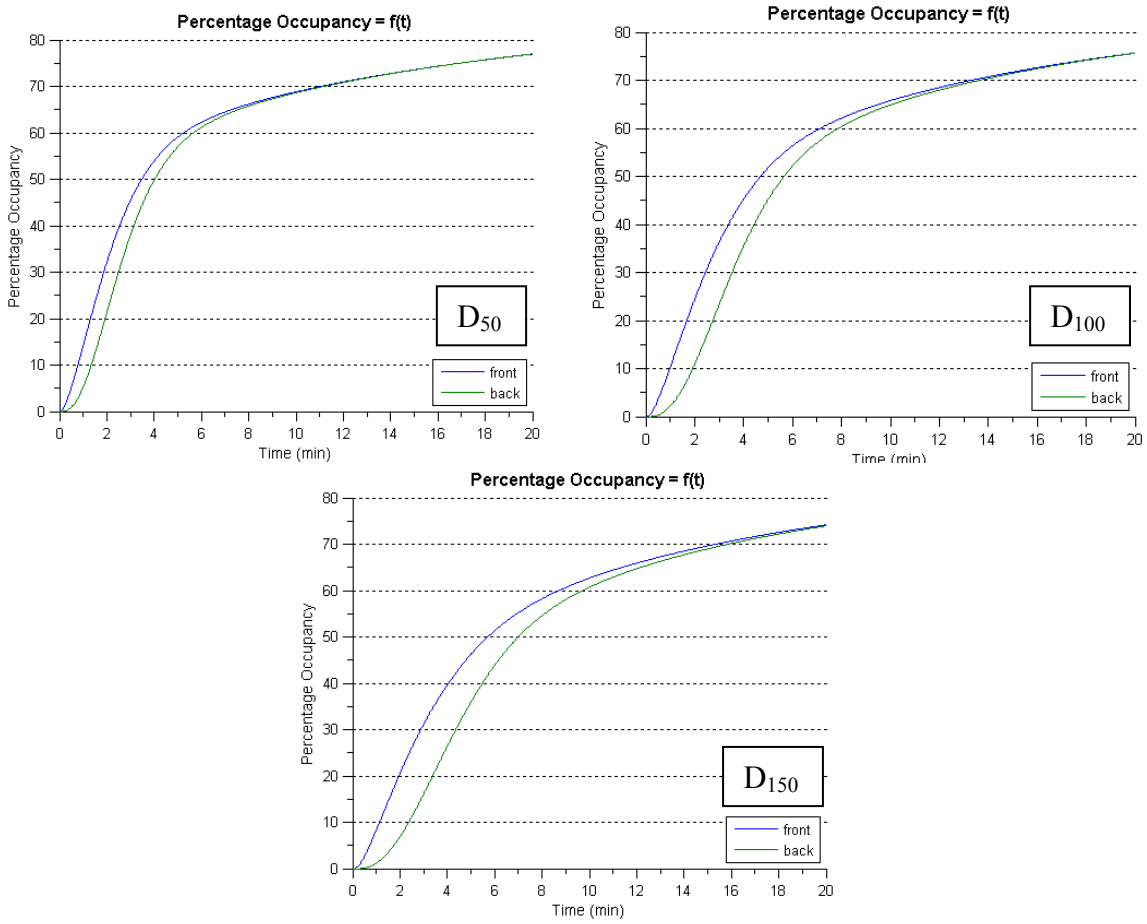

Figure 3-18: Comparison between front and back computed percentage occupancy (PO computed as per equation (36)) with respect to the point source of factor delivery for three different diffusion coefficient values. Maximum computed occupancy differences are indicated in red. Top left: $D_{50} = 3.69.10^{-12}$ m^2/s. Top right: $D_{100} = 1.84.10^{-12}$ m^2/s. Bottom left: $D_{150} = 1.23.10^{-12}$ m^2/s.

The plots above illustrate the "polarization window" available to reach a threshold on the front cell side while not initiating signals on the back cell side, hence activating the signaling pathway in a spatially controlled manner. The maximum computed window between the front and back cell side was reached during the first three minutes of the polarization process with a 10% window reached after two minutes for D_{50}, 13% after two minutes 30 seconds for D_{100} and 16% after three minutes for D_{150}. As the diffusion coefficient in the microenvironment was decreased, the maximum occupancy differential was reached at later time points but no later than three minutes post-delivery, time frame consistent with the previously identified 'velocity

polarized" state. Based on Schoeberl's analysis, their results demonstrated that heterogeneity of occupancy levels on the cell surface were not compatible with asymmetric activation of Erk in the cytoplasmic compartment after three minutes as all systems will have reached the lower threshold of 15% PO on the back cell side by this time. Occupancy levels were completely or near-completely homogeneous after 10 minutes. This demonstrates that the constant release of factor in the cell vicinity may not be consistent with achieving polarization, and that shorter lengths of EGF pulses should be studied. Engineered microenvironments of soluble factor can be translated in heterogeneous occupancy levels on the cell surface at early time points (< 3 min), thus offering the possibility for transient signals activated in a spatially controlled manner.

Experimental Results

Delivery experiments of FITC in collagen were performed to estimate gel viscosity and define necessary collagen concentrations to ensure consistency with preliminary computations. Experimentally, several technical difficulties were encountered:

- The concentration of collagen consistent with preliminary computations and analysis was not compatible with imaging and the high gel density did not allow for brightfield / phase contrast / DIC imaging;
- Collagen autofluorescence was observed in the FITC channel, along with autofluorescence from the culture media;
- Collagen adherence in glass chambers was limited and cast gels detached from the glass surface upon media addition. To circumvent this issue, collagen coating of glass was performed with no observed improvements;

- Collagen dehydration was observed, even when the gel was submerged in culture media and it was hypothesized this was caused by the high gel density;
- The micropositioning of the delivery system in the cell vicinity significantly disturbed the collagen matrix. Thus the diffusion properties of EGF molecules in the cell microenvironment could have been considerably altered.

We were not able to accurately measure the diffusion of FITC in collagen gels and hence evaluate experimentally gel viscosity and diffusivity. Also, these challenges illustrated the difficulty associated with high resolution fluorescent imaging of cells cultivated in collagen matrices necessary for polarization analysis *in vitro*.

Summary

We demonstrated how a two-dimensional finite-element model of diffusing ligand with binding to surface receptors could be used to analyze the spatial distribution of molecules. We developed a set of metrics to analyze and quantify the degree of both asymmetry and occupancy at the single cell level. Two successive stages were identified during the controlled delivery process: a "velocity polarized" state followed by a "concentration polarized" phase, the latter being the most influenced by the diffusion coefficient in the media. The analysis of PI demonstrated the transient nature of bound molecules asymmetry on the cell surface and how a decrease of the diffusion coefficient in the microenvironment could contribute to improvements of PI at early time points. Even with high mass transfer limitation, the evaluation of occupancy levels indicated that local concentrations were consistent with the activation of downstream signaling pathways such as MAPK/Erk. When studying the occupancy differentials, we

demonstrated that a polarization window can be created during the first minutes. In conjunction with the velocity polarized state, the first minutes of the delivery offer the possibility for spatially controlled signals both in terms of intensity and specificity. Spatial heterogeneities in the velocity of formation of target members of the pathway could be responsible for various kinetics of internalization and associated pools of cytoplasmic adaptor proteins. Nonetheless, these effects would be transient as computed velocities of formation were homogeneous after ten minutes along with occupancy levels. As such, polarization could be achieved only if it is correlated with the cell cycle, thus ensuring the cell will divide before asymmetry is lost.

3.4.5 Diffusion in the Micropipette as a Controlled Variable

In this section, a second strategy for controlled EGF release was evaluated. For this model, the cell was cultured in media (diffusion of EGF in water at 20ºC), and polarized delivery was accomplished through a micropipette loaded with a gel of controlled porosity. Acrylamide was selected and preliminary experiments were performed to evaluate the diffusion coefficient in acrylamide gels at different percentage of cross-linking. Initial experiments were performed in glass tubes (length of four centimeters, diameter of 5 millimeters) loaded with Fluorescein IsoThioCyanate (FITC, Molecular Probes, Canada) at a concentration of 50 μg/mL. FITC Release experiments from acrylamide gels were performed to evaluate gel viscosity and further assess the diffusion coefficient of EGF in the micropipette.

Material and Methods

Samples of various polyacrylamide gels were prepared as outlined in Table 3.

Volume (mL)	gel %						
	5	7.5	9	10	12	15	20
Acrylamide/Bis-acrylamide (30%/0.8%)	0.5	0.76	0.9	1	1.2	1.5	2
gel buffer PBS 2X	1.5	1.5	1.5	1.5	1.5	1.5	1
Distilled water	1	0.74	0.6	0.5	0.3	0	0

Table 3: Preparation of polyacrylamide gels.

The various gels were prepared by mixing the reported volumes of 30% / 0.8% Acrylamide/Bis-acrylamide stock solution (Invitrogen, Canada), phosphate buffer solution (PBS 2x, Invitrogen Canada) and de-ionized water. FITC solution was added to the gels and the mixture was subsequently degassed for two to five minutes. After degassing, 10 µL of Ammonium PerSulfate (APS, Gibco, Canada) and TEtraMethylEthyleneDiamine (TEMED, Invitrogen, Canada) were added to the solution to initiate gelling. The mixture was immediately transferred into a tube and covered with a lightly greased cover slip to prevent oxygen from entering the system.

A Cary Eclipse spectrofluorimeter (courtesy of Professor Guillemette, Department of Chemistry, University of Waterloo) was used to measure sample fluorescence. Each cuvette was filled with a PBS buffer solution and a micro-stir bar was inserted to ensure proper homogenization and accurate fluorescence readings. The loaded tube to be examined was inverted and placed on top of the cuvette to ensure contact with PBS solution. The diffusion of FITC through various gel concentrations was determined by examining the increase of fluorescence of each sample in the cuvette. The following setup was used for analysis:

- Carry Eclipse: kinetics mode
- Excitation Wavelength: 485 nm ; Excitation Slit: 2.5 nm
- Emission: 520 nm; Emission Slit: 5 nm
- Average time: 1 s

Experimental Results

The release of FITC from various polyacrylamide gels and increase of FITC fluorescence in the cuvette is presented in Figure 3-19:

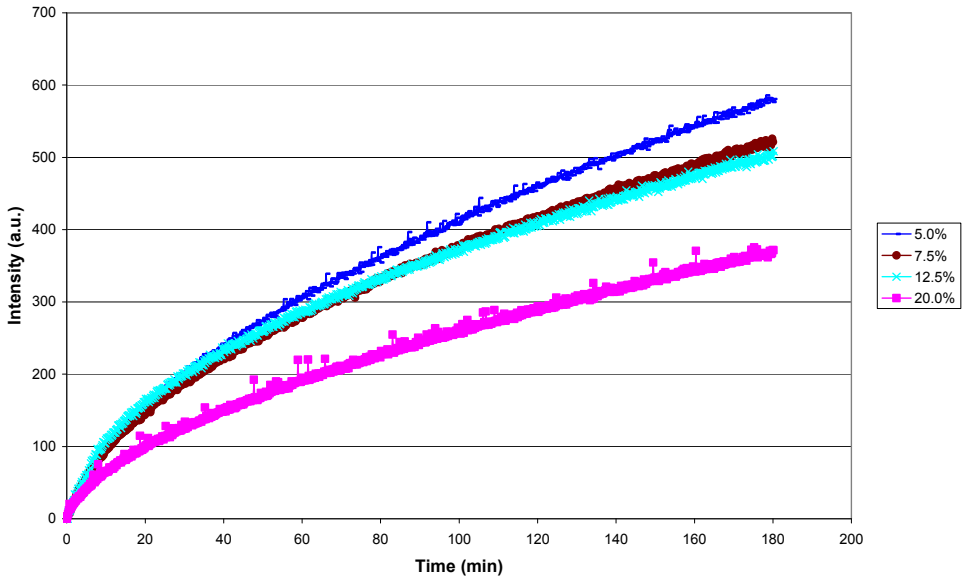

Figure 3-19: Fluorescence time-course of FITC release from gels of various % polyacrylamide. 5% polyacrylamide: Dark blue; 7.5% polyacrylamide: Brown; 12.5% polyacrylamide: Light blue; 20% polyacrylamide: Pink.

The data presented above demonstrated a correlation between polyacrylamide gel percentage and release of FITC from the gel. Lower percentage gels released FITC more rapidly in the cuvette but some discrepancy was observed between the 7.5% and 12.5% polyacrylamide gels; possible causes will be discussed below. This data was further used to estimate the initial release rate from the macrotube as shown in Figure 3-20:

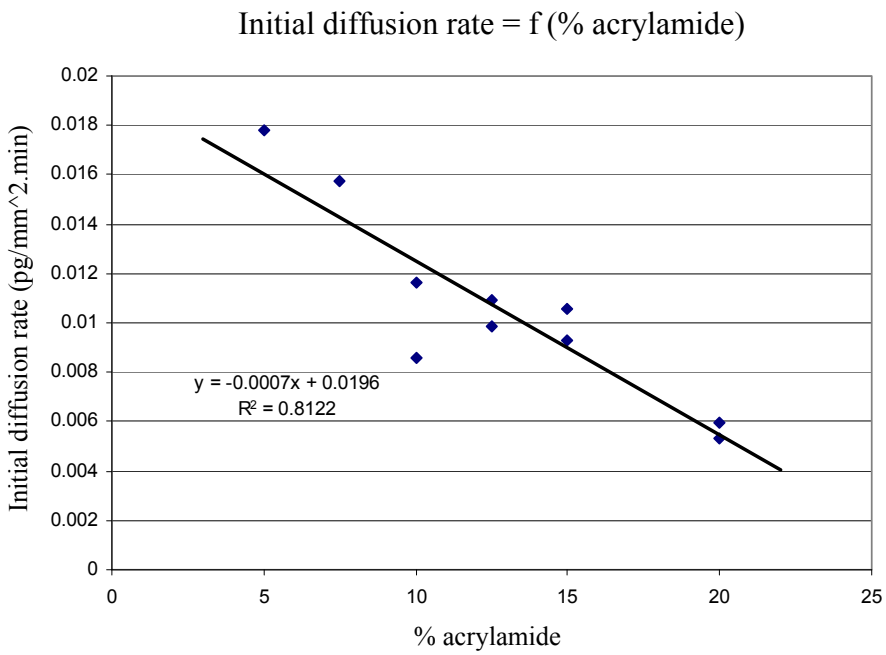

Figure 3-20: Initial Diffusion Rates of FITC from polyacrylamide gels at various percentages.

The results above exhibited a linear relationship between the initial diffusion rate of FITC and the gel concentrations. Using Fick's first law, we calculated the diffusion coefficient for three percentages of cross-linking (5%, 10% and 20%). The Stokes-Einstein equation, the molecular weight and density of FITC (MW = 389.38 Da; $\rho = 1.548$ g/cm^3) were further used to assess the viscosity of each gel:

- 5% : $D_{FITC1} = 2.4 \times 10^{-13}$ m^2/s and $\mu_1 = 1.46$ kg/m.s
- 10% : $D_{FITC2} = 1.6 \times 10^{-13}$ m^2/s and $\mu_2 = 2.2$ kg/m.s
- 20% : $D_{FITC3} = 8 \times 10^{-13}$ m^2/s and $\mu_3 = 4.39$ kg/m.s

Using these viscosity values, the diffusion of EGF in these gels was measured:

- $D_5 = 1.26e^{-13}$ m^2/s;
- $D_{10} = 8.4e^{-14}$ m^2/s;
- $D_{20} = 4.2e^{-14}$ m^2/s.

During FITC delivery experiments, several technical difficulties were encountered. First, rapid cross-linking of highly viscous solutions (cross-linking > 10%) prevented homogeneous loading of macrotubes. Even for lower cross-linking values, gel loading was affected by bubble formation occurring during the degassing step. Following loading, gels exhibited some contraction from the macrotube walls, thereby increasing the surface directly in contact with the media and potentially affecting the actual release rate. This phenomenon could explain the discrepancy observed between the 7.5% and 12.5% polyacrylamide gels. Finally, the loading process was unsuccessful during scale-down experiments, raising a feasibility concern with respect to the preparation of homogeneously loaded micropipettes in the μm range.

Concentrations

In this section, we focus on the differences observed with respect to the first delivery strategy. The two-dimensional finite-element model used in COMSOL was identical to the one used in the previous section apart from the changes for the diffusion coefficient. The diffusion coefficient in the media was defined based on diffusion in water at 20ºC (D_{med} = 1.84 e-10 m^2/s). Diffusion in the micropipette was a controlled variable (D_5, D_{10} and D_{20}).

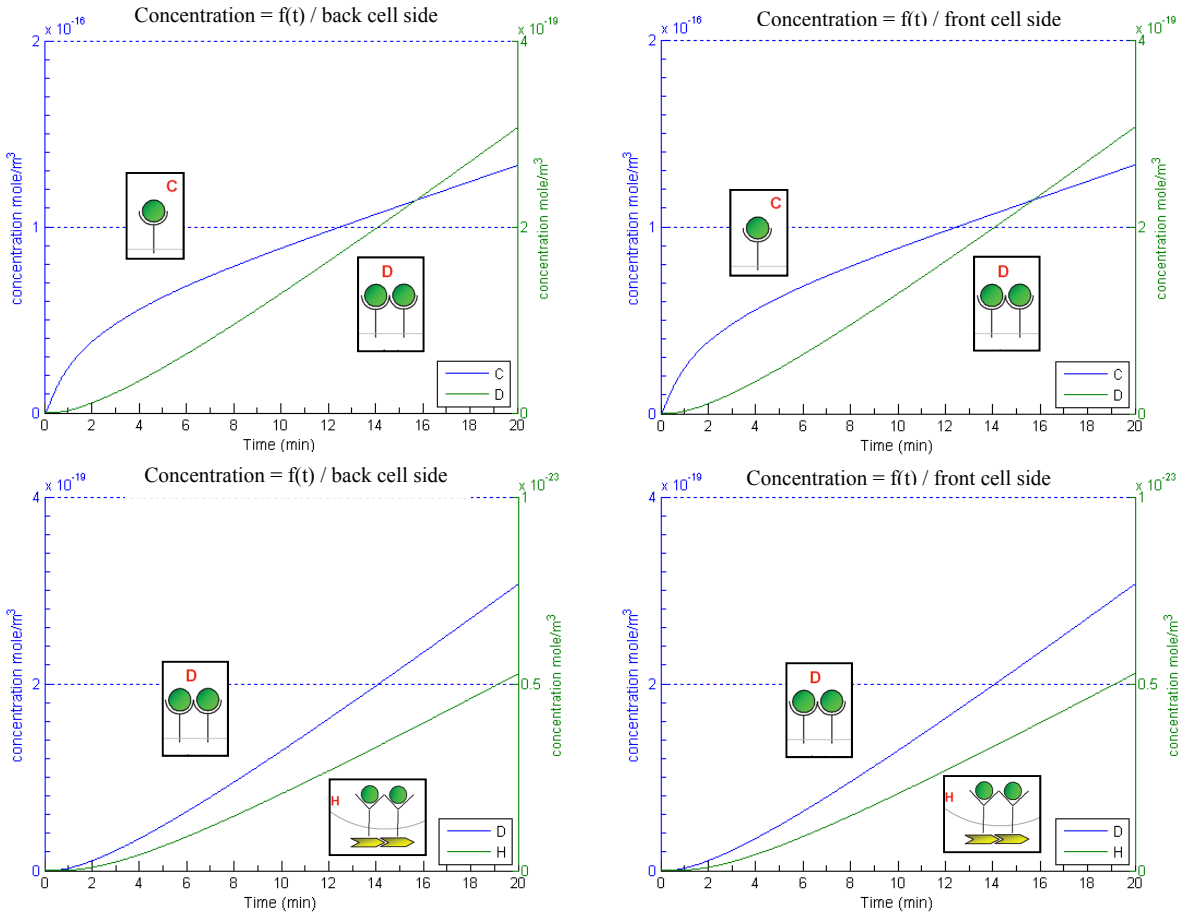

Figure 3-21: Analysis of computed concentrations of various members of the kinetic system (receptor-ligand complexes *C*, dimerized receptor-ligand complexes in the smooth pits *D*, dimerized receptor-ligand complexes in the coated pits *H*) for $D_5 = 1.26 \times 10^{-13}$ m^2/s in the delivery system. Top left: Computed concentration of *C* (blue) and *D* (green) on the back cell side. Top right: Computed concentration of *C* (blue) and *D* (green) on the front cell side. Bottom left: Computed concentration of *D* (blue) and *H* (green) on the back cell side. Bottom right: Computed concentration of *D* (blue) and *H* (green) on the front cell side.

We first analyzed computed concentrations of *C*, *D* and *H* on the front and back cell surface for the highest diffusion coefficient D_5 as shown in Figure 3-21. In the acrylamide system, these values were on average two orders of magnitude lower than in the collagen system. Based on the apparent diffusion coefficient in the micropipette, this approach significantly reduced the amount of EGF molecules delivered in the media but did not slow down the motion

of EGF molecules following release. Concentrations were increasing steadily over the course of the computations, indicating ligand was limiting and that the system did not reach saturation.

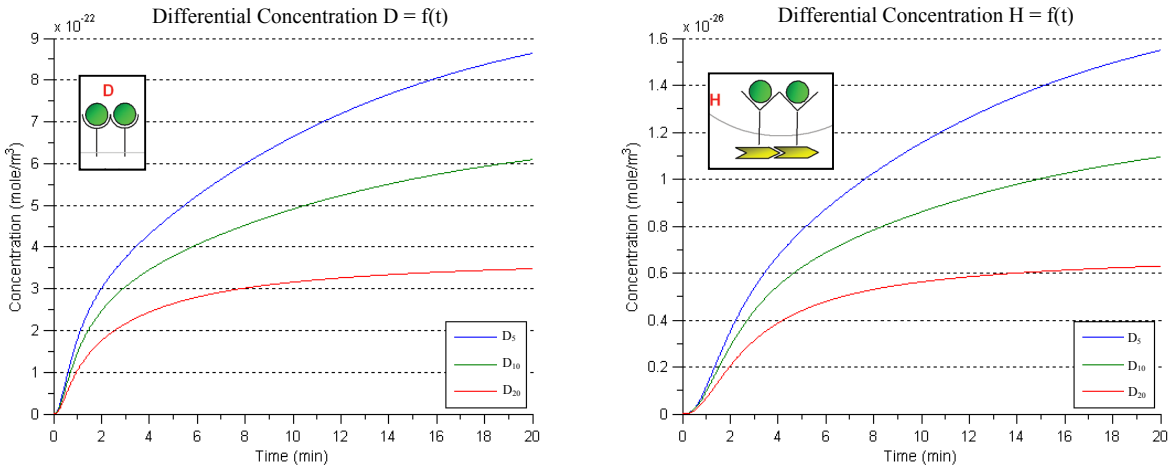

Figure 3-22: The measurement of the differential concentration between the front and back cell side for three different diffusion coefficients exhibits opposite response to mass transfer limitation compared to the collagen system. Left: differential of *D* concentration computed as per equation (40). Right: differential of *H* concentration computed as per equation (41). ($D_5 = 1.29x10^{-13}$ m^2/s, $D_{10} = 8.4x10^{-14}$ m^2/s, $D_{20} = 4.2x10^{-14}$ m^2/s)

When looking at the differential concentration of dimerized receptor-ligand complexes in the smooth pits (*D*) and coated pits (*H*), significant differences were observed when compared to the collagen system as shown in Figure 3-22. First, the computed differences were significantly smaller (four orders of magnitude smaller for *D*, three for *H*), thus raising the possibility that a polarization window was not effectively created in this system on the basis of surface concentrations. Also, the effect of the diffusion coefficient in this system was reversed: decreasing the diffusion coefficient in the micropipette led to a reduction of differential concentrations. Without diffusion limitation in the direct cell microenvironment, limiting the amount of molecules delivered had no beneficial effect on polarization as diffusion between the front and back cell side occurs rapidly. Consistent with these findings, no time shift could be observed to reach the maximum differential when the diffusion coefficient was decreased,

indicating the diffusion in the media was governing once EGF molecules are released. We next analyzed the velocity of formation of (*D*) and (*H*) on the cell surface.

Velocities of Formation

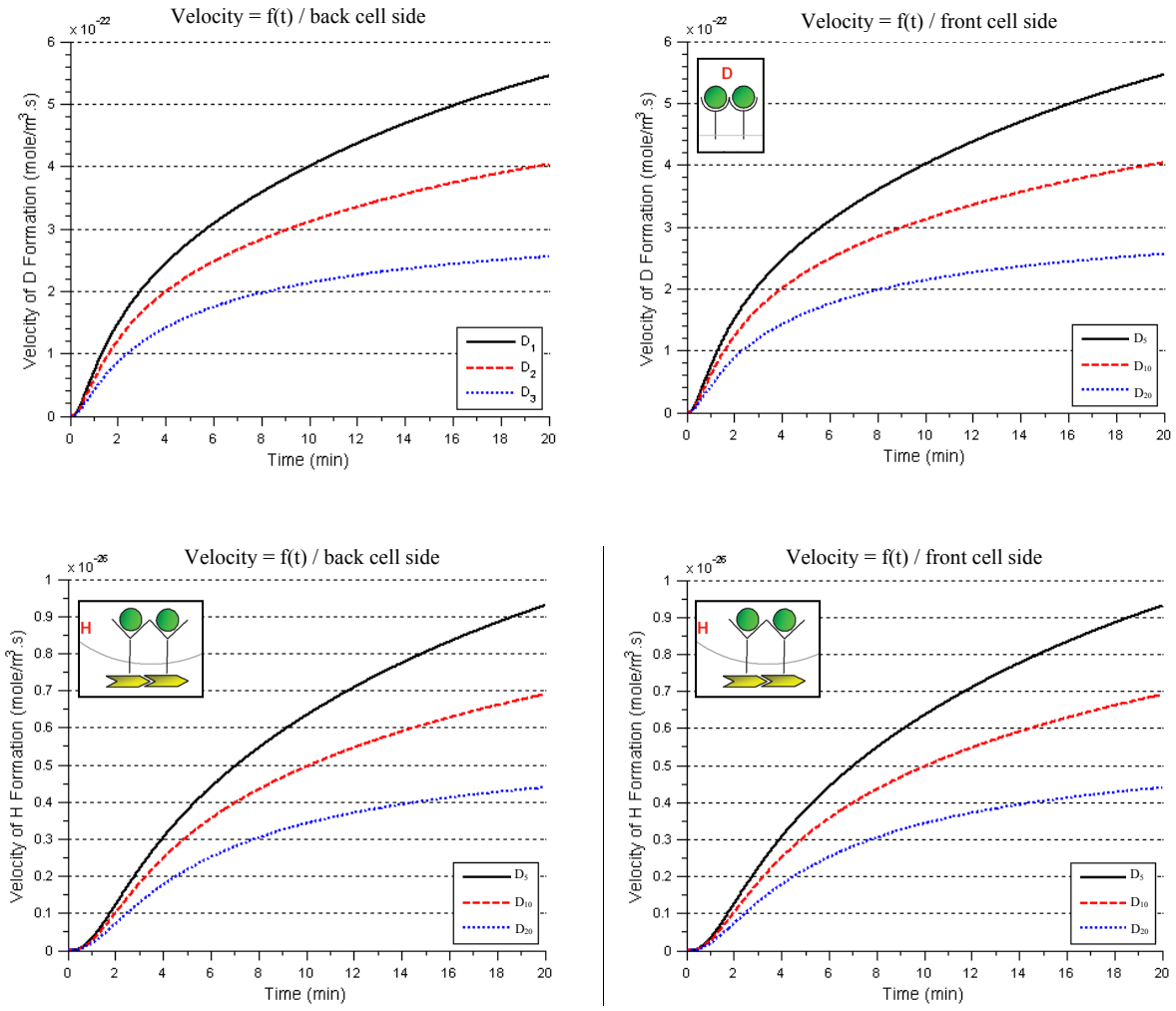

Figure 3-23: Velocity of formation of dimerized receptor-ligand complexes in the smooth pits *D* and dimerized receptor-ligand complexes in the coated pits *H* for three different diffusion coefficients and illustration of the effect of mass transport limitation on the velocity profiles. Top left: Velocity of formation of *D* on the back cell side computed as per equation (42). Top right: Velocity of formation of *D* on the front cell side computed as per equation (43). Bottom left: Velocity of formation of *H* on the back cell side computed as per equation (44). Bottom right: Velocity of formation of *H* on the front cell side computed as per equation (45). ($D_5 = 1.29x10^{-13}$ m^2/s, $D_{10} = 8.4x10^{-14}$ m^2/s, $D_{20} = 4.2x10^{-14}$ m^2/s).

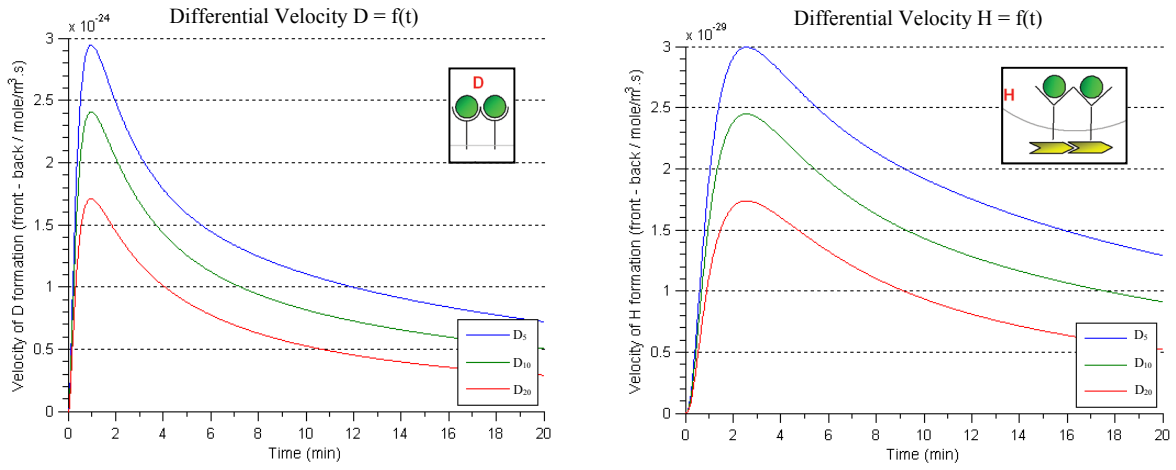

Figure 3-24: The measurement of the differential velocities between the front and back cell side for three diffusion coefficients demonstrates the effect of mass transfer limitations for the creation of spatial heterogeneity of velocities. Left: differential of *D* velocity computed as per equation (46). Right: differential of *H* velocity computed as per equation (47). ($D_5 = 1.29x10^{-13}$ m^2/s, $D_{10} = 8.4x10^{-14}$ m^2/s, $D_{20} = 4.2x10^{-14}$ m^2/s)

The analysis of velocities of formation of *D* and *H* demonstrated the lower order of magnitude of computed velocities compared to the collagen system as shown in Figure 3-23. Velocity profiles were non-monotonic with maximum differential reached in the first five minutes for all diffusion coefficients tested. Nonetheless, computed differences were smaller than in the collagen system (three orders of magnitude on average) as shown in Figure 3-24 raising the possibility these differentials may not be significant in the context of signaling. The effect of the diffusion coefficient was reversed compared to the collagen system, and no time shift was observed for the maximal differential when mass transfer limitation was increased in the delivery system.

Polarization Index

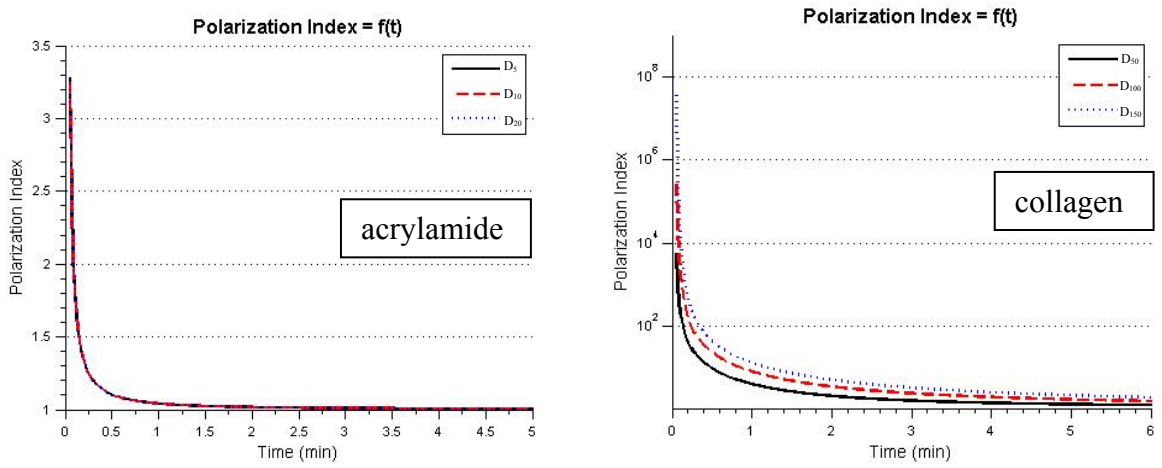

Figure 3-25: The acrylamide system (left) exhibits an important loss of polarization when molecules freely diffuse in the cell microenvironment compared to collagen embedding technique (right). For the acrylamide system: $D_5 = 1.29x10^{-13}$ m^2/s, $D_{10} = 8.4x10^{-14}$ m^2/s, $D_{20} = 4.2x10^{-14}$ m^2/s. For the collagen system: $D_{50} = 3.69x10^{-12}$ m^2/s, $D_{100} = 1.84x10^{-12}$ m^2/s, $D_{150} = 1.23x10^{-12}$ m^2/s. PI was computed as per equation (32).

A shown in Figure 3-25, the diffusion in water in the direct cell vicinity triggered a significant decrease in computed PI values, with a maximum of 3.25 for the first time point. PI decreased to 1.1 in 30 seconds, indicative of the speed at which asymmetry was lost in this system. A decrease of the diffusion coefficient in the micropipette exhibited no effect on PI profile which demonstrated the asymmetry of soluble molecules binding on the cell surface is dependent upon mass transfer limitation in the cell microenvironment rather than on the amount of soluble molecules released from a point source when diffusion around the cell is rapid.

Percentage Occupancy

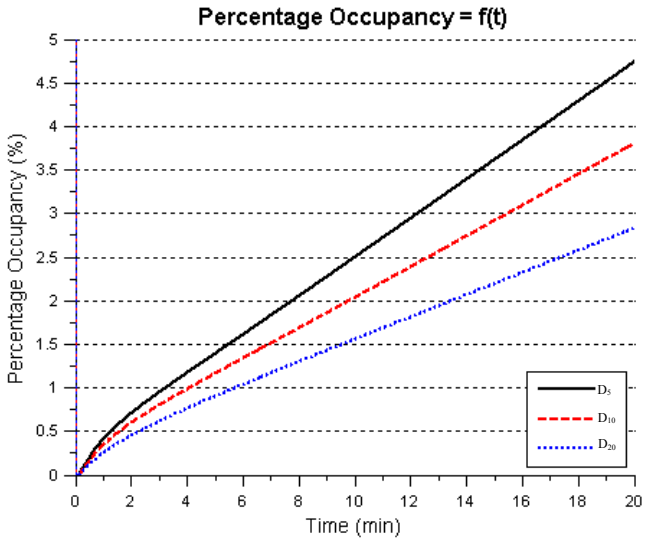

Figure 3-26: Percentage of receptor occupancy. The computations indicate that levels of binding on the cell surface are not consistent with signaling levels in the acrylamide system and a reduction of the diffusion coefficient in the micropipette did not produce significant changes of occupancy profiles ($D_5 = 1.29x10^{-13}$ m^2/s, $D_{10} = 8.4x10^{-14}$ m^2/s, $D_{20} = 4.2x10^{-14}$ m^2/s). PO was computed as per equation (36).

Finally, the computed occupancy levels as shown in Figure 3-26 demonstrated PO was below 5% at all times, thus indicating that levels of EGF in the culture media were not consistent with MAPK activation. The comparison between front and surface occupancies demonstrate that spatial heterogeneity was not achieved in this system, with a maximum computed PO difference below 1e-3% in the first minute of the process (data not shown).

3.5 Conclusions and Future Directions

We have developed a comprehensive two-dimensional finite-element model of single cell polarization with soluble factors that considers mass transfer and reaction kinetics to analyze the creation of controlled polarized microenvironments *in vitro*. Metrics were developed that account for (I) the asymmetry of ligand binding on the cell surface (PI); (ii) the percentage of occupancy

of receptors on the cell surface; and (iii) the concentration and velocity differentials for dimerized ligand-receptor complexes in the smooth (*D*) and coated (*H*) pits with respect to the point source of delivery. Focusing on the applicability of this computational framework to other signaling pathways, general definitions were proposed that can be adapted for other binding and trafficking models. Structured metrics and parameter sets are needed for informatics-based *post hoc* analysis.

We initially analyzed the effect of system geometry on response profiles for the Polarization Index PI and the Percentage of receptor Occupancy PO, which illustrate both the asymmetry and signaling potential following controlled release. The advantages of finite-element models were illustrated, as geometrical effects were important at the single-cell level. The analysis of surface response profiles allowed for the definition of working micropipette dimensions and distance from the target cell. Of relevance, the importance of the cell diameter was demonstrated, highlighting the need for predefined cellular systems. Based on the proposed metrics and the defined micropipette configuration, our analysis subsequently focused on two distinct strategies for controlled EGF release: one in which EGF was delivered from a micropipette (i.e. point source of delivery) in a collagen matrix in which the cell was embedded, and one in which the cell was cultured in media (diffusion in water) with controlled EGF release from a micropipette loaded with an acrylamide gel of controlled porosity.

In a system in which collagen limits the diffusion of molecules in the cell microenvironment, polarization is high. Slowed motion of EGF molecules around the cell increases the time needed for diffusing molecule to go from the front to the back cell side with

respect to the point source of delivery. Hence, the polarization window is improved and a initial conditions allowed for occupancy levels consistent with downstream signaling through the MAPK/Erk pathway. When looking at the diffusion effect on concentrations and velocities of formation of key pathway members, we observed a biphasic response in which the system was initially "velocity polarized" and subsequently "concentration polarized", phenomenon further amplified by the reduction of the diffusion coefficient in the direct cell vicinity. The velocity polarized system is of particular relevance in the case of EGF as this type of kinetic information is consistent with activation of downstream signaling cascades, such as intracellular Erk. We demonstrated that heterogeneities in local EGF concentrations can be translated in heterogeneities of occupancy levels on a single cell surface with respect to the point source of delivery, thus enabling polarization windows in which different levels of MAPK activation can be reached on the front and back cell sides. Several reports (as previously stated) indicate the velocity of receptor activation can control the specificity of docking proteins and internalization through the clathrin-mediated pathway. Elicited signals could thereby be different based on different kinetic states and different subcellular localization of dimerized complexes. Controlled EGF release could thus transiently enable different signal intensity but also specificity between the front and back cell side with respect to the point source of delivery.

When the delivery was exclusively controlled through the porosity of a gel inside the micropipette, no improvements of polarization were observed as the rapid diffusion of EGF molecules around the cell did not allow for the asymmetric delivery of molecules. Also, levels of occupancy computed for experimental values of acrylamide gel viscosity were not compatible with MAPK signal responses.

At the single cell level, limiting the diffusion of soluble molecules in the cell vicinity is a requirement for polarization and the translation of asymmetric environment of soluble factors to an asymmetry of receptor occupancy on the cell surface. *In vivo*, diffusion of soluble molecules is restricted in the cell microenvironment as local gradients of factors can be created by entrapment of molecules in the extracellular matrix (Dowd, Cooney et al. 1999). This indicates that natural tissues have a predisposition to polarize cells as molecules in the extracellular matrix exhibit a slower apparent diffusion coefficient. As a result, culture system design should move towards more biomimetic transport rates to allow for the development of polarization.

In the literature, different percentages of the total cell volume have been used to model the endosomal compartment, ranging from 0.00003% (Schoeberl *et al*., 2002) to 100% (Athale, Mansury et al. 2005). A modification of the endosomal volume would have significant effects on our computations, and this raises concerns with respect to the inclusion of the endosomal fraction in the model. To improve model relevance, the system should be tailored for a specific cell type that can be studied experimentally. In this context, the HeLa CCL2 system (expressing EGFR) was selected due to its wide availability, ease of culture and extensive literature available for estimation of kinetic parameters. Additionally, to ensure model relevance, the system should also be simplified to include kinetic parameters that can be measured experimentally. The two strategies for controlled EGF release demonstrated technical challenges. Also, the stiffness of the extracellular matrix can influence the differentiation of stem cells (Even-Ram *et al*., 2006). This indicates that cultivating cells in a matrix could provide environmental signals that would bias our analysis of polarization with soluble factors. The effect of local absorbing and non-absorbing boundaries in the cell microenvironment should be studied as an alternative to embedding in

collagen as collagen embedding may perturb cell fate decisions independent of soluble factor gradients. Local boundaries could limit the free diffusion of molecules around a cell and could possibly help potentiate polarized signals *in vitro*. For all these reasons, we propose the following improvements to the existing model:

- Modeling should be performed in three dimensions and the effect of the local geometry (addition of reflective surfaces to model adherent culture conditions) on the delivery strategy should be evaluated;
- Diffusion in water should be preferred in the analysis but the effect of neighboring cells on polarization should be investigated;
- The kinetic model should be developed according to the HeLa cell system and the finite-element model should be updated to account for a cell diameter of 20 μm;
- A new strategy of delivery should be experimented in which we compare different lengths of delivery pulse;
- Model should be simplified to include experimentally identifiable parameters and evaluation of kinetic constants for the selected cell system should be performed (k_f and R_{init});
- The model should be correlated to experimental PI measurements.

4 Chapter 4: Three-Dimensional Finite-Element Modeling of Controlled EGF Release to a Single Cell

4.1 Overview

Receptor Tyrosine Kinases (RTKs) have been studied for over three decades and their mechanism of activation and signal transduction are well understood (Cohen and Carpenter 1975). Once a factor binds to its specific receptor, the newly formed complex is internalized and triggers the activation of cytoplasmic proteins through phosphorylation. This cascade of protein and small molecules moves to the nucleus where they act as transcription factors to control the expression of target genes and initiate cellular responses. Regulatory mechanisms involve early and late endosomal compartments in which complexes are dissociated, growth factors directed towards lysosomes for subsequent degradation and receptors recycled to the cell surface (Vieira, Lamaze et al. 1996; Zheng, Lavoie et al. 2004; Mizuno, Iura et al. 2005; Sorkin and Goh 2009). Among this family of receptors, the Epidermal Growth Factor (EGF) and EGF receptor (EGFR) have been studied extensively. EGFR signaling is involved in a variety of stages in embryonic/post-natal and tumorigenic development (Carpenter 1987; Steinbach, Borchers et al. 1998) and can elicit various cellular responses including proliferation, growth inhibition, differentiation, cell migration and apoptosis (Carpenter 1987; Darcy, Wohlhueter et al. 1999; Schlessinger 2000; Schlessinger 2004). Upon EGF binding, receptors dimerize which triggers the transphosphorylation step of the EGFR cytoplasmic domain. Src homology domain 2 (SH2) or phosphotyrosine binding (PTB) domain-containing transducers are then recruited which initiates the phosphorylation cascade (Schlessinger and Ullrich 1992; Schlessinger 2002).

Ultimately, target genes are activated through several signaling pathways including the Mitogen Activated Protein Kinase / Extracellular Regulated Kinase (MAPK/Erk).

In the context of cell fate, the subcellular localization of factors, associated receptors, proteins and RNA at the time of mitosis is responsible for many cell fate decisions. For example, asymmetric EGFR distribution (or EGFR polarization) at the time of mitosis has been correlated with control of cell fate in cancer keratinocytes and mouse cortical stem cells *in vitro* (Le Roy, Zuliani et al. ; Sun, Goderie et al. 2005). It is unclear whether EGFR localization in these systems is the result of an intrinsic genetic program or extrinsic heterogeneities in the cell microenvironment such as local gradients. The controlled release of soluble factors *in vitro* and analysis of polarization at the single cell level will elucidate the existence of the extrinsic mechanism in the context of EGF.

Gradients of soluble factors are biologically significant as illustrated during embryogenesis. Spatial and temporal modulation of gradients creates heterogeneous cell populations which ultimately give rise to differentiated specialized tissues. Manipulating and controlling gradients *in vitro* is thus a necessary step towards more comprehensive and physiological culture systems and can provide clues with respect to the control of cell identities both at the colony and single cell level. To date, several approaches have been investigated to create linear or radial gradients and control the release of soluble factors over time: optical tweezers (Kress, Park et al. 2009); biological hydrogels (Foxman, Campbell et al. 1997; Chen, He et al. 1998); micropipettes (Zhelev, Alteraifi et al. 1996; Servant, Weiner et al. 1999; Servant, Weiner et al. 2000; Dehghani Zadeh, Seveau et al. 2003; Zadeh and Keller 2003; Zhelev,

Alteraifi et al. 2004; Wong, Pertz et al. 2006); Zigmond chamber (Zigmond 1977); Dunn chambers (Zicha, Dunn et al. 1997) and microfluidic devices (Dertinger, Jiang et al. 2002; Li Jeon, Baskaran et al. 2002; Fosser and Nuzzo 2003; Burdick, Khademhosseini et al. 2004; Chung, Flanagan et al. 2005; Gunawan, Choban et al. 2005; Lin, Nguyen et al. 2005; Abhyankar, Lokuta et al. 2006; Gunawan, Silvestre et al. 2006). Understanding the interplay between gradients and differential signaling responses at the colony and single cell level will benefit from further characterization, both theoretically and experimentally.

Gradients of factors such as EGF can be analyzed by modeling diffusion and convection. Finite-element models are of interest as they can incorporate complex two or three-dimensional geometries with diffusive models and reactive boundary conditions. As such, diffusion of soluble molecules should be investigated with cell-representing reflecting or adsorbing boundaries in various culture systems and cell colony configurations. The combination of finite-element models of diffusion with kinetic models of binding and trafficking on cell surfaces can provide a valuable framework to elucidate complex signaling responses at the single cell level. The EGF system has pioneered the development of kinetic models of cell growth and signaling both at the receptor (Starbuck and Lauffenburger 1992) and signaling intermediate levels (Schoeberl, Eichler-Jonsson et al. 2002; Aksan and Kurnaz 2003). The extensive kinetic data available in the literature in conjunction with EGF biological significance makes it ideal for the development of such a framework.

To test the relevance of the model, the experimental system should resolve the technical difficulties associated with colony and sub-colony level analysis of gradient effects. The ideal system should allow for: long-term culture and imaging of cells; control of delivery intensity and duration; delivery reproducibility; fluorescence measurement online and endpoint immunofluorescence analysis of the cell(s). We selected a combinatorial approach of live-cell imaging with micropipette delivery. Our group has developed an expertise in the development of culture chambers for long-term imaging in which cell colonies can be restricted to a monolayer (Moogk, Hanley et al. 2007; Ramunas, Montgomery et al. 2007) and immunofluorescence performed *in situ*. An automated system for long-term imaging and tracking was developed which includes a robotic axis for micropipette positioning with sub-micrometer accuracy. This system allows for on-demand spatially and temporally controlled delivery with single-cell level accuracy for asymmetric delivery of molecules to a cell (Zhelev, Alteraifi et al. 2004).

Herein we present the *in silico* design analysis for asymmetric delivery of factors to single cells and/or cell subpopulations *in vitro*. We developed a three-dimensional finite-element model in which continuous diffusive transport delivers EGF to a cell surface at which a model for EGF binding and trafficking is defined (i.e. reactive boundary conditions) based on published HeLa kinetics. To our knowledge, this study is the first to analyze the subcellular localization of receptor-ligand complexes to enable the study of receptor-ligand asymmetry across a cell. In a first step, a sensitivity analysis is performed to identify the significant kinetic constants based on a defined set of metrics to simplify and permit experimental validation of the kinetic model. By characterizing the delivery in terms of factor asymmetry and percentage of receptor occupancy, we compare two strategies for controlled EGF release in the media and analyze the effect of

culture system geometry and mass transfer limitation on polarization. We demonstrate that limiting diffusion of molecules in the cell microenvironment, either through a reduced diffusion coefficient or increased tortuosity in the cell vicinity greatly enhances polarization and the potential for asymmetric signaling. Our conclusions are confirmed experimentally using a combination of point source and bulk delivery approaches as the polarization index is measured experimentally and correlated with model predictions in two different cell systems. This computational framework is readily applicable to other cell systems and signaling networks to investigate the extrinsic nature of asymmetric factor partitioning and cell fate decisions.

4.2 Material and Methods

4.2.1 **Micropipette Manufacture**

A horizontal automated P-97 flaming micropipette puller (Sutter Instrument Company, Novato, USA) was used (collaboration with Professor J. Spafford, University of Waterloo) with standard wall borosilicate tubings of 0.86mm inner diameter (ID) and 1.5mm outer diameter (OD) (ref. BF-150-86-15, Sutter Instrument Company, Novato, USA). Initial ramp tests were performed and measured a melting temperature of 241^{o}C that was used in the following program for the manufacture of micropipettes with ID = 5 ± 2 µm:

	Temperature (ºC)	Pulling Force	Velocity	Time	Pressure
Line 1 (*4)	Ramp +10	30	50	150	300

Table 4: Selected program for the manufacture of micropipettes with ID = 5 ± 2 µm.

4.2.2 **Cell Culture and Time-Lapse Imaging**

EGF and TRITC-EGF were obtained from Gibco and Molecular Probes (Invitrogen, USA). EGF stock was resuspended in PBS 0.5% BSA (Bovine Serum Albumin) and aliquoted at a final concentration of 100 ng/mL. TRITC-EGF was reconstituted in deionized water at a concentration of 40 μg/mL and aliquots were stored at -35ºC protected from light.

HeLa CCL2 cells expressing EGFR were obtained from ATCC and cultivated in DMEM-F12 (Gibco, Canada) supplemented with 10% FBS (Gibco, Canada) in a controlled atmosphere 37^{o}C / 5% CO_2 until confluent upon which cells were split following trypsin (Sigma, Canada) treatment. The gap chamber culture system illustrated in Figure 4-1 was selected for time-lapse imaging and was assembled and loaded as previously described (Ramunas, Illman et al. 2006; Moogk, Hanley et al. 2007). One ounce, 22 mm by 60 mm, No. 1 coverslips (VWR Scientific, West Chester PA) were used as a culture surface. Glass tubing with an internal diameter of 15 mm was cut to a length of roughly 1 cm and one axial edge of the tube was lightly coated with silicon type A medical adhesive Silastic (Dow Corning, MI, USA), pressed gently on the coverslip surface and allowed to dry overnight. To construct a lid for the well, a similar length of tubing with an internal diameter of 18 mm was cut and glued to a 22 mm by 22 mm, No. 1.5 coverslip (VWR Scientific, West Chester, PA) and allowed to dry. Prior to use the wells and lids were autoclaved while submersed in deionized water in an enclosed beaker. Following sterilization, the water was removed and the wells were dried in a sterile laminar flow hood.

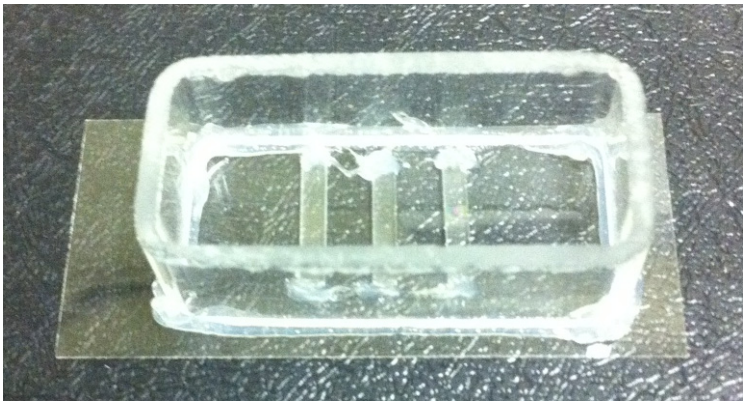

Figure 4-1: A 1 mm by 8 mm piece of microscope slide is cut and positioned in the center of a coverslip with medical grade silicone used at both sides. Polystyrene beads are used in the cell population cultured. The beads act as spacers between the coverslip and cut glass segment, which otherwise are held firmly together by the adhesive.

Cells were treated for 5 minutes with trypsin, resuspended in DMEM-F12 and centrifugated for 5 minutes at 1000 rpm. Following supernatant removal, cells were resuspended in DMEM-F12 10% FBS with 10 μm polystyrene beads at a concentration of $1x10^4$ beads/mL (Polysciences, USA) and loaded in gap chambers at a concentration of $2x10^7$ cells/mL. The bead size defines the thickness of the two-dimensional cell culture. For TRITC-EGF delivery experiments, bulk media change (infinite source) and micropipette (point source) approaches were tested. For the bulk delivery, cells were washed in phenol-free DMEM-F12 (Gibco, Canada) for 10 minutes and then 2 mL of phenol-free DMEM-F12 containing 100 ng/mL TRITC-EGF was added in the culture chamber for 2 minutes. 2 mL of phenol-free DMEM-F12 was subsequently added to the culture chamber and time-lapse imaging was started at a time interval of 6 minutes in brightfield and fluorescence. For the point source delivery, micropipette positioning was performed using a x,y,z-axis controlled stage with sub-micrometer accuracy. The pipette holder was implemented on a motorized axis (referred to as w-axis) to enable automated entrance and removal from the imaging region with minimum perturbation. A micropipette was pre-loaded with phenol-free DMEM-F12 containing 100 ng/mL TRITC EGF

and the region of delivery was selected based on cell density and configuration. The micropipettes were sealed following loading using medical adhesive Silastic to ensure that the delivery of TRITC-EGF through the micropipette boundary was diffusive only. Once micropipette tip focus was achieved and target distance from the cell / colony reached, image acquisition was started at a time interval of two/three minutes in brightfield and fluorescence.

Imaging was performed on an Axiovert 200 inverted microscope with a 40x objective (Zeiss, Germany) on a humidified stage with controlled temperature and a digital camera XCD-SX900 (Sony, Japan) was used for image acquisition using custom software.

4.2.3 Image Analysis

Image analysis was performed in Image J (NIH, USA). For single cells, the threshold level of fluorescent images was used to identify cells boundaries. This method exhibits satisfactory time accuracy as masks can be redefined at each time point, thus accounting for minute variations in cell shape and positioning. Following threshold adjustment, masks whose size was greater than 1000 pixels^2 were selected and the mask of interest defined as a Region of Interest (ROI) used for fluorescence intensity measurements. As fluorescence intensities were low for the first time point, the threshold selection was not efficient and the second fluorescent image was used to generate a mask for the first two images. Background removal was performed prior to fluorescence intensity measurements. For polarization index measurements, a macro was developed to split ROIs vertically into two equal surfaces (see Appendix C) and extract mean gray values. For multicellular system, the threshold approach was not applicable and masks were drawn manually. In the context of cell colonies, the axis of separation for PI measurements was

not defined with respect to the source of factor delivery but accordingly to the orientation of membrane surfaces available to the media.

4.2.4 **Parameters Estimation**

HeLa CCL2 cells were cultivated in T75 flasks in DMEM-F12 10% FBS (Invitrogen, CA) until confluent. 12 hours prior to the experiment, cells were FBS starved and incubated in phenol-free DMEM-F12 with 0.75% Bovine Serum Albumin (BSA) (Invitrogen, CA). Following FBS starvation, cells were incubated in 3 mL of phenol-free DMEM-F12, 5% BSA with 5 ng/mL TRITC-EGF (Invitrogen, CA). Gentle agitation was performed to ensure homogenous covering of the flask surface. Cells were incubated for various times (1, 3, 5, 10, 30 and 45 min) after which cells counts were performed and residual fluorescence intensity in the media measured on a Quantamaster^{TM} Fluorimeter (Photon Technology International, USA) with lamp power supply LPS220B. The excitation wavelength was set to 555 nm and the emission spectrum was scanned between 568 and 585 nm with an integration time of 3 seconds and a step of 1 nm. Three replicates were performed on every sample for subsequent data analysis. The concentration of TRITC-EGF in each sample was subtracted from the average emission from the samples that contained unlabeled EGF (10-fold excess) and this difference was used to calculate the number of molecules of bound TRITC-EGF per cell. Data was fitted to a simple on-binding model using a non-linear regression in MATLAB and k_f and R_{init} were estimated.

4.3 Mathematical Model

In this section, the chosen kinetic model is presented in Figure 4-2:

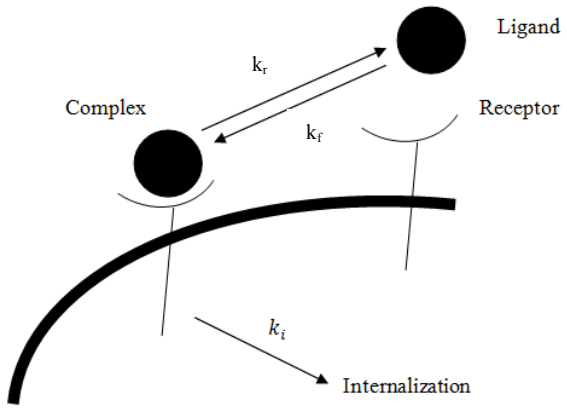

Figure 4-2: EGF binding and trafficking model. Shortly after the reversible binding of EGF (*L*) to EGFR (*R*), the newly formed complex (*C*) is internalized. This model is simplified from Figure 3-2.

The binding of EGF (*L*) on a receptor (*R*) triggers the formation of a ligand-receptor complex (*C*). The complex is internalized (*I*) towards the endosomal compartment modeled on the cell surface. k_l is the second order forward rate constant for binding of EGF on the receptor, and k_i is a first order rate constant for internalization of the complex. The parameters estimates were identified in the literature for the HeLa cell line and are presented in Table 5 (Teramura, Ichinose et al. 2006; Schmidt-Glenewinkel, Reinz et al. 2009; Yu, Hale et al. 2009).

Model 1: $$R + L \xrightarrow{k_f/k_r} C \xrightarrow{k_i} I$$

$$\frac{dR}{dt} = \frac{dL}{dt} = -k_f RL + k_r C$$

$$\frac{dC}{dt} = k_f RL - (k_r + k_i)C$$

$$\frac{dI}{dt} = k_i C$$

Model 2: $R + L \xrightarrow{k_f} C$

$$\frac{dR}{dt} = \frac{dL}{dt} = -k_f RL$$

$$\frac{dC}{dt} = k_f RL$$

Parameter	Value
k_f	$20150\left(\frac{\mathrm{m}^3}{\mathrm{mol}\cdot\mathrm{sec}}\right)$
k_r	$4.17 \times 10^{-3}\,\frac{1}{\mathrm{sec}}$
k_i	$8.34 \times 10^{-3}\,\frac{1}{\mathrm{sec}}$
R_{init}	47000 receptors

Table 5: Kinetic parameters for the three-dimensional model.

4.3.1 Model Equations

As in the two-dimensional analysis, EGF transport in the media was assumed diffusive only. The diffusion coefficient in the media and in the micropipette was set to $D_{med} = D_{tube} = 1.89 \times 10^{-10}$ m^2/s calculated for EGF using the Einstein-Stokes equation and published R_G value

(Lemmon, Bu et al. 1997). Initial EGF concentration in the delivery pipette was set to 10 and 200 ng/mL for the sensitivity analysis and 100 ng/mL in subsequent simulations.

4.3.2 **Finite-Element Model Setup**

Finite-element modeling was performed in COMSOL Multiphysics (version 3.5, USA) with MATLAB (version 2008b, Mathworks, Inc., Natick, MA) and model sketches are presented in Figure 4-3. The batch-type culture region was defined as a cube of 100 μm sides containing the growth medium (diffusion D_{med}). The delivery system was modeled as a cylinder with an inner diameter of 5 μm, wall thickness of 0.5 μm (dimensions consistent with readily manufactured micropipettes) and a length of 10 μm positioned at a distance of 10 μm from the cell surface. Similar micropipette designs have previously been used to asymmetrically deliver chemoattractant molecules to human neutrophils (Zhelev, Alteraifi et al. 1996; Zhelev, Alteraifi et al. 2004). A diameter of 20 μm was selected for HeLa cells based on experimental measurements of HeLa cells diameter. The cell was depicted as a sphere with a radius of 10 μm in the suspension model, a semi-sphere with a radius of 12.6 μm in the adherent system and a cylinder of 11.55 μm radius and 5 μm height in the gap chamber to ensure conservation of volume. In the case of the gap chamber, the delivery system was positioned 1 μm outside the gap chamber interface.

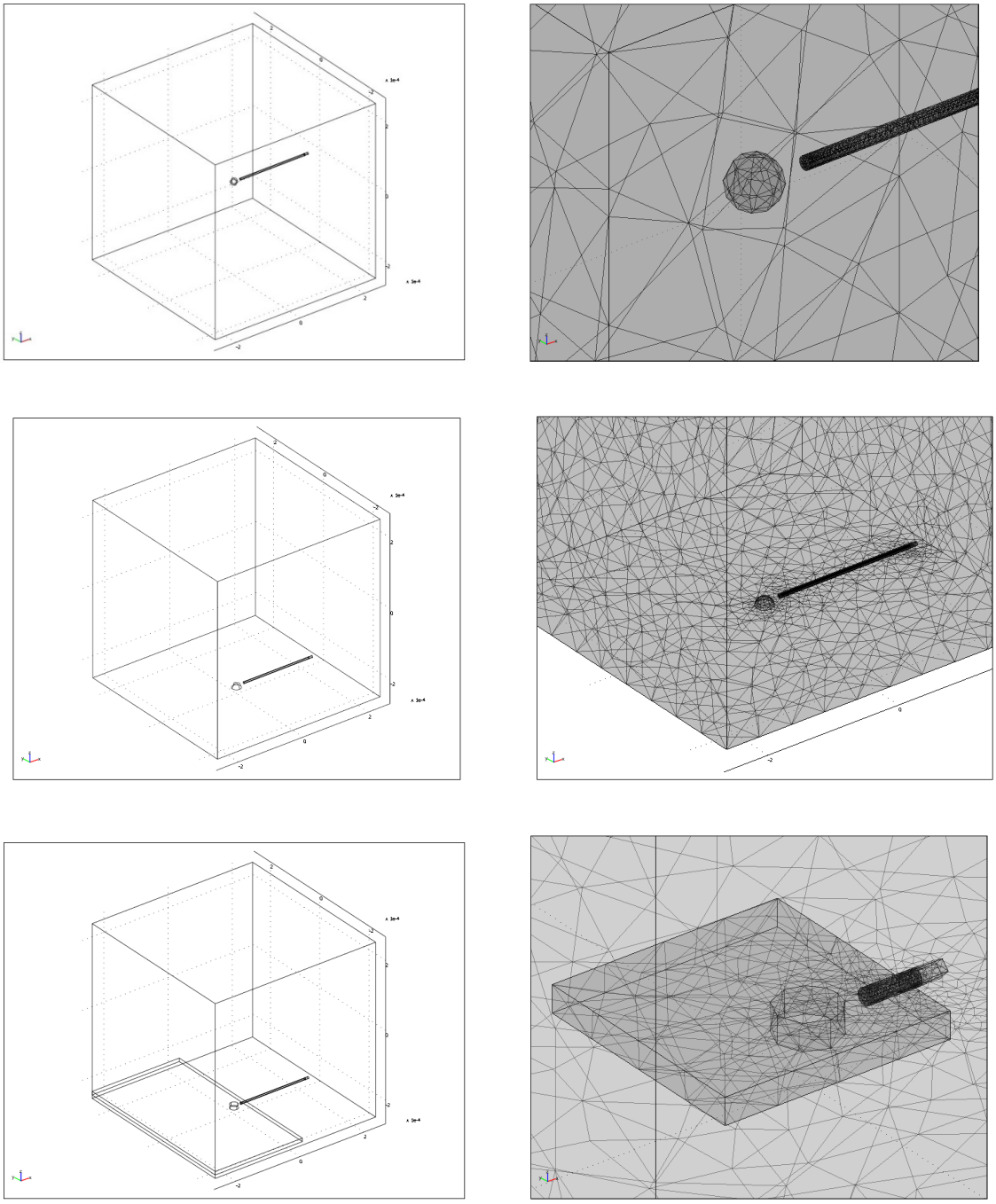

Figure 4-3: Finite-element model sketches (left) and meshes (right) for the three different culture systems. Top: suspension system. Middle: adherent system. Bottom: gap chamber system.

4.3.3 **Boundary Conditions**

Reflective surfaces in the adherent and gap chamber culture systems as well as the culture chamber boundaries are accounted for using an insulation / symmetry condition in which:

$$N_0 = 0$$

The culture chamber walls were defined distant enough from the point source not to affect EGF profile in the cell vicinity. The cell boundaries are defined with the following inward flux of EGF in mol/m^2.s in which the rate of flux is equal to the kinetic rate at the boundary:

Model 1: $$N_0 = -k_f RL + k_r C$$

Model 2: $$N_0 = -k_f RL$$

The reaction and surface diffusion system on the cell surface (D_R = 1x10^{-13} m^2/s; D_C = 1x10^{-14} m^2/s; D_I = 0) (Shvartsman, Wiley et al. 2001) were defined as coupled, linear PDEs as shown in Table 6. Similar to model design in the two-dimensional analysis, internalized complexes were modeled on the cell surface.

Component	PDE Model 1	PDE Model 2
R	$\frac{\partial R}{\partial t} = \nabla \cdot D_R \nabla R + k_r C - k_f RL$	$\frac{\partial R}{\partial t} = \nabla \cdot D_R \nabla R - k_f RL$
C	$\frac{\partial C}{\partial t} = \nabla \cdot D_C \nabla C + k_f RL - C(k_r + k_i)$	$\frac{\partial C}{\partial t} = \nabla \cdot D_C \nabla C + k_f RL$
I	$\frac{\partial I}{\partial t} = k_i C$	None

Table 6: System of equations for the computation of surface concentrations in COMSOL.

4.3.4 **Non-Dimensional Parameters**

We defined a matrix of initial conditions $\overline{O}$ in which the simulation results are valid: [$Q_{i=1,\ldots,J}$; $R_{k=1,\ldots,L}$; $S_{m=1,\ldots,N}$; $T_{o=1,\ldots,P}$] where Q is the set of J initial kinetic conditions including all rate constants; R is the set of L initial chemical conditions including initial concentrations, diffusion values; S is the set of N initial physical conditions including model geometry, micropipette distance and diameter, array volume/surface and boundary conditions; T is the set of simulation parameters including tolerances, type and settings of the numerical solver used. The cell surface was split into two half-domains (frontS and backS) with respect to the position of the source of factor delivery. The polarization index (PI) was defined by comparing surface concentration integrals of bound entities on the front and back cell sides:

Model 1: $$PI(t,\bar{O}) = \frac{\int_{frontS}(C)dS+\int_{frontS}(I)dS}{\int_{backS}(C)dS+\int_{backS}(I)dS} \quad (48)$$

Model 2: $$PI(t,\bar{O}) = \frac{\int_{frontS}(C)dS}{\int_{backS}(C)dS} \quad (49)$$

This equation was derived, giving:

$$PI(t,\bar{O}) = \frac{\frac{1}{2}\int_{S}(R_i)dS-\int_{frontS}(R)dS}{\frac{1}{2}\int_{S}(R_i)dS-\int_{backS}(R)dS} \quad (50)$$

R_i is the initial number of receptors. The integrals were the appropriately oriented surface integrals over the cell surface facing ($_{front}$S) and away ($_{back}$S) from the source(s) of free ligand. The domain of these surface integrals can be assigned as desired, but orthonormal projection of the cell relative to the delivery pipette were used. The percentage of receptor occupancy (PO) was computed (on the entire cell surface S, $_{front}$S and $_{back}$S) to assess the potential for signaling following delivery:

Model 1: $$PO(t,\bar{O}) = \frac{\int(C)dS+\int(I)dS}{\int(C)dS+\int(I)dS+\int(R)dS} \quad (51)$$

Model 2: $$PO(t,\bar{O}) = \frac{\int(C)dS}{\int(C)dS+\int(R)dS} \quad (52)$$

This equation was derived, giving:

$$PO(t,\bar{O}) = \left[1 - \left(\frac{\int_{frontS}(R)dS+\int_{backS}(R)dS}{\int_S (R_i)dS}\right)\right] \quad (53)$$

As absolute occupancy levels cannot be evaluated experimentally at the single cell level, PI will be used for model correlation with experimental data. The Damköhler number was also computed for different diffusion coefficient values to assess the effect of mass transport versus kinetic limitations in the system:

$$\mathrm{Da} = \frac{k_1 \times Surface\ Receptor\ Density \times Radius}{D_{med}} \quad (54)$$

The receptor density on the cell surface was calculated as the ratio between the receptor concentration and the cell surface area and was adjusted for the three geometries studied to ensure conservation of the initial number of receptors.

4.3.5 Numerical Solution, Solver Parameter and Model Validation

A time-dependent solver was used in COMSOL with a time step of one second and a time scale of 1200 seconds. The accuracy and stability of computed concentrations were evaluated based on the convergence of computations with progressive finite-element mesh refinement. The solver selected uses a time stepping algorithm with both an absolute and relative tolerance (A_{tol} and R_{tol}) and the error vector *(e)* is calculated such that the following equation is satisfied before the solver proceeds to the next iteration:

$$|e(i)| \leq Rtol \times |y(i)| + Atol(y(i)) \tag{55}$$

e is the error vector, *y* the vector of dependent variables and *i* is the iteration step. R_{tol} should be set at least one order of magnitude lower than the expected deviation.

4.3.6 **Sensitivity Analysis**

The COMSOL with MATLAB software package was used to perform the statistical analysis. The following formulation of the experimental design was incorporated into a MATLAB code (see Appendix B) that solves the COMSOL model for all of the experimental runs as proposed. A 2^{7-2} factorial design (resolution V) was selected as it allows for the analysis of two-factor interactions which are generally significant in the context of signaling kinetics (Mahdavi, Davey et al. 2007). All kinetic parameters were included along with the diffusion coefficient D_{med} and initial number of EGF receptors (R_i). The kinetic parameters and initial number of receptors were varied by 10-fold. The bounds for the diffusion coefficient were 6.34×10^{-11} – 1.84×10^{-10} m^2/s and 10 – 200 ng/mL for initial EGF concentration. Regarding the diffusion coefficient, the higher bond was evaluated using the diffusion of EGF in water at 40 ºC and the lower bound was estimated using viscosity measurements of the normal leg tissue of a mouse (Halpern, Chandramouli et al. 1999). Effects were measured after 2 and 10 minutes using the following equations:

$$PI\ effect(t, \bar{O}) = \overline{PI}_x^+ - \overline{PI}_x^- \tag{56}$$

$$PO\ effect(t, \bar{O}) = \overline{PO}_x^+ - \overline{PO}_x^- \tag{57}$$

with x the independent variable (or two-factor interaction) being studied and $\overline{PI}_x^+$ ($\overline{PO}_x^+$) and $\overline{PI}_x^-$ ($\overline{PO}_x^-$) the averaged computed PI (PO) at higher and lower bounds respectively. The effects were presented using Pareto charts in MATLAB.

4.3.7 EGF Binding Kinetics: Model Fit, k_f and R_i Estimation

Following the sensitivity analysis, the simplified kinetic model is used and as shown previously:

$$R + L \overset{k_f}{\rightarrow} C$$

Hence

$$\frac{dR}{dt} = -k_f RL$$

$$\frac{dL}{dt} = -k_f RL$$

$$\frac{dC}{dt} = k_f RL$$

With the initial conditions in mol/m^3:

$R(0) = R_{init}$

$L(0) = L_0$

$C(0) = 0$

It can be observed that

$$\frac{dR}{dt} = \frac{dL}{dt} = -\frac{dC}{dt}$$

Hence

$$L = R + k_1$$

with k_1 equal to the difference between L_0 and R_{init} (as in this system L>>R)

$$k_1 = L_0 - R_{init}$$

Then

$$\frac{dL}{dt} = k_f L\big(L - (L_0 - R_{init})\big) = k_f L(L + R_{init} - L_0) \tag{58}$$

The solution of this differential equation can be obtained using the separation of variables and partial fraction decomposition as shown in Appendix, leading to the following solution:

$$L = \frac{R_{init} - L_0}{\frac{R_{init}}{L_0}\exp[k_f t(L_0 - R_{init})] - 1} \tag{59}$$

The fluorescence data was fitted to this function in MATLAB using a non-linear regression and the forward rate constant k_f and initial number of free receptors R_{init} were estimated.

4.4 Results

4.4.1 Sensitivity Analysis

The sensitivity analysis was performed on the suspension system using a constant release of factor (100 ng/mL EGF) from a point source of delivery (micropipette) as described previously. The Polarization Index (PI) was measured as the ratio of front versus back bound entities on the cell surface with respect to the source of factor delivery (EGF-EGFR complexes C and internalized complexes I in model 1, equation 50). As the kinetic model in the study did not include downstream effectors of the EGF pathway, the percentage of receptor occupancy (PO) was studied to evaluate the capacity to initiate signal transduction, as shown in equation (53). As discussed in Chapter 3, the bounds of 15 and 55% occupancy levels on the cell surface to ensure between 70 and 90% of maximum downstream Erk activation will be used in this analysis. The

sensitivity analysis performed on model 1 using published kinetic data was used to identify parameters significantly affecting PI and PO.

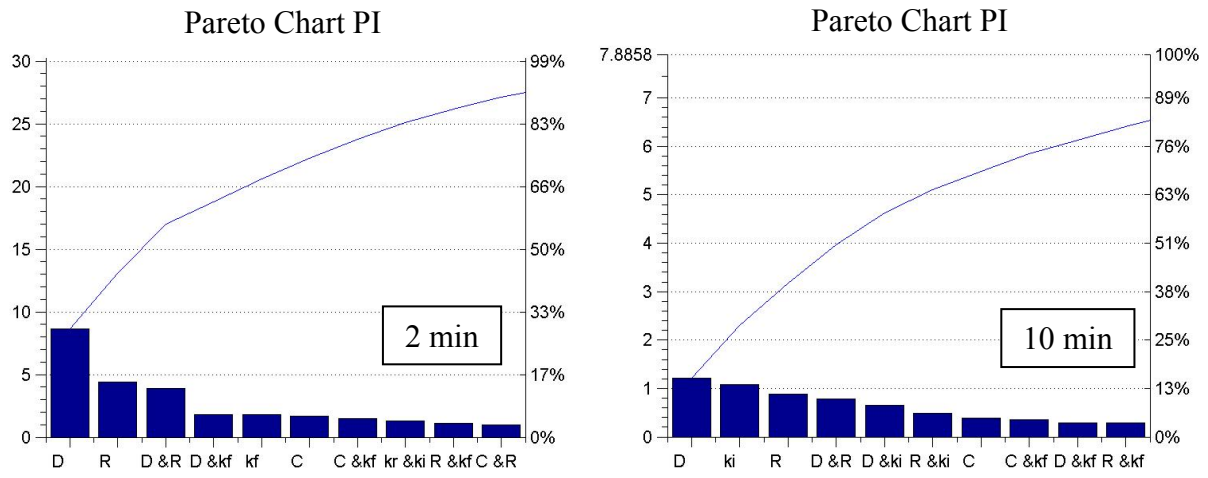

Figure 4-4: Pareto chart for the sensitivity analysis on PI as a dependant variable after two minutes (left) and ten minutes (right). The blue line represents the cumulative computed effects for the independent variables (right y-scale).

As illustrated in Figure 4-4, after two minutes, PI is strongly influenced by the diffusion coefficient in the media ($D = D_{med}$), the initial number of receptor (R_i) and the interaction between D and R_i, which together account for over 50% of the overall computed effects. Initially, polarization is driven by the motion of molecules in the cell environment. High diffusion values will allow for the rapid motion of soluble molecules to front and back cell surfaces hence triggering the loss of asymmetry. This is illustrated by the system desensitization as the absolute effect of the diffusion coefficient exhibits a six-fold decrease after ten minutes. The concentration of soluble EGF becomes gradually homogeneous around the cell which only induces transient asymmetry.

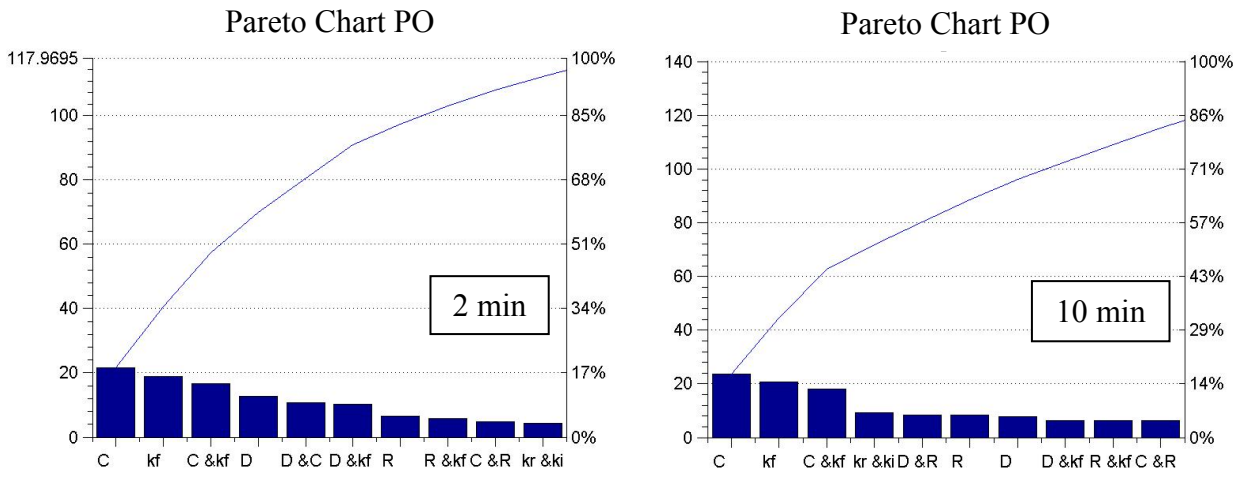

Figure 4-5: Pareto chart for the sensitivity analysis on PO as a dependant variable after two minutes (left) and ten minutes (right). The blue line represents the cumulative computed effects for the independent variables (right y-scale).

As shown in Figure 4-5, the sensitivity analysis for PO demonstrated the importance of the initial concentration of ligand L_0, forward constant of binding k_1 as well as the diffusion coefficient D, the combination of these three parameters accounting for over 70% of the computed effects. The reverse rate k_r and internalization constant k_f were found to have minor effects on PO and PI. The diffusion coefficient D and initial EGF concentration L_0 are controllable variables that can be optimized for target PI and PO values and such analysis provides clues with respect to possible strategies for the engineering of polarization. In this context, the effect of the diffusion coefficient in the culture media should be studied along with strategies to control the amount of EGF molecules released in the media through pulses of adjustable length. Finally, as k_r and k_i demonstrated no significant effects on polarization independently of the metric studied, the kinetic model was further simplified by reducing it to a simple on-binding step (k_f only, model 2) which was measured experimentally along with the initial number of free receptors R_i to improve model significance.

4.4.2 Measurement of Forward Rate Constant k_f and Initial Number of Receptors R_i

Depletion experiments of TRITC-EGF in HeLa cultures cultivated in phenol-free DMEM-F12 were performed as described in Material and Methods and results are presented in Figure 4-6. Model fit was performed in MATLAB using a non-linear regression (see Appendix A) and estimated k_f = 1.3 x 10^5 m^3/mol.s and R_i = 47362 receptors were used in subsequent simulations.

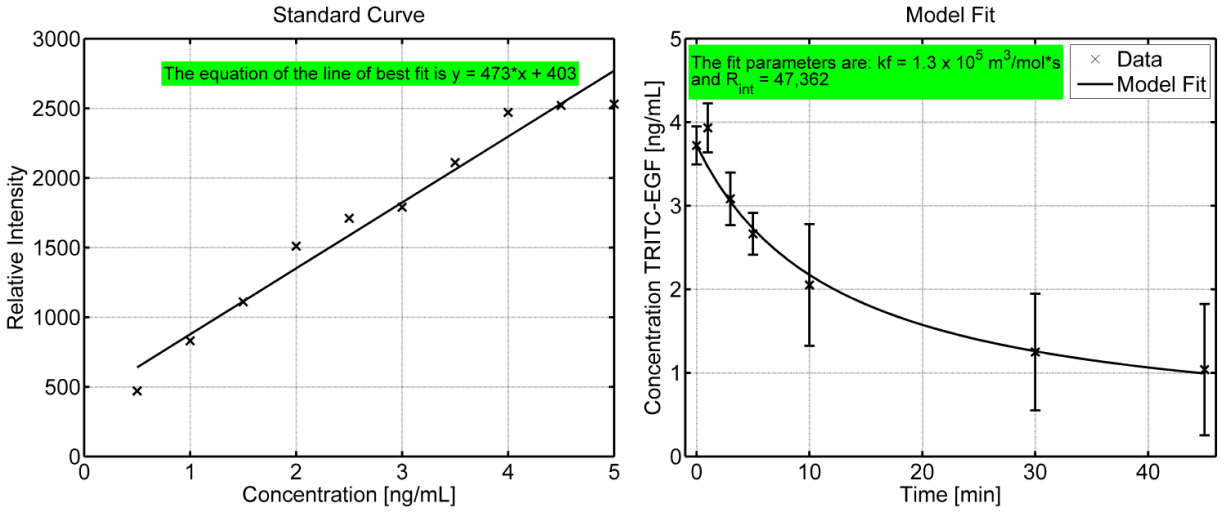

Figure 4-6: Model fit to experimental data. Left: Calibration curve for various concentration of TRITC-EGF on the Quantmaster™ spectrofluorimeter. Right: Model fit to experimental data for TRITC-EGF depletion experiments in HeLa cultures as described in Material and Methods. Error bars represent one standard deviation.

4.4.3 Temporal Profiles

In this section we analyzed the temporal profiles of PI and PO and compared the three different culture systems (suspension, adherent and gap chamber) as described in Material and Methods. Two delivery strategies were investigated: continuous EGF release and a two-minute

EGF pulse both at a concentration L_0 = 100 ng/mL in the micropipette. Computations for the pulse delivery were performed in two steps: model was solved as previously described for two minutes and solutions were used as initial conditions of a second model solved for 18 minutes with $L_0 = 0$.

Polarization Index

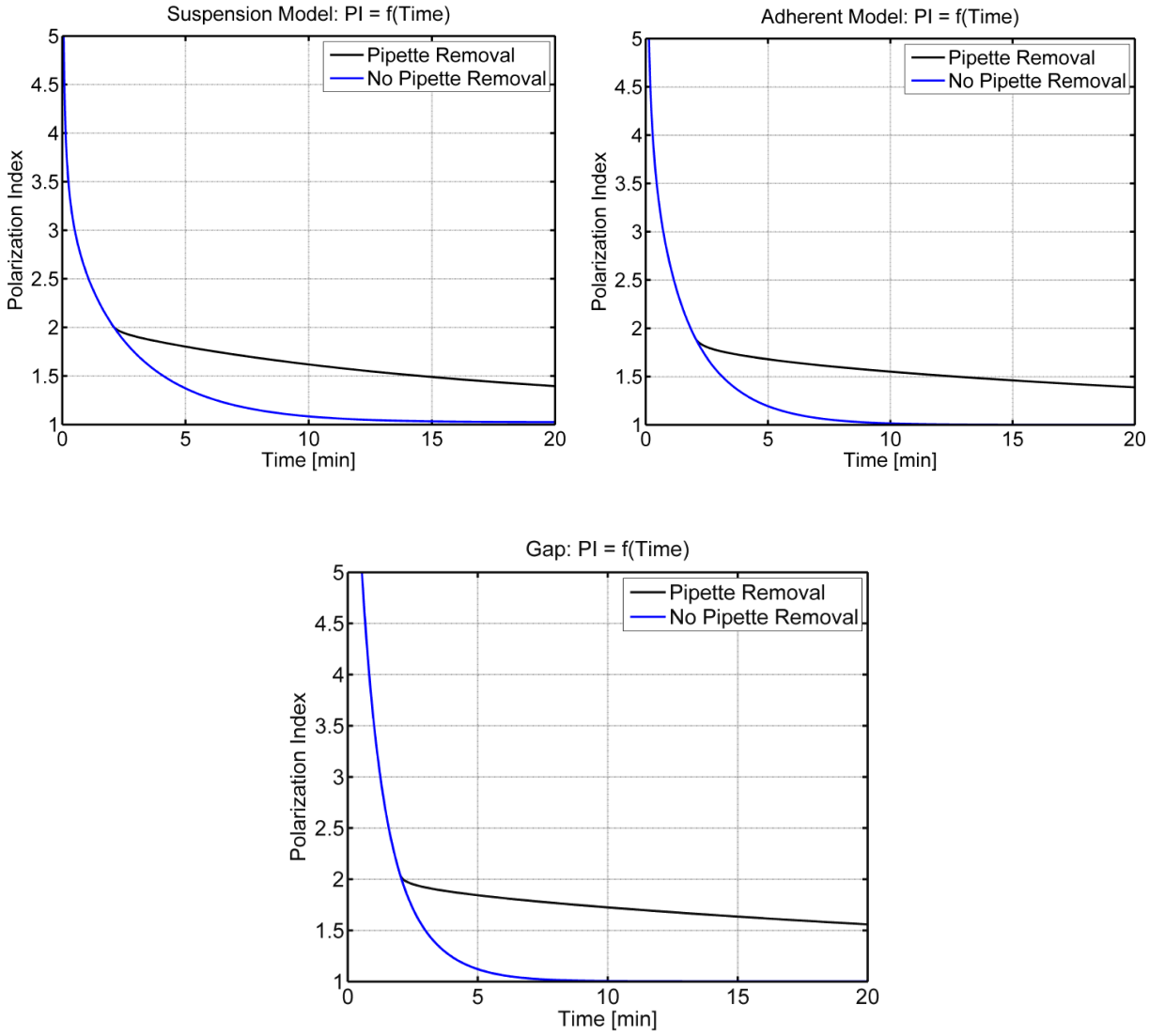

Figure 4-7: Analysis of Polarization Index PI computed as per equation (50). Top left: suspension system. Top right: adherent system. Bottom: gap chamber. Blue line: constant EGF release. Black line: two-minute EGF pulse.

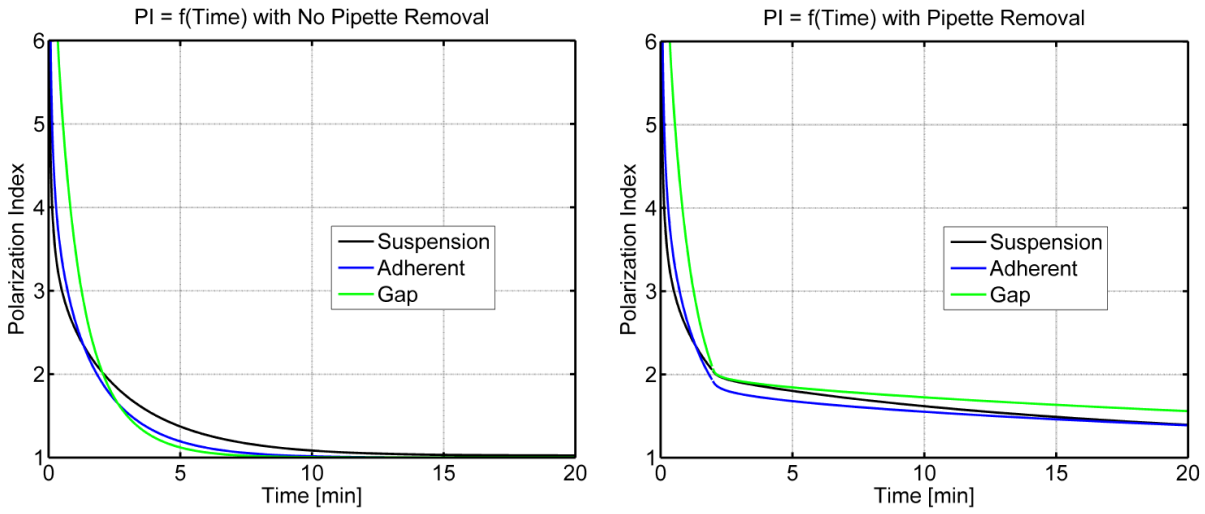

Figure 4-8: Analysis of Polarization Index PI computed as per equation (50) for the three different culture systems and illustration of the effect of reflective boundaries in the cell microenvironment. Left: constant EGF release. Right: two-minute EGF pulse. Black line: suspension system. Blue line: Adherent system. Green line: Gap chamber.

Figure 4-7 and 4-8 depict typical simulation results for PI with a maximum value of 11.33 for the hypothetical suspension system at the first time point. Asymmetric delivery is a transient process with a PI value of 1.08 after 10 minutes and 1.02 after 20 minutes indicating the loss of polarization. The fast diffusion of molecules around the cell is responsible for the rapid decrease of asymmetry on the cell surface. The two-minute pulse of EGF exhibited some improvements, with a PI value of 1.61 after 10 minutes. When release from the point source of delivery is stopped, homogenization of concentrations around the cell surface in a purely diffusive system is slowed down, thus contributing to the maintenance of a higher polarization degree over the course of computations. The implementation of the adherent system demonstrated improvements in terms of initial PI values (maximum value of 18.6) while PI values were below computed values for the suspension system after 1.2 minutes. Two combinatorial effects can be hypothesized; the absolute number of paths towards the back cell

surface is reduced when a reflective surface is added and reflection of diffusing molecules on the bottom surface contributes to a local increase in EGF concentrations. This increase is initially observed facing the point source of delivery and gradually spreads around the cell, thus contributing to a decrease in PI values at later time points compared to the suspension system. It should be noted the time at which reversal of effects occurs (i.e. 1.2 minutes in Figure 4-8 left panel) is entirely dependent upon initial conditions and system design. When EGF was pulsed for two minutes, PI was improved following pipette removal compared to the constant release in all culture conditions until the end of computations (Figure 4-8 right panel). Of relevance, the suspension system exhibited the most rapid decrease in PI values until the end of computations, highlighting the positive effect of reflective boundaries on the maintenance of asymmetry. Using the pulse approach, the gap chamber system demonstrated the highest PI values at all time which indicates the addition of reflective surfaces in the cell environment potentiates the increase in computed PI values with pulse delivery. Interestingly, this effect was reversed with constant EGF release, as the gap chamber while presenting the highest initial PI values became the least efficient system after two minutes.

The effect of the culture system geometry is double: at early time points reflective surfaces contribute to an increase in local EGF concentrations facing the point source of delivery, leading to an increase in computed PI values. At later time points, local EGF concentrations are increased around the entire cell surface and asymmetry is lost more rapidly with the addition of reflective boundaries. Using a pulse approach, heterogeneity in concentrations around the cell surface is improved at all times, with the effect further amplified by the addition of reflective surfaces. The culture system is thus a major effector of the polarization process. Depending on delivery strategies, we demonstrated that geometry effects

can potentiate or impair polarization signals at the single cell level, illustrating the benefits of finite-element models in the context of soluble factor signaling analysis.

Percentage of Receptor Occupancy

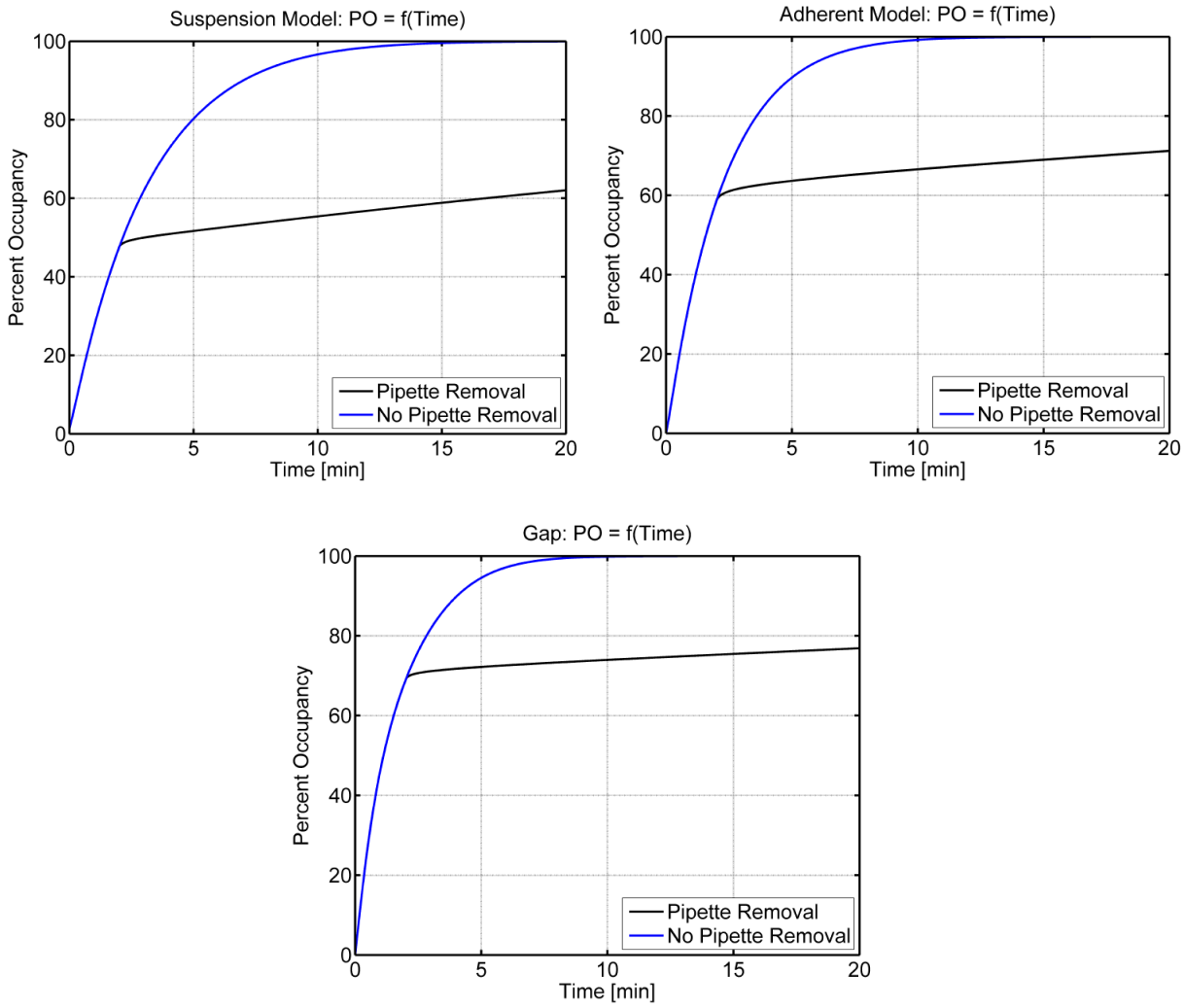

Figure 4-9: Analysis of Percentage Occupancy PO computed as per equation (53). Top left: suspension system. Top right: adherent system. Bottom: gap chamber. Blue line: constant EGF release. Black line: two-minute EGF pulse.

Figure 4-9 depicts typical simulation results in which PO exhibits a monotonic profile with 48% occupancy reached in two minutes, 80% occupancy in five minutes and near cell saturation by the end of the delivery in the suspension system using constant EGF release. The

pulse approach significantly reduces the amount of factor delivered in the media and PO decreases to 62% by the end of the computations in the suspension system. The effects observed with the addition of one or two reflective surfaces confirm the previous hypothesis as PO increases after two minutes to 60% and 69%, respectively. In these systems, occupancy levels exhibited a 7 to 10% increase by the end of simulations following pipette removal, indicating the pulse approach allows for a relative stabilization of PO values to two-minute occupancy levels. These occupancy values also indicate the pulse delivery strategy is consistent with downstream MAPK/Erk activation in all culture systems as discussed previously. To further characterize asymmetric signaling potential, PO was computed on the front and back cell side (PO_{front} and PO_{back} respectively) to differentiate signaling potential with respect to delivery asymmetry.

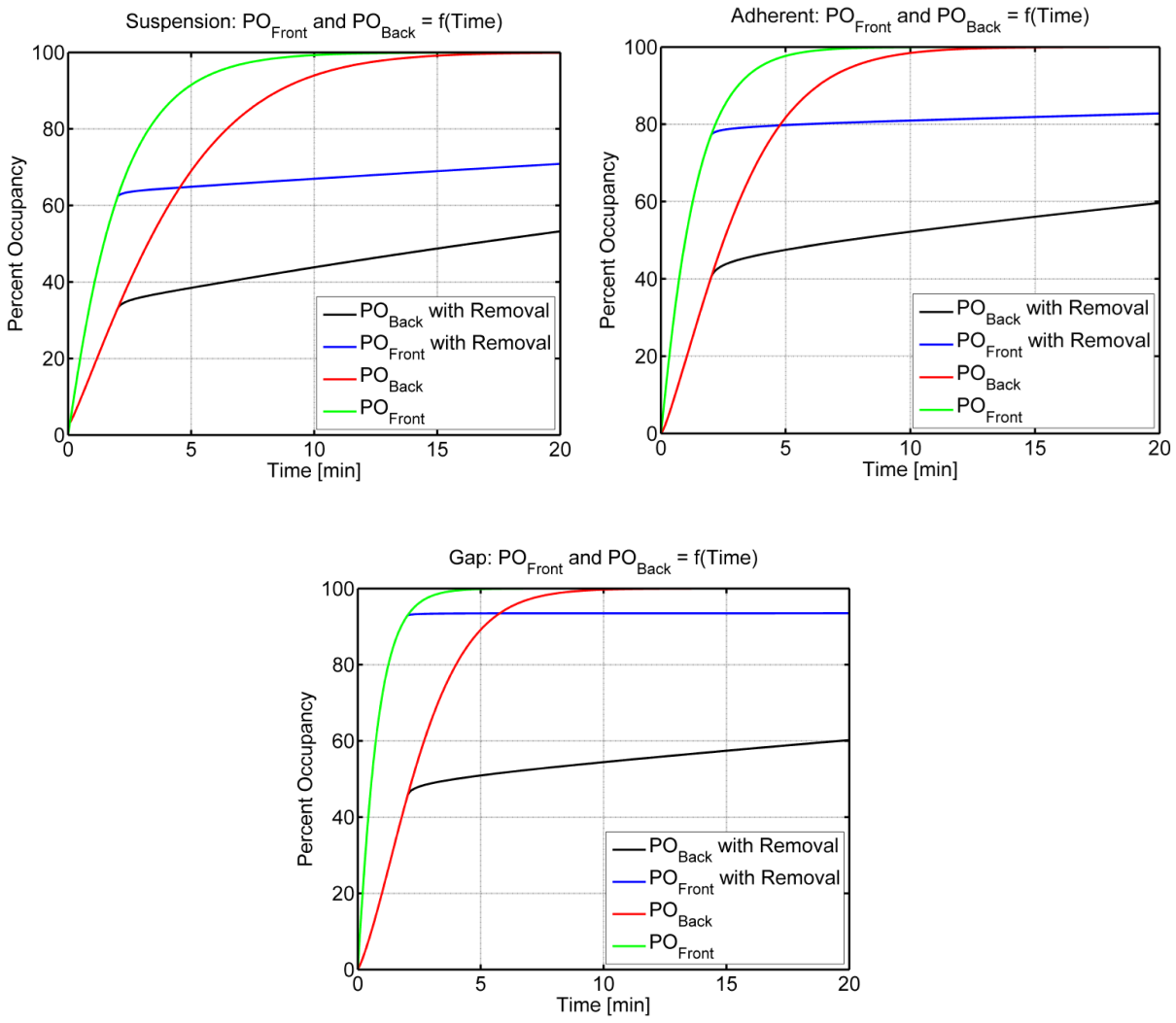

Figure 4-10: Analysis of Percentage Occupancy PO computed on the front and back cell side respectively as per equation (53). Top left: suspension system. Top right: adherent system. Bottom: gap chamber. Red line: PO_{back} constant EGF release. Green line: PO_{front} constant EGF release. Black line: PO_{back} two-minute EGF pulse. Blue line: PO_{front} two-minute EGF pulse.

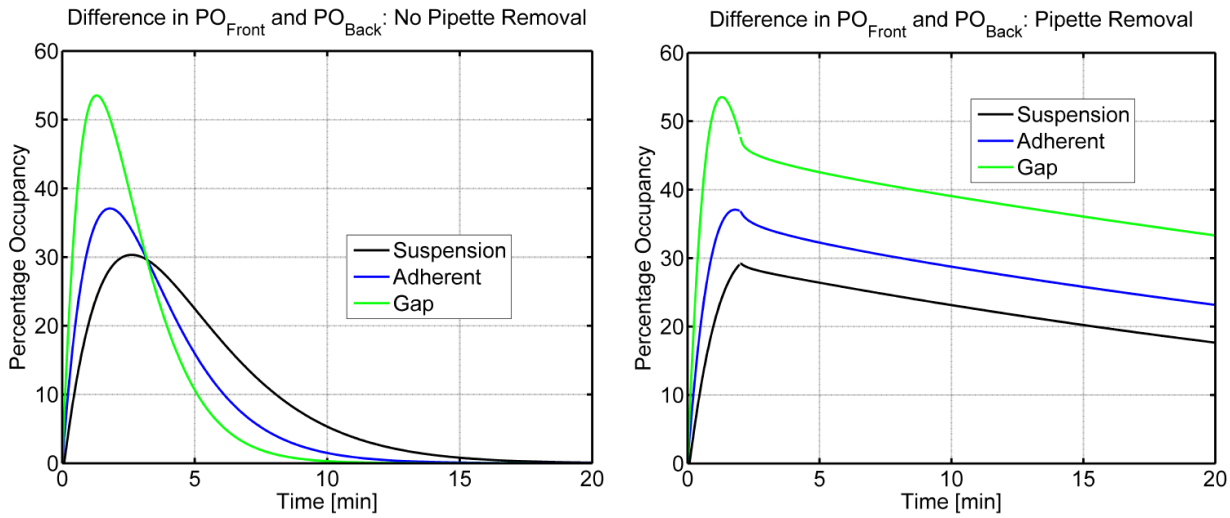

Figure 4-11: Analysis of PO differential between the front and back cell surfaces with respect to the point source of factor delivery for the three different culture systems. Left: Constant EGF release. Right: two-minute EGF pulse. Black line: suspension system. Blue line: adherent system. Green line: gap chamber.

As shown in Figure 4-10 and 4-11, Computed PO_{front} and PO_{back} exhibited different values, indicating controlled release of EGF from a point source can be translated in spatially heterogeneous occupancy levels on the cell surface. In the suspension system, the maximum differential of 30% was computed after two minutes and 30 seconds, with 72% occupancy on the front cell side and 42% on the back cell side. Occupancy levels demonstrated saturation of both cell sides by the end of experiment. Pipette removal stabilizes the occupancy difference to a relatively steady level until the end of computations (from 29% differential after two minutes to 18% after 20 minutes) indicating pulse delivery provides improvements for the generation of occupancy differentials in the case of the suspension system. With the addition of one reflective boundary, the effect of pipette removal was further improved: the initial increase in local EGF concentrations contributed to higher occupancy levels on the front cell side (78% after two minutes compared to 63% in the suspension system) while occupancy levels at the back cell side were slightly increased (42% compared to 34% in the suspension system). Hence, a higher

differential was reached at all times following EGF pulse with the addition of one reflective boundary. In this system, the benefit of pipette removal compared to constant release was observed after three minutes with higher computed occupancy differentials. This confirms that Brownian motion of molecules hitting reflective boundaries increases local EGF concentrations. When release is constant, the differential PO is transient, as concentration around the cell rapidly homogenizes, whereas the pulse approach allows for higher differential occupancy levels with reflective boundaries in the cell microenvironment (Figure 4-11). This was confirmed with the gap chamber system in which PO = 93% was reached after two minutes on the front cell side, and pipette removal allowed for occupancy differential levels up to 47% after two minutes and 33% by the end of computations. This represents significant improvements compared to the constant EGF release, as in this case saturation of the entire cell was reached in ten minutes.

As signal amplification along the MAPK/Erk pathway allows for subsequent 70% Erk duo-phosphorylation with PO as low as 15%, a stringent asymmetry of occupancy levels is required on the cell surface to reach conditions for asymmetric Erk activation. While differentials were improved with the addition of one and two reflective boundaries in the pulse approach, the range of computed occupancy values was increased and demonstrated the gap chamber was not compatible with asymmetric signaling as PO>15% on the back cell side after 50 seconds.

In vivo, cells are confined in complex three-dimensional environments constituted of neighboring cells and extracellular matrix limiting diffusion of soluble molecules. Soluble factors experience restricted diffusion in tissue in which gradients can be generated by entrapment in the extracellular matrix (Dowd, Cooney et al. 1999). This is a prerequisite for the formation of polarized systems such as epitheliums in which relative positional information allows for the creation of basal, lateral and apical membrane domains. It indicates that the

addition of supplementary artificial boundaries in a cell microenvironment may be one logical step towards further improvement of *in vitro* culture techniques. Also, the preliminary results of the sensitivity analysis led us to introduce the Damköhler number (D_a) to study the effect of mass transport limitations in the system.

4.4.4 **Effect of the Diffusion Coefficient**

In this section we analyzed how transport limitation of soluble molecules in the cell microenvironment affects the polarization process as PI and PO were computed for 10 different apparent diffusion coefficient values (D). The bounds for D were defined using the viscosity of water at 20ºC and microviscosity of a normal mouse leg tissue (Halpern, Chandramouli et al. 1999). D_a was calculated as per equation (54) and the EGF pulse approach was selected for analysis. The correlation between diffusion coefficients and the specific D_a values used is presented in Appendix D.

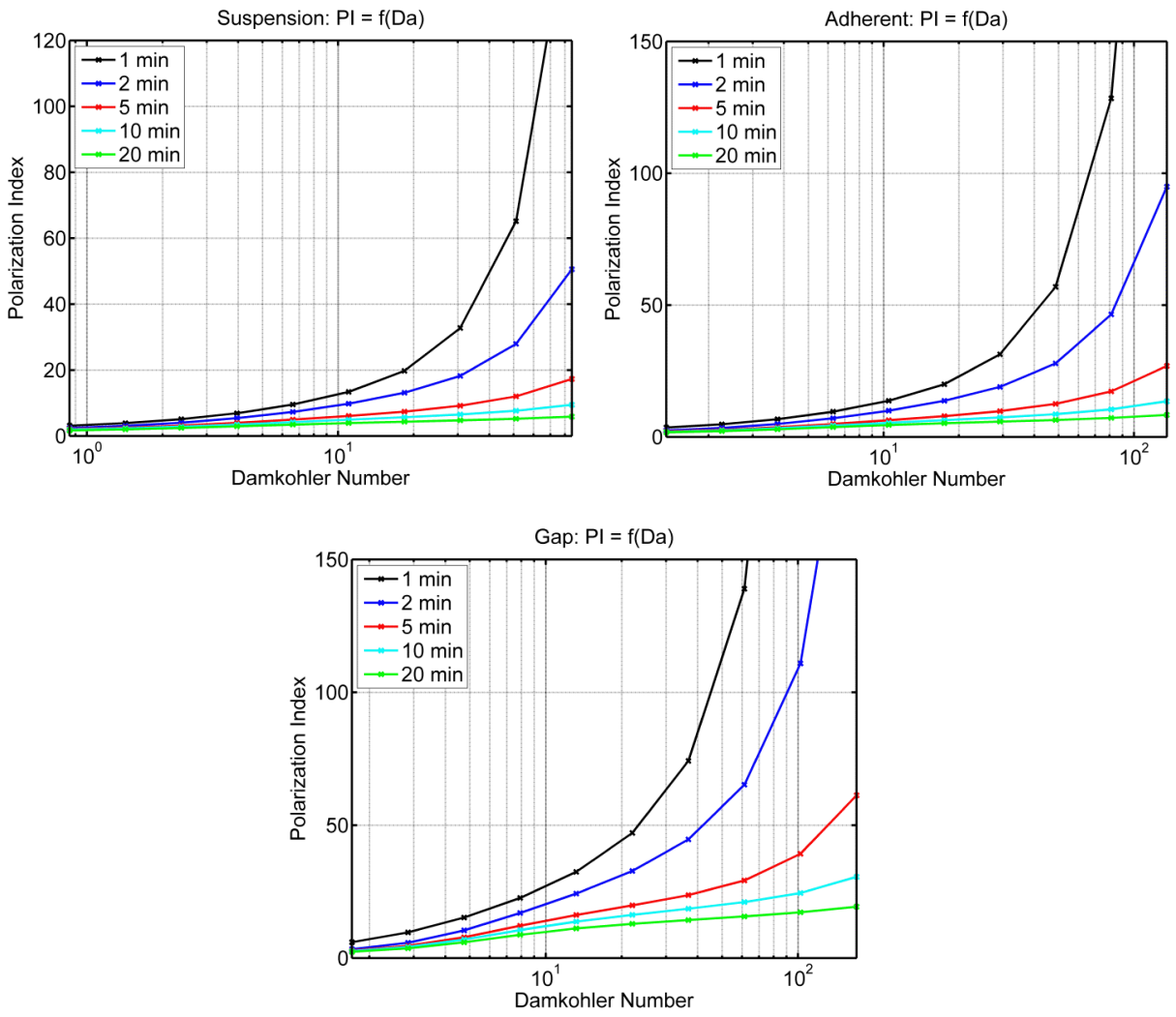

Figure 4-12: Effect of mass transfer limitation on PI computed as per equation (50) for the three different culture systems. High D_a values indicate high mass transfer limitations in the cell vicinity. PI was computed after 1 (black line), 2 (blue line), 5 (red line), 10 (cyan line) and 20 minutes (green line). Top left: suspension system. Top right: adherent system. Bottom: gap chamber.

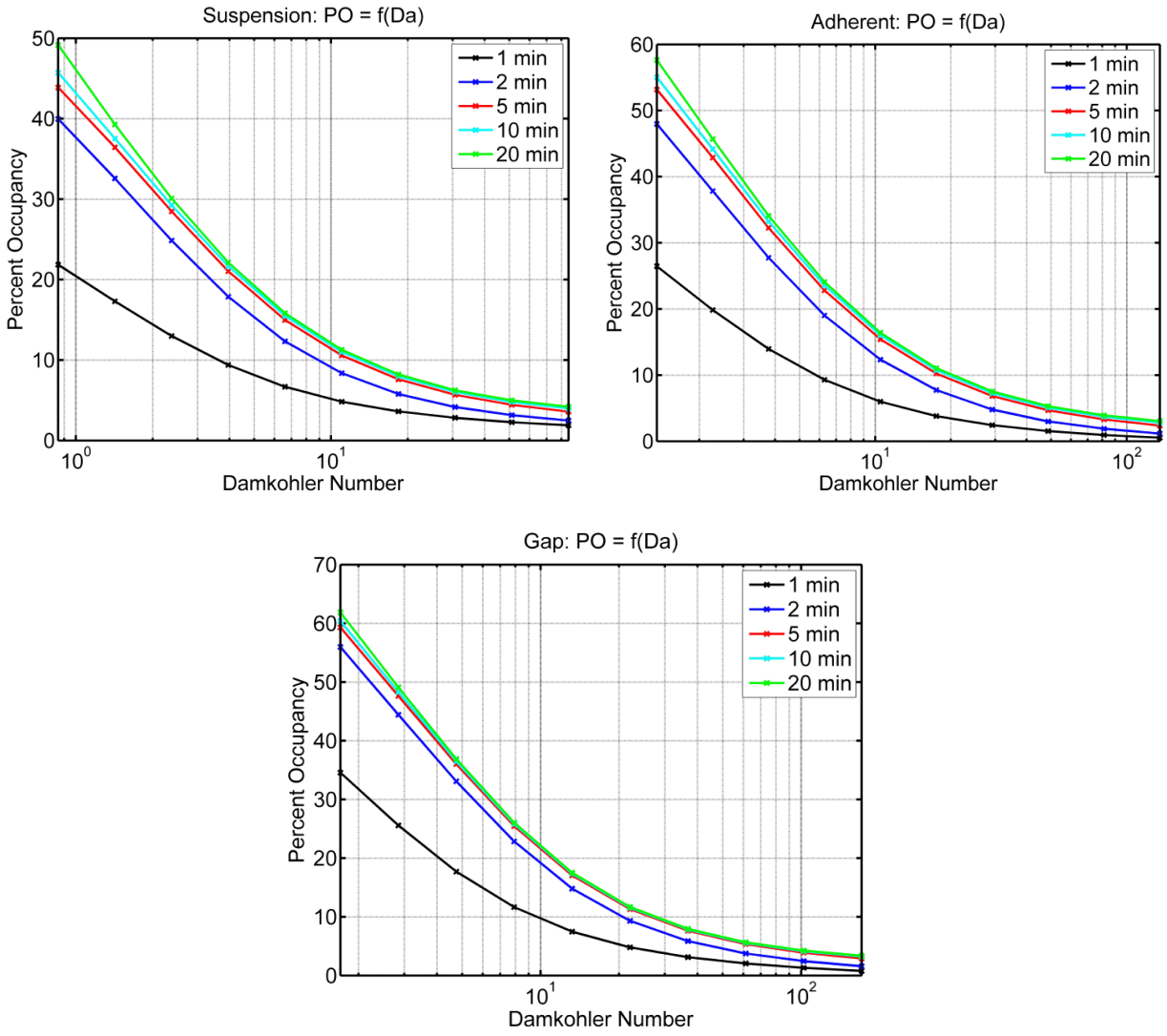

Figure 4-13: Effect of mass transfer limitation on PO computed as per equation (53) on the entire cell surface for the three different culture systems. PO was computed after 1 (black line), 2 (blue line), 5 (red line), 10 (cyan line) and 20 minutes (green line). Top left: suspension system. Top right: adherent system. Bottom: gap chamber.

Figure 4-12 exhibits the significant increase in computed PI values with mass transport limitation at early time points (PI > 20 as $D_a > 18$ after one minute). With $D_a = 10$ ($D = 0.0095e^{-10}$ m^2/s), some improvements in PI could be observed up to 20 minutes in the suspension system while polarization was rapidly lost when EGF diffused in media at 20ºC. This indicates the slow motion of EGF in the cell microenvironment potentiates polarized signals in the short and long

term. The addition of reflective surfaces in the cell vicinity contributed to significant improvements of PI at early time points for $D_a \geq 20$ and minor improvements were also observed at later time points compared to the suspension system. The gap chamber exhibited the most pronounced improvements with increased computed PI over the entire spectrum of D_a values. Significantly, PI = 18 can be maintained until the end of delivery with $D_a = 100$ in the gap chamber, indicating that with a low diffusion coefficient, homogenization of EGF concentrations around the entire cell occurs slowly, phenomenon further amplified by the addition of reflective boundaries in the cell vicinity. Hence, tissue-type culture conditions in which the apparent diffusion is reduced in the extracellular space potentiate polarized signals.

The positive effect of mass transport limitation on PI occurs at the expense of occupancy values, as shown in Figure 4-13. In the suspension system, computed PO values were below 15% occupancy levels after two minutes with $D_a \geq 5$ indicating mass transport limitation could be responsible for low levels of Erk activation. The adherent and gap chamber systems exhibited improvements, allowing for occupancy levels consistent with high MAPK activation with higher mass transfer limitations. Specifically in the case of the gap chamber system, D_a values as high as 13 were consistent with a minimum of 15% occupancy after two minutes. A perfectly asymmetric system may thus not be able to elicit cellular responses, whereas a perfectly signal-potent system may not be asymmetric. A balance must be reached to ensure the creation of a polarized environment capable of triggering signaling responses in a spatially controlled manner, as shown with the analysis of PO_{front} and PO_{back}.

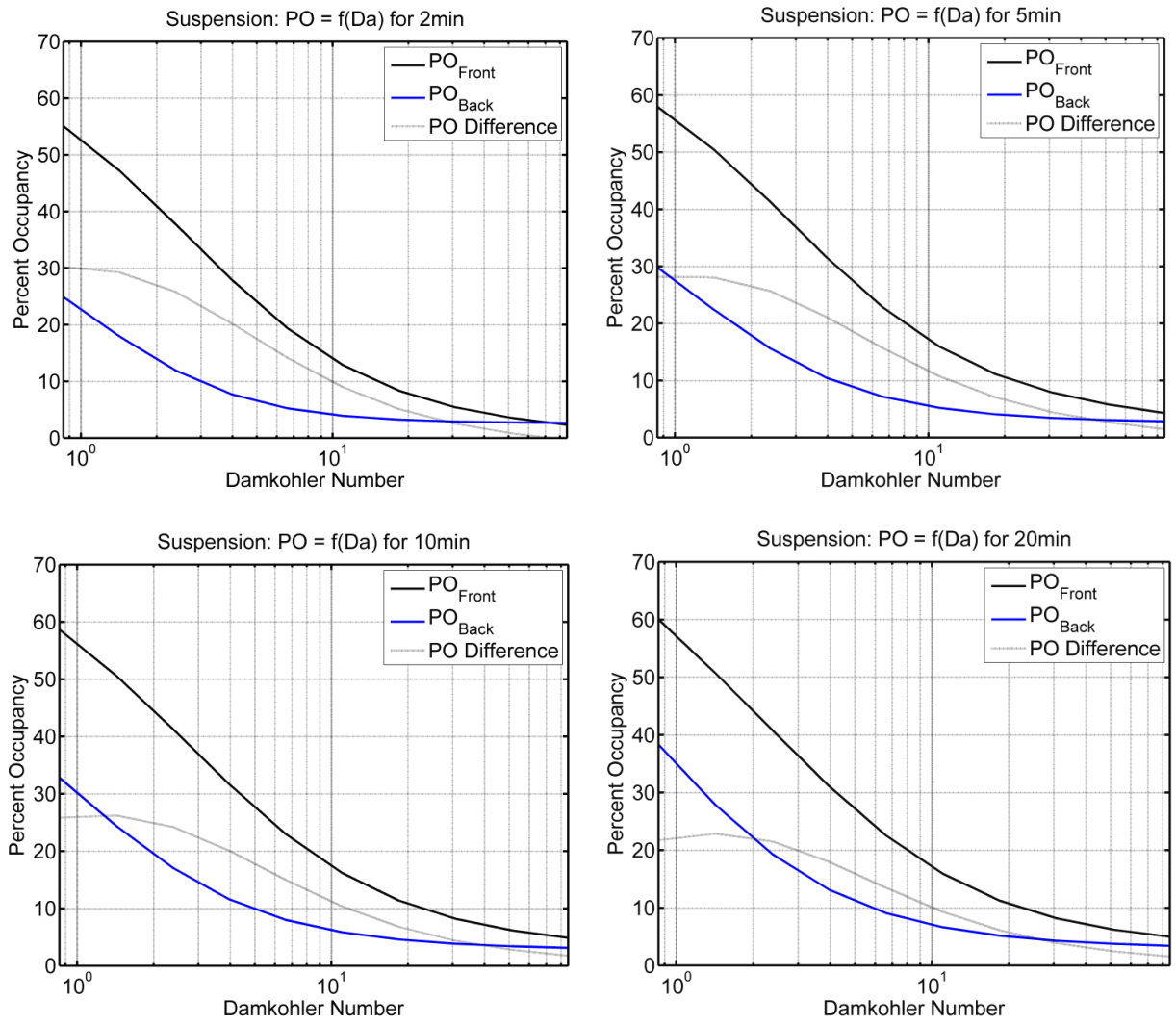

Figure 4-14: Effect of mass transfer limitation on PO computed as per equation (53) on the front and back cell surfaces for the suspension system. PO_{front}: Black line. PO_{back}: Blue line. PO difference between the front and back surfaces: grey line. Top left: Computation results after two minutes. Top right: Computation results after five minutes. Bottom left: Computation results after ten minutes. Bottom right: Computation results after 20 minutes.

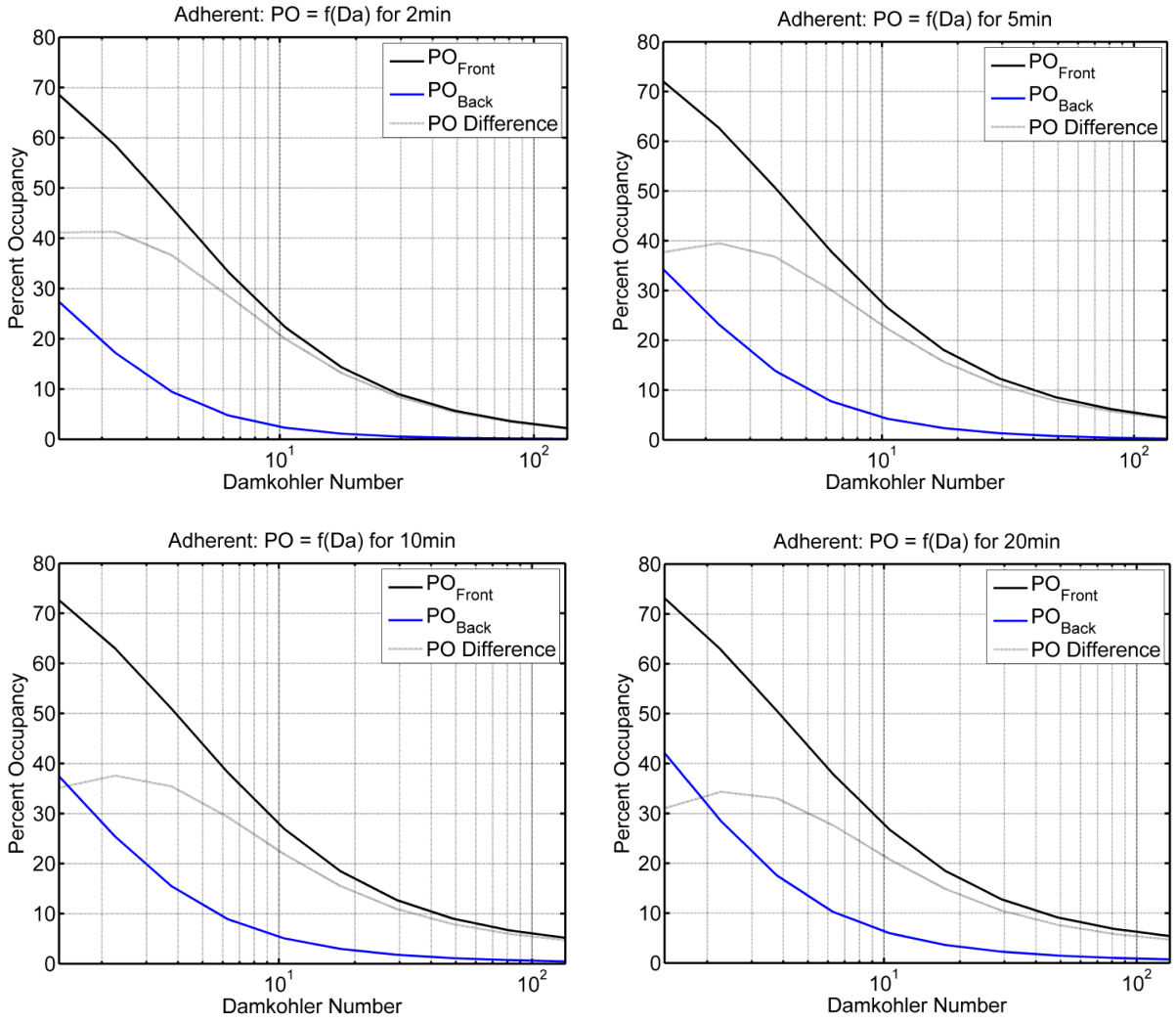

Figure 4-15: Effect of mass transfer limitation on PO computed as per equation (53) on the front and back cell surfaces for the adherent system. PO_{front}: black line. PO_{back}: Blue line. PO difference between the front and back surfaces: grey line. Top left: Computation results after two minutes. Top right: Computation results after five minutes. Bottom left: Computation results after ten minutes. Bottom right: Computation results after 20 minutes.

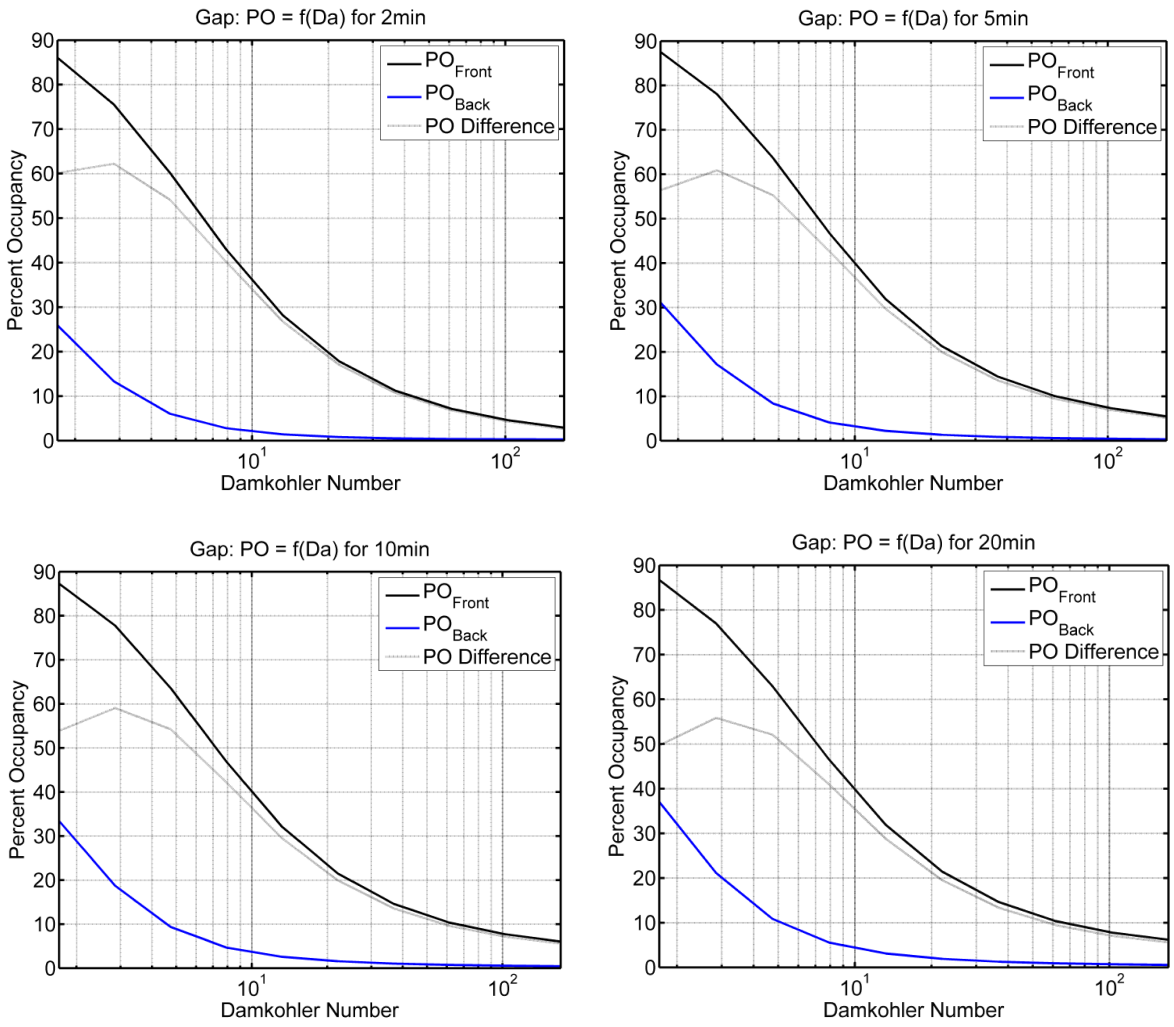

Figure 4-16: Effect of mass transfer limitation on PO computed as per equation (53) on the front and back cell surfaces for the gap chamber. PO_{front}: black line. PO_{back}: Blue line. PO difference between the front and back surfaces: grey line. Top left: Computation results after two minutes. Top right: Computation results after five minutes. Bottom left: Computation results after ten minutes. Bottom right: Computation results after 20 minutes.

When further analyzing the PO_{front} and PO_{back} values as shown in Figure 4-14, 4-15 and 4-16, we demonstrated that mild transport limitations in the cell vicinity ($D_a > 4$ in all systems) allowed for occupancy levels on the distal cell side below 15% at all times and thus represent conditions for spatially controlled elicited signals in the cytoplasm. This analysis also demonstrated the differential occupancy level could be maximized for a specific D_a value ($D_a = 3$

in all systems) indicating a balance is needed to ensure enough binding of molecules on one cell side while limiting the diffusion of EGF to the back cell side. The combination of mass transfer limitation and reflective boundaries in the direct cell vicinity generates the highest computed polarized signals at the single cell level as the computed differentials increase with the addition of reflective boundaries (28% after five minutes in the suspension system, compared to 40% and 61% in the adherent and gap chamber systems respectively after five minutes for $D_a = 3$).

While this analysis may not be applicable experimentally to the gap chamber system, these plots illustrate conditions practically applicable to adherent culture systems in which cells are grown in various matrices. The use of the Damkhöler number enables one to define D_a values for specific cellular / signaling systems and specific matrix viscosities, hence allowing one to evaluate asymmetric MAPK potential for the specific geometry analyzed. Nonetheless, the use of matrices for cell culture also involves potential limitations of oxygen and nutrients. As the microenvironment is a strong effector of polarization, we decided to further analyze the impact of neighboring cells on polarization.

4.4.5 **Effect of the Cell Configuration**

A single-cell system offers numerous advantages both computationally and experimentally. The absence of cellular neighbors also affects the cell microenvironment in terms of potential cell-cell and cell-ECM interactions. In this context, it is possible the designed microenvironment will lack primordial cues to translate polarized signals of soluble factors into changes of genetic and metabolic activity leading to controlled cell fate decisions. In this section, we analyze the effect of neighboring cells and specifically the creation of cellular “walls” on

polarization. Two and four cells were added on the lateral sides (y-axis) of the cell of interest with respect to the point source of delivery as shown in Figure 4-17 and the x-axis was left unencumbered.

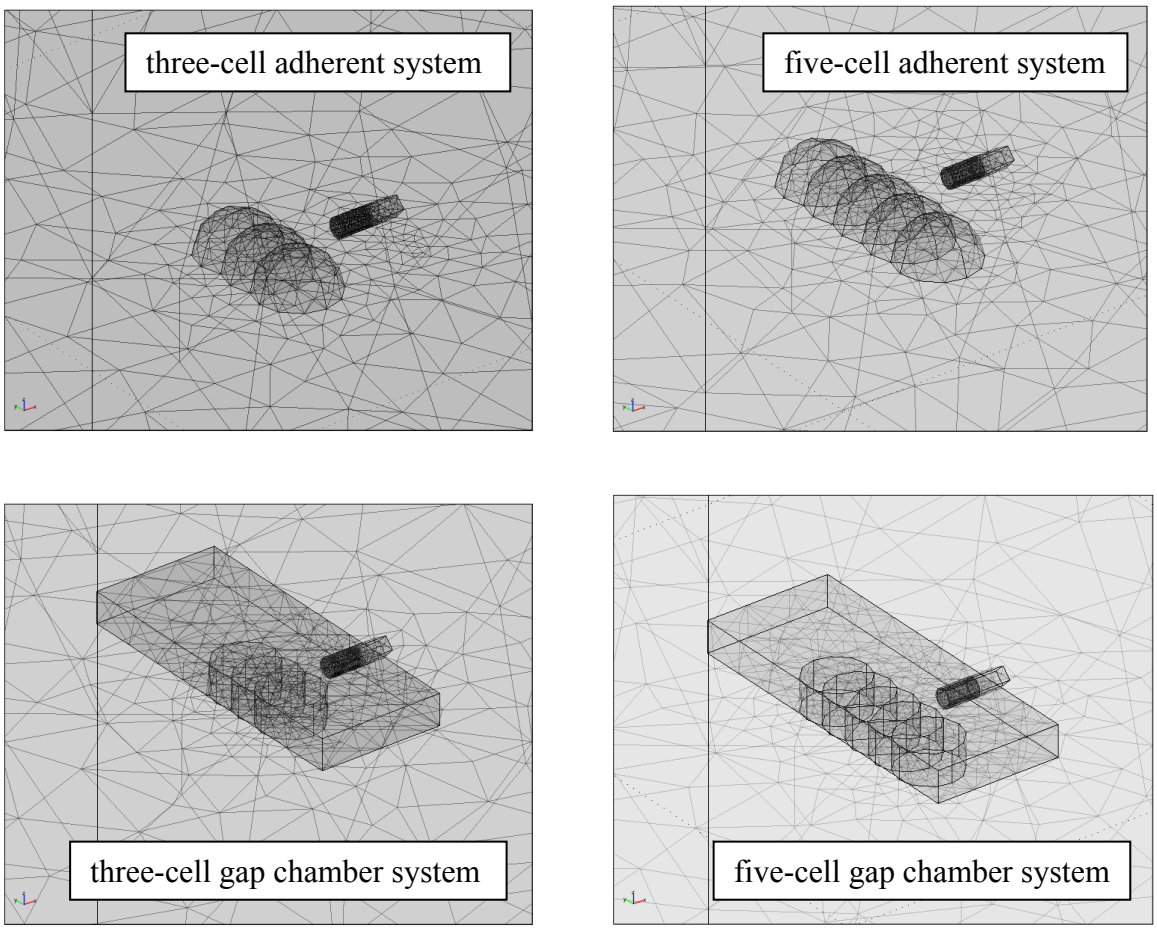

Figure 4-17: Meshes of finite-element models used for the analysis of neighboring cell effects on PI and PO. Top left: three-cell adherent system. Top right: five-cell adherent system. Bottom left: three-cell gap chamber system. Bottom right: five-cell gap chamber system.

The effect of neighboring cells in the z-axis was not studied as the gap chamber model does not allow for the addition of cells in this direction. Newly added cells were defined non-reflective using model 2 and their respective center defined at ten μm from neighbors to ensure

overlap between cellular volumes. Internal surfaces were inactivated in COMSOL and receptor density kept constant for available surfaces. A two-minute 100 ng/mL EGF pulse was simulated with diffusion in media at 20ºC.

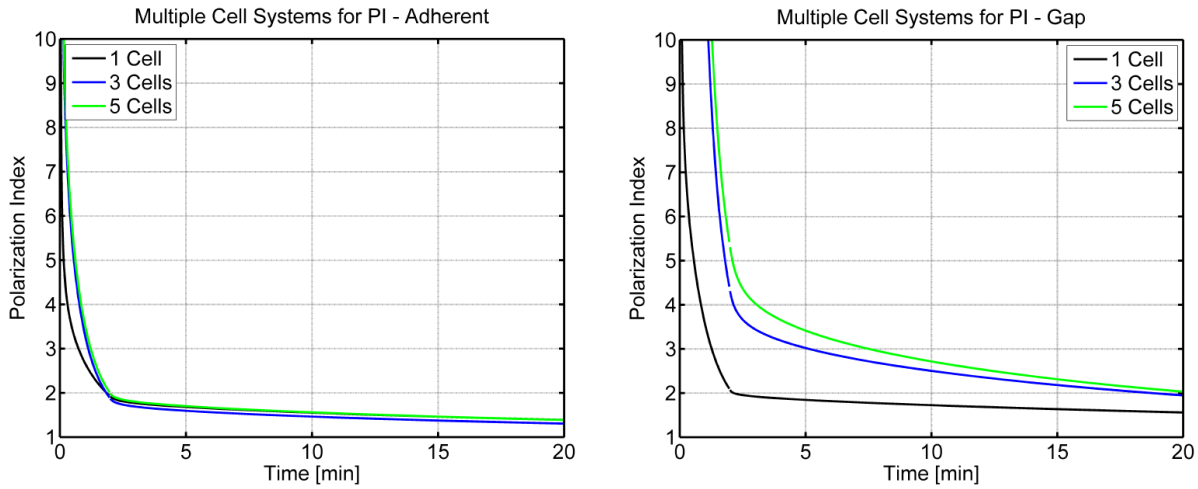

Figure 4-18: Effect of neighboring cells on PI computed as per equation (50). Left: adherent system. Right: gap chamber. Black line: one-cell system. Blue line: three-cell system. Green line: five-cell system.

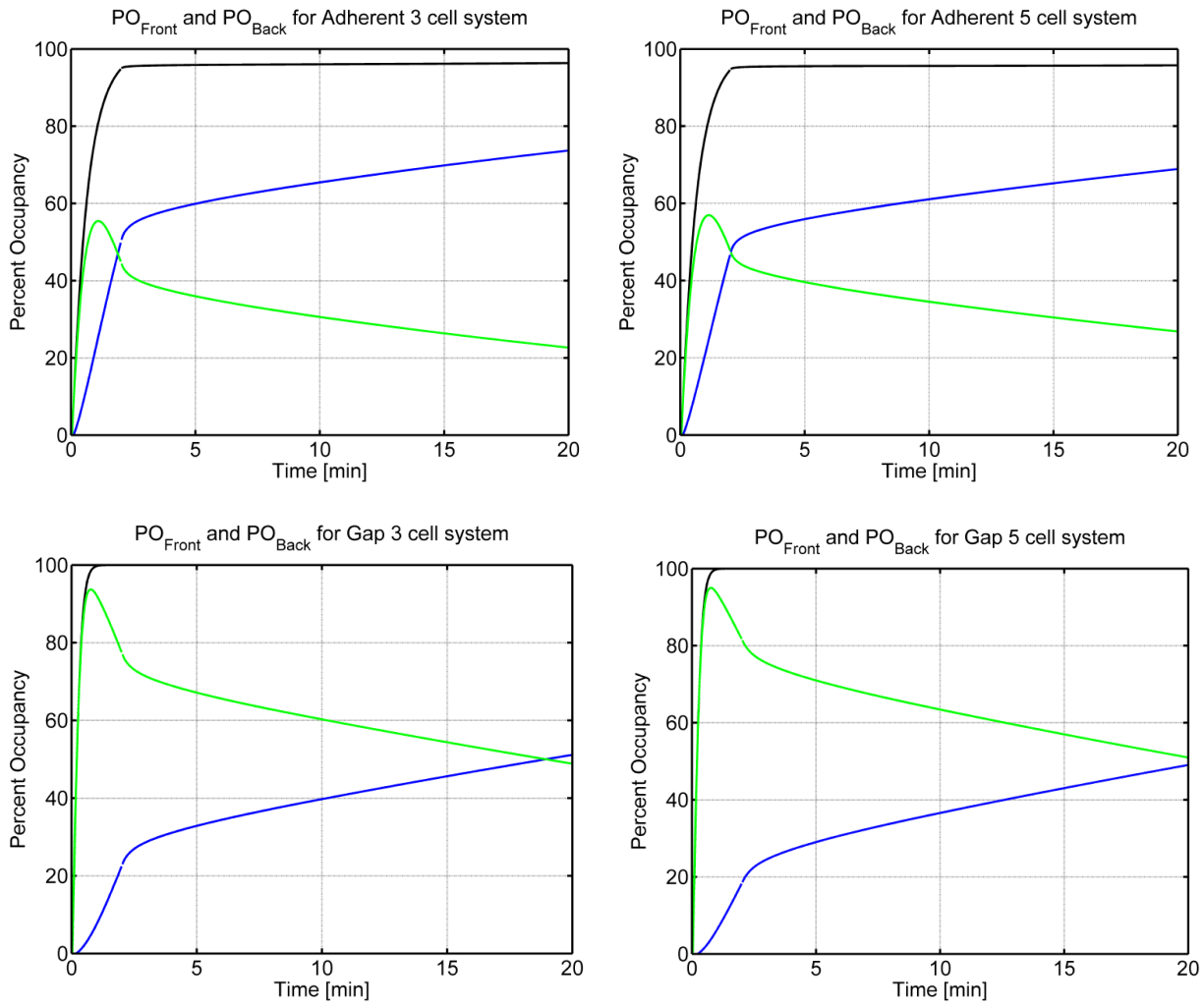

Figure 4-19: Effect of neighboring cells on PO computed as per equation (53) for the front and back cell surfaces with respect to the point source of delivery. Top Left: three-cell adherent system. Top right: five-cell adherent system. Bottom left: three-cell gap chamber system. Bottom right: five-cell gap chamber system. Black line: PO_{front}. Blue line: PO_{back}. Green line: PO difference between the front and back surfaces.

As shown in Figure 4-18, the addition of neighboring cells in the suspension system did not contribute to improvements of PI values. The presence of adjacent cells contributed to a local increase in diffusing EGF concentration initially on the front cell surface and gradually around the entire cell surface over time. This behavior is similar to what was observed with the addition of reflective boundaries around a single cell *in silico*. In the adherent culture system, the addition of two and four cells in the cell vicinity demonstrated improvements of computed PI during the

first two minutes, time after which the results were almost identical to the one-cell system. The physical obstruction of diffusion paths towards the distal cell side with a combination of reflective and non-reflective boundaries allows for minor PI improvements at early time points, result of local increase in EGF concentration on the side facing the point source of delivery. As the apical domain was left unencumbered, improvements were reduced over time compared to the single cell system due to the homogenization of EGF concentration around the cell. In the adherent system, the addition of more than two neighbors in the y-axis demonstrated no further improvements of PI. The gap chamber system exhibited the most significant improvements in terms of PI. While a single cell could maintain PI > 2 for approximately 2.5 minutes, the three-cell system allowed for PI > 3 for almost three minutes and PI > 2 until the end of simulations. Compared to the adherent system, the gap chamber allowed for complete obstruction of diffusion paths in the cell vicinity, thus effectively increasing the shortest distance to the distal cell side and tortuosity. Results were further improved in the five-cell system as shown in Figure 4-18 and values were greater than the three-cell system at all times.

Effects observed on occupancy levels were similar as shown in Figure 4-19. In the adherent system, the addition of two or four neighboring cells demonstrated significant improvements of occupancy differential values (from 37% after two minutes in a single-cell system to 56% in the three-cell system) while no further improvements were observed in the five-cell system. Hence, the presence of neighbors contributes to the local increase of concentrations on the front cell side while the reduction of the number of paths towards the back side improves the asymmetric potential of the EGF pulse. It should be noted that occupancy levels on the front and back cell sides are still consistent with a minimum of 70% subsequent Erk

activation in less than one minute, indicating that the cell configuration can shift the differential range out of target for spatially controlled activated Erk in the intracellular compartment. In the gap chamber, results were different as occupancy levels at the back cell side were below 15% for up to two minutes in the three-cell and five-cell systems while allowing near saturation on the front cell side in approximately one minute (30 seconds for the five-cell system). Only when the tortuosity was increased by the addition of both reflective (culture chamber surface) and non reflective boundaries (cells) could we produce conditions consistent with significant spatial differences in the kinetics and amplitude of Erk activation for two minutes based on Schoeberl's analysis. This behavior indicates a complete adhesion to neighboring cells and both basal and apical surfaces is necessary for the potentiation of polarization. Polarization inside a five-cell wall with diffusion in media at 20ºC demonstrated a higher differential after two minutes than any system previously tested with mass transfer limitation in the cell microenvironment (section 4.4.4) while keeping occupancy levels on the back cell side to a maximum of 15%. The formation of cellular walls or colonies is an intrinsic property of *in vitro* cultures that increases the shortest distance to the distal cell side of a cell with respect to a point source of delivery. Cell colony structure will dictate various responses to soluble signals and careful selection of cellular configurations, cell colony shapes and sizes allows for the engineering of local microenvironments *in vitro*.

4.4.6 **Model Correlation with Experimental Data**

In these simulations, the concentration of TRITC-EGF in the point source of delivery was 100 ng/mL. The delivery length was two minutes after which the point source of delivery was

removed from the culture system and fluorescent imaging was then performed with a time interval of three minutes as described in Material and Methods.

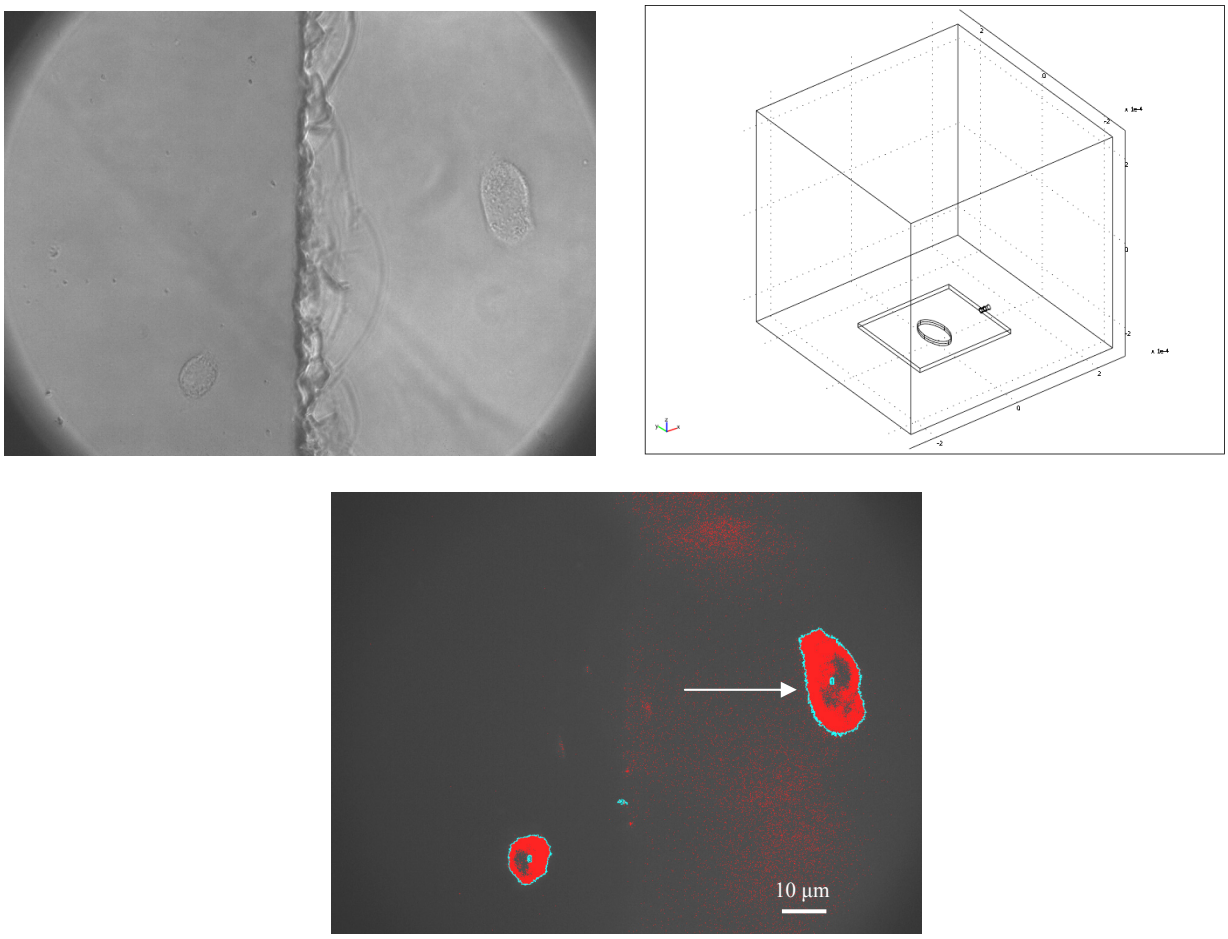

Figure 4-20: Single cell delivery of TRITC-EGF from a point source (micropipette) for model correlation. Top left: 40X brightfield image of a single HeLa cell cultivated in a gap chamber and visualization of the gap edge. Top right: finite-element sketch of a single cell culture in a gap chamber (54 µm major axis). The cell was modeled as an ellipse and model dimensions were evaluated based on the brightfield image. Bottom: 40X fluorescent imaging after two minutes following a two-minute EGF pulse. Adjustment of intensity threshold was used to define cell boundaries and define a ROI further used for PI measurement (white arrow).

Masks were defined as described in Material and Methods and split into two equal surfaces vertically for measurement of fluorescence intensity (mean gray value). For model correlation, we developed a three-dimensional model of a gap chamber in which the cell was approximated as an ellipse, kinetic model 2 defined on the cell surface and same boundary conditions as defined previously were used. The cell dimensions, micropipette tip diameter, distance from the cell and gap chamber thickness were modeled accordingly to the experimental setup as shown in Figure 4-20. The first experimental time point was one minute due to the time needed for final positioning of the micropipette, capture of brightfield image, adjustment of acquisition settings for fluorescence (one frame per second) and initial image capture. To estimate the effect of ROI boundary definition uncertainty on PI measurements, ROI boundaries were resized to generate +/- 10% changes in ROI surface (see appendix). Time-course imaging of delivery after background subtraction is presented in Figure 4-21.

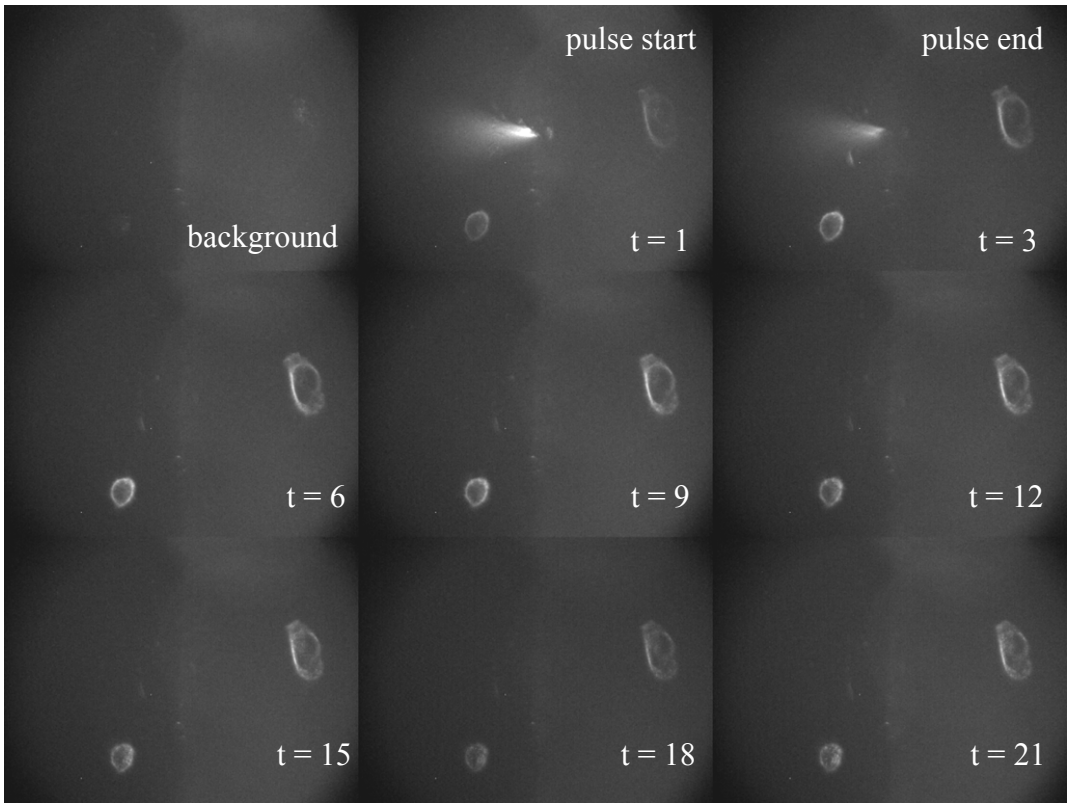

Figure 4-21: 40X fluorescent time-course of a two-minute pulse delivery of 100 ng/mL TRITC-EGF to a single HeLa cell after background removal with a three-minute time interval. t = 18 was not considered for model correlation due to the lower level of fluorescence intensity. Time in minutes.

PI measurements and simulation results are presented in Figure 4-22:

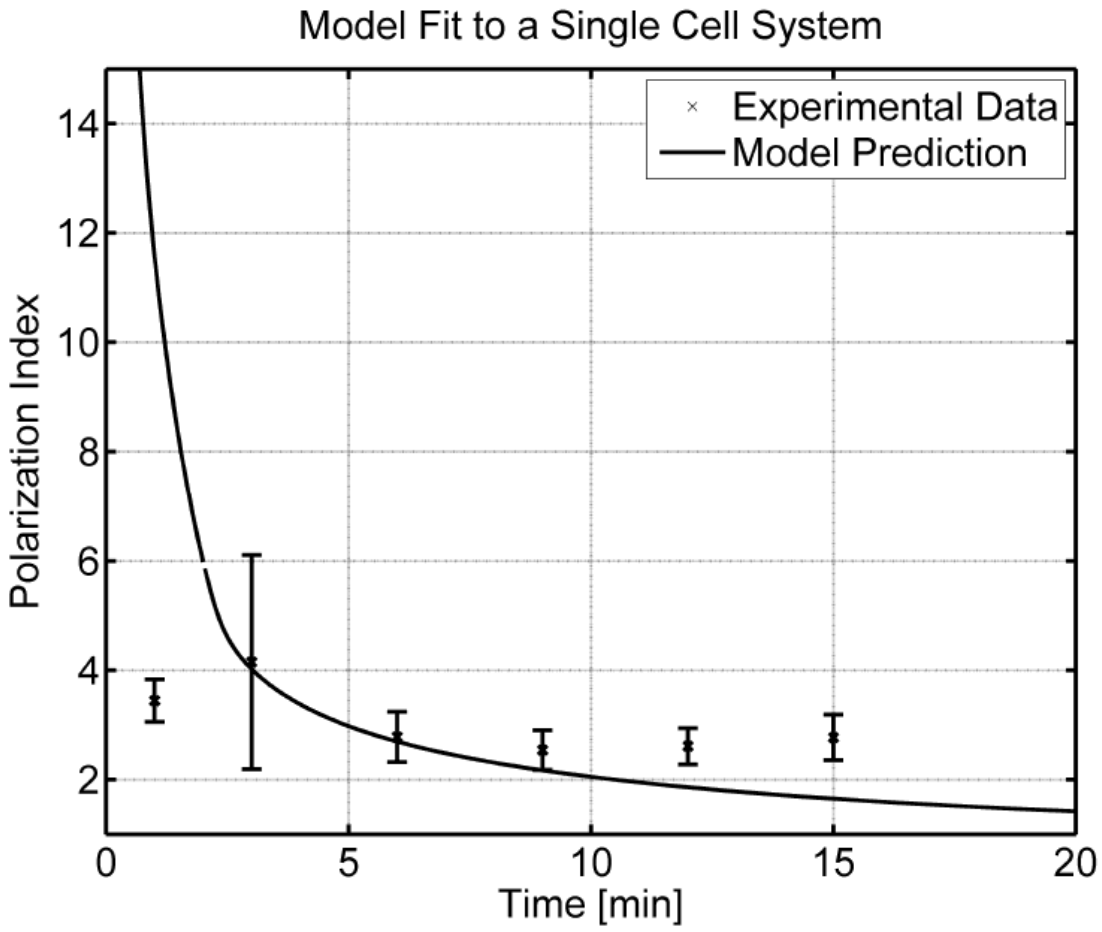

Figure 4-22: Model correlation with experimental data of a two-minute 100 ng/mL EGF pulse. Solid line: model results for the defined geometry with PI computed as per equation (50). Error bars indicate one standard deviation.

A satisfactory fit between model simulation and experimental data is observed up to 10 minutes. Except for the first time point, the decrease of PI as concentrations gradually homogenizes around the cell is confirmed with computed PI = 4 after three minutes down to PI = 3.2 after ten minutes. The effect of ROI boundary uncertainty is maximal after three minutes and can be attributed to residual fluorescence in the culture media resulting from freely diffusing EGF molecules following delivery. Therefore, increasing or reducing the ROI surface will significantly affect average pixel intensity. After ten minutes, experimental data exhibited

slightly higher PI compared to model predictions. Figure 4-23 illustrates the cell of interest after six and 21 minutes post delivery and demonstrates the vesicular nature of fluorescence signal by the end of the experiment. As the model does not include internalization, events occurring at later time points are not accurately depicted such as movements of endosomal vesicles through cytoskeletal motion. Internalization thus appears to stabilize polarization at later time points.

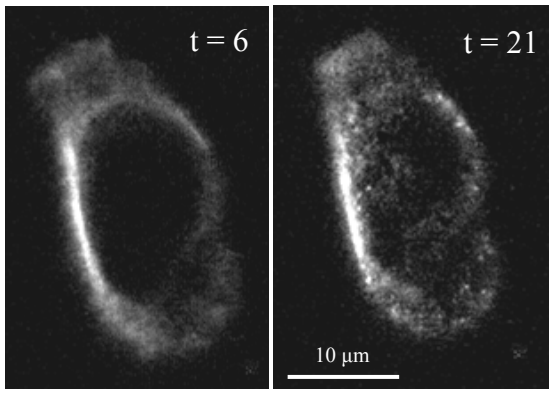

Figure 4-23: Comparison of fluorescence profiles after six (left) and 21 minutes (right) demonstrating the vesicular nature of fluorescence signals at later time points.

We further decided to evaluate model significance with another single cell system in a gap chamber. The cell of interest exhibited a significantly different shape, as shown in Figure 4-24:

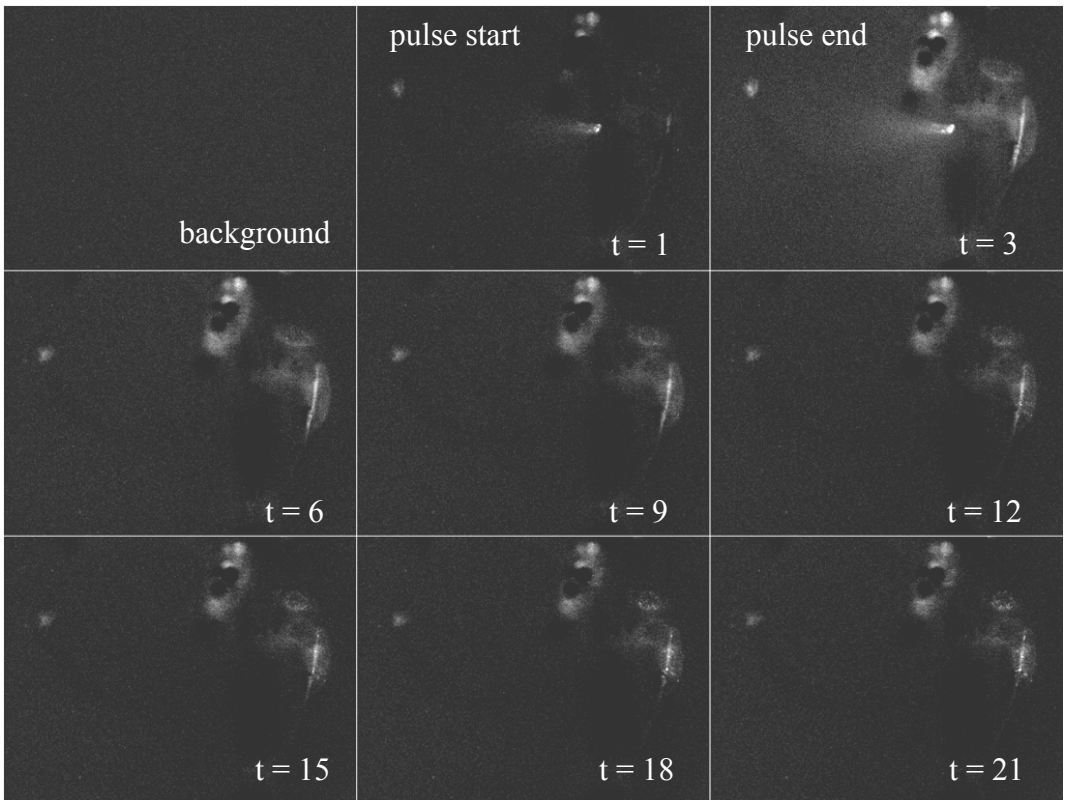

Figure 4-24: 40X fluorescent time-course of a two-minute pulse delivery of 100 ng/mL TRITC-EGF to a single HeLa cell after background removal with a three-minute time interval. Time in minutes.

The threshold approach was not effective as fluorescence signal coming from the media did not allow for the proper identification of cell boundaries. In this case, we used the fluorescence image at five minutes to manually draw the outline of the cell and the three-dimensional computational model was designed based on the experimental system dimensions, as shown in Figure 4-25:

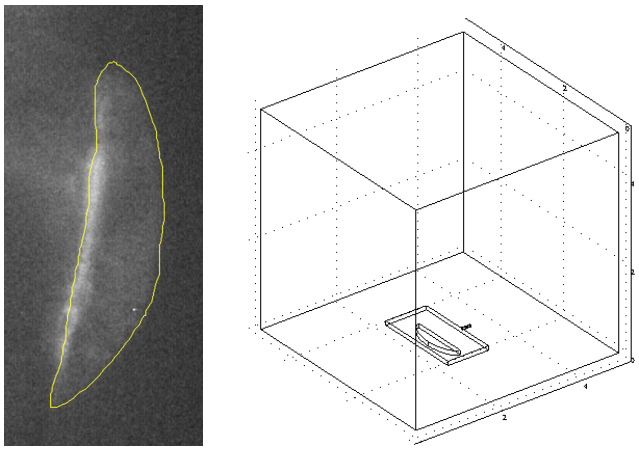

Figure 4-25: Manual identification of cell boundaries based on fluorescence image (left) and finite-element model sketch (right).

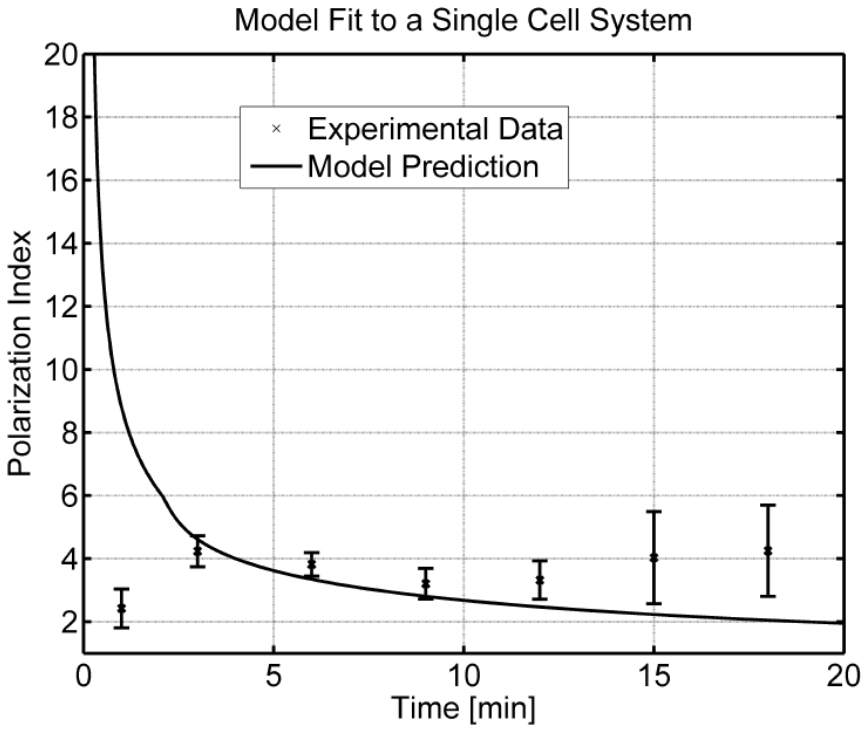

Figure 4-26: Model correlation with experimental data of a two-minute 100 ng/mL EGF pulse. Solid line: model results for the defined geometry with PI computed as per equation (50). Error bars indicate one standard deviation.

Due to the particular shape of the cell selected for pulse delivery, the cell was depicted as half-ellipse in COMSOL to increase model significance. Compared to the previous model fit, computation results exhibited greater PI at all times due to the change in cell shape. As shown in Figure 4-26, the proper depiction of the single cell was necessary as slight changes in cell shape demonstrated significant effects on computed PI (switch from half-ellipse to ellipse for example). The model exhibited satisfactory fit between one and ten minutes, after which experimental PI values were greater than computations. This is again indicative of the potentiating effect of internalization with vesicles concentrated on the cell side facing the point source of delivery.

This section demonstrated model significance using finite-element systems specifically tailored for the experimental conditions. Of relevance, we demonstrated that assuming simple diffusion in the gap chamber system was a reasonable assumption and allowed for the capture of polarization events at the single cell level. In COMSOL, internal boundaries are inactive and computing PI for a cell in direct contact with neighboring cells would necessitate omitting some of the cellular surface for measurements. This situation may or may not be acceptable depending on the ability to measure surface integrals for both a front and back domain. Therefore, cells part of compact spherical colonies will not be candidate for modeling as the back surface could not be defined in COMSOL.

4.4.7 Analysis of Cell Colony Effects

Point Source

For the reasons cited previously, the analysis of colony effects was performed experimentally and PI was measured as described in Material and Methods following a two-minute pulse of 100 ng/mL TRITC-EGF. Five cells were selected for analysis as shown in Figure 4-27.

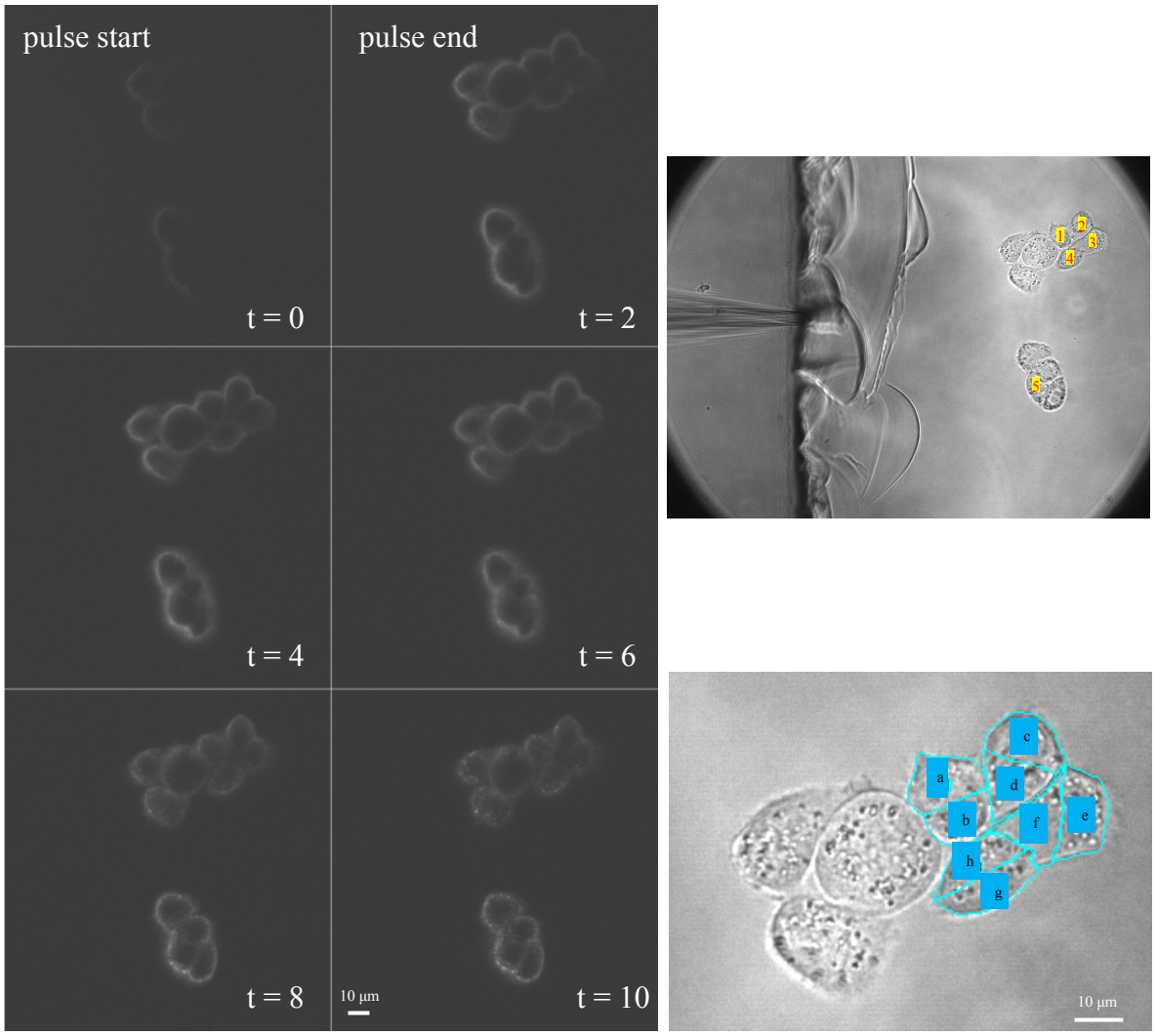

Figure 4-27: Two-minute pulse delivery of 100 ng/mL TRITC-EGF to HeLa colonies cultivated in a gap chamber. Top right: 40X brightfield image of two HeLa colonies (one seven-cell and one four-cell colony) with the micropipette on the left gap edge and identification of the five cells selected for analysis. The gap edge ad micropipette can be identified on the left side. Bottom right: manual drawing of masks (a, b, c, d, e, f, g and h) for front and back domains of single cells based on the orientation of available surfaces as described in Materials and Methods. Left: 40X fluorescent time-course of a two-minute pulse delivery of 100 ng/mL TRITC-EGF to HeLa colonies after background removal with a two-minute time interval. Time in minutes.

The identification of the axis of separation was made as described in Material and Methods and masks were defined manually. Results of PI measurements are presented in Figure 4-28.

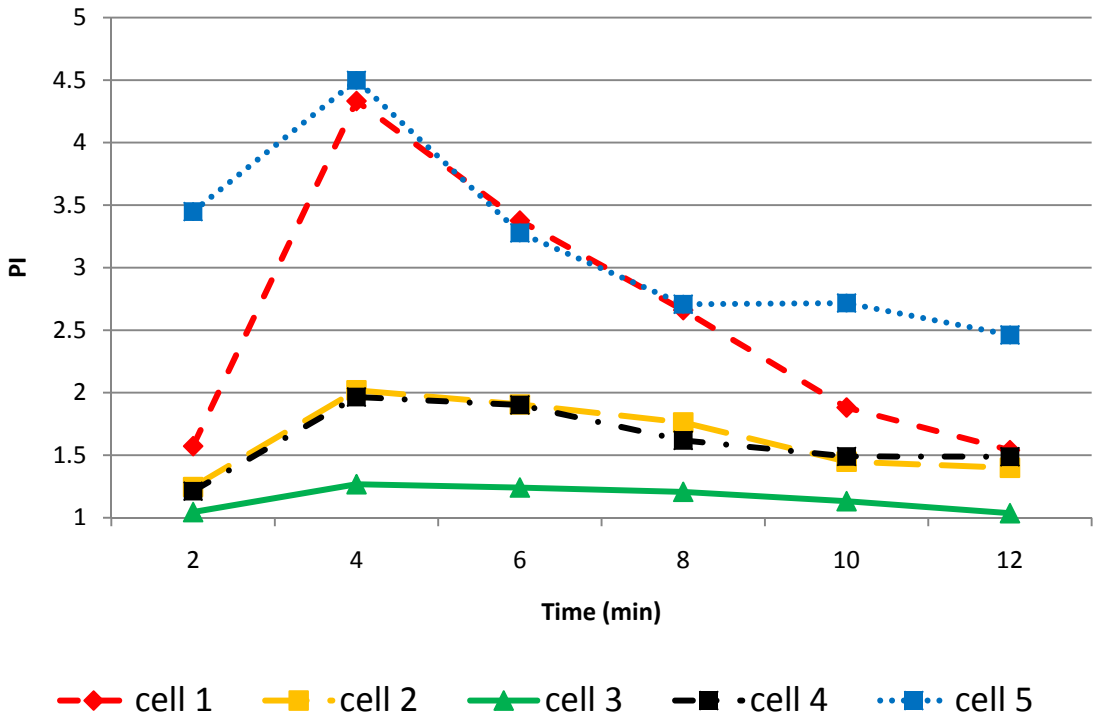

Figure 4-28: Analysis of colony effects on experimental PI measurements. Cells 1 and 5 (dark blue and light blue line) exhibited highest PI measurements.

With a two-minute pulse, the most distal cell of the system (3) demonstrated the lowest PI with a maximum of 1.27 after four minutes as shown in Figure 4-28. Other cells on the distal side such as (2) and (4) exhibited intermediate PI values with maximum of two after four minutes and PI = 1.5 by the end of the experiment. For these cells, the axis of separation between the front and back cell side was defined according to orientation of cell membranes available to freely diffusing EGF. Two cells exhibited significantly higher PI values (1 and 5). Cell (5) was located on the front of a small four-cell colony and was expected to be highly polarized, with a maximum PI of four after four minutes and PI = 2.5 by the end of experiment. Interestingly, cell (1) exhibited similar values between four and eight minutes and PI went as low as 1.6 after 12 minutes. Cell (1) was located further from the point source and the direct path with respect to the point source of delivery was encumbered with cells in the colony as shown in Figure 4-27. The

fraction of cell membrane available to the media seems a possible cause for this phenomenon, with lower ratio of membrane available to freely diffusing EGF responsible for higher computed PI thus compensating the increased shortest distance to the point source. Cell (5) exhibited a higher fraction of available membrane and higher PI values by the end of the time-course. A close inspection of fluorescence images demonstrated the apparition of endocytic vesicles as soon as eight minutes following delivery which was not observed in any other cell. After ten and 12 minutes, the high vesicular nature of EGF signal was clear as shown in Figure 4-29 and larger cytoplasmic volumes could contribute to higher polarization following internalization due to the limited mobility of endosomal vesicles. On the opposite, smaller cytoplasmic volumes could be responsible for a more rapid homogenization of cytoplasmic signal following internalization while the reduction of membrane surface could potentiate the negative effect of receptor lateral diffusion on polarization.

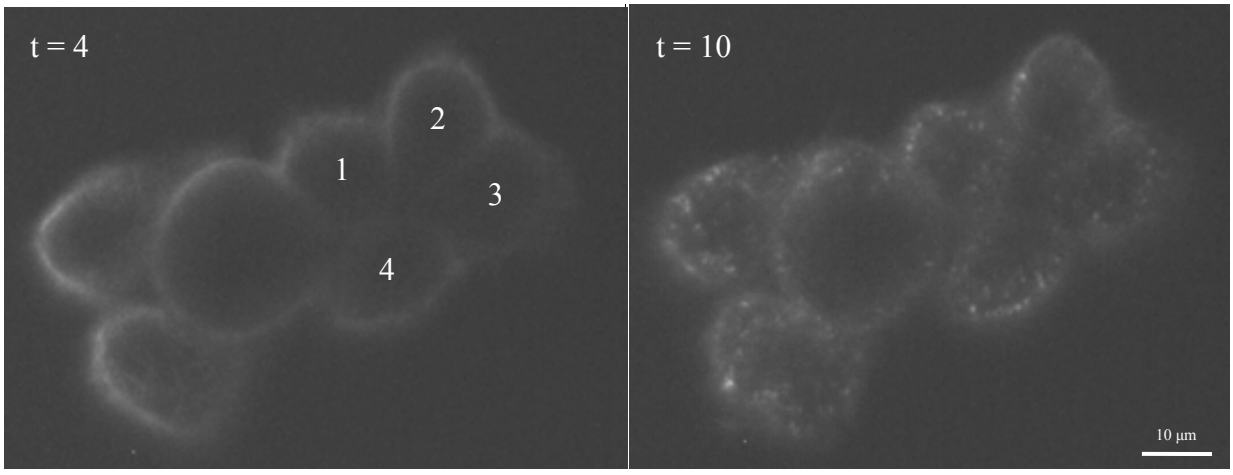

Figure 4-29: TRITC-EGF signal in HeLa cells after four minutes (left) and ten minutes (right) illustrating the vesicular nature of fluorescence signals at later time points. Time in minutes.

It has been previously reported that the kinetics of EGFR dimerization is a regulator of EGFR internalization (Wang, Villeneuve et al. 2005). Hence, different quantities of bound EGF on different cells could be responsible for different kinetics of internalization which could further impair or stabilize polarization depending on the cellular volume. Finally, all PI profiles exhibited the same behavior as previously reported, with low measured PI for the first time point (two minutes) indicating the acquisition system sensitivity did not allow for the capture of early polarized events due to low detected signal intensity.

Bulk Source

While the pulse delivery through a point source allowed for fine positioning with respect to single cells and cell colonies, we analyzed the potential for bulk delivery in the context of polarization. This approach enabled the polarization of a large amount of colonies of various sizes and shapes in a single experiment. HeLa cell colonies were cultivated in gap chambers as shown in Figure 4-30 and media containing 10 ng/mL TRITC-EGF was added to the culture for two minutes.

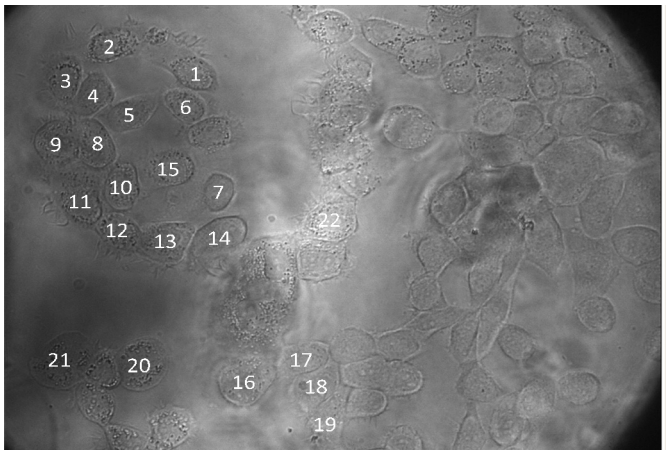

Figure 4-30: Brightfield image of a HeLa colony prior to two-minute pulse delivery of 10ng/mL TRITC-EGF and cell identification.

Figure 4-31 depicts a typical two minutes pulse of medium containing 100 ng/mL TRITC-EGF followed by time-lapse imaging at six minutes time interval.

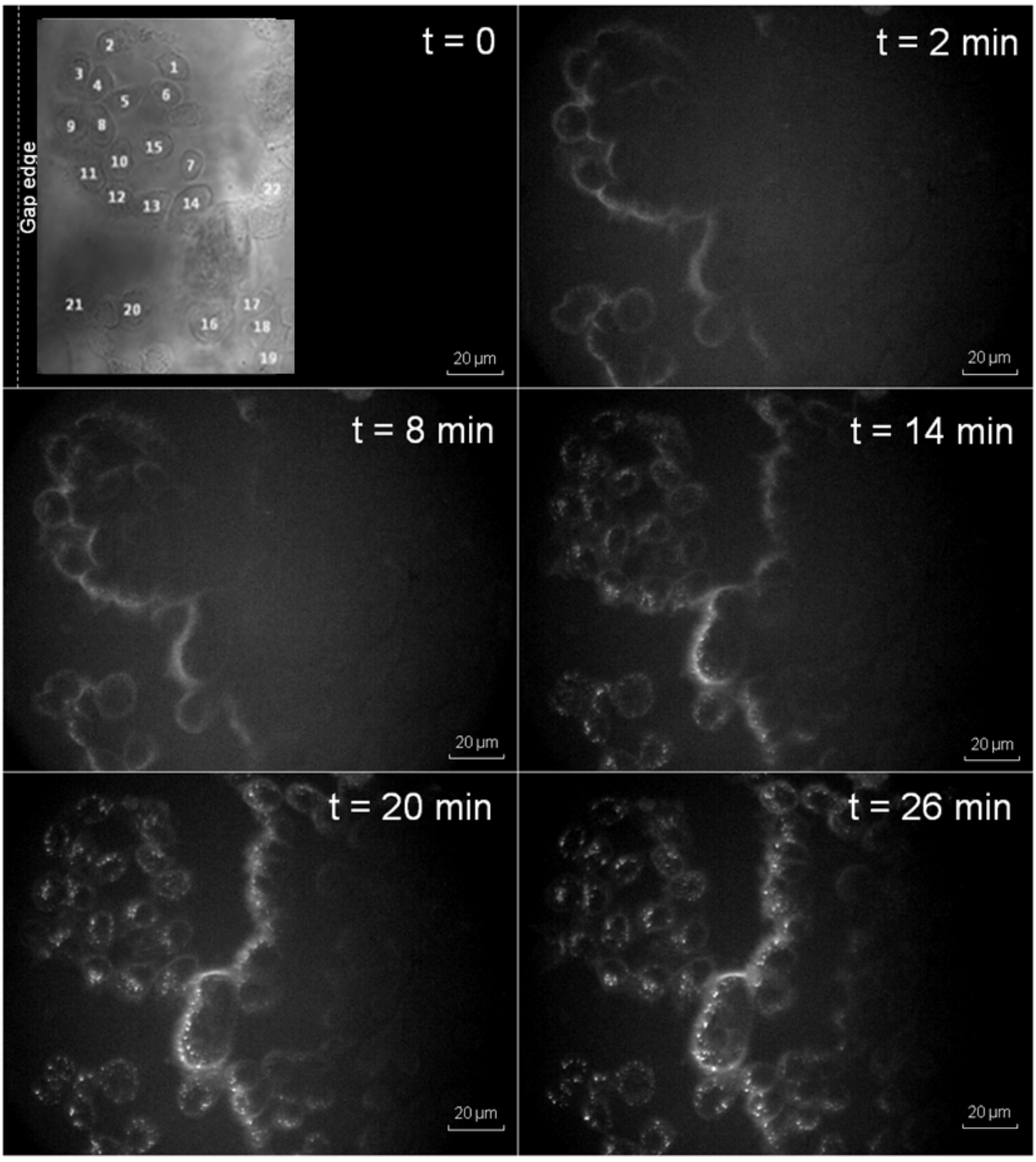

Figure 4-31: 40X fluorescent time-course of a two-minute pulse delivery of 10 ng/mL TRITC-EGF (bulk media change) to HeLa colonies after background removal with a six-minute time interval.

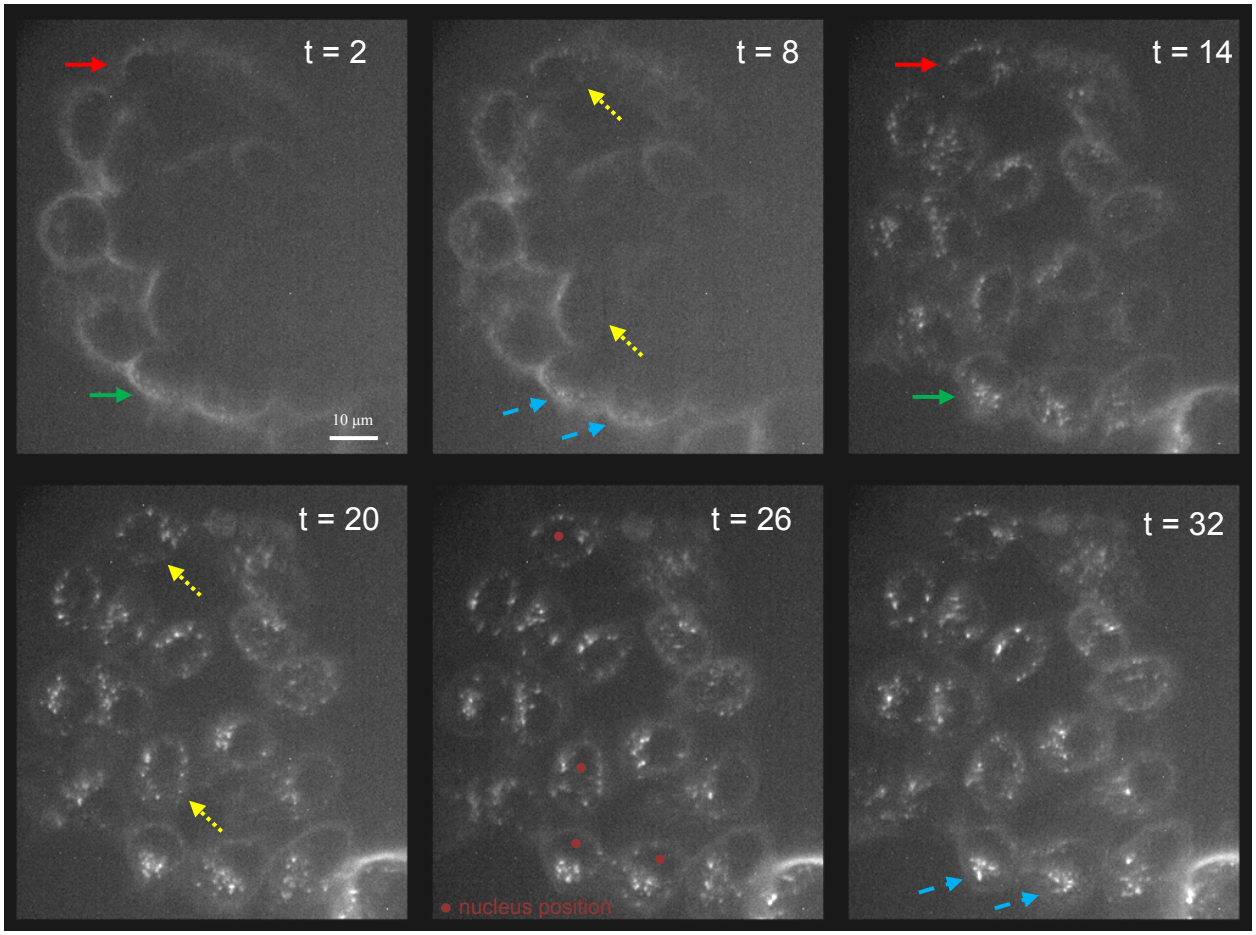

Figure 4-32: Illustration of a polarized colony and effect of cell nucleus position on the polarization of the cytoplasmic compartment. Time in minutes.

When further comparing cells with lower (red arrows) and higher levels of TRITC-EGF (green arrows), we observed the formation of patches on the cell membrane after eight minutes and internalization became apparent after 14 minutes, as shown in Figure 4-32. This indicates significant differences in terms of the amount of EGF molecules delivered to a single cell did not affect the kinetic of internalization. After eight minutes, we isolated two cells exhibiting strong to intermediate degrees of EGF polarization (yellow arrows) and observed that by 20 minutes post-delivery, endocytic vesicles were localized throughout the entire cytoplasm. Conversely, other cells were polarized and did demonstrate a much higher degree of polarization up to 32

minutes post-delivery (blue arrows). A careful examination indicated cells with a central nuclear position (yellow) lost cytoplasmic polarization rapidly which highlighted the potential for rapid and long-distance mobility (in the μm range) of endosomal vesicles in the cytoplasm. When the nucleus exhibited an eccentric position, vesicles charged with growth factors appeared restricted to a given cell side due to a restriction of the cytoplasmic volume.

In Chapter 2, we reviewed fundamental mechanisms of asymmetric cell division and described a mechanism in which the cell spindle could be asymmetrically positioned at the time of division, thus leading to the formation of daughter cells with different size and fate potential. We thereby propose non-central positioning of the nucleus could allow for the restricted movement of endosomal vesicles in a given subsection of the cytoplasmic compartment. Associated with the proper orientation of the mitotic spindle at the time of mitosis, this could allow for control of the repartitioning of activated signaling pathway intermediates such as the MAPK but also a variety of other cytoplasmic molecules and proteins relevant in the context of polarization.

4.5 Discussion

In this chapter, we developed a three-dimensional computational framework for the analysis of asymmetric environments of soluble factors *in vitro*. Diffusive transport from a point source delivers soluble EGF onto a cell surface on which a kinetic model of binding and internalization was developed. Using PI and PO, we performed a sensitivity analysis that identified significant parameters of the system with respect to the defined metrics. We demonstrated the importance of the forward rate constant, initial concentration of free receptors

and diffusion coefficient, which led us to simplify the kinetic model to a simple on-binding step in which k_f and R_i were estimated experimentally to improve model significance.

Using Schoeberl's analysis as a reference, we aimed at identifying experimental conditions consistent with asymmetric MAPK activation following controlled EGF release and especially conditions in which PO_{back}<15%. The complexity of geometry effects was illustrated by comparing the two methods for EGF delivery, constant release and EGF pulse. With constant release, the addition of reflective boundaries in the cell vicinity contributed to reduced occupancy differentials on the cell surface as EGF concentration around the cell rapidly homogenized. When EGF was pulsed for two minutes, concentrations were increased on the front cell surface and this phenomenon was amplified in the adherent and gap chamber systems. We demonstrated that while improving the degree of polarization *per se*, the culture system is a major effector of polarization. Depending on selected delivery strategies, the effect of reflective boundaries in the cell microenvironment is reversed and this could not have been elucidated without the combinatorial use of finite-element modeling and boundary value problems. Simple diffusion of molecules in media at 20ºC did not allow for polarized signals at the single cell level as we demonstrated MAPK activation was homogeneous on the front and back cell side based on occupancy levels.

The diffusion coefficient in the cell vicinity is a major effector of the polarization. Slowing down diffusion of soluble molecules triggers high PI values while still allowing for occupancy levels consistent with signal transduction, especially in the case of the gap chamber. Hence the culture system needs to be carefully considered in the context of polarization. Of relevance, this analysis allowed for the definition of experimental conditions in which MAPK activation was triggered exclusively on a specific cell side with occupancy levels below 15% on

the distal cell side at all times. *In vivo*, diffusion of soluble molecules in tissues will allow for polarized signals at the single cell level and source distance from the target cell, concentration of released factor, extracellular matrix viscosity as well as the presence of neighboring emitting or reflecting cells could provide control mechanisms for target thresholds.

When looking at the effect of neighboring cells, we further demonstrated the beneficial effect of increasing the shortest distance to the back cell side with respect to the point source of delivery. Neighboring cells did not affect significantly polarization in the adherent system, as the apical / basal domains of the cells still allowed for free diffusion of EGF molecules. A significant improvement of PI and PO differential was computed in the gap chamber especially in the five-cell system, demonstrating the interplay between the culture system and cell colony configuration. In this case, it was possible to reduce occupancy levels on the distal cell side to ensure below 70% MAPK/Erk activation with near saturation on the front side for two minutes. These highly asymmetric conditions of occupancy have the potential to generate various levels of downstream MAPK activation in the cytoplasm based on the position of the point source of delivery.

In vivo, cells are confined in complex three-dimensional environments constituted of neighboring cells and extracellular matrix limiting the diffusion of soluble molecules. Soluble factors experience restricted diffusion in tissue in which gradients can be created by factor entrapment in the extracellular matrix (Dyson and Gurdon 1998; Dowd, Cooney et al. 1999). This is a prerequisite for the formation of polarized systems such as epitheliums in which relative positional information allows for the creation of basal, lateral and apical membrane domains. It indicates that the addition of supplementary artificial boundaries in the cell vicinity may be one

logical step towards further improvement of *in vitro* culture techniques as demonstrated in the gap chamber.

Even though specific culture conditions provide major improvements of the potential for asymmetric delivery, the time frame during which asymmetric conditions were obtained was short. Occupancy levels moderately increase after pipette removal (as shown in Figure 4-9), which indicates long term asymmetric potential was not achieved at the single cell level. In this context it is important to mention that additional cells were not introduced in the model due to the higher complexity of meshes and difficulty for model convergence and accuracy. Our results demonstrated a trend that is likely applicable to larger cell aggregates and also to more complex colony shapes. Hence, the polarization of cells inside larger colonies has the potential for asymmetric MAPK profiles longer than the ones demonstrated in this computational analysis.

The model was fitted to experimental data for a single cell cultivated in a gap chamber, demonstrating the relevance of a three-dimensional finite-element model of diffusion and boundary value problem in the context of elucidating polarized soluble signals *in vitro*. Proper analysis and prediction of polarized signals will require the accurate representation of culture conditions, cell shape, cell number, cell colony configuration and dimensions. We thereby propose that conventional culture systems lack the ability to generate polarized signals at the single cell level. Cultivating cell colonies in a gap chamber can increase the shortest distance to the back cell membrane as long as cells are attached to both gap surfaces, thus mimicking the limited diffusion of molecules in the complex matrix while allowing diffusion in water.

After user-based definitions of ROIs, CAD export and finite-element model setup can be automated to significantly increase the speed at which complex multicellular three-dimensional

models can be generated and analyzed. While this analysis was performed post-delivery, it is now possible to envision systems in which colonies will be analyzed prior to controlled factor release and potential for polarization assessed according to system geometry. Target PI, PO and differential values could be defined and used for the optimization of system parameters (pulse length and factor concentration), thus enabling on demand prediction of polarization *in vitro* as shown in Figure 4-33.

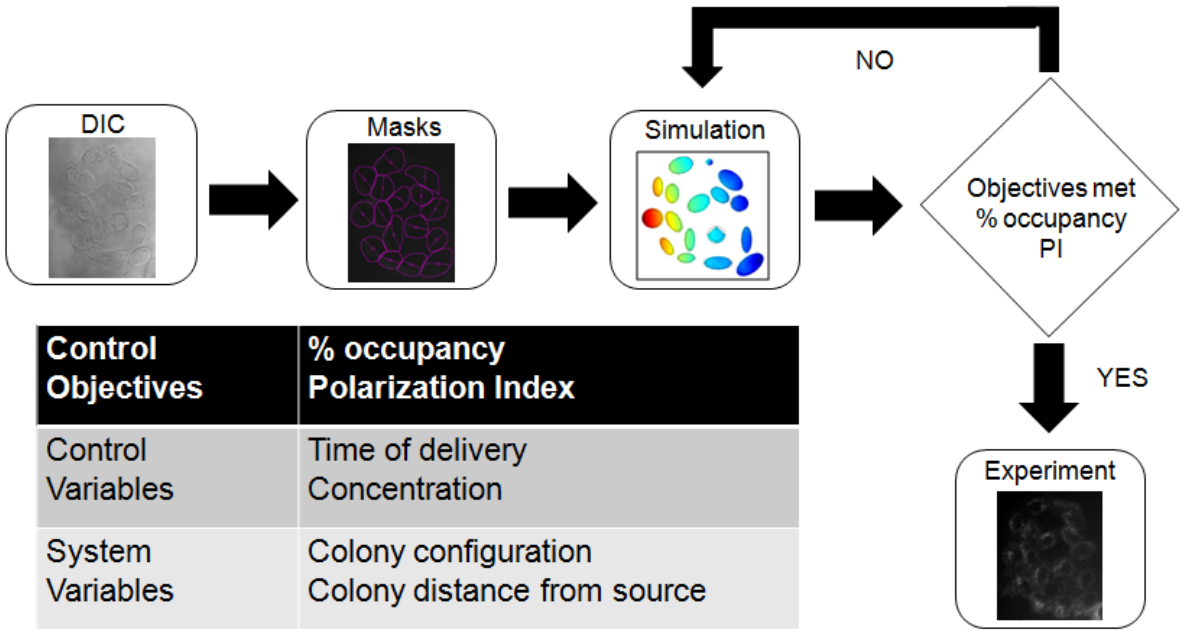

Control Objectives	% occupancy Polarization Index
Control Variables	Time of delivery Concentration
System Variables	Colony configuration Colony distance from source

Figure 4-33: Automation and prediction of polarization *in silico*.

Quantitative differences in signaling intermediates can generate different levels of early genes activation based on simple enzyme biochemistry and law of mass action. As several early genes products act as homo-heterodimeric transcription factors for late genes, it appears quantitative differences at the signaling level have the potential to elicit qualitative changes at the cellular level. Also, the length of MAPK activation controlled by removal of the point source in our system can dictate important specificity of repertoire of Jun and Fos proteins expressed

(Kovary and Bravo 1991; Kovary and Bravo 1992; Cook, Aziz et al. 1999). While the activation of MAPK/Erk can be asymmetrically triggered on a single-cell surface, all MAPK signals will converge towards the same nucleus and ultimately control the activity of transcription factors regulating the expression of two copies of the identical target gene(s). Polarization of signaling pathways at the single cell level will be physiologically relevant only in the context of appropriate cell cycle positioning. Numerous approaches are used to synchronize cells in culture such as serum removal or the addition of chemicals such as nocodazole and these allow for cell blockage at various cell cycle position (G1/S or G2/M for example) (Hoebeke, Van Nijen et al. 1976). Polarization at the time of mitosis will enable asymmetric repartitioning of pools of activated transduction proteins which could then elicit different patterns of gene activation in the daughter cells. This also indicates that short time frames of asymmetric MAPK profiles as demonstrated in the gap chamber with five cells can be significant if they are properly correlated with the cell cycle.

We demonstrated the experimental feasibility of polarization and the relevance of finite-element models for the definition measurable metrics in the context of delivery efficiency and asymmetry. The next chapter will study both short-term and long-term effects of polarization and we will analyze the subcellular localization of duo-phosphorylated MAPK (the active form of MAPK) and several proteins either involved in polarization complexes (Par) or acting as cell fate determinants (Numb) both in HeLa cells and primary cell lines. We will finally evaluate the potential long-term effects of polarization through long-term live-cell imaging of HeLa colonies cultivated in gap chambers following TRITC-EGF pulse.

5 Chapter 5: Physiological Effects of Pulse Delivery

Chapters 3 and 4 have demonstrated how a computational framework of diffusion and reaction on a cell surface can be useful for the definition of a set of metrics for polarization analysis. These were used to demonstrate that both the culture systems and neighboring cells were important and should be considered in the context of polarization. Models can adequately capture experimental data based on the partitioning of fluorescent molecules on a cell surface and also be used for prediction as long as the experimental setup is accurately depicted. These computational approaches are a framework useful in the engineering of delivery strategies based on target occupancy levels (PO) and polarization index (PI) values. The physiological relevance of controlled pulses to single cells should now be investigated.

In a first step, short term effects following the pulse will be studied using immunocytochemical analysis of key molecules in the context of EGF signaling, polarization proteins and cell fate determinants. While informative, the shortcoming of this approach is its destructive nature, as cells must be destroyed or fixed in order to obtain the desired information. To further evaluate the long-term effects of pulse delivery and polarization *in vitro*, methods are needed that enable the acquisition of data in time and space and allow for the identification of lineage-related effects. These systems could be used for the analysis of asymmetric properties between daughter cells, such as cell cycle time, morphological features, migration pathways and distances as well as the expression of various proteins. To achieve this, live-cell imaging stations should allow for the observation of cellular systems in a near-continuous manner.

Time course imaging and cell tracking methods were developed and implemented in the 1960s, initially for studying generation times of monolayer cell cultures (Hsu 1960; Earle 1962; Froese 1964). Since then, the improvement of microscopic and computer technology has allowed such studies to include extraction of morphological (Geng, Cosman et al. 2004) and locomotory phenotypes (Niggemann, Maaser et al. 1997). More recent studies have tracked single cell movement through three-dimensional substrates (Niggemann, Maaser et al. 1997; Demou and McIntire 2002; Rabut and Ellenberg 2004). In these cases it is obvious that continuous observation of the system is imperative in order to obtain accurate temporal data, such as cell cycle time, or spatial data, such as cell migration pathways. Such studies will require the combination of unique imaging systems, image processing and cell tracking software, as well as feature extraction and pattern classification algorithms. In a second step, we will investigate the potential for lineage tracking in the context of cell polarization. A specific set of features are needed to evaluate the potential for asymmetric factor delivery and assess long-term metabolic and phenotypical effects of pulse delivery. HeLa colonies cultivated in gap chambers will be tracked for up to five days using a custom imaging system and tracking software. Analysis of data will focus on variations in cell cycle time based on their localization among polarized colonies or the time until first division following TRITC-EGF pulse.

5.1 Material and Methods

5.1.1 Long-Term Imaging and Tracking System

In order to be adapted for live-cell imaging, a custom-built cell culture chamber has been implemented on the stage of a Zeiss Axiovert 200 inverted microscope as shown in Figure 5-1.

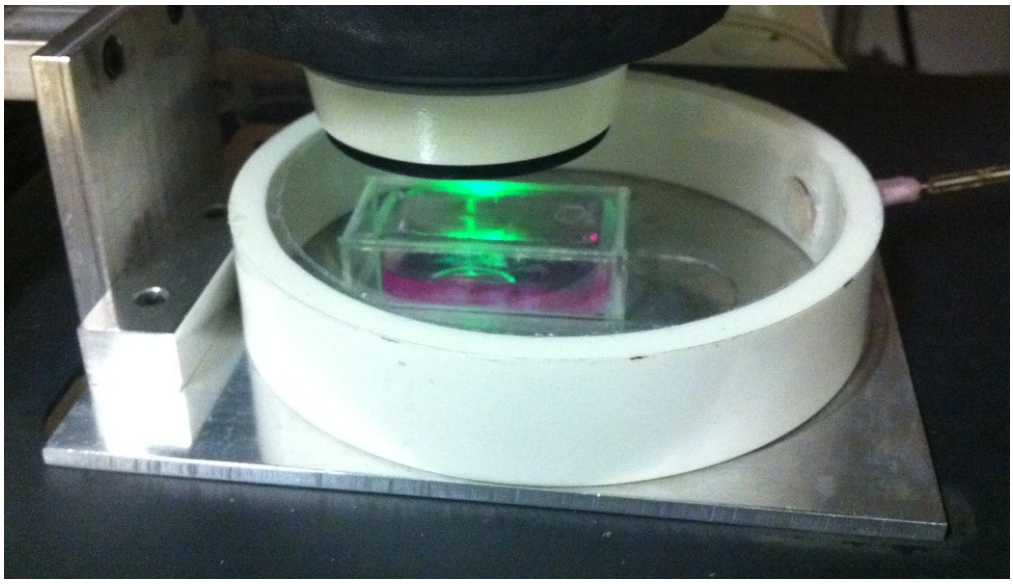

Figure 5-1: Cell culture environment chamber that provides control for temperature, humidity and CO_2 during long term live cell imaging.

Cell culture is processed in the inner chamber surrounded by a water reservoir to control humidity. The outer chamber offers a control for CO_2 by passive gas exchange with 5% CO_2 balance air and temperature is regulated in the whole microscope environment. The microscopy system has been installed in a laminar flow hood that ensures sterility in the microscope environment and allows for cellular micromanipulations with an open inner chamber. The microscope has also been implemented with a motorized stage that allows a fine control of the stage positioning in the x, y and z directions. The stage is controlled using a custom-built interface and software that allows the directed positioning of the live sample in culture while it is translated through the microscope's focal point, as shown in Figure 5-2:

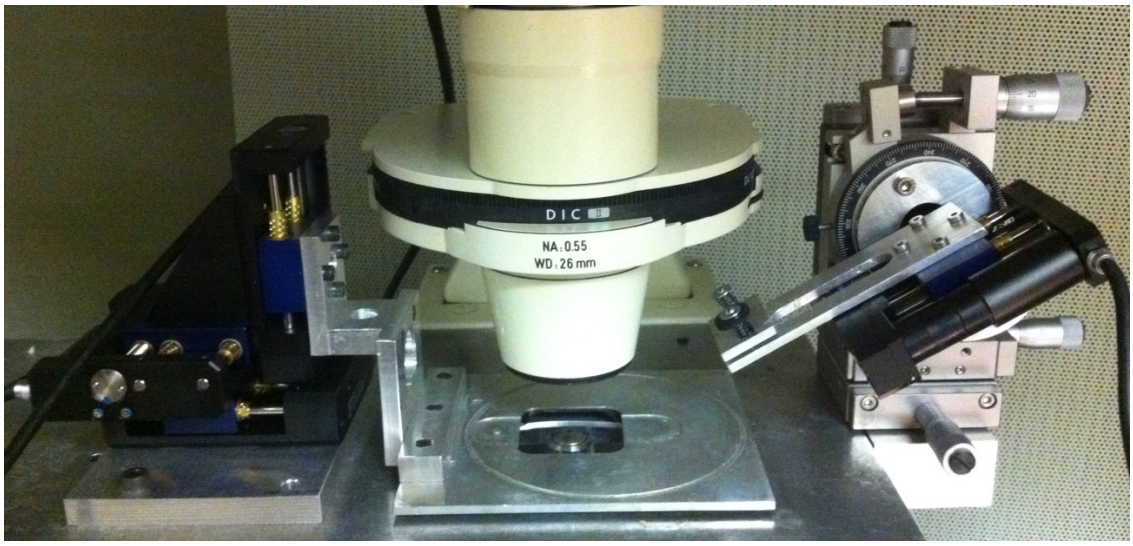

Figure 5-2: The complete three-axis robotic stage (x,y and z-axis) is on the left and the micropipette positioning system (or w-axis) is on the right.

Custom software enables the creation of imaging "blocks" corresponding to successive defined positions through which the microscope stage moves sequentially and repetitively over time. This feature enables long-term live cell imaging (LTLCI) of relatively large fields of view (1cm x 1cm).

5.1.2 Cell Culture

HeLa cell culture was performed as described in Chapter 4. Mouse cortical neural stem cells (NSC 002) were obtained from R&D systems. NSC basal media was supplemented with Penicillin-Streptomycin (1X final) EGF and bFGF at a final concentration of 20 ng/mL. Aliquots were stored at -35ºC until use. For adherent cultures of mNSCs, TC-treated culture flasks were coated with poly-L-ornithine (Invitrogen, Canada) overnight at 37ºC. Flasks were subsequently rinsed three times and allowed to incubate overnight at 37° C and 5% CO_2. A 1 µg/mL solution of Bovine Fibronectin (R&D Systems, USA) was freshly prepared by adding fibronectin in

sterile PBS and performing gentle inversion. PBS was discarded and flasks were rinsed with 10 mL PBS and 10 mL of 1 μg/mL bovine fibronectin solution was subsequently added to each flask. Incubation was performed at 37° C and 5% CO_2 for 3 - 30 hours after which fibronectin solution was discarded, flasks rinsed once with 10 mL PBS and used immediately. For adherent culture of mNSCs, cells were seeded on fibronectin coated flasks at a concentration of 2.0 x 10^5 cells/mL. After 24 hours, 1 μL of 1000X FGF basic stock and 1 μL of 1000X EGF stock per mL of culture were added. Every second day, medium was replaced with fresh NSC Media. Cells were passaged when reaching 70-80% confluence and were cultivated up to three passages according to the manufacturer's instructions. For TRITC-EGF delivery experiments, mouse cortical stem cells were cultivated in gap chambers coated with fibronectin as described previously. Cell loading was performed as described in Chapter 3 and the bead size selected for culture was seven μm.

5.1.3 Immunofluorescence

Samples of interests were fixed using 4% paraformaldehyde for 25 minutes at room temperature. Chamber was rinsed three times with PBS 1x and initial blocking was performed in PBS 5X Bovine Serum Albumin (BSA, Invitrogen, CA) overnight at 4ºC. Primary antibodies for EGFR (ab2430, ABCAM, USA), phospho-MAPK (ab50011, ABCAM, USA), Par-6 (ab45394, ABCAM, USA), Numb (ab14140, ABCAM, USA) were used at an assay-dependant dilution and prepared in PBS 1% BSA. Incubation was performed overnight at 4ºC. Chambers were rinsed three times in PBS 1X then secondary antibodies goat anti rabbit FITC (ab7086, ABCAM, USA) and goat anti mouse Cy5 (ab6563, ABCAM, USA) were used at an assay-dependant dilution in PBS 1% BSA and incubated overnight at 4ºC. Chambers were rinsed three times in PBS 1X and

stained with a DAPI / antifade solution at 20 µg/mL for 25 minutes. Chambers were rinsed three times in PBS 1X and protected from light. Confocal imaging was performed on an Olympus Fluoview FV1000 confocal microscope.

5.1.4 Cell Cycle Time Analysis

To evaluate the long term effects of polarized delivery, HeLa CCL2 colonies cultivated in gap chambers were pulsed for two minutes with a bulk media change of phenol-free DMEM-F12 containing 10 ng/mL TRITC-EGF as described previously. Media was removed, phenol-free DMEM-F12 added to the culture and fluorescent imaging of gaps was performed to assess polarized cells following delivery. Cells were subsequently cultivated in DMEM-F12 and tracked for four days using DIC imaging with a time interval of five minutes on a Zeiss Axiovert 200 inverted microscope in controlled atmosphere (37 ºC, 5% CO_2). Lineages trees were generated in MATLAB using custom software CellHunter. For this purpose, cells of interest were manually tracked frame by frame by users.

5.2 Results

5.2.1 Short-Term Polarization Effects

HeLa System

In this section, we present the immunocytochemical analysis of members of the EGFR signaling pathway, polarization complexes and cell fate determinants in various polarized and non polarized colonies of HeLa cells and mouse cortical stem cells.

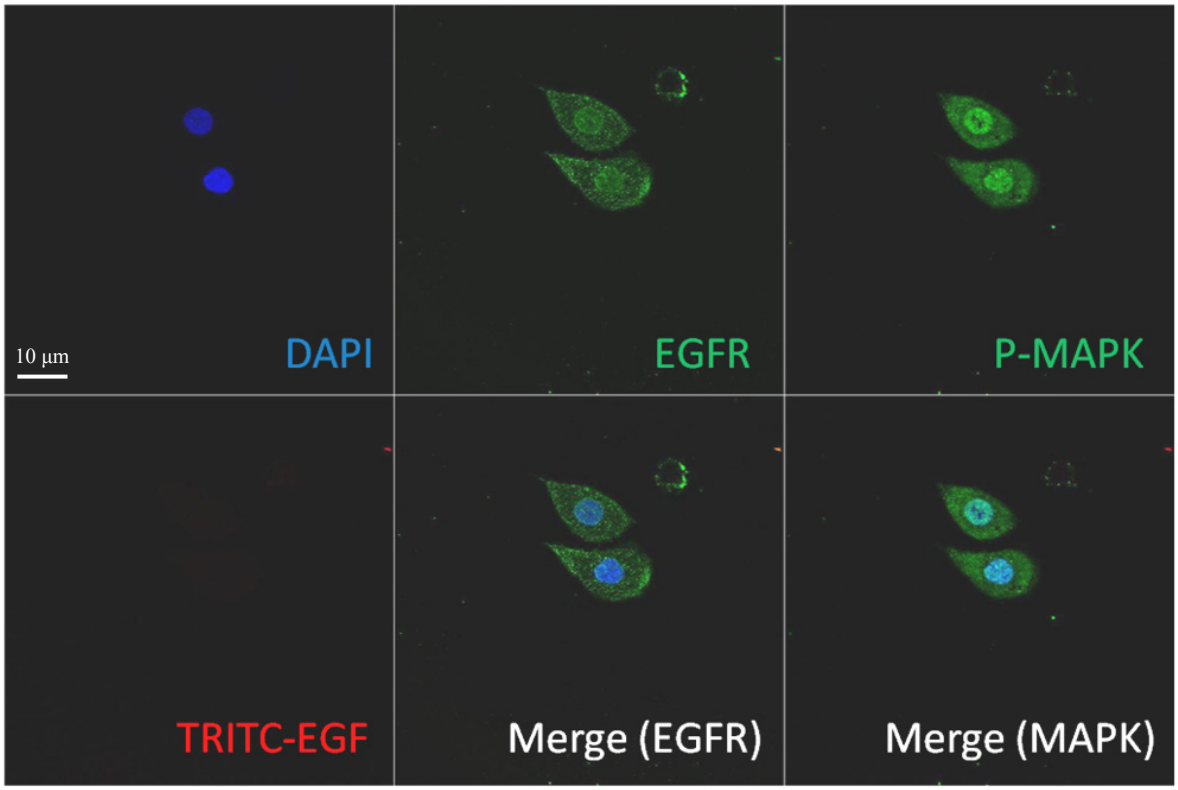

Figure 5-3: Immunofluorescence of non polarized HeLa cells cultivated in a gap chamber (40X). Blue: DAPI. Red: TRITC-EGF. Green: EGFR (middle) and duo-phosphorylated MAPK (right).

As shown in Figure 5-3, the localization of EGFR on the cell surface is homogeneous without EGF polarization and EGFR exhibits both a nuclear and surface localization in HeLa cells. The analysis of the duo-phosphorylated MAPK demonstrated nuclear and cytoplasmic localization and indicated a high level of basal expression. In Figure 5-4, a two-cell colony was pulsed with TRITC-EGF and EGF polarization on the cell surface is depicted after four minutes post delivery.

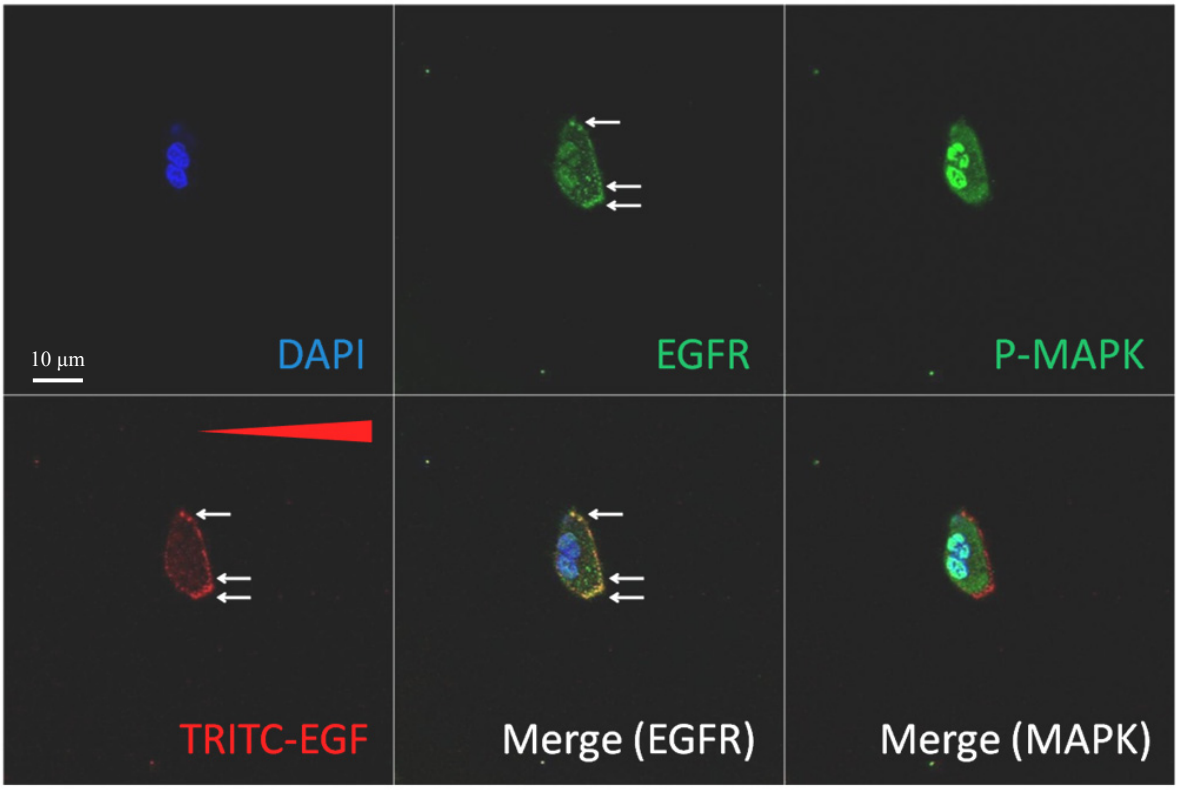

Figure 5-4: Immunofluorescence of a polarized two-cell HeLa colony after four minutes post-delivery of 100 ng/mL TRITC-EGF (40X). Gap edge is on the right side of the cell and TRITC-EGF gradient is depicted accordingly. The merge image demonstrates the polarization of EGFR on the cell surface as a result of EGF polarization. Blue: DAPI. Red: TRITC-EGF. Green: EGFR (middle) and duo-phosphorylated MAPK (right).

The localization of EGFR was not homogeneous and concentrated areas of receptors could be observed overlapping with EGF signal. The merge image demonstrated colocalization of EGF and EGFR, indicating that a polarized soluble signal could induce the polarization of surface receptors. To our knowledge, this is the first report indicating polarization of EGFR can be a result of asymmetric soluble EGF signals in the cell microenvironment *in vitro*. The activated MAPK staining exhibited higher intensity in the nuclear compartment which was consistent with prior reports of activated MAPK translocation towards the nucleus for the activation of target nuclear proteins, transcription factors and ultimately genes.

Partitioning Defective 6 (Par-6) is involved in fate determination as demonstrated in *Drosophila* in which it is asymmetrically partitioned at the time of mitosis among the Par-3 / Par-6 / atypical Protein Kinase C (aPKC) complex (Wodarz, Ramrath et al. 2000; Ohno 2001; Petronczki and Knoblich 2001). Some of the Par proteins including Par-3 and Par-6 regulate the assembly of tight junctions in *Drosophila* and Par-3 phosphorylation has been shown to occur through EGF-mediated Src kinase signaling (Wang, Du et al. 2006). We analyzed Par-6 localization profiles after four and 18 minutes post pulse delivery of 100 ng/mL TRITC-EGF, as shown in Figure 5-6 and 5-7.

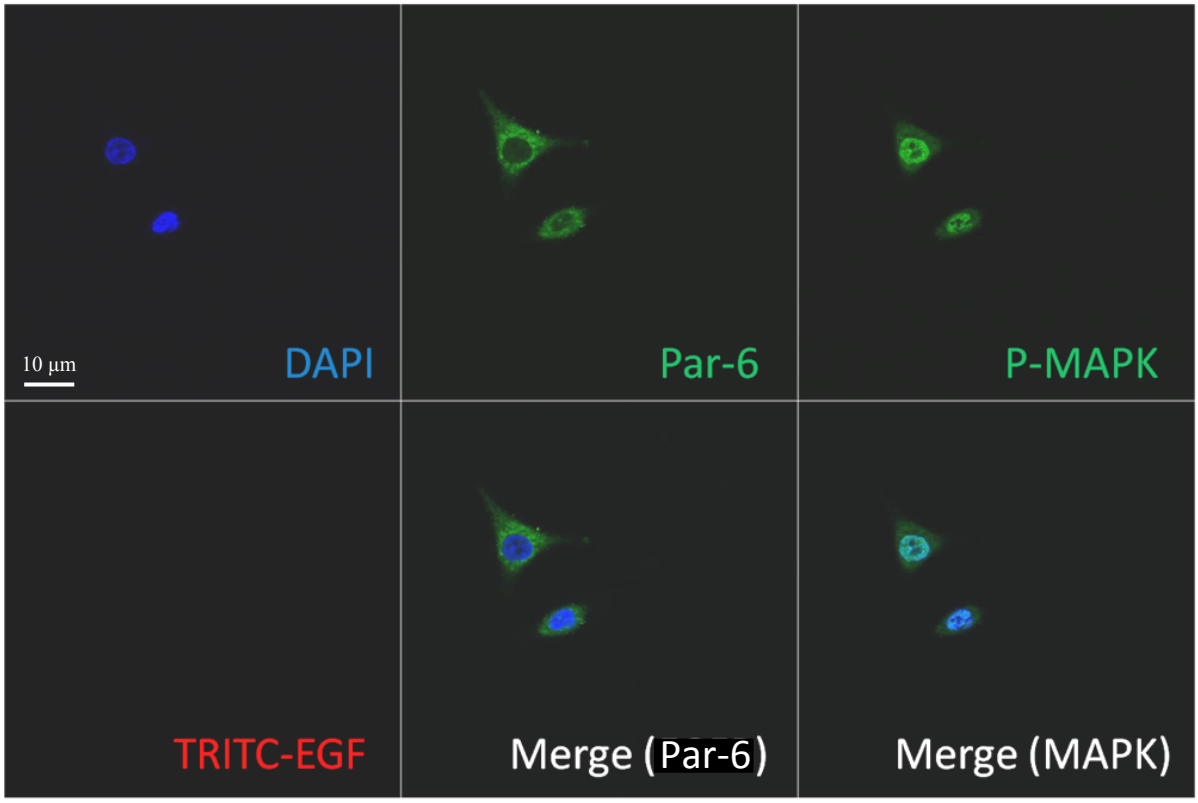

Figure 5-5: Immunofluorescence of non polarized HeLa cells cultivated in a gap chamber (40X). Blue: DAPI. Red: TRITC-EGF. Green: Par-6 (middle) and duo-phosphorylated MAPK (right).

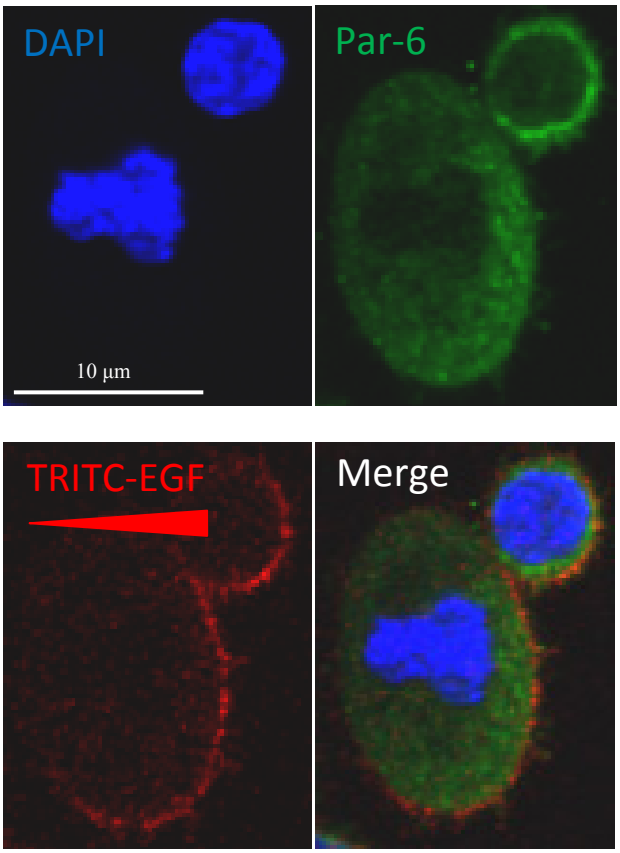

Figure 5-6: Immunofluorescence of a polarized mitotic HeLa cell after four minutes post-delivery of 100 ng/mL TRITC-EGF (40X). Gap edge is on the left side of the cell and TRITC-EGF gradient is depicted accordingly. Blue: DAPI. Red: TRITC-EGF. Green: Par-6.

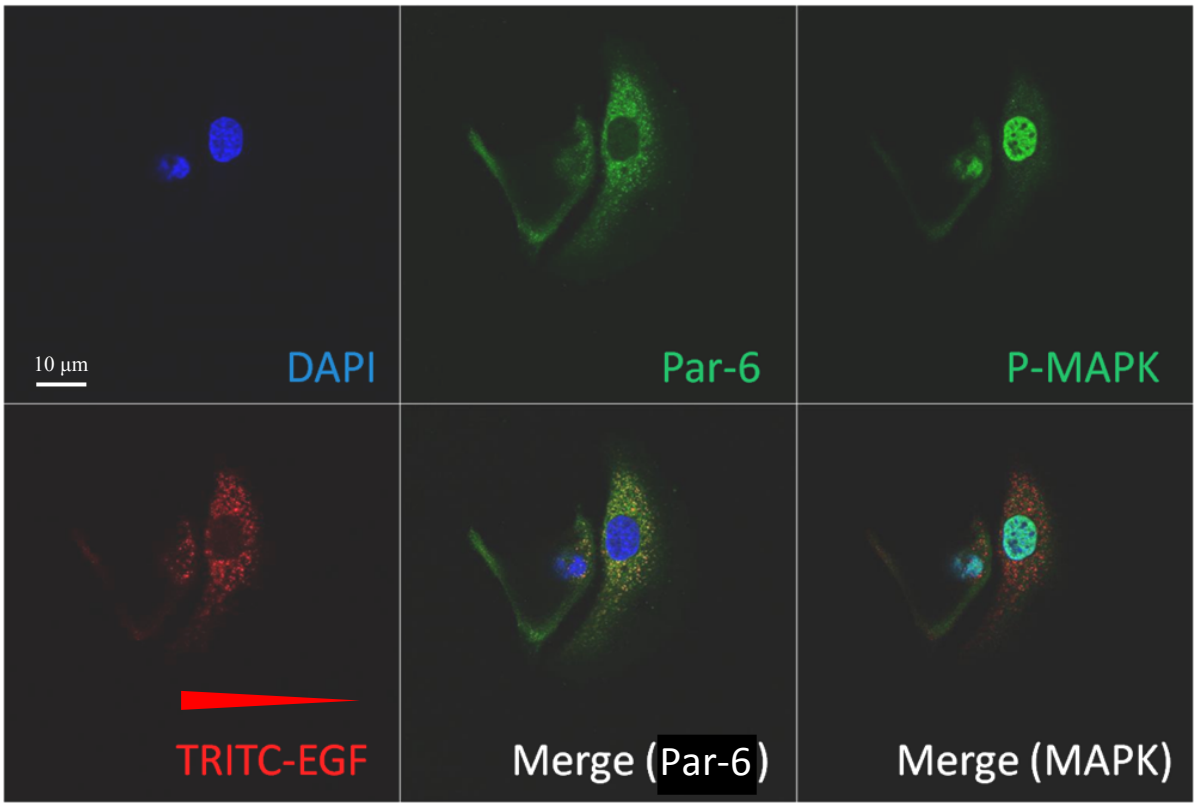

Figure 5-7: Immunofluorescence of a polarized HeLa cell after 18 minutes post-delivery of 100 ng/mL TRITC-EGF (40X). Gap edge is on the left side of the cell and TRITC-EGF gradient is depicted accordingly. Blue: DAPI. Red: TRITC-EGF. Green: Par-6 (middle) and duo-phosphorylated MAPK (right).

In regular culture conditions, Par-6 expression was homogeneous in the cytoplasm as shown in Figure 5-5 and some cells exhibited a higher perinuclear profile. Four minutes following TRITC-EGF pulse, Par-6 expression profile correlated with EGF polarization as non polarized cells exhibited homogeneous cytoplasmic expression while highly polarized cells demonstrated cytoplasmic polarization of Par-6 according to the EGF profile. A mitotic cell was able to integrate the EGF gradient and generated a polarized Par-6 response as shown in Figure 5-6. This indicates single dividing cells can capture asymmetric signals at the time of division and control of soluble factors in correlation with cell cycle time could allow for asymmetric partitioning of cell fate determinants in daughter cells. 18 minutes after polarized delivery, cells

exhibited a vesicular EGF profile with no apparent polarization with respect to the source of pulse delivery. Interestingly, the Par-6 staining demonstrated colocalization with EGF vesicles as shown in the merge image. It has been demonstrated in HeLa cells that Par-6 was necessary for the regulation of endocytic trafficking (Balklava, Pant et al. 2007) which raises the possibility EGF-containing endosomal vesicles and Par-6 interact during active vesicular transport. This demonstrates polarization of endosomal vesicles could be responsible for the asymmetric partitioning of polarization proteins such as members of the Par family.

Amongst cell fate determinants, Numb is also important in the regulation of cell fate as it contributes to the downregulation of Notch signaling (Frise, Knoblich et al. 1996). When we analyzed the Numb expression profile of polarized and non polarized cells, we observed homogeneous cytoplasmic expression of Numb at early (data not shown) and late time points following pulse delivery (22 minutes), thereby indicating no polarization dependant effect on Numb following asymmetric EGF signals as shown in Figure 5-8 and 5-9.

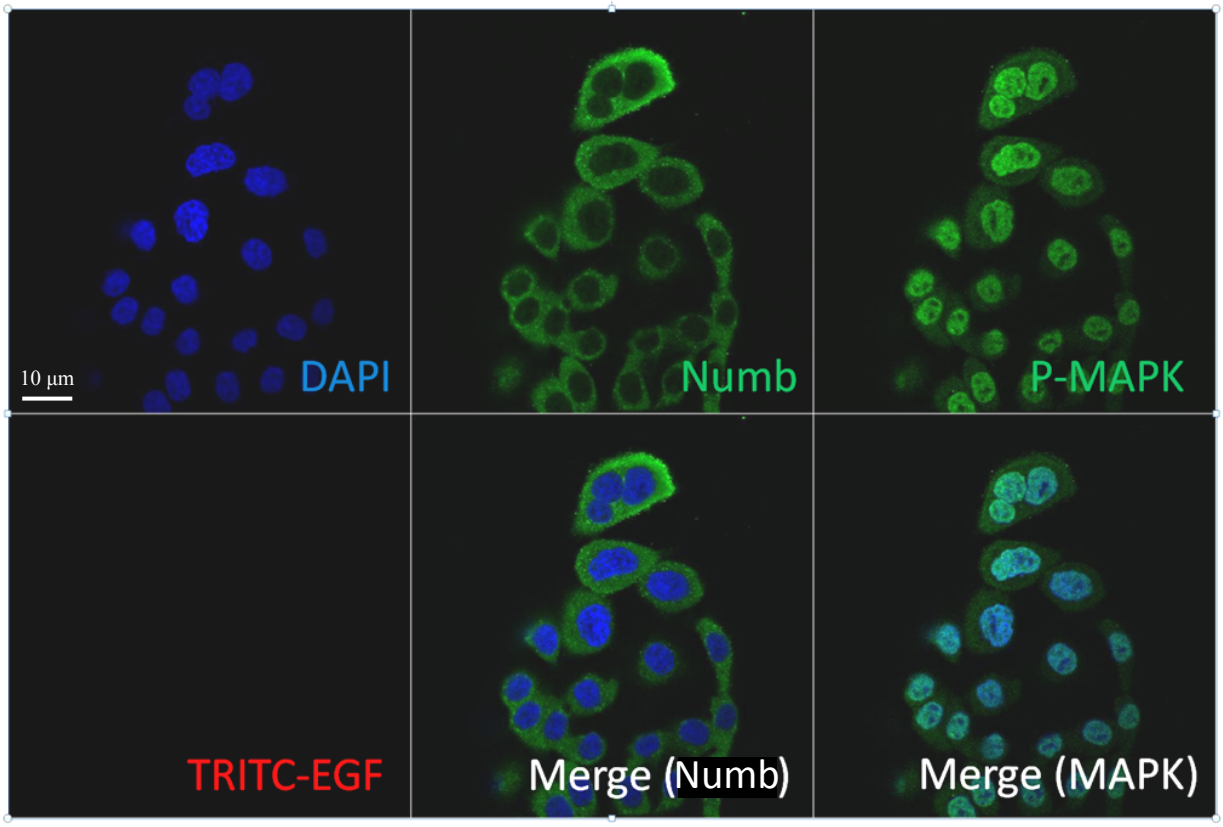

Figure 5-8: Immunofluorescence of non polarized HeLa cells cultivated in a gap chamber (40X). Blue: DAPI. Red: TRITC-EGF. Green: Numb (middle) and duo-phosphorylated MAPK (right).

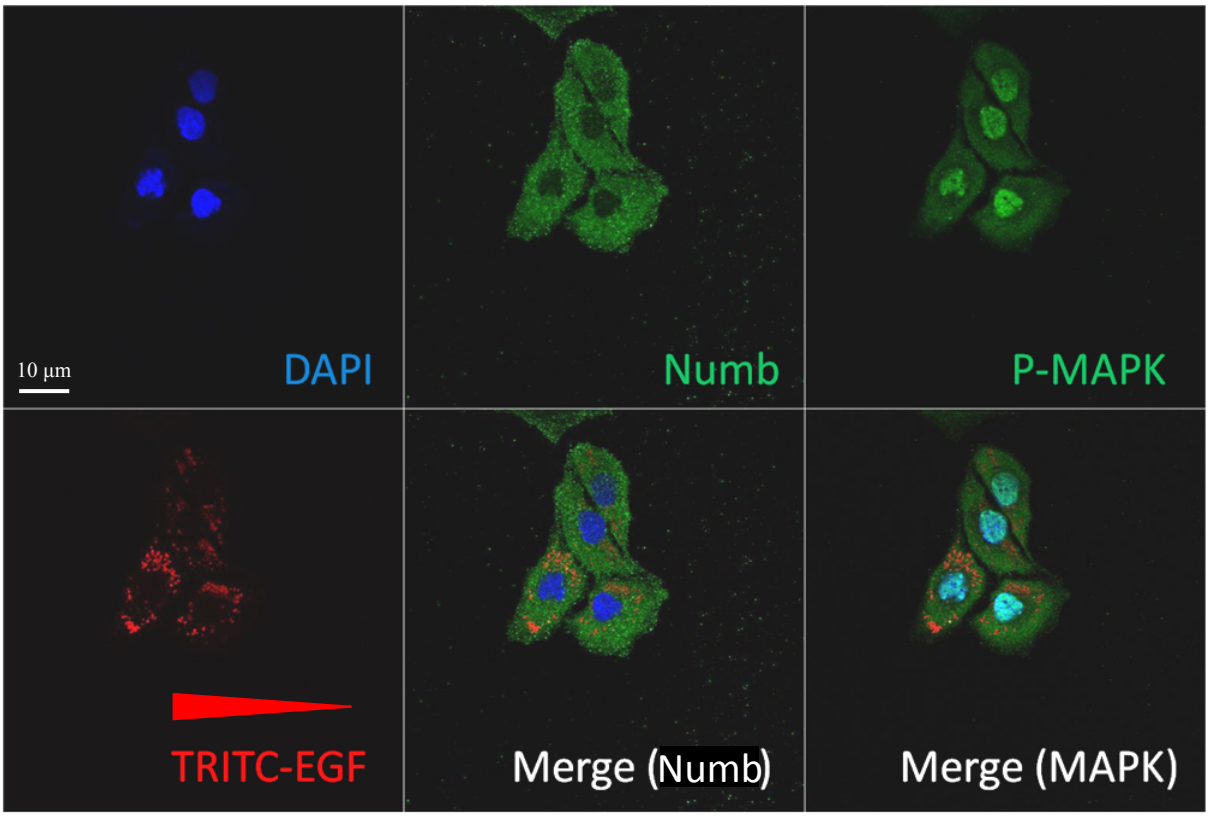

Figure 5-9: Immunofluorescence of a polarized HeLa cell after 22 minutes post-delivery of 100 ng/mL TRITC-EGF (40X). Gap edge is on the left side of the cell and TRITC-EGF gradient is depicted accordingly. Blue: DAPI. Red: TRITC-EGF. Green: Numb (middle) and duo-phosphorylated MAPK (right).

While the computational analysis was based on asymmetric levels of MAPK activation in the cell cytoplasm, HeLa cells exhibited a high degree of basal MAPK duo-phosphorylation with both cytoplasmic and nuclear expression profiles. We did not observe changes of this expression profile in cells polarized with TRITC-EGF, indicating the HeLa cell line is not well suited for this experimental validation. While the engineered system did not demonstrate effects on the partitioning of activated signaling pathway molecules, we did demonstrate the asymmetric partitioning of polarization proteins such as Par-6 in response to EGF gradient. This is significant in the context of asymmetric cell division as members of these complexes contribute to the

polarization of the cortical domains, prerequisite to asymmetric cell divisions. Therefore, this indicates that asymmetric environments could contribute to cell fate decisions.

Asymmetric cell divisions were first described in the context of stem cells, and while the HeLa system was a good choice for model and delivery system development due to the ease of culture, homogeneity of cell populations, cell size and also the extensive literature available for kinetic studies, the physiological relevance will require the translation of these findings towards stem cell systems. In the next section, we will describe preliminary experiments performed in mouse cortical stem cells based on preliminary reports of EGFR polarization in mouse neural stem cells from the ventricular and subventricular zones (Sun, Goderie et al. 2005).

Mouse cortical stem cells

We performed pulse delivery of 10 ng/mL TRITC-EGF (bulk media change) to mNSCs cultivated in gap chambers as described previously and results are presented in Figure 5-10.

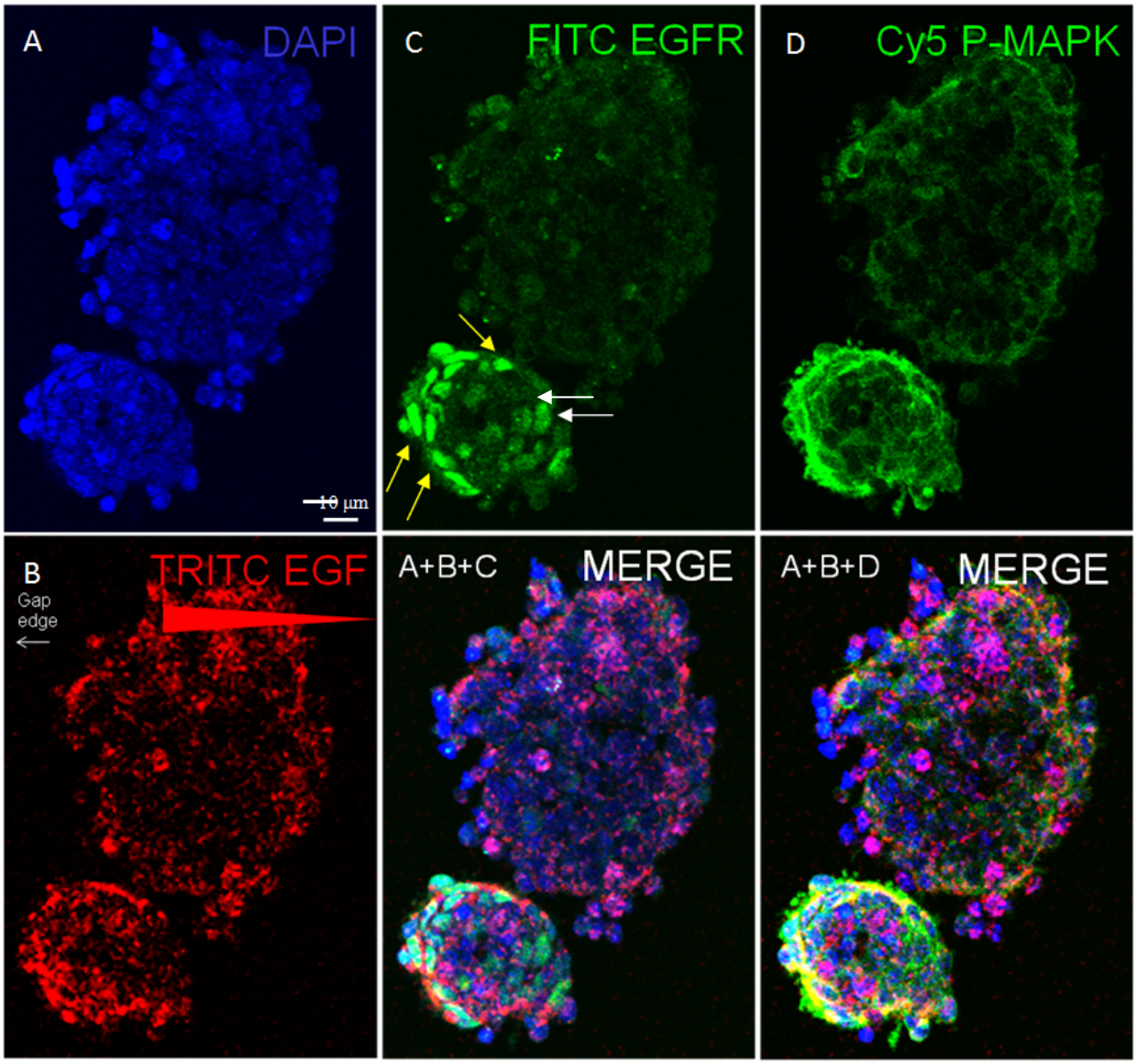

Figure 5-10: Immunofluorescence of polarized mNSCs colonies after ten minutes post-delivery of 10 ng/mL TRITC-EGF (40X). Gap edge is on the left side of the cell and TRITC-EGF gradient is depicted accordingly. A: DAPI. B: TRITC-EGF. C: FITC EGFR. D: Cy5 duo-phosphorylated MAPK.

The analysis of TRITC-EGF signal demonstrated a less obvious polarization compared to what was observed with HeLa cells. The larger top colony exhibited no apparent polarization while the bottom colony exhibited some degree of polarization after ten minutes with respect to the source of TRITC-EGF. This illustrated some properties of primary cells that will complicate the analysis of polarization in these systems. mNSCs are significantly smaller than HeLa cells and we discussed in Chapter 3 the effect of cell diameter on computed PI values. Smaller single cells did not reach high PI values and the degree of asymmetry was not maintained for long periods of time. Also, the density of mNSC colonies did not seem to reach density levels of HeLa colonies *in vitro*. As such, media could infiltrate various intracellular regions and thus contribute to a decrease of polarization at the colony level. Finally, the reduced cell size led us to hypothesize that some colonies could exhibit attachment only to a single surface of the culture chamber, thus leading to poor polarization as demonstrated in the three-dimensional finite-element model. Several challenges will need to be considered for full implementation of polarization strategies in primary cells.

In the polarized bottom colony, analysis of EGFR signals demonstrated the existence of a population with high EGFR levels. Amongst these cells, some were consistent with TRITC-EGF polarization (yellow arrows) while some cells on the rightmost side exhibited high EGFR levels without apparent TRITC-EGF signal (white arrow). EGFR levels highlight a troublesome property of primary cells as these lines are heterogeneous. This will affect polarization responses at the single cell level as some cells may be more receptive or refractory to the molecule of interest based on number of available receptors and occupancy levels. Compared to the HeLa system, polarization of EGFR at the single cell level was not demonstrated, as it was

hypothesized this was a result of the limited EGF polarization of the system. Improvements will need to be implemented allowing for increased polarized signals based on reduced bead size (five μm vs seven μm), full attachment of colonies on both chamber surface and increased colony density. At the colony level, EGF polarization demonstrated some correlation with levels of EGFR expression.

While mNSCs demonstrated some shortcomings in the context of polarization, this system seems more suited for the analysis of asymmetric activated MAPK. The level of expression of MAPK was low in untreated cells and no nuclear expression was detected as shown in Figure 5-10. In the case of the polarized colony, higher levels of duo-phosphorylated MAPK were detected partially overlapping with the TRITC-EGF signal. Higher resolution imaging will be needed to fully evaluate the potential for asymmetric MAPK signals following TRITC-EGF delivery.

5.2.2 Long-Term Polarization Effects

We were finally interested in the long term effect of EGF polarization. Following EGF pulse, the quantitative differences produced in signaling pathways intermediates such as duo-phosphorylated Erk could affect the gene expression of immediate early genes such as *jun* and *fos*. As discussed in Chapter 2, these can further control the expression of late genes and affect metabolic processes. While it appears the polarization of EGF can translate into a polarized EGFR state on the cell surface, we were not able to observe polarization of activated MAPK in the intracellular compartment. Nonetheless, proteins such as Par-6, member of conserved cell fate complexes asymmetrically partitioned at the time of mitosis, exhibited a polarized profile

which seems to be lost over the course of delivery. It is unclear whether a gene's response could be triggered differentially in polarized cells versus non polarized cells following mitosis. We performed two-minute pulse delivery of 10 ng/mL TRITC-EGF in HeLa colonies (bulk media change) as described in Material and Methods and analyzed the potential for asymmetric lineages over the course of five days using a long-term live cell imaging approach.

The analysis of asymmetric lineage can be performed in a variety of ways. We hypothesized HeLa cells subject to pulses of growth factor such as EGF could exhibit a lineage asymmetry between daughter cells. Asymmetry could be observed through different cell cycle times between daughter cells (quantitative difference) or survival of only one of the daughter cells (qualitative difference). Long-term live cell imaging allows for the analysis of qualitative and quantitative information and the mosaic of polarized cells is presented in Figure 5-11:

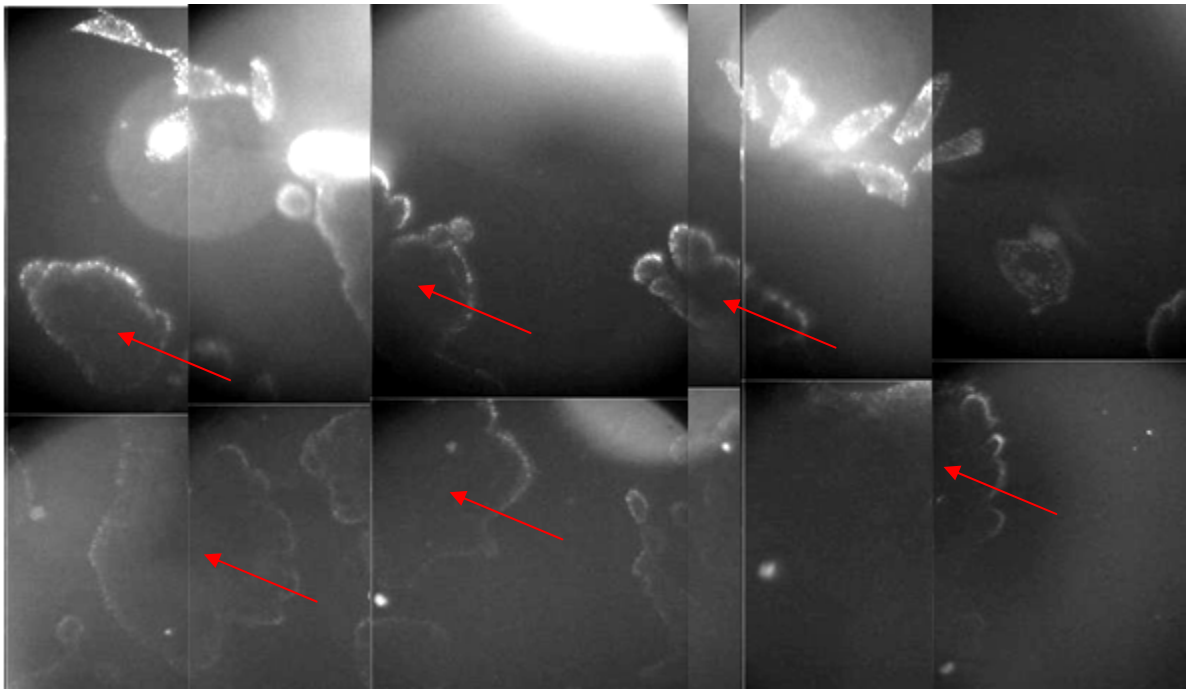

Figure 5-11: Reconstructed mosaic of the polarized gap chamber and identification of polarized colonies (gap edge is on the top). Six polarized colonies were identified and selected for subsequent cell tracking (red arrows). Manual acquisition was performed for fluorescent imaging which explains the significant overlap between images.

The time resolution of the acquisition system should allow for the unambiguous identification of cell identities at every time step. In this respect, the time interval was set to five minutes which enabled cell tracking with absolute certainty. Our group has developed a custom software for the acquisition of large fields of view using a robotic controller implemented on a microscope stage as described in Material and Methods. The long-term live cell imaging approach enables the generation of a mosaic of images of a cell culture (Figure 5-11) at regular time intervals for hours, days or weeks in brightfield/DIC imaging or fluorescence. Cells can be tracked by a user at every step, thus enabling the accurate identification of cell progenies over time. Large-scale analysis of colonies allows for the generation of lineage trees, representing the

"genealogy" of the entire culture and linking cells with their parents and daughters. In the specific case of this analysis, fluorescent imaging can be used to score cells at time t = 0 for a given property such as the presence of a polarized EGF signal. This information could then be used to gate specific cells inside a complex lineage tree and look for specific features. One can also envision performing immunocytochemical analysis at the end of the culture and then run the movie backwards to correlate a given phenotype with properties acquired during imaging.

For this particular analysis, HeLa colonies were cultivated in gap chambers until cell density was considered high enough to ensure compact colonies and high potential for polarization. After a two-minute pulse of 10 ng/mL TRITC-EGF, two gaps of interest were panned using fluorescence imaging to assess the degree of polarization of target colonies and cells. Imaging was started at the end of acquisition and cells imaged for up to five days. In parallel, a control was cultivated and imaged in identical conditions except that the bulk media change did not contain 10 ng/mL TRITC-EGF. Movies produced during imaging were further loaded in the custom MATLAB software CellHunter for tracking. During tracking, cell death and loss of cell identity (either due to movement out of the imaging region or loss of trackable features) were scored accordingly. MATLAB queries were performed to access information relative to cells of interest (cell IDs query). The selection of cells to include in the analysis was performed in two different ways:

- Selection method 1: Cells that divided in the five hours following EGF pulse for which polarization data may or may not have been available. If no fluorescence information was available, cells were selected based on their location inside a colony (no internal cells) and polarization potential.

- Selection method 2: Cells for which polarization data univocally demonstrated polarization following EGF pulse as shown in Figure 5-12 and for which the two daughter cells divided.

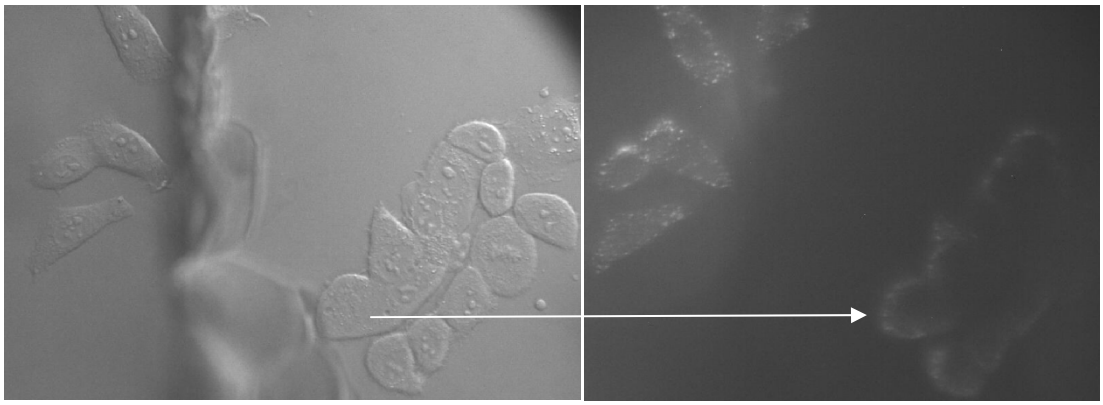

Figure 5-12: Identification of polarized HeLa colonies following two-minute pulse of 10 ng/mL TRITC-EGF. Identification of polarized cells was made based on fluorescent profile captured following delivery and cell IDs of polarized cells were isolated for future analysis versus non-polarized cells (inside cells from a colony for example and untreated control).

The length of five hours following delivery was selected based on reported lengths of G2 and M phase in various human tissues to ensure cells chosen for analysis were either in G2 or M phase during polarization (Lipkin, Bell et al. 1963; Lipkin 1965; Frindel, Malaise et al. 1968; Winawer and Lipkin 1969). In total, 118 cells were selected in the treated block for subsequent analysis and 196 cells in the control block. In the case of the first selection method, only 15 cells in the EGF-pulsed chamber divided in the defined time frame and were selected, which indicates results presented in this section will be qualitative and focus primarily on the information that can be extracted from these systems in the context of polarization analysis. Out of these 15 cells, two of them did not divide over the course of the entire experiment and were not included in the analysis. For the control, we identified 22 cells that divided in the five hours following bulk

media change (no TRITC-EGF) and out of these cells seven were removed from the analysis as they were identified as internal cells amongst colonies. The signals occurring inside multicellular structures through direct cell-cell interaction or contact with the extracellular matrix go outside of the scope of this analysis and for consistency purposes cells were selected exclusively based on the direct contact with the culture media in the context of a colony. We compared average daughters cell cycle time differences following mitosis between the treated and control chambers and results are presented in Tables 7 and 8 respectively.

Cell ID	Daughter A	Daughter B	Cycle time Difference
38714	17.0858	17.5719	0.4861
38399	15.0025	15.0025	0
38822	22.8333	21.9167	0.9166
39148	19.3333	20.3333	1
39141	24.4164	17.1689	7.2475
39122	20.0117	23.8475	3.8358
39106	32.4886	23.8242	8.6644
39099	16.0811	19.0811	3
39113	2	18.5833	None
38944	24.1694	21.6575	2.5119
38743	16.6667	19.1664	2.4997
38626	26.2408	26.9886	0.7478
38572	2	2	None
38460	2	2	None
38413	18.3331	16.6667	1.6664

Table 7: Analysis of cell cycle time asymmetry in EGF treated HeLa cells selected using method 1 (cell cycle time in hours). 2 indicates cells died during tracking. Cell cycle time difference average is 2.96 hours, standard deviation is 2.69 hours.

Cell ID	Daughter A	Daughter B	Cycle time Difference
39966	19.9928	21.6667	1.6739
39690	1	1	None
39891	25.3308	24.7475	0.5833
39770	28.4186	32.3125	3.8939
39717	26.8228	25.5	1.3228
39702	19.0833	18.4797	0.6036
39683	22.9956	22.7581	0.2375
39528	27.5	19.1914	8.3086
39437	20.6033	29.7581	9.1548
39388	25.8561	30.7628	4.9067
39315	18.5711	24.8106	6.2395
38861	34.9747	25.8331	9.1416
38529	22.4767	24.1458	1.6691
39920	20	22.5072	2.5072
39860	31.6492	24.1617	7.4875

Table 8: Analysis of cell cycle time asymmetry in control (untreated) HeLa cells selected using method 1 (cell cycle time in hours). 1 indicates cells did not divide during the tracking period. Cell cycle time difference average is 4.12 hours, standard deviation is 3.36 hours.

The results demonstrated no significance with very high standard deviations. Some daughter cells exhibiting almost no difference in cell cycle time (as low as 30 minutes) while others exhibited up 9 hours difference both in the treated and control cells. This data set illustrates the complexity and heterogeneity of microenvironments at the single cell level. Heterogeneity and non-consistency in the results could arise from changes in the number of neighboring cells, contact with the extracellular matrix or even from the distance with the gap edge (potentially leading to oxygen and nutrient gradients and limitation when cell density is high). Hence, the proper analysis of long-term phenotypical effects needs to take into account variations in local cell environments arising from cell movements, trajectories but also the motion and trajectories of neighboring cells over the course of the imaging period. We thereby

propose collected data will need to be gated for specific properties of the culture to enable proper analysis and interpretation of polarization over several generations:

- Cell distance from the gap edge;
- Contacts with other cells (number of neighboring cells, position inside a colony);
- Scoring for morphological features (does the cell look “healthy”?);
- Variations of all these properties with respect to time.

The dynamic nature of these cultures demonstrate that environmental conditions should be matched between cells for proper analysis of data in the short term, and the changes in these conditions should be matched for long-term studies.

We discussed previously the importance of correlating polarization with cell division to ensure different states of cell signaling activation are transmitted in the daughter cells. Observation of imaging data highlighted an interesting property of dividing cells on the edge of colonies, as shown in Figure 5-13:

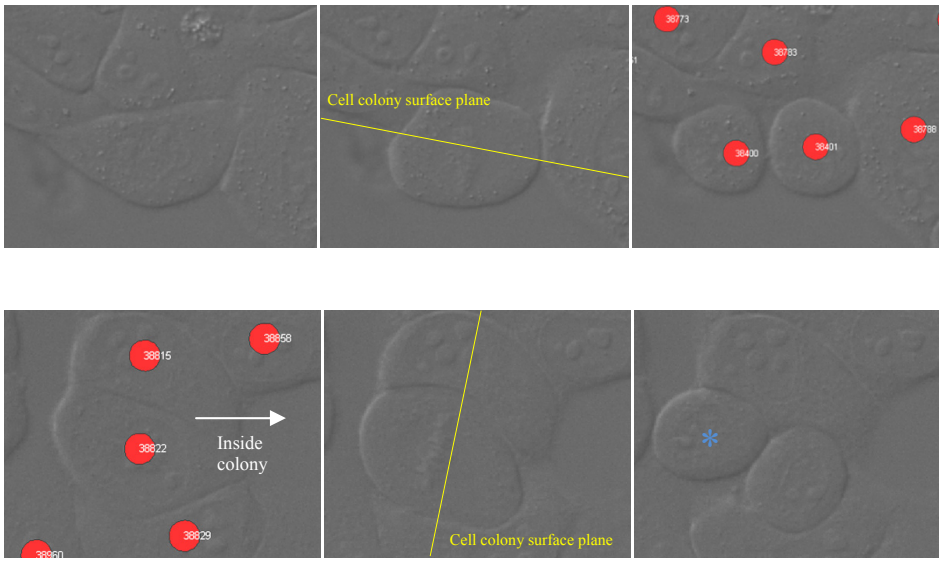

Figure 5-13: Example of two modes of cell division: parallel to the colony surface (top) and perpendicular to the colony surface (bottom). In the bottom panel, the cell indicated in blue has the potential to keep the polarized signal following delivery.

Most of the cells on the edge of colonies divided parallel to the colony surface. This demonstrates the polarization could be completely cancelled by the orientation of cell division in the context of the colony. In the treated sample, only three cells out of the 15 analyzed did not divide parallel to the colony surface, as shown in the bottom panel of Figure 5-13. Cell division perpendicular to the colony surface is needed for the potentiation of polarization and to enable asymmetric MAPK signaling between daughter cells.

Therefore, correlation between cell division and polarization needs to be performed at two levels in time and space. In Figure 5-14 we present the lineage trees for the three cells that divided perpendicularly to the colony surface. Figure 5-15 depicts the cellular context over the course of imaging for these three cells.

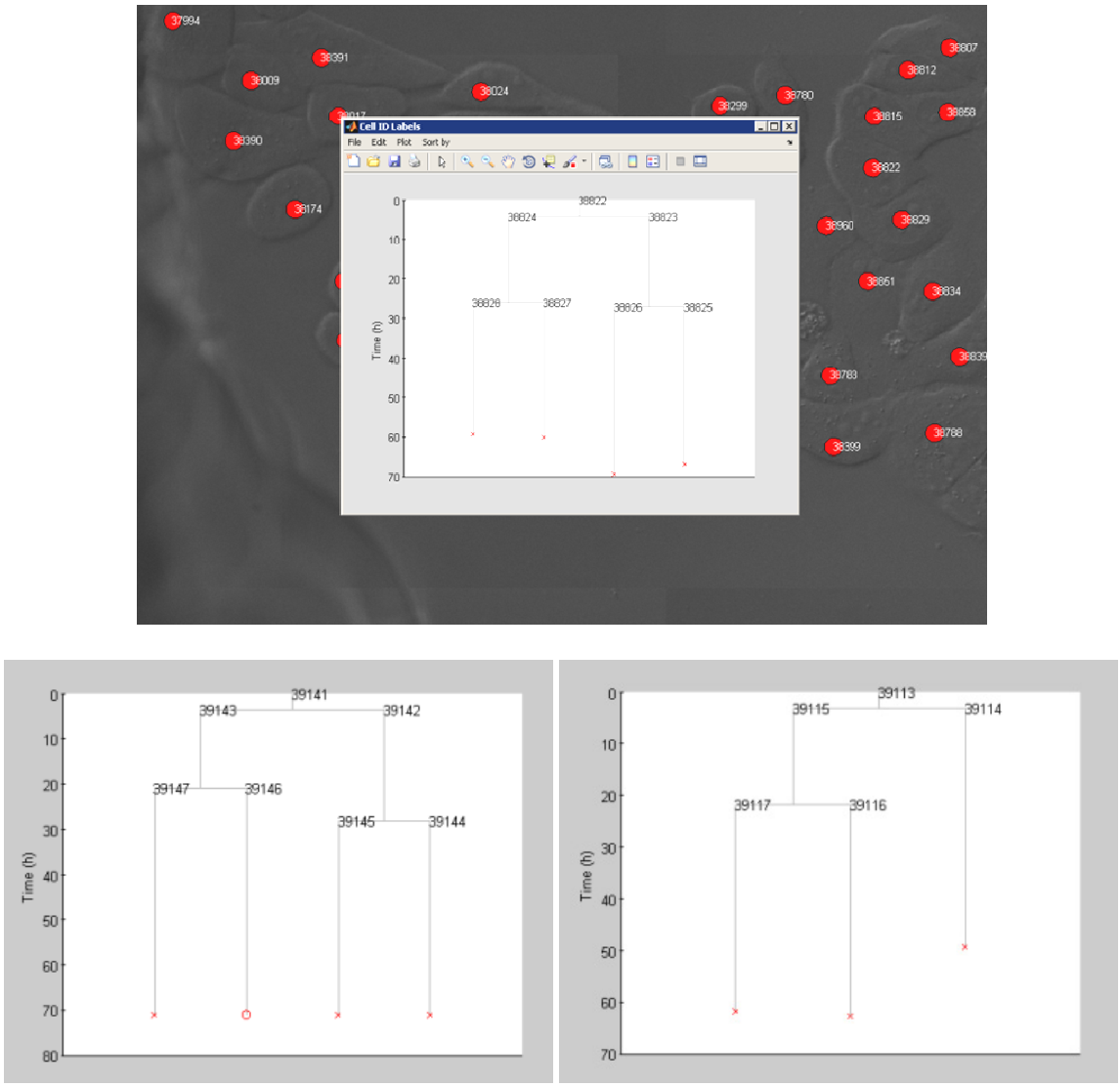

Figure 5-14: Lineages trees for the three cells (ID 38822, 39141 and 39113) that divided perpendicular to the cell colony surface in the treated HeLa culture.

Two cells demonstrated an asymmetric lineage; one was quantifiable as daughter cells exhibited difference in cell cycle time (7.25 hours) while the other one demonstrated qualitative significance as only one of the two daughter cells divided again over the course of the experiment.

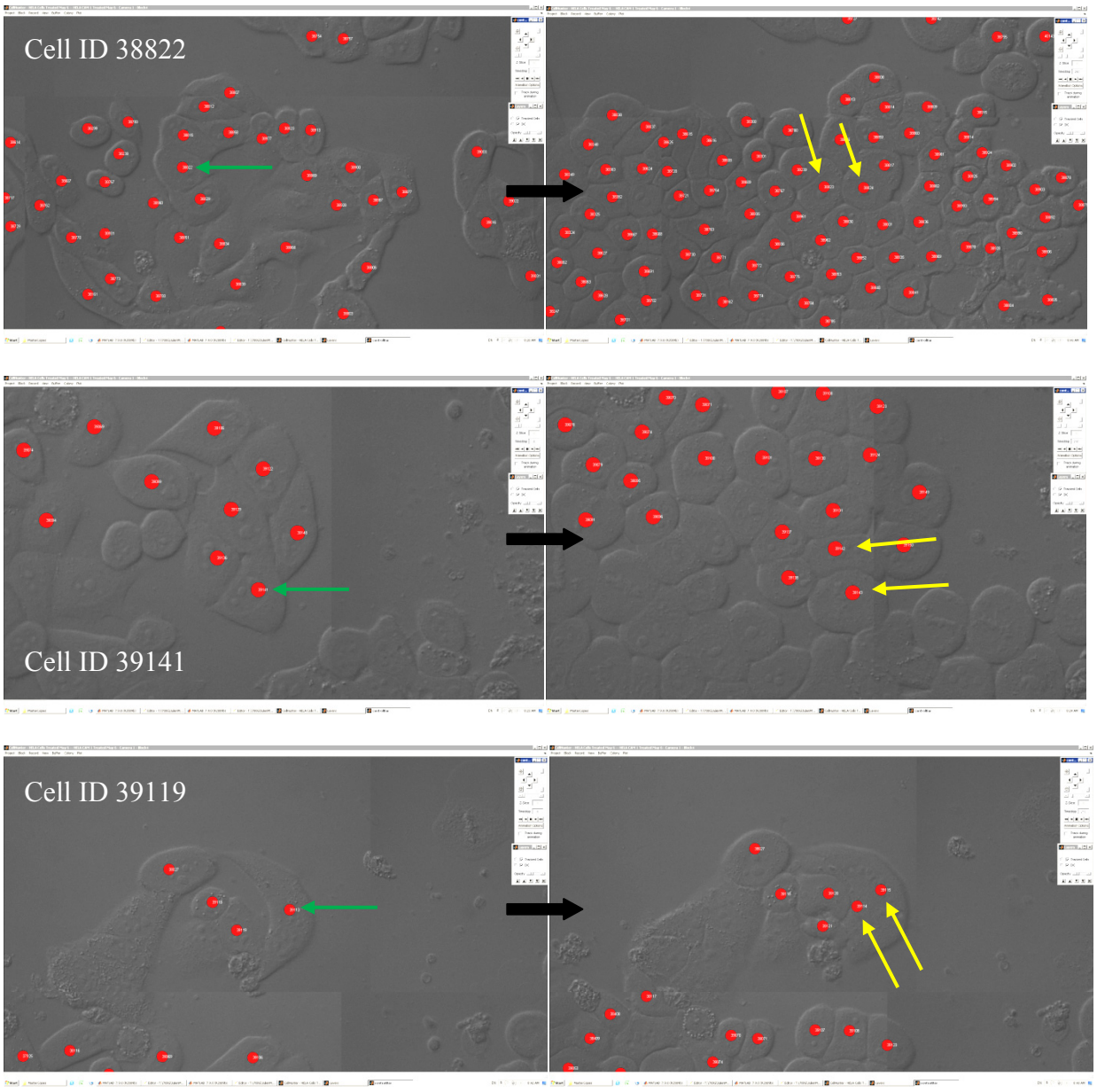

Figure 5-15: Identification of cellular context of daughters from cells dividing perpendicular to the colony surface plane. Left panels: initial tracking image and identification of mother cells (green arrows)

When analyzing these cells in more detail, we observed that the daughters of cell ID 38822 which exhibited a symmetric lineage were both located on the inside of the colony before their respective divisions with no direct contact with the media. In the case of cell ID 39141 and 39119, one of the daughters exhibited contact with the media by the time they divided, indicating

that the asymmetry in their local microenvironment could be a factor in the asymmetric lineages observed. Hence, careful analysis of environmental data at the single cell level is needed for proper analysis of asymmetric lineage trees.

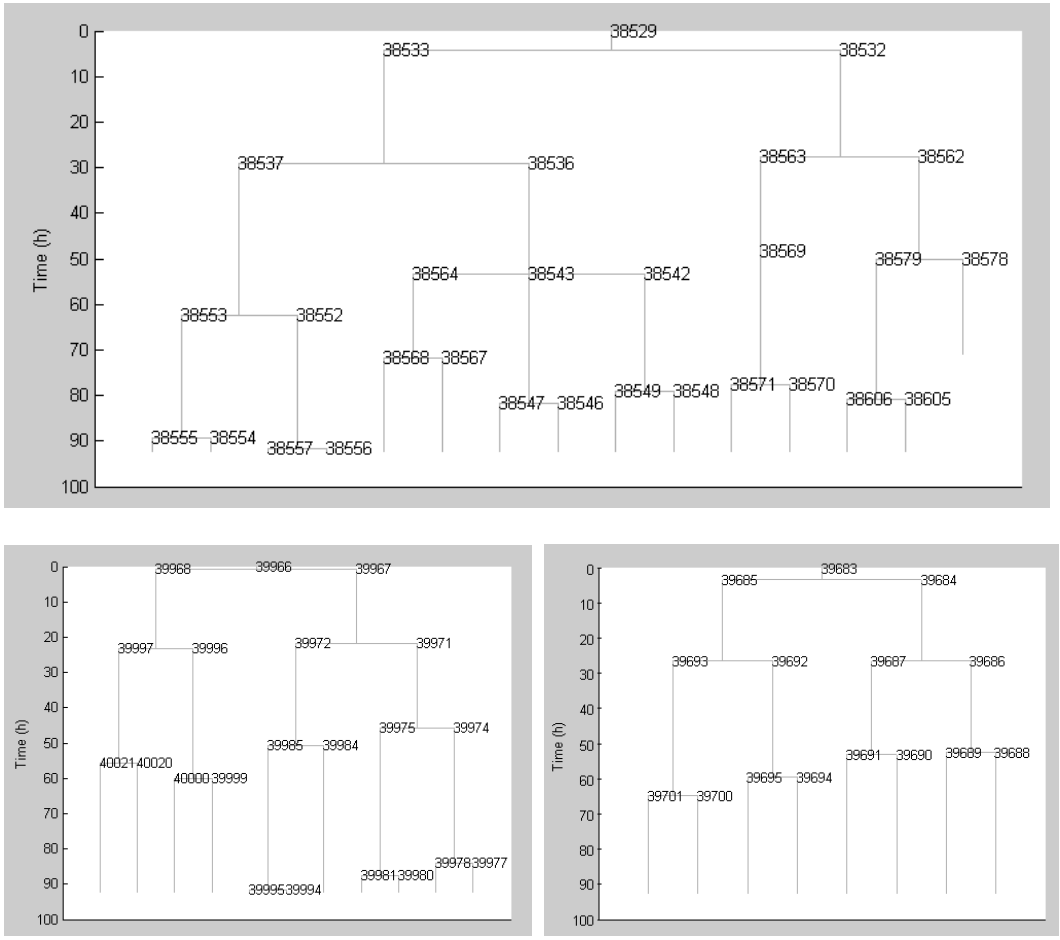

Figure 5-16: Lineages trees for the three cells (ID 38529, 39966 and 39683) that divided perpendicular to the cell colony surface in the control HeLa culture.

Interestingly, the three lineage trees of cell dividing perpendicularly to the colony surface in the control exhibited a high degree of symmetry with respect to the time until division of the two daughter cells (cycle time difference of 1.66, 1.67 and 0.23 hours respectively) as shown in Figure 5-16. Cells in the control also divided significantly more than the cells in the treated

chamber. An overview of the chambers demonstrated the control system was significantly denser which could have affected the proliferative potential over the course of five days. This again demonstrates that several parameters need to be taken into account to ensure the consistency between treated and control HeLa colonies.

When cell selection method 2 (cells for which polarization data univocally demonstrated) was used, we identified only seven cells in the treated culture and results are presented in Table 9.

Cell ID	Daughter A	Daughter B	Cycle time Difference
38153	26.7408	42.4908	**15.75**
38700	22.2475	21.7619	**0.4856**
38391	16.6667	19.1667	**2.5**
38024	22.5022	18.3447	**4.1575**
38614	22.905	21.9906	**0.9144**
38091	22.8331	23.655	**0.8219**
38069	18.8214	15.8192	**3.0022**

Table 9: Analysis of cell cycle time asymmetry in EGF treated HeLa cells selected using method 2 (cell cycle time in hours). Cell cycle time difference average is 3.94 hours, standard deviation is 5.37 hours.

This analysis illustrated significant challenges in the context of long-term effects of polarization. First, even with several colonies analyzed and a total number of cells tracked cells exceeding 300 cells for both the treated and control chambers, the stringent conditions for cell selection based either on division in the appropriate timeframe or fluorescence polarization led to small number of cells for analysis. These numbers were too small for statistically significant analysis and demonstrate the field of view will need to be significantly larger to allow for the acquisition of statistically relevant data. While effects were not shown, this framework is

particularly well suited for the analysis of asymmetric cell division. Single-cell level tracking allows for the generation of lineages trees which can be analyzed for asymmetric properties such as cell cycle time or asymmetry of survival. The mosaic of environments in which the cell will develop complicates the analysis of polarization effects over generations and the acquisition of supplementary data for each cell (distance from the gap edge, number of direct neighbors and location in a colony) will enable the comparison between cells in similar conditions. Also, a focus on the first division following mitosis would significantly reduce the complexity of these systems in the context of polarization analysis. We demonstrated that a very small fraction of analyzed cells divide on a cell surface following an orientation that could enable the persistence of polarized signals following mitosis. Divisions symmetric to the colony surface will symmetrically partition a polarized signal in the context of a colony (and potentially, polarity proteins such as Par-6 as demonstrated previously) while a division perpendicular to the colony surface could lead to the formation of only one daughter cell keeping the polarized signal. The further context of the daughter cells in the colony may be significant in the generation of asymmetric lineage trees.

6 Chapter 6: Conclusions and Future Work

We initially performed a two-dimensional analysis of EGF diffusion from a point source in culture (micropipette) with binding to a single cell using literature values for EGF binding and trafficking in the context of the B82 fibroblast (HMEC) cell line. This approach enabled the design of a polarization system using a set of metrics to characterize delivery asymmetry (polarization index PI) and signaling potential (percentage occupancy PO). By analyzing temporal profiles of PI, PO, concentrations and velocity of formation of various members of the system significant in the context of downstream pathway activation (dimerized receptor-ligand complexes in the smooth *D* and coated pits *H*), we were able to decipher complex behavioral responses following controlled EGF release and evaluate two delivery strategies for the creation of asymmetric EGF microenvironments. Using published threshold values for MAPK/Erk activation, we analyzed the system in the context of generating an asymmetry of bound entities at the single cell level. Controlling EGF delivery in the media through a micropipette loaded with a gel of controlled porosity did not allow for asymmetric partitioning or occupancy levels consistent with signaling. When EGF was released through a micropipette in a collagen matrix in which the cell was embedded, asymmetry could be generated on a single cell surface consistent with asymmetric MAPK activation. Nonetheless, preliminary experiments demonstrated the technical difficulties associated with fluorescent imaging in collagen cultures. We further developed a three-dimensional model to analyze geometry effects to evaluate alternate strategies in the context of polarization in culture media with diffusive properties similar to water.

In this second step, we improved model significance by evaluating kinetic parameters (forward rate constant k_f and initial number of free EGF receptors R_{init}) for the HeLa cell system

and used these values in a three-dimensional model in which we analyzed geometry effects from the culture chamber and neighboring cells. We demonstrated that culture systems with reflective surfaces greatly contribute to polarized signals at the single cell level and can potentiate pulsed growth factor signals in the cell vicinity. Nonetheless, no single cell culture system was able to maintain asymmetric MAPK activation based on target threshold levels. When analyzing the effect of neighboring cells, we demonstrated that the combination of reflective (culture chamber) and absorbing (neighboring cells) surfaces around a cell significantly potentiates polarization and allows for asymmetric delivery consistent with asymmetric MAPK activation levels. The gap chamber system developed in professor Jervis' laboratory demonstrated the highest potential due to the effective increase in tortuosity as was selected for subsequent model validation. The model significance was demonstrated through fitting with experimental data in various cell configurations thereby confirming Hypothesis 2 - ***single cell level methods and experiments permit the analysis and prediction of soluble factor binding***.

When further evaluating the physiological effects of pulse delivery, we demonstrated that polarized receptors on a single cell surface can be the result of the asymmetric delivery of soluble molecules and hence validated Hypothesis 4 - ***Asymmetric environments of soluble factors (EGF) can be translated in the asymmetric partitioning of receptor-ligand complexes (EGF-EGFR) at the single cell level***. While we were not able to demonstrate polarized MAPK signaling at the single cell level, the HeLa system showed that single cells can respond to polarized soluble factor signaling in terms of the localization of polarization proteins such as Par-6. We observed polarization of Par-6 in a cell undergoing mitosis that correlated with the induced TRITC-EGF gradient, demonstrating engineered polarization could be triggered during

mitosis and lead to the asymmetric partitioning of polarization proteins. Nonetheless, we did not observe the asymmetric partitioning of the cell fate determinant Numb in HeLa cells. We further analyzed polarization effects in primary cells (mouse cortical stem cells). Heterogeneity of cell populations within the colonies (i.e. mixed progenitor populations) will be an issue to address and future improvements will be needed for the polarization of cells relevant in the context of regenerative medicine.

Long-term live cell imaging is a valuable tool for the analysis of polarization over several rounds of division. The generation of lineage trees and identification of cellular events in a near continuous manner over the course of several days is necessary for elucidating asymmetric events at the single cell level. This approach enables cell cycle time analysis, the generation of migration maps and distances and the scoring of morphological features. In the context of polarization, we analyzed asymmetry in cell cycle time between daughter cells following a two-minute pulse of TRITC-EGF. While using imaging blocks covering at least six cell colonies, less than 15 cells could be used for data analysis using two different approaches for cell gating. Non-division of one of the daughter cells, loss of tracking features, death or movement outside of the field of view all contribute to the reduction of the sample for data analysis. One of the biggest challenges to overcome in the context of long-term phenotypical effects of polarization will be the ability to collect large samples of experimental data *in vitro*. While not providing us enough information to answer Hypothesis 5 - ***Asymmetric partitioning of receptor-ligand complexes at the single-cell level can lead to asymmetric cell fate decisions***, this analysis demonstrated the long-term live cell imaging approach is well suited for the analysis of polarization. The results obtained with Par-6 confirm that polarized soluble EGF signals have the potential to dictate cell

fate decisions at the single cell level in the context of Hypothesis 3 - ***Soluble factor signaling alone can dictate the symmetry of cell division***. The analysis of long-term phenotypical effects of controlled EGF release and polarization in stem cell populations will be needed to fully answer this question.

Several improvements would contribute to increase model significance and improve our understanding of polarization while allowing for the engineering of biomimetic systems. As discussed in Chapter 3, actual endosomal volumes are not known which severely limits endosomal modeling. Recently, considerable progress has been made in understanding the two and three-dimensional structure of complex subcellular systems such as the endosomal compartment or endoplasmic reticulum (Murk, Humbel et al. 2003; Means, Smith et al. 2006). We propose these approaches should be implemented with diffusion and boundary value problems for the generation of a new class of biological models that would consider both quantitative and spatial properties of cellular systems.

In the specific case of EGFR, several reports indicate receptors are not homogeneously distributed over the entire cell surface, but organized in clusters whose distribution may be regulated by lipid rafts (Irwin, Mueller et al. 2010). Two classes of EGFR have also been demonstrated in the context of EGF signaling, with some receptors existing in the form of predimers with different ligand binding kinetics compared to monomeric receptors. We propose that the inclusion of these factors will contribute to an increase of model quality and significance. Finally, interpretation of our computational results was based on published data associated with the MAPK/Erk signaling pathway. The inclusion of adaptor proteins and signaling pathway

intermediates up to the MAPK level will allow for better engineering of delivery strategies in the context of soluble factor signaling and activation of downstream signaling cascades. In the context of complex three-dimensional geometries of cell structure, it is possible to envision different pools of adaptor proteins (varying concentrations) associated with a specific subcellular localization around various endosomal regions (early and late). Multicellular models should be investigated and solutions for modeling of compact colonies should be investigated. The inclusion of three dimensions also allows for the creation of complex microenvironments that could be designed to mimic niches *in vitro* and further used to elucidate the complex interplay between niches and soluble signals *in vivo*. For example, recent published reviews on stem cell niche structure and functions (Li and Xie, 2005; Scadden, 2006) could be used for finite-element design. These types of models would represent a step forward in the engineering of biomimetic systems.

The long-term analysis of polarization effects at the single cell and colony levels demonstrated cell numbers should be significantly increased in culture to allow for statistically significant analysis of polarization and asymmetric cell division at the single cell level. Increasing the number of tracked cells and colonies present a challenge to address as the time resolution needed for single cell tracking limits panning of very large areas of culture. Also, endpoint immunocytochemical analysis as well as the use of cell lines expressing GFP-fusion proteins would significantly increase our ability to extract information during and after imaging. For example, cell lines expressing a GFP-Par6 fusion protein would allow for the analysis of polarization during the early stages following delivery. Fluorescence data acquired during and after mitosis would enable the accurate evaluation of polarization at the single cell level. Finally,

the importance of the cell division orientation in the context of polarization demonstrates that approaches to control the cell division orientation during delivery would significantly increase the proportion of polarized cells.

Our overall goal, Hypothesis 1 - ***single cell level control of asymmetric division is needed for the generation of a population of cells of desired purity and composition***, represents the ideal level of cell culture control. This work sought to demonstrate that heterogeneities in cultures may affect long-term phenotypical effects following engineered polarization. We have shown that polarization of single cells with soluble factors is feasible and that long-term live cell imaging offers the possibility to identify these various environmental conditions in the context of polarized cells within colonies. We developed methods and metrics to enable the induction and quantification of cell polarization, tracking of progenies with asymmetric fate and selection of cells of interest based on microenvironmental conditions. Our analysis has led to a new appreciation of the complexities and challenges of producing homogeneous populations of cells in culture; within a culture each cell exists within its own microenvironment that can lead to unique concentration gradients around individual cells thereby affecting fate decisions.

References

Abhyankar, V. V., M. A. Lokuta, et al. (2006). "Characterization of a membrane-based gradient generator for use in cell-signaling studies." Lab Chip 6(3): 389-393.

Adler, P. N. (1992). "The genetic control of tissue polarity in Drosophila." Bioessays 14(11): 735-741.

Aksan, I. and M. L. Kurnaz (2003). "A computer-based model for the regulation of mitogen activated protein kinase (MAPK) activation." J Recept Signal Transduct Res 23(2-3): 197-209.

Alison, M. R., M. H. Golding, et al. (1996). "Pluripotential liver stem cells: facultative stem cells located in the biliary tree." Cell Prolif 29(7): 373-402.

Arasada, R. R. and G. Carpenter (2005). "Secretase-dependent tyrosine phosphorylation of Mdm2 by the ErbB-4 intracellular domain fragment." J Biol Chem 280(35): 30783-30787.

Aroian, R. V., M. Koga, et al. (1990). "The let-23 gene necessary for Caenorhabditis elegans vulval induction encodes a tyrosine kinase of the EGF receptor subfamily." Nature 348(6303): 693-699.

Artavanis-Tsakonas, S., M. D. Rand, et al. (1999). "Notch signaling: cell fate control and signal integration in development." Science 284(5415): 770-776.

Athale, C., Y. Mansury, et al. (2005). "Simulating the impact of a molecular 'decision-process' on cellular phenotype and multicellular patterns in brain tumors." J Theor Biol 233(4): 469-481.

Balklava, Z., S. Pant, et al. (2007). "Genome-wide analysis identifies a general requirement for polarity proteins in endocytic traffic." Nat Cell Biol 9(9): 1066-1073.

Batzer, A. G., P. Blaikie, et al. (1995). "The phosphotyrosine interaction domain of Shc binds an LXNPXY motif on the epidermal growth factor receptor." Mol Cell Biol 15(8): 4403-4409.

Benveniste, M., E. Livneh, et al. (1988). "Overexpression of epidermal growth factor receptor in NIH-3T3-transfected cells slows its lateral diffusion and rate of endocytosis." J Cell Biol 106(6): 1903-1909.

Berkers, J. A., P. M. van Bergen en Henegouwen, et al. (1991). "Three classes of epidermal growth factor receptors on HeLa cells." J Biol Chem 266(2): 922-927.

Bertics, P. J. and G. N. Gill (1985). "Self-phosphorylation enhances the protein-tyrosine kinase activity of the epidermal growth factor receptor." J Biol Chem 260(27): 14642-14647.

Betschinger, J. and J. A. Knoblich (2004). "Dare to be different: asymmetric cell division in Drosophila, C. elegans and vertebrates." Curr Biol 14(16): R674-685.

Betschinger, J., K. Mechtler, et al. (2003). "The Par complex directs asymmetric cell division by phosphorylating the cytoskeletal protein Lgl." Nature 422(6929): 326-330.

Blume-Jensen, P. and T. Hunter (2001). "Oncogenic kinase signalling." Nature 411(6835): 355-365.

Bottaro, D. P., A. Liebmann-Vinson, et al. (2002). "Molecular signaling in bioengineered tissue microenvironments." Ann N Y Acad Sci 961: 143-153.

Brehm, M., T. Zeus, et al. (2002). "Stem cells--clinical application and perspectives." Herz 27(7): 611-620.

Brou, C., F. Logeat, et al. (2000). "A novel proteolytic cleavage involved in Notch signaling: the role of the disintegrin-metalloprotease TACE." Mol Cell 5(2): 207-216.
Bublil, E. M. and Y. Yarden (2007). "The EGF receptor family: spearheading a merger of signaling and therapeutics." Curr Opin Cell Biol 19(2): 124-134.
Buday, L. and J. Downward (1993). "Epidermal growth factor regulates p21ras through the formation of a complex of receptor, Grb2 adapter protein, and Sos nucleotide exchange factor." Cell 73(3): 611-620.
Burdick, J. A., A. Khademhosseini, et al. (2004). "Fabrication of gradient hydrogels using a microfluidics/photopolymerization process." Langmuir 20(13): 5153-5156.
Burgess, A. W., H. S. Cho, et al. (2003). "An open-and-shut case? Recent insights into the activation of EGF/ErbB receptors." Mol Cell 12(3): 541-552.
Burke, P., K. Schooler, et al. (2001). "Regulation of epidermal growth factor receptor signaling by endocytosis and intracellular trafficking." Mol Biol Cell 12(6): 1897-1910.
Carpenter, G. (1987). "Receptors for epidermal growth factor and other polypeptide mitogens." Annu Rev Biochem 56: 881-914.
Chambers, I., D. Colby, et al. (2003). "Functional expression cloning of Nanog, a pluripotency sustaining factor in embryonic stem cells." Cell 113(5): 643-655.
Chambers, I. and A. Smith (2004). "Self-renewal of teratocarcinoma and embryonic stem cells." Oncogene 23(43): 7150-7160.
Chapman, G., L. Liu, et al. (2006). "High levels of Notch signaling down-regulate Numb and Numblike." J Cell Biol 175(4): 535-540.
Chen, H., Z. He, et al. (1998). "Semaphorin-neuropilin interactions underlying sympathetic axon responses to class III semaphorins." Neuron 21(6): 1283-1290.
Cho, H. S., K. Mason, et al. (2003). "Structure of the extracellular region of HER2 alone and in complex with the Herceptin Fab." Nature 421(6924): 756-760.
Chu-Lagraff, Q., D. M. Wright, et al. (1991). "The prospero gene encodes a divergent homeodomain protein that controls neuronal identity in Drosophila." Development Suppl 2: 79-85.
Chung, B. G., L. A. Flanagan, et al. (2005). "Human neural stem cell growth and differentiation in a gradient-generating microfluidic device." Lab Chip 5(4): 401-406.
Clayton, A. H., M. L. Tavarnesi, et al. (2007). "Unligated epidermal growth factor receptor forms higher order oligomers within microclusters on A431 cells that are sensitive to tyrosine kinase inhibitor binding." Biochemistry 46(15): 4589-4597.
Cohen, P. (1997). "The search for physiological substrates of MAP and SAP kinases in mammalian cells." Trends Cell Biol 7(9): 353-361.
Cohen, S. and G. Carpenter (1975). "Human epidermal growth factor: isolation and chemical and biological properties." Proc Natl Acad Sci U S A 72(4): 1317-1321.
Cohen, S. and A. A. Hyman (1994). "Cell fate determination. When is a determinant a determinant?" Curr Biol 4(5): 420-422.
Cook, S. J., N. Aziz, et al. (1999). "The repertoire of fos and jun proteins expressed during the G1 phase of the cell cycle is determined by the duration of mitogen-activated protein kinase activation." Mol Cell Biol 19(1): 330-341.
Coulombel, L. (2007). "[Adult stem cells: their scientific interest and therapeutic future]." Gynecol Obstet Fertil 35(9): 806-810.

Darcy, K. M., A. L. Wohlhueter, et al. (1999). "Selective changes in EGF receptor expression and function during the proliferation, differentiation and apoptosis of mammary epithelial cells." Eur J Cell Biol 78(7): 511-523.
De Robertis, E. M., J. Larrain, et al. (2000). "The establishment of Spemann's organizer and patterning of the vertebrate embryo." Nat Rev Genet 1(3): 171-181.
Defize, L. H., D. J. Arndt-Jovin, et al. (1988). "A431 cell variants lacking the blood group A antigen display increased high affinity epidermal growth factor-receptor number, protein-tyrosine kinase activity, and receptor turnover." J Cell Biol 107(3): 939-949.
Dehghani Zadeh, A., S. Seveau, et al. (2003). "Chemotactically-induced redistribution of CD43 as related to polarity and locomotion of human polymorphonuclear leucocytes." Biol Cell 95(5): 265-273.
Demou, Z. N. and L. V. McIntire (2002). "Fully automated three-dimensional tracking of cancer cells in collagen gels: determination of motility phenotypes at the cellular level." Cancer Res 62(18): 5301-5307.
Dertinger, S. K., X. Jiang, et al. (2002). "Gradients of substrate-bound laminin orient axonal specification of neurons." Proc Natl Acad Sci U S A 99(20): 12542-12547.
Dho, S. E., M. B. French, et al. (1999). "Characterization of four mammalian numb protein isoforms. Identification of cytoplasmic and membrane-associated variants of the phosphotyrosine binding domain." J Biol Chem 274(46): 33097-33104.
Dowd, C. J., C. L. Cooney, et al. (1999). "Heparan sulfate mediates bFGF transport through basement membrane by diffusion with rapid reversible binding." J Biol Chem 274(8): 5236-5244.
Dyson, S. and J. B. Gurdon (1998). "The interpretation of position in a morphogen gradient as revealed by occupancy of activin receptors." Cell 93(4): 557-568.
Earle, W. R. (1962). "Some morphologic variations of certain cells under controlled experimental conditions." Natl Cancer Inst Monogr 7: 213-236.
Feig, L. A. (1999). "Tools of the trade: use of dominant-inhibitory mutants of Ras-family GTPases." Nat Cell Biol 1(2): E25-27.
Feiguin, F., M. Hannus, et al. (2001). "The ankyrin repeat protein Diego mediates Frizzled-dependent planar polarization." Dev Cell 1(1): 93-101.
Ferguson, K. M., M. B. Berger, et al. (2003). "EGF activates its receptor by removing interactions that autoinhibit ectodomain dimerization." Mol Cell 11(2): 507-517.
Fosser, K. A. and R. G. Nuzzo (2003). "Fabrication of patterned multicomponent protein gradients and gradient arrays using microfluidic depletion." Anal Chem 75(21): 5775-5782.
Foxman, E. F., J. J. Campbell, et al. (1997). "Multistep navigation and the combinatorial control of leukocyte chemotaxis." J Cell Biol 139(5): 1349-1360.
Friedenstein, A. J., U. F. Deriglasova, et al. (1974). "Precursors for fibroblasts in different populations of hematopoietic cells as detected by the in vitro colony assay method." Exp Hematol 2(2): 83-92.
Friedenstein, A. J., J. F. Gorskaja, et al. (1976). "Fibroblast precursors in normal and irradiated mouse hematopoietic organs." Exp Hematol 4(5): 267-274.
Frindel, E., E. Malaise, et al. (1968). "Cell proliferation kinetics in five human solid tumors." Cancer 22(3): 611-620.
Frisch, T. and O. Thoumine (2002). "Predicting the kinetics of cell spreading." J Biomech 35(8): 1137-1141.

Frise, E., J. A. Knoblich, et al. (1996). "The Drosophila Numb protein inhibits signaling of the Notch receptor during cell-cell interaction in sensory organ lineage." Proc Natl Acad Sci U S A 93(21): 11925-11932.
Froese, G. (1964). "The Distribution and Interdependence of Generation Times of Hela Cells." Exp Cell Res 35: 415-419.
Fujioka, A., K. Terai, et al. (2006). "Dynamics of the Ras/ERK MAPK cascade as monitored by fluorescent probes." J Biol Chem 281(13): 8917-8926.
Gadella, T. W., Jr. and T. M. Jovin (1995). "Oligomerization of epidermal growth factor receptors on A431 cells studied by time-resolved fluorescence imaging microscopy. A stereochemical model for tyrosine kinase receptor activation." J Cell Biol 129(6): 1543-1558.
Garrett, T. P., N. M. McKern, et al. (2003). "The crystal structure of a truncated ErbB2 ectodomain reveals an active conformation, poised to interact with other ErbB receptors." Mol Cell 11(2): 495-505.
Geng, W., P. Cosman, et al. (2004). "Automatic tracking, feature extraction and classification of C elegans phenotypes." IEEE Trans Biomed Eng 51(10): 1811-1820.
Goldstein, B. and I. G. Macara (2007). "The PAR proteins: fundamental players in animal cell polarization." Dev Cell 13(5): 609-622.
Gomperts, B. N. and R. M. Strieter (2007). "Stem cells and chronic lung disease." Annu Rev Med 58: 285-298.
Grifoni, D., F. Garoia, et al. (2004). "The human protein Hugl-1 substitutes for Drosophila lethal giant larvae tumour suppressor function in vivo." Oncogene 23(53): 8688-8694.
Gunawan, R. C., E. R. Choban, et al. (2005). "Regiospecific control of protein expression in cells cultured on two-component counter gradients of extracellular matrix proteins." Langmuir 21(7): 3061-3068.
Gunawan, R. C., J. Silvestre, et al. (2006). "Cell migration and polarity on microfabricated gradients of extracellular matrix proteins." Langmuir 22(9): 4250-4258.
Gurdon, J. B. and P. Y. Bourillot (2001). "Morphogen gradient interpretation." Nature 413(6858): 797-803.
Haigler, H. T., J. A. McKanna, et al. (1979). "Direct visualization of the binding and internalization of a ferritin conjugate of epidermal growth factor in human carcinoma cells A-431." J Cell Biol 81(2): 382-395.
Halpern, H. J., G. V. Chandramouli, et al. (1999). "Diminished aqueous microviscosity of tumors in murine models measured with in vivo radiofrequency electron paramagnetic resonance." Cancer Res 59(22): 5836-5841.
Haugh, J. M. and D. A. Lauffenburger (1998). "Analysis of receptor internalization as a mechanism for modulating signal transduction." J Theor Biol 195(2): 187-218.
Hess, J., P. Angel, et al. (2004). "AP-1 subunits: quarrel and harmony among siblings." J Cell Sci 117(Pt 25): 5965-5973.
Ho, H. O., C. W. Lin, et al. (2001). "Diffusion characteristics of collagen film." Journal of Controlled Release 77(1-2): 97-105.
Hoebeke, J., G. Van Nijen, et al. (1976). "Interaction of oncodazole (R 17934), a new antitumoral drug, with rat brain tubulin." Biochem Biophys Res Commun 69(2): 319-324.
Holbro, T. and N. E. Hynes (2004). "ErbB receptors: directing key signaling networks throughout life." Annu Rev Pharmacol Toxicol 44: 195-217.

Honegger, A. M., R. M. Kris, et al. (1989). "Evidence that autophosphorylation of solubilized receptors for epidermal growth factor is mediated by intermolecular cross-phosphorylation." Proc Natl Acad Sci U S A 86(3): 925-929.
Horvitz, H. R. and I. Herskowitz (1992). "Mechanisms of asymmetric cell division: two Bs or not two Bs, that is the question." Cell 68(2): 237-255.
Howe, A., A. E. Aplin, et al. (1998). "Integrin signaling and cell growth control." Curr Opin Cell Biol 10(2): 220-231.
Hsu, T. C. (1960). "Generation time of HeLa cells determined from cine records." Tex Rep Biol Med 18: 31-33.
Hu, Y. and D. D. Bowtell (1996). "Sos1 rapidly associates with Grb2 and is hypophosphorylated when complexed with the EGF receptor after EGF stimulation." Oncogene 12(9): 1865-1872.
Hynes, N. E. and H. A. Lane (2005). "ERBB receptors and cancer: the complexity of targeted inhibitors." Nat Rev Cancer 5(5): 341-354.
Irwin, M. E., K. L. Mueller, et al. (2010). "Lipid raft localization of EGFR alters the response of cancer cells to the EGFR tyrosine kinase inhibitor gefitinib." J Cell Physiol.
Izaki, T., S. Kamakura, et al. (2005). "Phosphorylation-dependent binding of 14-3-3 to Par3beta, a human Par3-related cell polarity protein." Biochem Biophys Res Commun 329(1): 211-218.
Izumi, Y., N. Ohta, et al. (2006). "Drosophila Pins-binding protein Mud regulates spindle-polarity coupling and centrosome organization." Nat Cell Biol 8(6): 586-593.
Jenny, A., R. S. Darken, et al. (2003). "Prickle and Strabismus form a functional complex to generate a correct axis during planar cell polarity signaling." EMBO J 22(17): 4409-4420.
Jenny, A., J. Reynolds-Kenneally, et al. (2005). "Diego and Prickle regulate Frizzled planar cell polarity signalling by competing for Dishevelled binding." Nat Cell Biol 7(7): 691-697.
Jessell, T. M. (2000). "Neuronal specification in the spinal cord: inductive signals and transcriptional codes." Nat Rev Genet 1(1): 20-29.
Jura, N., N. F. Endres, et al. (2009). "Mechanism for activation of the EGF receptor catalytic domain by the juxtamembrane segment." Cell 137(7): 1293-1307.
Karin, M. and T. Hunter (1995). "Transcriptional control by protein phosphorylation: signal transmission from the cell surface to the nucleus." Curr Biol 5(7): 747-757.
Kim-Ha, J., J. L. Smith, et al. (1991). "oskar mRNA is localized to the posterior pole of the Drosophila oocyte." Cell 66(1): 23-35.
Kim, H. and W. J. Muller (1999). "The role of the epidermal growth factor receptor family in mammary tumorigenesis and metastasis." Exp Cell Res 253(1): 78-87.
Kirkin, V. and I. Dikic (2007). "Role of ubiquitin- and Ubl-binding proteins in cell signaling." Curr Opin Cell Biol 19(2): 199-205.
Klingensmith, J., R. Nusse, et al. (1994). "The Drosophila segment polarity gene dishevelled encodes a novel protein required for response to the wingless signal." Genes Dev 8(1): 118-130.
Knoblich, J. A. (2008). "Mechanisms of asymmetric stem cell division." Cell 132(4): 583-597.
Kovary, K. and R. Bravo (1991). "Expression of different Jun and Fos proteins during the G0-to-G1 transition in mouse fibroblasts: in vitro and in vivo associations." Mol Cell Biol 11(5): 2451-2459.

Kovary, K. and R. Bravo (1992). "Existence of different Fos/Jun complexes during the G0-to-G1 transition and during exponential growth in mouse fibroblasts: differential role of Fos proteins." Mol Cell Biol 12(11): 5015-5023.
Kraut, R., W. Chia, et al. (1996). "Role of inscuteable in orienting asymmetric cell divisions in Drosophila." Nature 383(6595): 50-55.
Kress, H., J. G. Park, et al. (2009). "Cell stimulation with optically manipulated microsources." Nat Methods 6(12): 905-909.
Kunath, T., M. K. Saba-El-Leil, et al. (2007). "FGF stimulation of the Erk1/2 signalling cascade triggers transition of pluripotent embryonic stem cells from self-renewal to lineage commitment." Development 134(16): 2895-2902.
Kusumi, A., Y. Sako, et al. (1993). "Confined lateral diffusion of membrane receptors as studied by single particle tracking (nanovid microscopy). Effects of calcium-induced differentiation in cultured epithelial cells." Biophys J 65(5): 2021-2040.
Kyriakis, J. M. and J. Avruch (2001). "Mammalian mitogen-activated protein kinase signal transduction pathways activated by stress and inflammation." Physiol Rev 81(2): 807-869.
Le Roy, H., T. Zuliani, et al. "Asymmetric distribution of epidermal growth factor receptor directs the fate of normal and cancer keratinocytes in vitro." Stem Cells Dev 19(2): 209-220.
Lemmon, M. A., Z. Bu, et al. (1997). "Two EGF molecules contribute additively to stabilization of the EGFR dimer." EMBO J 16(2): 281-294.
Levkowitz, G., H. Waterman, et al. (1998). "c-Cbl/Sli-1 regulates endocytic sorting and ubiquitination of the epidermal growth factor receptor." Genes Dev 12(23): 3663-3674.
Li Jeon, N., H. Baskaran, et al. (2002). "Neutrophil chemotaxis in linear and complex gradients of interleukin-8 formed in a microfabricated device." Nat Biotechnol 20(8): 826-830.
Lin, F., C. M. Nguyen, et al. (2005). "Neutrophil migration in opposing chemoattractant gradients using microfluidic chemotaxis devices." Ann Biomed Eng 33(4): 475-482.
Lipkin, M. (1965). "Cell Replication in the Gastrointestinal Tract of Man." Gastroenterology 48: 616-624.
Lipkin, M., B. Bell, et al. (1963). "Cell Proliferation Kinetics in the Gastrointestinal Tract of Man. I. Cell Renewal in Colon and Rectum." J Clin Invest 42(6): 767-776.
Lund, K. A., L. K. Opresko, et al. (1990). "Quantitative analysis of the endocytic system involved in hormone-induced receptor internalization." J Biol Chem 265(26): 15713-15723.
Luo, Y., Z. Cheng, et al. (2011). "Endosomal signalling of epidermal growth factor receptors contributes to EGF-stimulated cell cycle progression in primary hepatocytes." Eur J Pharmacol 654(2): 173-180.
Lutolf, M. P. and J. A. Hubbell (2005). "Synthetic biomaterials as instructive extracellular microenvironments for morphogenesis in tissue engineering." Nat Biotechnol 23(1): 47-55.
Lynch, T. J., D. W. Bell, et al. (2004). "Activating mutations in the epidermal growth factor receptor underlying responsiveness of non-small-cell lung cancer to gefitinib." N Engl J Med 350(21): 2129-2139.
Mahdavi, A., R. E. Davey, et al. (2007). "Sensitivity analysis of intracellular signaling pathway kinetics predicts targets for stem cell fate control." PLoS Comput Biol 3(7): e130.

Masui, S., Y. Nakatake, et al. (2007). "Pluripotency governed by Sox2 via regulation of Oct3/4 expression in mouse embryonic stem cells." Nat Cell Biol 9(6): 625-635.
Mayo, K. H., M. Nunez, et al. (1989). "Epidermal growth factor receptor binding is not a simple one-step process." J Biol Chem 264(30): 17838-17844.
Means, S., A. J. Smith, et al. (2006). "Reaction diffusion modeling of calcium dynamics with realistic ER geometry." Biophys J 91(2): 537-557.
Mizuno, E., T. Iura, et al. (2005). "Regulation of epidermal growth factor receptor down-regulation by UBPY-mediated deubiquitination at endosomes." Mol Biol Cell 16(11): 5163-5174.
Montcouquiol, M., N. Sans, et al. (2006). "Asymmetric localization of Vangl2 and Fz3 indicate novel mechanisms for planar cell polarity in mammals." J Neurosci 26(19): 5265-5275.
Moogk, D., S. Hanley, et al. (2007). "Design and analysis of a long-term live-cell imaging chamber for tracking cellular dynamics within cultured human islets of Langerhans." Biotechnol Bioeng 97(5): 1138-1147.
Morrison, D. K. and R. E. Cutler (1997). "The complexity of Raf-1 regulation." Curr Opin Cell Biol 9(2): 174-179.
Muller, A. M., A. Medvinsky, et al. (1994). "Development of hematopoietic stem cell activity in the mouse embryo." Immunity 1(4): 291-301.
Murk, J. L., B. M. Humbel, et al. (2003). "Endosomal compartmentalization in three dimensions: implications for membrane fusion." Proc Natl Acad Sci U S A 100(23): 13332-13337.
Muthuswamy, S. K., M. Gilman, et al. (1999). "Controlled dimerization of ErbB receptors provides evidence for differential signaling by homo- and heterodimers." Mol Cell Biol 19(10): 6845-6857.
Nakakuki, T., N. Yumoto, et al. (2008). "Topological analysis of MAPK cascade for kinetic ErbB signaling." PLoS One 3(3): e1782.
Nichols, J. T., A. Miyamoto, et al. (2007). "Notch signaling--constantly on the move." Traffic 8(8): 959-969.
Niggemann, B., K. Maaser, et al. (1997). "Locomotory phenotypes of human tumor cell lines and T lymphocytes in a three-dimensional collagen lattice." Cancer Lett 118(2): 173-180.
Nipper, R. W., K. H. Siller, et al. (2007). "Galphai generates multiple Pins activation states to link cortical polarity and spindle orientation in Drosophila neuroblasts." Proc Natl Acad Sci U S A 104(36): 14306-14311.
Niwa, H., J. Miyazaki, et al. (2000). "Quantitative expression of Oct-3/4 defines differentiation, dedifferentiation or self-renewal of ES cells." Nat Genet 24(4): 372-376.
Noda, Y., R. Takeya, et al. (2001). "Human homologues of the Caenorhabditis elegans cell polarity protein PAR6 as an adaptor that links the small GTPases Rac and Cdc42 to atypical protein kinase C." Genes Cells 6(2): 107-119.
Oda, K., Y. Matsuoka, et al. (2005). "A comprehensive pathway map of epidermal growth factor receptor signaling." Mol Syst Biol 1: 2005 0010.
Ohno, S. (2001). "Intercellular junctions and cellular polarity: the PAR-aPKC complex, a conserved core cassette playing fundamental roles in cell polarity." Curr Opin Cell Biol 13(5): 641-648.
Olayioye, M. A., R. M. Neve, et al. (2000). "The ErbB signaling network: receptor heterodimerization in development and cancer." EMBO J 19(13): 3159-3167.
Orkin, S. H. and L. I. Zon (2008). "Hematopoiesis: an evolving paradigm for stem cell biology." Cell 132(4): 631-644.

Ortega-Perez, I., K. Murray, et al. (2007). "The how and why of adult neurogenesis." J Mol Histol 38(6): 555-562.
Paez, J. G., P. A. Janne, et al. (2004). "EGFR mutations in lung cancer: correlation with clinical response to gefitinib therapy." Science 304(5676): 1497-1500.
Pao, W., V. Miller, et al. (2004). "EGF receptor gene mutations are common in lung cancers from "never smokers" and are associated with sensitivity of tumors to gefitinib and erlotinib." Proc Natl Acad Sci U S A 101(36): 13306-13311.
Pawson, T. (1995). "Protein modules and signalling networks." Nature 373(6515): 573-580.
Pawson, T. (2004). "Specificity in signal transduction: from phosphotyrosine-SH2 domain interactions to complex cellular systems." Cell 116(2): 191-203.
Pearse, B. M. and M. S. Robinson (1990). "Clathrin, adaptors, and sorting." Annu Rev Cell Biol 6: 151-171.
Pera, M. F., B. Reubinoff, et al. (2000). "Human embryonic stem cells." J Cell Sci 113 (Pt 1): 5-10.
Petronczki, M. and J. A. Knoblich (2001). "DmPAR-6 directs epithelial polarity and asymmetric cell division of neuroblasts in Drosophila." Nat Cell Biol 3(1): 43-49.
Pinkas-Kramarski, R., L. Soussan, et al. (1996). "Diversification of Neu differentiation factor and epidermal growth factor signaling by combinatorial receptor interactions." EMBO J 15(10): 2452-2467.
Plowman, G. D., J. M. Culouscou, et al. (1993). "Ligand-specific activation of HER4/p180erbB4, a fourth member of the epidermal growth factor receptor family." Proc Natl Acad Sci U S A 90(5): 1746-1750.
Plowman, G. D., G. S. Whitney, et al. (1990). "Molecular cloning and expression of an additional epidermal growth factor receptor-related gene." Proc Natl Acad Sci U S A 87(13): 4905-4909.
Rabut, G. and J. Ellenberg (2004). "Automatic real-time three-dimensional cell tracking by fluorescence microscopy." J Microsc 216(Pt 2): 131-137.
Ramunas, J., M. Illman, et al. (2006). "True monolayer cell culture in a confined 3D microenvironment enables lineage informatics." Cytometry A 69(12): 1202-1211.
Ramunas, J., H. J. Montgomery, et al. (2007). "Real-time fluorescence tracking of dynamic transgene variegation in stem cells." Mol Ther 15(4): 810-817.
Riese, D. J., 2nd and D. F. Stern (1998). "Specificity within the EGF family/ErbB receptor family signaling network." Bioessays 20(1): 41-48.
Saso, K., G. Moehren, et al. (1997). "Differential inhibition of epidermal growth factor signaling pathways in rat hepatocytes by long-term ethanol treatment." Gastroenterology 112(6): 2073-2088.
Schaefer, K. L., K. Brachwitz, et al. (2006). "Constitutive activation of neuregulin/ERBB3 signaling pathway in clear cell sarcoma of soft tissue." Neoplasia 8(7): 613-622.
Schlessinger, J. (2000). "Cell signaling by receptor tyrosine kinases." Cell 103(2): 211-225.
Schlessinger, J. (2002). "Ligand-induced, receptor-mediated dimerization and activation of EGF receptor." Cell 110(6): 669-672.
Schlessinger, J. (2004). "Common and distinct elements in cellular signaling via EGF and FGF receptors." Science 306(5701): 1506-1507.
Schlessinger, J. and M. A. Lemmon (2003). "SH2 and PTB domains in tyrosine kinase signaling." Sci STKE 2003(191): RE12.

Schlessinger, J. and A. Ullrich (1992). "Growth factor signaling by receptor tyrosine kinases." Neuron 9(3): 383-391.
Schmidt-Glenewinkel, H., E. Reinz, et al. (2009). "Systems biological analysis of epidermal growth factor receptor internalization dynamics for altered receptor levels." J Biol Chem 284(25): 17243-17252.
Schoeberl, B., C. Eichler-Jonsson, et al. (2002). "Computational modeling of the dynamics of the MAP kinase cascade activated by surface and internalized EGF receptors." Nat Biotechnol 20(4): 370-375.
Seale, P. and M. A. Rudnicki (2000). "A new look at the origin, function, and "stem-cell" status of muscle satellite cells." Dev Biol 218(2): 115-124.
Seifert, J. R. and M. Mlodzik (2007). "Frizzled/PCP signalling: a conserved mechanism regulating cell polarity and directed motility." Nat Rev Genet 8(2): 126-138.
Servant, G., O. D. Weiner, et al. (2000). "Polarization of chemoattractant receptor signaling during neutrophil chemotaxis." Science 287(5455): 1037-1040.
Servant, G., O. D. Weiner, et al. (1999). "Dynamics of a chemoattractant receptor in living neutrophils during chemotaxis." Mol Biol Cell 10(4): 1163-1178.
Shvartsman, S. Y., H. S. Wiley, et al. (2001). "Spatial range of autocrine signaling: modeling and computational analysis." Biophys J 81(4): 1854-1867.
Sibilia, M., J. P. Steinbach, et al. (1998). "A strain-independent postnatal neurodegeneration in mice lacking the EGF receptor." EMBO J 17(3): 719-731.
Sibilia, M. and E. F. Wagner (1995). "Strain-dependent epithelial defects in mice lacking the EGF receptor." Science 269(5221): 234-238.
Silva, J. and A. Smith (2008). "Capturing pluripotency." Cell 132(4): 532-536.
Sorkin, A. and G. Carpenter (1993). "Interaction of activated EGF receptors with coated pit adaptins." Science 261(5121): 612-615.
Sorkin, A., P. P. Di Fiore, et al. (1993). "The carboxyl terminus of epidermal growth factor receptor/erbB-2 chimerae is internalization impaired." Oncogene 8(11): 3021-3028.
Sorkin, A. and L. K. Goh (2009). "Endocytosis and intracellular trafficking of ErbBs." Exp Cell Res 315(4): 683-696.
Starbuck, C. and D. A. Lauffenburger (1992). "Mathematical model for the effects of epidermal growth factor receptor trafficking dynamics on fibroblast proliferation responses." Biotechnol Prog 8(2): 132-143.
Steinbach, F., K. Borchers, et al. (1998). "Dendritic cells presenting equine herpesvirus-1 antigens induce protective anti-viral immunity." J Gen Virol 79 (Pt 12): 3005-3014.
Sun, Y., S. K. Goderie, et al. (2005). "Asymmetric distribution of EGFR receptor during mitosis generates diverse CNS progenitor cells." Neuron 45(6): 873-886.
Tam, P. P. and R. R. Behringer (1997). "Mouse gastrulation: the formation of a mammalian body plan." Mech Dev 68(1-2): 3-25.
Taupin, P. (2006). "Adult neural stem cells, neurogenic niches, and cellular therapy." Stem Cell Rev 2(3): 213-219.
Taylor, J., N. Abramova, et al. (1998). "Van Gogh: a new Drosophila tissue polarity gene." Genetics 150(1): 199-210.
Teramura, Y., J. Ichinose, et al. (2006). "Single-molecule analysis of epidermal growth factor binding on the surface of living cells." EMBO J 25(18): 4215-4222.
Thomson, J. A., J. Itskovitz-Eldor, et al. (1998). "Embryonic stem cell lines derived from human blastocysts." Science 282(5391): 1145-1147.

Till, J. E., E. A. McCulloch, et al. (1964). "A Stochastic Model of Stem Cell Proliferation, Based on the Growth of Spleen Colony-Forming Cells." Proc Natl Acad Sci U S A 51: 29-36.
Tree, D. R., J. M. Shulman, et al. (2002). "Prickle mediates feedback amplification to generate asymmetric planar cell polarity signaling." Cell 109(3): 371-381.
Ullrich, A. and J. Schlessinger (1990). "Signal transduction by receptors with tyrosine kinase activity." Cell 61(2): 203-212.
van Deurs, B., O. W. Petersen, et al. (1989). "The ways of endocytosis." Int Rev Cytol 117: 131-177.
Vetter, I. R. and A. Wittinghofer (2001). "The guanine nucleotide-binding switch in three dimensions." Science 294(5545): 1299-1304.
Vieira, A. V., C. Lamaze, et al. (1996). "Control of EGF receptor signaling by clathrin-mediated endocytosis." Science 274(5295): 2086-2089.
Wang, Q., G. Villeneuve, et al. (2005). "Control of epidermal growth factor receptor endocytosis by receptor dimerization, rather than receptor kinase activation." EMBO Rep 6(10): 942-948.
Wang, Y., D. Du, et al. (2006). "Tyrosine phosphorylated Par3 regulates epithelial tight junction assembly promoted by EGFR signaling." EMBO J 25(21): 5058-5070.
Wang, Y., S. Pennock, et al. (2002). "Endosomal signaling of epidermal growth factor receptor stimulates signal transduction pathways leading to cell survival." Mol Cell Biol 22(20): 7279-7290.
Wasserman, J. D. and M. Freeman (1997). "Control of EGF receptor activation in Drosophila." Trends Cell Biol 7(11): 431-436.
Waterman, H., I. Sabanai, et al. (1998). "Alternative intracellular routing of ErbB receptors may determine signaling potency." J Biol Chem 273(22): 13819-13827.
Watt, F. M. and B. L. Hogan (2000). "Out of Eden: stem cells and their niches." Science 287(5457): 1427-1430.
Weiss, S., B. A. Reynolds, et al. (1996). "Is there a neural stem cell in the mammalian forebrain?" Trends Neurosci 19(9): 387-393.
Wharton, K. A., K. M. Johansen, et al. (1985). "Nucleotide sequence from the neurogenic locus notch implies a gene product that shares homology with proteins containing EGF-like repeats." Cell 43(3 Pt 2): 567-581.
Wiesmann, C., M. H. Ultsch, et al. (1999). "Crystal structure of nerve growth factor in complex with the ligand-binding domain of the TrkA receptor." Nature 401(6749): 184-188.
Wikstrand, C. J., C. J. Reist, et al. (1998). "The class III variant of the epidermal growth factor receptor (EGFRvIII): characterization and utilization as an immunotherapeutic target." J Neurovirol 4(2): 148-158.
Wiley, H. S. (1988). "Anomalous binding of epidermal growth factor to A431 cells is due to the effect of high receptor densities and a saturable endocytic system." J Cell Biol 107(2): 801-810.
Wiley, H. S. and P. M. Burke (2001). "Regulation of receptor tyrosine kinase signaling by endocytic trafficking." Traffic 2(1): 12-18.
Winawer, S. J. and M. Lipkin (1969). "Cell proliferation kinetics in the gastrointestinal tract of man. IV. Cell renewal in the intestinalized gastric mucosa." J Natl Cancer Inst 42(1): 9-17.
Wodarz, A. and W. B. Huttner (2003). "Asymmetric cell division during neurogenesis in Drosophila and vertebrates." Mech Dev 120(11): 1297-1309.

Wodarz, A., A. Ramrath, et al. (2000). "Drosophila atypical protein kinase C associates with Bazooka and controls polarity of epithelia and neuroblasts." J Cell Biol 150(6): 1361-1374.
Wolpert, L. (1989). "Positional information revisited." Development 107 Suppl: 3-12.
Wong, K., O. Pertz, et al. (2006). "Neutrophil polarization: spatiotemporal dynamics of RhoA activity support a self-organizing mechanism." Proc Natl Acad Sci U S A 103(10): 3639-3644.
Wu, J., T. J. Klein, et al. (2004). "Subcellular localization of frizzled receptors, mediated by their cytoplasmic tails, regulates signaling pathway specificity." PLoS Biol 2(7): E158.
Yarden, Y. and J. Schlessinger (1987). "Self-phosphorylation of epidermal growth factor receptor: evidence for a model of intermolecular allosteric activation." Biochemistry 26(5): 1434-1442.
Yarden, Y. and M. X. Sliwkowski (2001). "Untangling the ErbB signalling network." Nat Rev Mol Cell Biol 2(2): 127-137.
Yu, C., J. Hale, et al. (2009). "Receptor overexpression or inhibition alters cell surface dynamics of EGF-EGFR interaction: new insights from real-time single molecule analysis." Biochem Biophys Res Commun 378(3): 376-382.
Zadeh, A. D. and H. Keller (2003). "Chemotactically directed redistribution of alpha-actinin precedes morphological polarization and reversal of polarity in human polymorphonuclear leucocytes (PMNs)." Eur J Cell Biol 82(2): 93-96.
Zhang, H., A. Berezov, et al. (2007). "ErbB receptors: from oncogenes to targeted cancer therapies." J Clin Invest 117(8): 2051-2058.
Zhang, X., J. Gureasko, et al. (2006). "An allosteric mechanism for activation of the kinase domain of epidermal growth factor receptor." Cell 125(6): 1137-1149.
Zhelev, D. V., A. M. Alteraifi, et al. (2004). "Controlled pseudopod extension of human neutrophils stimulated with different chemoattractants." Biophys J 87(1): 688-695.
Zhelev, D. V., A. M. Alteraifi, et al. (1996). "F-actin network formation in tethers and in pseudopods stimulated by chemoattractant." Cell Motil Cytoskeleton 35(4): 331-344.
Zheng, B., C. Lavoie, et al. (2004). "Regulation of epidermal growth factor receptor degradation by heterotrimeric Galphas protein." Mol Biol Cell 15(12): 5538-5550.
Zicha, D., G. Dunn, et al. (1997). "Analyzing chemotaxis using the Dunn direct-viewing chamber." Methods Mol Biol 75: 449-457.
Zigmond, S. H. (1977). "Ability of polymorphonuclear leukocytes to orient in gradients of chemotactic factors." J Cell Biol 75(2 Pt 1): 606-616.

Textbooks

Welty J., Wicks C., Wilson R. and Rorrer G. Fundamentals of Momentum, Heat, and Mass Transfer. 5th edition. John Wiley & Sons Inc., 2007.

Lodish H., Berk A., Kaiser C., Krieger M., Scott M., Bretscher A., Ploegh H., Matsudaira P. Molecular Cell Biology. Wiley & Sons Inc., 2007.

Appendices

Appendix A: Derivation of Model Fit Equation and Model Fit

Statement of the Differential Rate Law

The equation of the reaction for this system is given below:

$$L + R \overset{k_f}{\rightarrow} C \ldots (1)$$

Based on the stoichiometry of the above equation, the following equivalence of rates of reaction with respect to specific species can be written:

$$\frac{dL}{dt} = \frac{dR}{dt} = -\frac{dC}{dt} \ldots (2)$$

The initial conditions for the concentration of each of the species, in units of $\frac{mol}{m^3}$ are given below:

$$L(0) = L_0; R(0) = R_{init}; C(0) = 0 \ldots (3)$$

Given the equivalence of the derivatives of L and R as shown in equation (2), their respective functions are equal up to an additive constant:

$$L = R + k_1 \ldots (4)$$

The additive constant k_1 would be equal to the difference between initial concentrations of L and R and is defined as:

$$k_1 = L_0 - R_{init} \ldots (5)$$

given that L>>R. The rate law for this second order reaction is given by:

$$r = k_f RL \ldots (6)$$

Substitution of (5) into (4) and then the result into (6) gives the following differential equation:

$$\frac{dL}{dt} = k_f L\big(L - (L_0 - R_{init})\big) = k_f L(L + R_{init} - L_0) \ldots (7)$$

Solution of the Differential Equation

Separation of Variables

$$\frac{dL}{L(L + R_{init} - L_0)} = k_f dt$$

Integrating both sides:

$$\int \frac{dL}{L(L + R_{init} - L_0)} = \int k_f dt = k_f t + k_2 \ldots (8)$$

where k_2 is the integration constant.

To integrate the right hand side, partial fraction expansion must be performed:

$$\frac{1}{L(L + R_{init} - L_0)} = \frac{A}{L} + \frac{B}{(L + R_{init} - L_0)} = \frac{A(L + R_{init} - L_0) + BL}{L(L + R_{init} - L_0)}$$

Then it can be noted that:

$$1 = A(L + R_{init} - L_0) + BL \ldots (9)$$

To solve for A, subsitutute $L = 0$ into (9):

$$1 = A(R_{init} - L_0) \rightarrow A = \frac{1}{(R_{init} - L_0)} \ldots (10)$$

To solve for B, substitute $L = L_0 - R_{int}$ into (9):

$$1 = A(L_0 - R_{init} + R_{init} - L_0) + B(L_0 - R_{init}) = B(L_0 - R_{init}) \rightarrow B = \frac{1}{(L_0 - R_{init})} \ldots (11)$$

Substitution of (10) and (11) into (8) results in:

$$\int \frac{dL}{L(L + R_{init} - L_0)} = \int \left[\frac{1}{(R_{init} - L_0)}\frac{1}{L} + \frac{1}{(L_0 - R_{init})}\frac{1}{(L + R_{init} - L_0)}\right] dL = k_f t + k_2$$

Factoring and integrating gives:

$$\int \left[\frac{1}{(R_{init} - L_0)}\frac{1}{L} + \frac{1}{(L_0 - R_{init})}\frac{1}{(L + R_{init} - L_0)}\right] dL$$

$$= \frac{1}{(L_0 - R_{init})}\int \left[\frac{1}{(L + R_{init} - L_0)} - \frac{1}{L}\right] dL$$

$$= \frac{1}{(L_0 - R_{init})}[\ln(L + R_{init} - L_0) - \ln L] + k_3 = k_f t + k_2 \ldots (12)$$

where k_3 is the integration constant.

Simplification of equation (12) gives:

$$\frac{1}{(L_0 - R_{init})}\ln\left[\frac{(L + R_{init} - L_0)}{L}\right] = k_f t + k_4$$

where $k_4 = k_2 - k_3$.

Further simplification results in the following:

$$\ln\left[\frac{(L + R_{init} - L_0)}{L}\right] = k_f t(L_0 - R_{init}) + k_5 \ldots (13)$$

where $k_5 = (L_0 - R_{init})k_4$.

Raising both sides of (13) to an exponent gives:

$$\frac{(L + R_{init} - L_0)}{L} = \exp\left[k_f t(L_0 - R_{init}) + k_5\right] \ldots (14)$$

Re-arranging for L: (note that $K = \exp(k_5)$)

$$L + R_{init} - L_0 = KL\exp\left[k_f t(L_0 - R_{init})\right] \rightarrow R_{init} - L_0 = L\{K\exp\left[k_f t(L_0 - R_{init})\right] - 1\}$$

Solving for L:

$$L = \frac{R_{init} - L_0}{K\exp\left[k_f t(L_0 - R_{init})\right] - 1} \ldots (15)$$

Application of the Initial Condition:

$$L(0) = L_0$$

Substitution into (15):

$$L(0) = L_0 = \frac{R_{init} - L_0}{K \exp\left[k_f 0(L_0 - R_{init})\right] - 1} = \frac{R_{init} - L_0}{K - 1}$$

Solving for K:

$$L_0(K-1) = R_{init} - L_0 \rightarrow L_0K - L_0 = R_{init} - L_0 \rightarrow L_0K = R_{init} \rightarrow K = \frac{R_{init}}{L_0} \ldots (16)$$

(16) into (15):

$$L = \frac{R_{init} - L_0}{\frac{R_{init}}{L_0} \exp\left[k_f t(L_0 - R_{init})\right] - 1}$$

Appendix B: Matlab m-files

This section covers the three-dimensional modeling. The files used for the two-dimensional analysis are not presented here but are similar in structure.

Model Fit and Kinetic Parameters Estimation

```
clear
close all
clc

%Code to fit Flourimeter Data to the Derrived Equation

%Input of Constants
EGFM = 6045;
AvanN = 6.02e23;
Volume = 3;
CellRadius = 5e-6;
CellNumber = 20886667;

%Standard Curve 1 - Input of Data and Fit to get b
StCurveRaw1 = [5760, 6120, 6400, 6800, 7000, 7080, 7400, 7760, 7810, 7820];
Blank1 = 5290;
StCurve1 = StCurveRaw1 - Blank1; %Subtract Blank
StCurveConc = [0.5:0.5:5]; %St Curve Concentrations
b1 = regress(StCurve1', [ones(10,1) StCurveConc']);
FittedLine1 = b1(1) + StCurveConc*b1(2);

% Plot the Standard Curve 1
plot(StCurveConc, StCurve1, 'kx',StCurveConc, FittedLine1, 'k-','LineWidth',2,'MarkerSize',10)
grid on
set(gca,'FontSize',18,'LineWidth',2)
xlabel('Concentration [ng/mL]','FontSize',18)
ylabel('Relative Intensity','FontSize',18)
title('Standard Curve','FontSize',18)
text(0.75,2750,['The equation of the line of best fit is y = ' num2str(round(b1(2)))...
   '*x + ' num2str(round(b1(1)))],'Background','g','FontSize',15)
axis([0 5 0 3e3])
print -dtiff -r600 StCurveJuly21.tif

%Input the EGF Binding Data 1
RawData1 = [mean([6920,6940]), 6740, 6520, 6390, mean([5970,6120]), 5930] - Blank1; %Substract Blank
ColdEGF1 = mean([7000,6890]) - Blank1; %Calculate Cold EGF Point
ConcData1 = (([ColdEGF1 RawData1]-b1(1))./b1(2))/(EGFM)*1e3; %Convert to nmol/L
Time = [0, 1, 3, 5, 10, 30, 45];

f = 7820/9725; %Standard Curve Correction

%Input the EGF Binding Data 2
RawData2 = [mean([8740,9000,8910]), 8120, 7900, 7340, 6825, 6720] - Blank1; %Substract Blank
ColdEGF2 = mean([8450,8800,8600]) - Blank1; %Calculate Cold EGF Point
ConcData2 = (([ColdEGF2 RawData2]*f-b1(1))./b1(2))/(EGFM)*1e3; %Convert to nmol/L - and correct for st. curve
```

```
ConcDataRaw = ([ColdEGF1 RawData1]+[ColdEGF2 RawData2]*f)/2;
ConcData = (ConcData1 + ConcData2)/2; %Average Concentraion Value

Error1 = [std([7000,6890,8450*f,8800*f,8600*f]) std([6920,6940,8740*f,9000*f,8910*f]) ...
   std([6740,8120*f]) std([6520,7900*f]) std([6390,7340*f]) std([5970,6120,6825*f]), std([5930,6720*f])];
%Calculation of an error based on all data points and standard deviation

%Calculate Error Bars
ConcDataU = ((ConcDataRaw + Error1 - b1(1))./b1(2))-ConcData/1e3*EGFM;
ConcDataL = ((ConcDataRaw - Error1 - b1(1))./b1(2))-ConcData/1e3*EGFM;

%Unit Conversion for Concentration, Define conc function
L0 = ConcData(1);
funfit = @(k,Time) (k(2)-L0)./(k(2)/L0*exp(k(1).*Time.*(L0-k(2)))-1);

%Fit kf using nlin fit - take 0.5 and 0.5 as a guess, calculate it
fit = nlinfit(Time,ConcData,funfit,[1 1]);
ConcFit = funfit(fit,0:45);

%Get Parameters
kf=fit(1)*1e6; %Take fit(1) and multiply by 1e6 to convert into m^3/mol*s =
(L/nmol*s)*(1m^3/1e3L)*(1e9nmol/mol)
Rint=fit(2)*1e-12*AvanN*Volume/CellNumber; %Take fit(2) and convert into R number =
(1L/1000mL)*(mol/10e9nmol)

%Plot the concentration graph
figure
errorbar(Time,ConcData*EGFM/1e3,ConcDataU,ConcDataL,'kx','LineWidth',2,'MarkerSize',10)
grid on
hold on
set(gca,'FontSize',18,'LineWidth',2)
plot(0:45,ConcFit/1e3*EGFM,'k-','LineWidth',2,'MarkerSize',10)
xlabel('Time [min]','FontSize',18)
ylabel('Concentration TRITC-EGF [ng/mL]','FontSize',18)
title('Model Fit','FontSize',18)
axis([-1  46 0 5])
legend('Data','Model Fit','Location','Best','FontSize',18)
text(-0.5,4.6,{'The fit parameters are: kf = 1.3 x 10^5 m^3/mol*s';...
   'and R_i_n_t = 47,362'},'Background','g','FontSize',15)
print -dtiff -r600 ModelFitJuly21.tif
```

Model definition, PI / PO plots and D_a analysis

Modelsus.m

```
function fem = modelsus(Time,D,Conc,fem0)

global kf RDensity C ATol RTol

if Conc == 1
   Var = 'L0';
else
   Var = 0;
```

```
end

% Geometry
g1=block3('5e-4','5e-4','5e-4','base','center','pos',{'0','0','0'},'axis',{'0','0','1'},'rot','0');
g2=sphere3('1e-5','pos',{'0','0','0'},'axis',{'0','0','1'},'rot','0');
g3=cylinder3('2.5e-6','2e-5','pos',{'2e-5','0','0'},'axis',{'1','0','0'},'rot','0');
g4=cylinder3('3e-6','2e-5','pos',{'2e-5','0','0'},'axis',{'0','0','1'},'rot','0');
g5=cylinder3('3e-6','2e-5','pos',{'2e-5','0','0'},'axis',{'1','0','0'},'rot','0');
g6=cylinder3('3.5e-6','1e-5','pos',{'4e-5','0','0'},'axis',{'1','0','0'},'rot','0');

% Analyzed geometry
clear s
s.objs={g1,g2,g3,g5,g6};
s.name={'Subdomain','Cell','OuterD','InnerD','End'};
s.tags={'g1','g2','g3','g5','g6'};

fem.draw=struct('s',s);
fem.geom=geomcsg(fem);

% Constants
fem.const = {'D',D, ...
  'kf',kf, ...
  'DC','1e-14', ...
  'DR','1e-14', ...
  'Rint',RDensity, ...
  'L0',C, ...
  'DI','1e-14'};

% Initialize mesh
fem.mesh=meshinit(fem, ...
                  'hauto',5);

% Application mode 1
clear appl
appl.mode.class = 'ConvDiff';
appl.dim = {'L'};
appl.module = 'CHEM';
appl.border = 'on';
appl.assignsuffix = '_chcd';
clear bnd
bnd.c0 = {0,0,0,Var};
bnd.N = {0,0,'-kf*L*R',0};
bnd.type = {'N0','cont','N','C'};
bnd.ind = [1,1,1,1,1,3,3,3,3,3,3,3,3,1,1,1,2,1,1,1,1,1,1,1,1,1,2,4,1,1, ...
  1,1];
appl.bnd = bnd;
clear equ
equ.D = {'D',1,'D'};
equ.init = {0,0,'L0'};
equ.usage = {1,0,1};
equ.ind = [1,2,2,3,2];
appl.equ = equ;
fem.appl{1} = appl;

% Application mode 2
clear appl
```

```
appl.mode.class = 'FlPDEWBoundary';
appl.dim = {'R','R_t'};
appl.assignsuffix = '_wb';
clear prop
clear weakconstr
weakconstr.value = 'off';
weakconstr.dim = {'lm2','lm3'};
prop.weakconstr = weakconstr;
appl.prop = prop;
clear bnd
bnd.dweak = {0,'R_test*R_time'};
bnd.init = {0,{'Rint';0}};
bnd.usage = {0,1};
bnd.weak = {0,'DR*(-RTx_test*RTx-RTy_test*RTy-RTz_test*RTz)+R_test*(surf_recept)'};
bnd.ind = [1,1,1,1,1,2,2,2,2,2,2,2,2,1,1,1,1,1,1,1,1,1,1,1,1,1,1,1,1,1,1, ...
  1,1];
appl.bnd = bnd;
fem.appl{2} = appl;

% Application mode 3
clear appl
appl.mode.class = 'FlPDEWBoundary';
appl.dim = {'C','C_t'};
appl.name = 'wb2';
appl.sshape = 2;
appl.assignsuffix = '_wb2';
clear prop
clear weakconstr
weakconstr.value = 'off';
weakconstr.dim = {'lm4','lm5'};
prop.weakconstr = weakconstr;
appl.prop = prop;
clear bnd
bnd.dweak = {0,'C_test*C_time'};
bnd.usage = {0,1};
bnd.weak = {0,'DC*(-CTx_test*CTx-CTy_test*CTy-CTz_test*CTz)+C_test*(surf_comp)'};
bnd.ind = [1,1,1,1,1,2,2,2,2,2,2,2,2,1,1,1,1,1,1,1,1,1,1,1,1,1,1,1,1,1,1, ...
  1,1];
appl.bnd = bnd;
fem.appl{3} = appl;
fem.frame = {'ref'};
fem.border = 1;
fem.outform = 'general';
clear units;
units.basesystem = 'SI';
fem.units = units;

% Boundary settings
clear bnd
bnd.ind = [1,1,1,1,1,2,2,2,2,2,2,2,2,1,1,1,1,1,1,1,1,1,1,1,1,1,1,1,1,1,1, ...
  1,1];
bnd.dim = {'L','R','C'};

% Boundary expressions
bnd.expr = {'surf_recept',{'','-kf*R*L'}, ...
  'surf_comp',{'','kf*R*L'}};
```

```
fem.bnd = bnd;

% ODE Settings
clear ode
clear units;
units.basesystem = 'SI';
ode.units = units;
fem.ode=ode;

% Multiphysics
fem=multiphysics(fem);

% Extend mesh
fem.xmesh=meshextend(fem);

if Conc == 1
% Solve problem
fem.sol=femtime(fem, 'symmetric','off', 'solcomp',{'C','R','L'}, ...
            'outcomp',{'R','C','L'}, 'blocksize','auto', ...
            'tlist',[colon(0,1,Time)], 'rtol',RTol, ...
            'tout','tlist', 'atol',ATol, 'linsolver','gmres', ...
            'prefun','amg');

else
fem.sol=femtime(fem,'init',fem0.sol,'symmetric','off','solcomp',{'R','C','L'}, ...
            'outcomp',{'C','R','L'},'blocksize','auto', ...
            'tlist',[colon(0,1,Time)],'rtol',RTol,'tout','tlist', ...
            'atol',ATol,'linsolver','gmres','prefun','amg');
end

% Save current fem structure for restart purposes
fem0=fem;
```

Modeladh.m

```
function fem = modeladh(Time,D,Conc,fem0)

global kf RDensity C ATol RTol

if Conc == 1
   Var = 'L0';
else
   Var = 0;
end

% Geometry
g1=block3('5e-4','5e-4','5e-4','base','center','pos',{'0','0','0'},'axis',{'0','0','1'},'rot','0');
g2=sphere3('12.599e-6','pos',{'0','0','-2.5e-4'},'axis',{'0','0','1'},'rot','0');
g3=geomcomp({g1,g2},'ns',{'g1','g2'},'sf','g1*g2','face','none','edge','all');
g4=block3('5e-4','5e-4','5e-4','base','center','pos',{'0','0','0'},'axis',{'0','0','1'},'rot','0');
g5=cylinder3('2.5e-6','2e-5','pos',{'2.2599e-5','0','-2.45e-4'},'axis',{'1','0','0'},'rot','0');
g6=cylinder3('3e-6','2e-5','pos',{'2.2599e-5','0','-2.45e-4'},'axis',{'1','0','0'},'rot','0');
g7=cylinder3('3e-6','1e-5','pos',{'4.2599e-5','0','-2.45e-4'},'axis',{'1','0','0'},'rot','0');
```

```
% Analyzed geometry
clear s
s.objs={g3,g4,g5,g6,g7};
s.name={'CO1','Subdomain','InnerD','OuterD','End'};
s.tags={'g3','g4','g5','g6','g7'};

fem.draw=struct('s',s);
fem.geom=geomcsg(fem);

% Constants
fem.const = {'D',D, ...
 'kf',kf, ...
 'DC','1e-14', ...
 'DR','1e-14', ...
 'Rint',RDensity, ...
 'L0',C};

% Initialize mesh
fem.mesh=meshinit(fem, ...
                  'hauto',5);

% Application mode 1
clear appl
appl.mode.class = 'ConvDiff';
appl.dim = {'L'};
appl.module = 'CHEM';
appl.sshape = 2;
appl.border = 'on';
appl.assignsuffix = '_chcd';
clear bnd
bnd.c0 = {0,0,0,Var};
bnd.N = {0,0,'-kf*L*R',0};
bnd.type = {'N0','cont','N','C'};
bnd.ind = [1,1,1,1,1,3,2,3,3,3,1,1,1,2,1,1,1,1,1,1,2,1,1,4,1,1,1,1];
appl.bnd = bnd;
clear equ
equ.D = {'D',1,'D'};
equ.init = {0,0,'L0'};
equ.usage = {1,0,1};
equ.ind = [1,2,2,3,2];
appl.equ = equ;
fem.appl{1} = appl;

% Application mode 2
clear appl
appl.mode.class = 'FlPDEWBoundary';
appl.dim = {'R','R_t'};
appl.sshape = 2;
appl.assignsuffix = '_wb';
clear prop
clear weakconstr
weakconstr.value = 'off';
weakconstr.dim = {'lm2','lm3'};
prop.weakconstr = weakconstr;
appl.prop = prop;
clear bnd
```

```
bnd.dweak = {0,'R_test*R_time'};
bnd.init = {0,{'Rint';0}};
bnd.usage = {0,1};
bnd.weak = {0,'DR*(-RTx_test*RTx-RTy_test*RTy-RTz_test*RTz)+R_test*(surf_recept)'};
bnd.ind = [1,1,1,1,1,2,1,2,2,2,1,1,1,1,1,1,1,1,1,1,1,1,1,1,1,1,1,1];
appl.bnd = bnd;
fem.appl{2} = appl;

% Application mode 3
clear appl
appl.mode.class = 'FlPDEWBoundary';
appl.dim = {'C','C_t'};
appl.name = 'wb2';
appl.sshape = 2;
appl.assignsuffix = '_wb2';
clear prop
clear weakconstr
weakconstr.value = 'off';
weakconstr.dim = {'lm4','lm5'};
prop.weakconstr = weakconstr;
appl.prop = prop;
clear bnd
bnd.dweak = {0,'C_test*C_time'};
bnd.usage = {0,1};
bnd.weak = {0,'DC*(-CTx_test*CTx-CTy_test*CTy-CTz_test*CTz)+C_test*(surf_comp)'};
bnd.ind = [1,1,1,1,1,2,1,2,2,2,1,1,1,1,1,1,1,1,1,1,1,1,1,1,1,1,1,1];
appl.bnd = bnd;
fem.appl{3} = appl;
fem.frame = {'ref'};
fem.border = 1;
fem.outform = 'general';
clear units;
units.basesystem = 'SI';
fem.units = units;

% Boundary settings
clear bnd
bnd.ind = [1,1,1,1,1,2,1,2,2,2,1,1,1,1,1,1,1,1,1,1,1,1,1,1,1,1,1,1];
bnd.dim = {'L','R','C'};

% Boundary expressions
bnd.expr = {'surf_recept',{'','-kf*R*L'}, ...
  'surf_comp',{'','kf*R*L'}};
fem.bnd = bnd;

% ODE Settings
clear ode
clear units;
units.basesystem = 'SI';
ode.units = units;
fem.ode=ode;

% Multiphysics
fem=multiphysics(fem);

% Extend mesh
```

```
fem.xmesh=meshextend(fem);

if Conc == 1
% Solve problem
fem.sol=femtime(fem, 'symmetric','off', 'solcomp',{'C','R','L'}, ...
            'outcomp',{'R','C','L'}, 'blocksize','auto', ...
            'tlist',[colon(0,1,Time)], 'rtol',RTol, ...
            'tout','tlist', 'atol',ATol, 'linsolver','gmres', ...
            'prefun','amg');

else
fem.sol=femtime(fem,'init',fem0.sol,'symmetric','off','solcomp',{'R','C','L'}, ...
            'outcomp',{'C','R','L'},'blocksize','auto', ...
            'tlist',[colon(0,1,Time)],'rtol',RTol,'tout','tlist', ...
            'atol',ATol,'linsolver','gmres','prefun','amg');
end

% Save current fem structure for restart purposes
fem0=fem;
```

Modelgap.m

```
function fem = modelgap(Time,D,Conc,fem0)

global kf RDensity C ATol RTol

if Conc == 1
   Var = 'L0';
else
   Var = 0;
end

% Geometry
g1=block3('5e-4','5e-4','5e-4','base','center','pos',{'0','0','0'},'axis',{'0','0','1'},'rot','0');
g3=cylinder3('2.5e-6','2e-5','pos',{'2.1547e-5','0','-2.45e-4'},'axis',{'1','0','0'},'rot','0');
g5=cylinder3('1.1547E-5','1.0E-5','pos',{'0','0','-2.45E-4'},'axis',{'0','0','1'},'rot','0');
g6=cylinder3('1.1547E-5','1.0E-5','pos',{'0','0','-2.5E-4'},'axis',{'0','0','1'},'rot','0');
g7=cylinder3('3e-6','2e-5','pos',{'2.1547e-5','0','-2.45e-4'},'axis',{'1','0','0'},'rot','0');
g8=cylinder3('3e-6','1e-5','pos',{'4.1547e-5','0','-2.45e-4'},'axis',{'1','0','0'},'rot','0');
g16=block3('2*4.3094E-5','2*4.3094E-5','1.0E-5','base','center','pos',{'-1.07735E-5*2','0','-2.35E-
4'},'axis',{'0','0','1'},'rot','0');

% Constants
fem.const = {'D',D, ...
 'kf',kf, ...
 'DC','1e-14', ...
 'DR','1e-14', ...
 'Rint',RDensity, ...
 'L0',C};

% Analyzed geometry
clear s
s.objs={g1,g3,g6,g7,g8,g16};
s.name={'Block','CYL1','Cell','CYL2','CYL3','BLK1'};
s.tags={'g1','g3','g6','g7','g8','g16'};
```

```
fem.draw=struct('s',s);
fem.geom=geomcsg(fem);

% Initialize mesh
fem.mesh=meshinit(fem, ...
                  'hauto',5);

% (Default values are not included)

% Application mode 1
clear appl
appl.mode.class = 'ConvDiff';
appl.dim = {'L'};
appl.module = 'CHEM';
appl.sshape = 2;
appl.border = 'on';
appl.assignsuffix = '_chcd';
clear bnd
bnd.c0 = {0,0,0,Var};
bnd.N = {0,0,'-kf*L*R',0};
bnd.type = {'N0','cont','N','C'};
bnd.ind = [1,1,1,1,1,1,1,1,1,1,3,3,2,2,3,3,1,1,1,1,2,1,1,1,1,1,1,2,1,1, ...
  4,1,1,1,1];
appl.bnd = bnd;
clear equ
equ.D = {'D',1,'D'};
equ.init = {0,0,'L0'};
equ.usage = {1,0,1};
equ.ind = [1,2,2,2,3,2];
appl.equ = equ;
fem.appl{1} = appl;

% Application mode 2
clear appl
appl.mode.class = 'FlPDEWBoundary';
appl.dim = {'R','R_t'};
appl.sshape = 2;
appl.assignsuffix = '_wb';
clear prop
clear weakconstr
weakconstr.value = 'off';
weakconstr.dim = {'lm2','lm3'};
prop.weakconstr = weakconstr;
appl.prop = prop;
clear bnd
bnd.dweak = {0,'R_test*R_time'};
bnd.init = {0,{'Rint';0}};
bnd.usage = {0,1};
bnd.weak = {0,'DR*(-RTx_test*RTx-RTy_test*RTy-RTz_test*RTz)+R_test*(surf_recept)'};
bnd.ind = [1,1,1,1,1,1,1,1,1,1,2,2,1,1,2,2,1,1,1,1,1,1,1,1,1,1,1,1,1,1, ...
  1,1,1,1,1];
appl.bnd = bnd;
fem.appl{2} = appl;

% Application mode 3
```

```
clear appl
appl.mode.class = 'FlPDEWBoundary';
appl.dim = {'C','C_t'};
appl.name = 'wb2';
appl.sshape = 2;
appl.assignsuffix = '_wb2';
clear prop
clear weakconstr
weakconstr.value = 'off';
weakconstr.dim = {'lm4','lm5'};
prop.weakconstr = weakconstr;
appl.prop = prop;
clear bnd
bnd.dweak = {0,'C_test*C_time'};
bnd.usage = {0,1};
bnd.weak = {0,'DC*(-CTx_test*CTx-CTy_test*CTy-CTz_test*CTz)+C_test*(surf_comp)'};
bnd.ind = [1,1,1,1,1,1,1,1,1,1,2,2,1,1,2,2,1,1,1,1,1,1,1,1,1,1,1,1,1,1, ...
  1,1,1,1,1];
appl.bnd = bnd;
fem.appl{3} = appl;
fem.frame = {'ref'};
fem.border = 1;
fem.outform = 'general';
clear units;
units.basesystem = 'SI';
fem.units = units;

% Boundary settings
clear bnd
bnd.ind = [1,1,1,1,1,1,1,1,1,1,2,2,1,1,2,2,1,1,1,1,1,1,1,1,1,1,1,1,1,1, ...
  1,1,1,1,1];
bnd.dim = {'L','R','C'};

% Boundary expressions
bnd.expr = {'surf_recept',{'','-kf*R*L'}, ...
  'surf_comp',{'','kf*R*L'}};
fem.bnd = bnd;

% ODE Settings
clear ode
clear units;
units.basesystem = 'SI';
ode.units = units;
fem.ode=ode;

% Multiphysics
fem=multiphysics(fem);

% Extend mesh
fem.xmesh=meshextend(fem);

if Conc == 1
% Solve problem
fem.sol=femtime(fem, 'symmetric','off', 'solcomp',{'C','R','L'}, ...
              'outcomp',{'R','C','L'}, 'blocksize','auto', ...
              'tlist',[colon(0,1,Time)], 'rtol',RTol, ...
```

```
            'tout','tlist', 'atol',ATol, 'linsolver','gmres', ...
            'prefun','amg');

else
fem.sol=femtime(fem,'init',fem0.sol,'symmetric','off','solcomp',{'R','C','L'}, ...
            'outcomp',{'C','R','L'},'blocksize','auto', ...
            'tlist',[colon(0,1,Time)],'rtol',RTol,'tout','tlist', ...
            'atol',ATol,'linsolver','gmres','prefun','amg');
end

% Save current fem structure for restart purposes
fem0=fem;
```

Susstart.m

```
clear
clc

global D kf RDensity C ATol RTol CellSurfaceArea

%Input of Constants
CellRadius = 10e-6; %m
AvangadroNumber = 6.02e23;
Concentration = 100; %ng/mL
CellSurfaceArea = 4*pi*CellRadius^2; %m^2
EGFMolarMass = 6045; %g/mol
ReceptorN = 47362; %Receptors
kf = 1.3627e5; %Forward Constant - m^3/mol*s

%Input of Ranges
TimePoints = linspace(0,1200,1200);
D = logspace(-10,-12,10);

%Solution Parameters
Time = 1200;
RTol = 1e-12;
ATol = 1e-12;

%Calculation of Specific Values
RDensity = ReceptorN/(AvangadroNumber*CellSurfaceArea);
C = Concentration/EGFMolarMass/1e3;
DaNumber = (kf*RDensity*CellRadius)./D;
D = [1.89e-10 D];

%============================MODEL=======================================

%Integrate - and return a matrix of D by Time
for z = 1:2
   if z == 1
for j = 1:11
fem = modelsus(120,D(j),1,0);
fem0=fem;

for k = 1:120
```

```
  Result = susint(k,fem);
  PIResult(k,j,z) = Result(1);
  POResult(k,j,z) = Result(2);
  POFront(k,j,z) = Result(3);
  POBack(k,j,z) = Result(4);
end

fem = modelsus(1200-120,D(j),2,fem0);

for k = 1:1200-120
  Result = susint(k,fem);
  PIResult(k+120,j,z) = Result(1);
  POResult(k+120,j,z) = Result(2);
  POFront(k+120,j,z) = Result(3);
  POBack(k+120,j,z) = Result(4);
end
end
    else
for j = 1:11
fem = modelsus(1200,D(j),1,0);
fem0=fem;

for k = 1:1200
  Result = susint(k,fem);
  PIResult(k,j,z) = Result(1);
  POResult(k,j,z) = Result(2);
  POFront(k,j,z) = Result(3);
  POBack(k,j,z) = Result(4);
end
end
    end

disp(['Runs Completed: ' num2str(j)])
xlswrite(['PIResult' num2str(j) '.xls'],PIResult(:,:,z),num2str(z))
xlswrite(['POResult' num2str(j) '.xls'],POResult(:,:,z),num2str(z))
xlswrite(['POFront' num2str(j) '.xls'],POFront(:,:,z),num2str(z))
xlswrite(['POBack' num2str(j) '.xls'],POBack(:,:,z),num2str(z))
end


%Adjust the matrix for the PI and PO vs. Da Plots
PIResult2 = PIResult([60,120,300,600,1200],2:11,1);
POResult2 = POResult([60,120,300,600,1200],2:11,1);

ColorLetters = {'k','b','r','c','g','m'};

%Additional Calculations
PODiff = - POBack + POFront;
TimePoints1 = [1, 2, 5, 10, 20]*60;

%Create the PI and PO Da Plot
figure
for i = 1:5
    semilogx(DaNumber,PIResult2(i,:),'Color',ColorLetters{i},'LineStyle','-','LineWidth',2,'Marker','x')
    hold on
    grid on
```

```
    axis([DaNumber(1) DaNumber(end) 0 120])
    xlabel('Damkohler Number','FontSize',12)
    ylabel('Polarization Index','FontSize',12)
    title('Suspension: PI = f(Da)','FontSize',12)
    set(gca,'FontSize',11)
end
legend('1 min','2 min','5 min','10 min','20 min','Location','Best')
print -dtiff -r600 SusDaPIPlot.tif

figure
for i = 1:5
    semilogx(DaNumber,POResult2(i,:),'Color',ColorLetters{i},'LineStyle','-','LineWidth',2,'Marker','x')
    hold on
    grid on
    axis([DaNumber(1) DaNumber(end) 0 50])
    xlabel('Damkohler Number','FontSize',12)
    ylabel('Percent Occupancy','FontSize',12)
    title('Suspension: PO = f(Da)','FontSize',12)
    set(gca,'FontSize',11)
end
legend('1 min','2 min','5 min','10 min','20 min','Location','Best')
print -dtiff -r600 SusDaPOPlot.tif

%Figure - PI vs Time Profile
figure
plot(TimePoints/60,PIResult(:,1,1),'k-',TimePoints/60,PIResult(:,1,2),'k--',...
    'LineWidth',2)
grid on
title('Suspension Model: PI = f(Time)','FontSize',12)
ylabel('Polarization Index','FontSize',12)
xlabel('Time [min]','FontSize',12)
set(gca,'FontSize',11)
axis([0 20 1 5])
legend('Pipette Removal after 2 min','No Pipette Removal','Location','Best')
print -dtiff -r600 SusPITimePlot.tif

%Figure - PO vs Time Profile
figure
plot(TimePoints/60,POResult(:,1,1),'k-',TimePoints/60,POResult(:,1,2),'k--',...
    'LineWidth',2)
grid on
title('Suspension Model: PO = f(Time)','FontSize',12)
ylabel('Percent Occupancy','FontSize',12)
xlabel('Time [min]','FontSize',12)
set(gca,'FontSize',11)
legend('Pipette Removal after 2 min','No Pipette Removal','Location','Best')
print -dtiff -r600 SusPOTimePlot.tif

figure
plot(TimePoints/60,POBack(:,1,1),'k-',TimePoints/60,POFront(:,1,1),'k:',...
 TimePoints/60,POBack(:,1,2),'k--',TimePoints/60,POFront(:,1,2),'k-.','LineWidth',2)
grid on
title('Suspension: PO Front and PO Back = f(Time)','FontSize',12)
xlabel('Time [min]','FontSize',12)
ylabel('Percent Occupancy','FontSize',12)
set(gca,'FontSize',11)
```

```
legend('PO Back','PO Front','PO Back with Removal','PO Front with Removal',...
   'Location','Best')
print -dtiff -r600 SusPOFrontBackPlot.tif

%PO Front and PO Back Da Plots
for i = 1:5
   figure
   semilogx(DaNumber,POFront(TimePoints1(i),2:11,1),'k-','LineWidth',2)
   hold on
   semilogx(DaNumber,POBack(TimePoints1(i),2:11,1),'b-','LineWidth',2)
   semilogx(DaNumber,PODiff(TimePoints1(i),2:11,1),'k:','LineWidth',2)
   legend('POFront','POBack','PO Difference','Location','Best')
   title(['Suspension: PO = f(Da) for ' num2str(TimePoints1(i)/60) 'min'],'FontSize',12)
   xlabel('Da Number','FontSize',12)
   ylabel('Percent Occupancy','FontSize',12)
   axis([DaNumber(1) DaNumber(end) 0 70])
   grid on
   print('-dtiff','-r600',['SusDaPlot' num2str(TimePoints1(i)/60)])
   close all
end
```

Adhstart.m

```
clear
clc

global D kf RDensity C ATol RTol CellSurfaceArea

%Input of Constants
CellRadius = 12.599e-6; %m
AvangadroNumber = 6.02e23;
Concentration = 100; %ng/mL
CellSurfaceArea = 2*pi*CellRadius^2; %m^2
EGFMolarMass = 6045; %g/mol
ReceptorN = 47362; %Receptors
kf = 1.3627e5; %Forward Constant - m^3/mol*s

%Input of Ranges
TimePoints = linspace(0,1200,1200);
D = logspace(-10,-12,10);

%Solution Parameters
Time = 1200;
RTol = 1e-12;
ATol = 1e-12;

%Calculation of Specific Values
RDensity = ReceptorN/(AvangadroNumber*CellSurfaceArea);
C = Concentration/EGFMolarMass/1e3;
DaNumber = (kf*RDensity*CellRadius)./D;
D = [1.89e-10 D];

%============================MODEL=======================================
```

```
%Integrate - and return a matrix of D by Time
for z = 1:2
   if z == 1
for j = 1:11
fem = modeladh(120,D(j),1,0);
fem0=fem;

for k = 1:120
  Result = adhint(k,fem);
  PIResult(k,j,z) = Result(1);
  POResult(k,j,z) = Result(2);
  POFront(k,j,z) = Result(3);
  POBack(k,j,z) = Result(4);
end

fem = modeladh(1200-120,D(j),2,fem0);

for k = 1:1200-120
  Result = adhint(k,fem);
  PIResult(k+120,j,z) = Result(1);
  POResult(k+120,j,z) = Result(2);
  POFront(k+120,j,z) = Result(3);
  POBack(k+120,j,z) = Result(4);
end
end
   else
for j = 1:11
fem = modeladh(1200,D(j),1,0);
fem0=fem;

for k = 1:1200
  Result = adhint(k,fem);
  PIResult(k,j,z) = Result(1);
  POResult(k,j,z) = Result(2);
  POFront(k,j,z) = Result(3);
  POBack(k,j,z) = Result(4);
end
end
   end

disp(['Runs Completed: ' num2str(j)])
xlswrite(['PIResult' num2str(j) '.xls'],PIResult(:,:,z),num2str(z))
xlswrite(['POResult' num2str(j) '.xls'],POResult(:,:,z),num2str(z))
xlswrite(['POFront' num2str(j) '.xls'],POFront(:,:,z),num2str(z))
xlswrite(['POBack' num2str(j) '.xls'],POBack(:,:,z),num2str(z))
end


%Adjust the matrix for the PI and PO vs. Da Plots
PIResult2 = PIResult([60,120,300,600,1200],2:11,1);
POResult2 = POResult([60,120,300,600,1200],2:11,1);

ColorLetters = {'k','b','r','c','g','m'};

%Additional Calculations
PODiff = - POBack + POFront;
```

```
TimePoints1 = [1, 2, 5, 10, 20]*60;

%Create the PI and PO Da Plot
figure
for i = 1:5
   semilogx(DaNumber,1./PIResult2(i,:),'Color',ColorLetters{i},'LineStyle','-','LineWidth',2,'Marker','x')
   hold on
   grid on
   axis([DaNumber(1) DaNumber(end) 0 150])
   xlabel('Damkohler Number','FontSize',12)
   ylabel('Polarization Index','FontSize',12)
   %title('Adherent: PI = f(Da)','FontSize',12)
   set(gca,'FontSize',11)
end
legend('1 min','2 min','5 min','10 min','20 min','Location','Best')
print -dtiff -r600 AdhDaPIPlot.tif

figure
for i = 1:5
   semilogx(DaNumber,POResult2(i,:),'Color',ColorLetters{i},'LineStyle','-','LineWidth',2,'Marker','x')
   hold on
   grid on
   axis([DaNumber(1) DaNumber(end) 0 60])
   xlabel('Damkohler Number','FontSize',12)
   ylabel('Percent Occupancy','FontSize',12)
   %title('Adherent: PO = f(Da)','FontSize',12)
   set(gca,'FontSize',11)
end
legend('1 min','2 min','5 min','10 min','20 min','Location','Best')
print -dtiff -r600 AdhDaPOPlot.tif

%Figure - PI vs Time Profile
figure
plot(TimePoints/60,1./PIResult(:,1,1),'k-',TimePoints/60,1./PIResult(:,1,2),'k--',...
   'LineWidth',2)
grid on
%title('Adherent Model: PI = f(Time)','FontSize',12)
ylabel('Polarization Index','FontSize',12)
xlabel('Time [min]','FontSize',12)
set(gca,'FontSize',11)
axis([0 20 1 5])
legend('Pipette Removal after 2 min','No Pipette Removal','Location','Best')
print -dtiff -r600 AdhPITimePlot.tif

%Figure - PO vs Time Profile
figure
plot(TimePoints/60,POResult(:,1,1),'k-',TimePoints/60,POResult(:,1,2),'k--',...
   'LineWidth',2)
grid on
%title('Adherent Model: PO = f(Time)','FontSize',12)
ylabel('Percent Occupancy','FontSize',12)
xlabel('Time [min]','FontSize',12)
set(gca,'FontSize',11)
legend('Pipette Removal after 2 min','No Pipette Removal','Location','Best')
print -dtiff -r600 AdhPOTimePlot.tif
```

```
figure
plot(TimePoints/60,POBack(:,1,1),'k-',TimePoints/60,POFront(:,1,1),'k:',...
 TimePoints/60,POBack(:,1,2),'k--',TimePoints/60,POFront(:,1,2),'k-.','LineWidth',2)
grid on
%title('Adherent: PO Front and PO Back = f(Time)','FontSize',12)
xlabel('Time [min]','FontSize',12)
ylabel('Percent Occupancy','FontSize',12)
set(gca,'FontSize',11)
legend('PO Back','PO Front','PO Back with Removal','PO Front with Removal',...
   'Location','Best')
print -dtiff -r600 AdhPOFrontBackPlot.tif

%PO Front and PO Back Da Plots
for i = 1:5
   figure
   semilogx(DaNumber,POFront(TimePoints1(i),2:11,1),'k-','LineWidth',2)
   hold on
   semilogx(DaNumber,POBack(TimePoints1(i),2:11,1),'b-','LineWidth',2)
   semilogx(DaNumber,PODiff(TimePoints1(i),2:11,1),'k:','LineWidth',2)
   legend('POFront','POBack','PO Difference','Location','Best')
   %title(['Adherent: PO = f(Da) for ' num2str(TimePoints1(i)/60) 'min'],'FontSize',12)
   xlabel('Da Number','FontSize',12)
   ylabel('Percent Occupancy','FontSize',12)
   axis([DaNumber(1) DaNumber(end) 0 80])
   grid on
   print('-dtiff','-r600',['AdhDaPlot' num2str(TimePoints1(i)/60)])
   close all
end
```

Gapstart.m

```
clear
clc

global D kf RDensity C ATol RTol CellSurfaceArea

%Input of Constants
CellRadius = 1.1547e-005; %m
AvangadroNumber = 6.02e23;
Concentration = 100; %ng/mL
CellSurfaceArea = 2*pi*CellRadius*10e-6; %m^2
EGFMolarMass = 6045; %g/mol
ReceptorN = 47362; %Receptors
kf = 1.3627e5; %Forward Constant - m^3/mol*s

%Input of Ranges
TimePoints = linspace(0,1200,1200);
D = logspace(-10,-12,10);

%Solution Parameters
Time = 1200;
RTol = 1e-12;
ATol = 1e-12;
```

```
%Calculation of Specific Values
RDensity = ReceptorN/(AvangadroNumber*CellSurfaceArea);
C = Concentration/EGFMolarMass/1e3;
DaNumber = (kf*RDensity*CellRadius)./D;
D = [1.89e-10 D];

%============================MODEL=====================================

%Integrate - and return a matrix of D by Time
for z = 1:2
   if z == 1
for j = 1:11
fem = modelgap(120,D(j),1,0);
fem0=fem;

for k = 1:120
  Result = gapint(k,fem);
  PIResult(k,j,z) = Result(1);
  POResult(k,j,z) = Result(2);
  POFront(k,j,z) = Result(3);
  POBack(k,j,z) = Result(4);
end

fem = modelgap(1200-120,D(j),2,fem0);

for k = 1:1200-120
  Result = gapint(k,fem);
  PIResult(k+120,j,z) = Result(1);
  POResult(k+120,j,z) = Result(2);
  POFront(k+120,j,z) = Result(3);
  POBack(k+120,j,z) = Result(4);
end
end
   else
for j = 1:11
fem = modelgap(1200,D(j),1,0);
fem0=fem;

for k = 1:1200
  Result = gapint(k,fem);
  PIResult(k,j,z) = Result(1);
  POResult(k,j,z) = Result(2);
  POFront(k,j,z) = Result(3);
  POBack(k,j,z) = Result(4);
end
end
   end

disp(['Runs Completed: ' num2str(j)])
xlswrite(['PIResult' num2str(j) '.xls'],PIResult(:,:,z),num2str(z))
xlswrite(['POResult' num2str(j) '.xls'],POResult(:,:,z),num2str(z))
xlswrite(['POFront' num2str(j) '.xls'],POFront(:,:,z),num2str(z))
xlswrite(['POBack' num2str(j) '.xls'],POBack(:,:,z),num2str(z))
end
```

```
%Adjust the matrix for the PI and PO vs. Da Plots
PIResult2 = PIResult([60,120,300,600,1200],2:11,1);
POResult2 = POResult([60,120,300,600,1200],2:11,1);

ColorLetters = {'k','b','r','c','g','m'};

%Additional Calculations
PODiff = - POBack + POFront;
TimePoints1 = [1, 2, 5, 10, 20]*60;

%Create the PI and PO Da Plot
figure
for i = 1:5
   semilogx(DaNumber,PIResult2(i,:),'Color',ColorLetters{i},'LineStyle','-','LineWidth',2,'Marker','x')
   hold on
   grid on
   axis([DaNumber(1) DaNumber(end) 0 150])
   xlabel('Damkohler Number','FontSize',12)
   ylabel('Polarization Index','FontSize',12)
   %title('Gap: PI = f(Da)','FontSize',12)
   set(gca,'FontSize',11)
end
legend('1 min','2 min','5 min','10 min','20 min','Location','Best')
print -dtiff -r600 GapDaPIPlot.tif

figure
for i = 1:5
   semilogx(DaNumber,POResult2(i,:),'Color',ColorLetters{i},'LineStyle','-','LineWidth',2,'Marker','x')
   hold on
   grid on
   axis([DaNumber(1) DaNumber(end) 0 70])
   xlabel('Damkohler Number','FontSize',12)
   ylabel('Percent Occupancy','FontSize',12)
   %title('Gap: PO = f(Da)','FontSize',12)
   set(gca,'FontSize',11)
end
legend('1 min','2 min','5 min','10 min','20 min','Location','Best')
print -dtiff -r600 GapDaPOPlot.tif

%Figure - PI vs Time Profile
figure
plot(TimePoints/60,PIResult(:,1,1),'k-',TimePoints/60,PIResult(:,1,2),'k--',...
   'LineWidth',2)
grid on
%title('Gap: PI = f(Time)','FontSize',12)
ylabel('Polarization Index','FontSize',12)
xlabel('Time [min]','FontSize',12)
set(gca,'FontSize',11)
axis([0 20 1 5])
legend('Pipette Removal after 2 min','No Pipette Removal','Location','Best')
print -dtiff -r600 GapPITimePlot.tif

%Figure - PO vs Time Profile
figure
plot(TimePoints/60,POResult(:,1,1),'k-',TimePoints/60,POResult(:,1,2),'k--',...
   'LineWidth',2)
```

```
grid on
%title('Gap: PO = f(Time)','FontSize',12)
ylabel('Percent Occupancy','FontSize',12)
xlabel('Time [min]','FontSize',12)
axis([0 20 0 100])
set(gca,'FontSize',11)
legend('Pipette Removal after 2 min','No Pipette Removal','Location','Best')
print -dtiff -r600 GapPOTimePlot.tif

figure
plot(TimePoints/60,POBack(:,1,1),'k-',TimePoints/60,POFront(:,1,1),'k:',...
 TimePoints/60,POBack(:,1,2),'k--',TimePoints/60,POFront(:,1,2),'k-.','LineWidth',2)
grid on
%title('Gap: PO Front and PO Back = f(Time)','FontSize',12)
xlabel('Time [min]','FontSize',12)
ylabel('Percent Occupancy','FontSize',12)
axis([0 20 0 100])
set(gca,'FontSize',11)
legend('PO Back','PO Front','PO Back with Removal','PO Front with Removal',...
   'Location','Best')
print -dtiff -r600 GapPOFrontBackPlot.tif

%PO Front and PO Back Da Plots
for i = 1:5
   figure
   semilogx(DaNumber,POFront(TimePoints1(i),2:11,1),'k-','LineWidth',2)
   hold on
   semilogx(DaNumber,POBack(TimePoints1(i),2:11,1),'b-','LineWidth',2)
   semilogx(DaNumber,-PODiff(TimePoints1(i),2:11,1),'k:','LineWidth',2)
   legend('POFront','POBack','PO Difference','Location','Best')
   title(['Gap: PO = f(Da) for ' num2str(TimePoints1(i)/60) 'min'],'FontSize',12)
   xlabel('Da Number','FontSize',12)
   ylabel('Percent Occupancy','FontSize',12)
   axis([DaNumber(1) DaNumber(end) 0 90])
   grid on
   print('-dtiff','-r600',['GapDaPlotT' num2str(TimePoints1(i)/60)])
   close all
end
```

Susint.m

```
function Result = susint(k,fem)

global RDensity CellSurfaceArea

TimePoints = linspace(0,1200,1200);

try
% Integrate - Back Half
I1=postint(fem,'C', 'unit','', 'recover','off', ...
        'dl',[6,7,8,9], 'edim',2, 'solnum',TimePoints(k));

% Integrate - Front Half
I2=postint(fem,'C', 'unit','', 'recover','off', ...
```

```
        'dl',[10,11,12,13], 'edim',2, 'solnum',TimePoints(k));

% Integrate - R
I3=postint(fem,'R', 'unit','', 'recover','off', ...
        'dl',[6,7,8,9,10,11,12,13], 'edim',2, 'solnum',TimePoints(k));

% Integrate - R
I4=postint(fem,'R', 'unit','', 'recover','off', ...
        'dl',[10,11,12,13], 'edim',2, 'solnum',TimePoints(k));

% Integrate - R
I5=postint(fem,'R', 'unit','', 'recover','off', ...
        'dl',[6,7,8,9], 'edim',2, 'solnum',TimePoints(k));

PIResult = I2/I1;
POResult = (1-I3/(CellSurfaceArea*RDensity))*100;
POFront = (1-I4/(CellSurfaceArea*RDensity/2))*100;
POBack = (1-I5/(CellSurfaceArea*RDensity/2))*100;

catch exception
   PIResult = NaN;
   POResult = NaN;
   POFront = NaN;
   POBack = NaN;
end

Result = [PIResult POResult POFront POBack];
```

Adhint.m

```
function Result = adhint(k,fem)

global RDensity CellSurfaceArea

TimePoints = linspace(0,1200,1200);

 try
% Integrate - Back Half
I1=postint(fem,'C', 'unit','', 'recover','off', ...
        'dl',[9,10], 'edim',2, 'solnum',TimePoints(k));

% Integrate - Front Half
I2=postint(fem,'C', 'unit','', 'recover','off', ...
        'dl',[6,8], 'edim',2, 'solnum',TimePoints(k));

% Integrate - R
I3=postint(fem,'R', 'unit','', 'recover','off', ...
        'dl',[6,8,9,10], 'edim',2, 'solnum',TimePoints(k));

% Integrate - R
I4=postint(fem,'R', 'unit','', 'recover','off', ...
        'dl',[9,10], 'edim',2, 'solnum',TimePoints(k));

% Integrate - R
```

```
I5=postint(fem,'R', 'unit','', 'recover','off', ...
          'dl',[6,8], 'edim',2, 'solnum',TimePoints(k));

PIResult = I2/I1;
POResult = (1-I3/(CellSurfaceArea*RDensity))*100;
POFront = (1-I4/(CellSurfaceArea*RDensity/2))*100;
POBack = (1-I5/(CellSurfaceArea*RDensity/2))*100;

catch exception
   PIResult = NaN;
   POResult = NaN;
   POFront = NaN;
   POBack = NaN;
end

Result = [PIResult POResult POFront POBack];
```

Gapint.m

```
function Result = gapint(k,fem)

global RDensity CellSurfaceArea

TimePoints = linspace(0,1200,1200);

 try
% Integrate - Back Half
I1=postint(fem,'C', 'unit','','recover','off', 'dl',[11,12], ...
          'edim',2, 'solnum',TimePoints(k));

% Integrate - Front Half
I2=postint(fem,'C', 'unit','', 'recover','off', 'dl',[15,16], ...
          'edim',2, 'solnum',TimePoints(k));

% Integrate - R
I3=postint(fem,'R', 'unit','', 'recover','off', ...
          'dl',[11,12,15,16], 'edim',2, 'solnum',TimePoints(k));

% Integrate - R
I4=postint(fem,'R', 'unit','', 'recover','off', ...
          'dl',[11,12], 'edim',2, 'solnum',TimePoints(k));

% Integrate - R
I5=postint(fem,'R', 'unit','', 'recover','off', ...
          'dl',[15,16], 'edim',2, 'solnum',TimePoints(k));

PIResult = I2/I1;
POResult = (1-I3/(CellSurfaceArea*RDensity))*100;
POFront = (1-I4/(CellSurfaceArea*RDensity/2))*100;
POBack = (1-I5/(CellSurfaceArea*RDensity/2))*100;

catch exception
   PIResult = NaN;
   POResult = NaN;
```

```
    POFront = NaN;
    POBack = NaN;
end

Result = [PIResult POResult POFront POBack];
```

Generateplot.m

```
clear
clc
close all

%Reads data from Excel
PI(:,1) = xlsread('SusPI.xls','1','A1:A1200');
PI(:,2) = xlsread('SusPI.xls','2','A1:A1200');
PI(:,3) = 1./xlsread('AdhPI.xls','1','A1:A1200');
PI(:,4) = 1./xlsread('AdhPI.xls','2','A1:A1200');
PI(:,5) = xlsread('GapPI.xls','1','A1:A1200');
PI(:,6) = xlsread('GapPI.xls','2','A1:A1200');
POFront(:,1) = xlsread('SusPOFront.xls','1','A1:A1200');
POFront(:,2) = xlsread('SusPOFront.xls','2','A1:A1200');
POFront(:,3) = xlsread('AdhPOFront.xls','1','A1:A1200');
POFront(:,4) = xlsread('AdhPOFront.xls','2','A1:A1200');
POFront(:,5) = xlsread('GapPOFront.xls','1','A1:A1200');
POFront(:,6) = xlsread('GapPOFront.xls','2','A1:A1200');
POBack(:,1) = xlsread('SusPOBack.xls','1','A1:A1200');
POBack(:,2) = xlsread('SusPOBack.xls','2','A1:A1200');
POBack(:,3) = xlsread('AdhPOBack.xls','1','A1:A1200');
POBack(:,4) = xlsread('AdhPOBack.xls','2','A1:A1200');
POBack(:,5) = xlsread('GapPOBack.xls','1','A1:A1200');
POBack(:,6) = xlsread('GapPOBack.xls','2','A1:A1200');

PODiff = POFront - POBack;
Time = linspace(0,1198,1198)'/60;
Time2 = linspace(0,1199,1199)'/60;

%Makes Plot 1
plot(Time,PI(:,1),'k-',Time,PI(:,3),'k:',Time,PI(:,5),'k--','LineWidth',2)
xlabel('Time [min]','FontSize',12)
ylabel('Polarization Index','FontSize',12)
title('PI = f(Time) with Pipette Removal','FontSize',12)
axis([0 20 1 6])
set(gca,'FontSize',11)
legend('Suspension','Adherent','Gap','Location','Best')
grid on
print -dtiff -r600 AllPIRemoval.tif

%Makes Plot 2
figure
plot(Time,PI(:,2),'k-',Time,PI(:,4),'k:',Time,PI(:,6),'k--','LineWidth',2)
xlabel('Time [min]','FontSize',12)
ylabel('Polarization Index','FontSize',12)
title('PI = f(Time) with No Pipette Removal','FontSize',12)
axis([0 20 1 6]);
```

```
set(gca,'FontSize',11)
legend('Suspension','Adherent','Gap','Location','Best')
grid on
print -dtiff -r600 AllPINoRemoval.tif

figure
plot(Time2,PODiff(:,2),'k-','LineWidth',2)
grid on
hold on
plot(Time2,PODiff(:,4),'k--','LineWidth',2)
plot(Time2,-PODiff(:,6),'k:','LineWidth',2)
title('Difference in PO Front and PO Back: No Pipette Removal','FontSize',12)
xlabel('Time [min]','FontSize',12)
ylabel('PO Value','FontSize',12)
axis([0 20 0 60])
legend('Suspension','Adherent','Gap','Location','Best')
print -dtiff -r600 AllPODiffNoRemoval.tif

figure
plot(Time2,PODiff(:,1),'k-','LineWidth',2)
grid on
hold on
plot(Time2,PODiff(:,3),'k--','LineWidth',2)
plot(Time2,-PODiff(:,5),'k:','LineWidth',2)
title('Difference in PO Front and PO Back: Pipette Removal','FontSize',12)
xlabel('Time [min]','FontSize',12)
ylabel('PO Value','FontSize',12)
axis([0 20 0 60])
legend('Suspension','Adherent','Gap','Location','Best')
print -dtiff -r600 AllPODiffRemoval.tif

close all
```

Tortuosity Analysis

Modeladh3.m

```
function fem = modeladh3(Time,Conc,fem0)

global kf RDensity C ATol RTol D

if Conc == 1
   Var = 'L0'
else
   Var = 0
end

% Geometry
g1=block3('5E-4','5E-4','5e-4','base','corner','pos',{'0','0','0'},'axis',{'0','0','1'},'rot','0');
g3=sphere3('12.599e-6','pos',{'2.5e-4','2.5e-4','0'},'axis',{'0','0','1'},'rot','0');
g5=sphere3('12.599e-6','pos',{'2.5e-4','2.5e-4+(12.599e-6)','0'},'axis',{'0','0','1'},'rot','0');
g6=sphere3('(12.599e-6)','pos',{'2.5e-4','2.5e-4-12.599e-6','0'},'axis',{'0','0','1'},'rot','0');
g8=geomcomp({g3,g5,g6},'ns',{'g3','g5','g6'},'sf','g3+g5+g6','face','none','edge','all');
g9=geomcomp({g1,g8},'ns',{'g1','g8'},'sf','g1*g8','face','none','edge','all');
```

```
g10=block3('0.5e-3','0.5e-3','0.5e-3','base','corner','pos',{'0','0','0'},'axis',{'0','0','1'},'rot','0');
g11=cylinder3('3.0E-6','1.0E-5','pos',{'2.6E-4+12.599e-6','2.5E-4','5.0E-6'},'axis',{'1','0','0'},'rot','0');
g14=cylinder3('2.5E-6','1.0E-5','pos',{'2.72599E-4','2.5E-4','5.0E-6'},'axis',{'1','0','0'},'rot','0');
g15=cylinder3('3.0e-6','1e-5','pos',{'2.7E-4+12.599e-6','2.5e-4','5e-6'},'axis',{'1','0','0'},'rot','0');

% Constants
fem.const = {'Rint',RDensity, ...
  'L0',C, ...
  'kf',kf, ...
  'DC','1e-14', ...
  'DR','1e-14', ...
  'D',D};

% Geometry

% Analyzed geometry
clear s
s.objs={g9,g10,g11,g14,g15};
s.name={'CO2','BLK1','CYL1','CYL2','CYL3'};
s.tags={'g9','g10','g11','g14','g15'};

fem.draw=struct('s',s);
fem.geom=geomcsg(fem);

% Initialize mesh
fem.mesh=meshinit(fem, ...
                  'hauto',5);

% (Default values are not included)

% Application mode 1
clear appl
appl.mode.class = 'ConvDiff';
appl.dim = {'L'};
appl.module = 'CHEM';
appl.sshape = 2;
appl.assignsuffix = '_chcd';
clear bnd
bnd.c0 = {0,0,0,Var};
bnd.N = {0,0,'-kf*L*R',0};
bnd.type = {'N0','cont','N','C'};
bnd.ind = [1,1,1,1,1,2,3,3,2,3,3,3,2,3,2,2,2,2,2,2,3,2,3,2,3,2,2,3,2,3, ...
  3,1,1,1,2,1,1,1,1,1,1,2,1,1,4,1,1,1,1];
appl.bnd = bnd;
clear equ
equ.D = {'D',1,'D'};
equ.init = {0,0,'L0'};
equ.usage = {1,0,1};
equ.ind = [1,2,2,2,2,2,2,3,2];
appl.equ = equ;
fem.appl{1} = appl;

% Application mode 2
clear appl
appl.mode.class = 'FlPDEWBoundary';
appl.dim = {'R','R_t'};
```

```
appl.sshape = 2;
appl.assignsuffix = '_wb';
clear prop
clear weakconstr
weakconstr.value = 'off';
weakconstr.dim = {'lm2','lm3'};
prop.weakconstr = weakconstr;
appl.prop = prop;
clear bnd
bnd.dweak = {0,'R_test*R_time'};
bnd.init = {0,{'Rint';0}};
bnd.usage = {0,1};
bnd.weak = {0,'DR*(-RTx_test*RTx-RTy_test*RTy-RTz_test*RTz)+R_test*(surf_recept)'};
bnd.ind = [1,1,1,1,1,1,2,2,1,2,2,2,1,2,1,1,1,1,1,1,2,1,2,1,2,1,1,2,1,2, ...
  2,1,1,1,1,1,1,1,1,1,1,1,1,1,1,1,1,1,1,1,1];
appl.bnd = bnd;
fem.appl{2} = appl;

% Application mode 3
clear appl
appl.mode.class = 'FlPDEWBoundary';
appl.dim = {'C','C_t'};
appl.name = 'wb2';
appl.sshape = 2;
appl.assignsuffix = '_wb2';
clear prop
clear weakconstr
weakconstr.value = 'off';
weakconstr.dim = {'lm4','lm5'};
prop.weakconstr = weakconstr;
appl.prop = prop;
clear bnd
bnd.dweak = {0,'C_test*C_time'};
bnd.usage = {0,1};
bnd.weak = {0,'DC*(-CTx_test*CTx-CTy_test*CTy-CTz_test*CTz)+C_test*(surf_comp)'};
bnd.ind = [1,1,1,1,1,1,2,2,1,2,2,2,1,2,1,1,1,1,1,1,2,1,2,1,2,1,1,2,1,2, ...
  2,1,1,1,1,1,1,1,1,1,1,1,1,1,1,1,1,1,1,1,1];
appl.bnd = bnd;
fem.appl{3} = appl;
fem.frame = {'ref'};
fem.border = 1;
fem.outform = 'general';
clear units;
units.basesystem = 'SI';
fem.units = units;

% Boundary settings
clear bnd
bnd.ind = [1,1,1,1,1,1,2,2,1,2,2,2,1,2,1,1,1,1,1,1,2,1,2,1,2,1,1,2,1,2, ...
  2,1,1,1,1,1,1,1,1,1,1,1,1,1,1,1,1,1,1,1,1];
bnd.dim = {'L','R','C'};

% Boundary expressions
bnd.expr = {'surf_recept',{'','-kf*R*L'}, ...
  'surf_comp',{'','kf*R*L'}};
fem.bnd = bnd;
```

```
% ODE Settings
clear ode
clear units;
units.basesystem = 'SI';
ode.units = units;
fem.ode=ode;

% Multiphysics
fem=multiphysics(fem);

% Extend mesh
fem.xmesh=meshextend(fem);

if Conc == 1
% Solve problem
fem.sol=femtime(fem,'symmetric','off', 'solcomp',{'R','C','L'},...
            'outcomp',{'C','R','L'}, 'blocksize','auto', ...
            'tlist',[colon(0,1,Time)], 'rtol',RTol, 'tout','tlist', ...
            'atol',ATol,'linsolver','gmres','prefun','amg');

else
fem.sol=femtime(fem,'init',fem0.sol,'symmetric','off','solcomp',{'R','C','L'}, ...
            'outcomp',{'C','R','L'},'blocksize','auto', ...
            'tlist',[colon(0,1,Time)],'rtol',RTol,'tout','tlist', ...
            'atol',ATol,'linsolver','gmres','prefun','amg');
end

% Save current fem structure for restart purposes
fem0=fem;
```

Modeladh5.m

```
function fem = modeladh5(Time,Conc,fem0)

global kf RDensity C ATol RTol D

if Conc == 1
   Var = 'L0';
else
   Var = 0;
end

% Geometry
g1=block3('0.5e-3','0.5e-3','0.5e-3','base','corner','pos',{'0','0','0'},'axis',{'0','0','1'},'rot','0');
g2=sphere3('12.599e-6','pos',{'2.5e-4','2.5e-4','0'},'axis',{'0','0','1'},'rot','0');
g4=sphere3('12.599e-6','pos',{'2.5e-4','2.5e-4+12.599E-6','0'},'axis',{'0','0','1'},'rot','0');
g5=sphere3('12.599E-6','pos',{'2.5E-4','2.5e-4-12.599E-6','0'},'axis',{'0','0','1'},'rot','0');
g6=sphere3('12.599E-6','pos',{'2.5E-4','2.5e-4+2*12.599E-6','0'},'axis',{'0','0','1'},'rot','0');
g7=sphere3('12.599E-6','pos',{'2.5e-4','2.5e-4-2*12.599E-6','0'},'axis',{'0','0','1'},'rot','0');
g8=geomcomp({g2,g4,g5,g6,g7},'ns',{'g2','g4','g5','g6','g7'},'sf','g2+g4+g5+g6+g7','face','none','edge','all');
g9=geomcomp({g1,g8},'ns',{'g1','g8'},'sf','g1*g8','face','none','edge','all');
g10=block3('0.5E-3','0.5E-3','0.5E-3','base','corner','pos',{'0','0','0'},'axis',{'0','0','1'},'rot','0');
g12=cylinder3('3E-6','1E-5','pos',{'2.6E-4+12.599E-6','2.5E-4','5.0E-6'},'axis',{'1','0','0'},'rot','0');
```

```
g14=cylinder3('2.5E-6','1.0E-5','pos',{'2.72599E-4','2.5E-4','5.0E-6'},'axis',{'1','0','0'},'rot','0');
g15=cylinder3('3e-6','1e-5','pos',{'2.7e-4+12.599e-6','2.5e-4','5e-6'},'axis',{'1','0','0'},'rot','0');

% Constants
fem.const = {'Rint',RDensity, ...
 'L0',C, ...
 'kf',kf, ...
 'DC','1e-14', ...
 'DR','1e-14', ...
 'D',D};

% Geometry

% Analyzed geometry
clear s
s.objs={g9,g10,g12,g14,g15};
s.name={'CO2','BLK1','CYL1','CYL2','CYL3'};
s.tags={'g9','g10','g12','g14','g15'};

fem.draw=struct('s',s);
fem.geom=geomcsg(fem);

% Initialize mesh
fem.mesh=meshinit(fem, ...
                  'hauto',5);

% (Default values are not included)

% Application mode 1
clear appl
appl.mode.class = 'ConvDiff';
appl.dim = {'L'};
appl.module = 'CHEM';
appl.sshape = 2;
appl.assignsuffix = '_chcd';
clear bnd
bnd.c0 = {0,0,0,Var};
bnd.N = {0,0,'-kf*L*R',0};
bnd.type = {'N0','cont','N','C'};
bnd.ind = [1,1,1,1,1,2,3,3,2,3,3,2,3,3,2,3,3,3,2,3,2,2,2,2,2,2,2,2,2, ...
  2,2,3,2,3,2,3,2,2,3,2,3,2,2,3,2,3,2,2,3,2,3,3,1,1,1,2,1,1,1,1,1,1,2,1, ...
  1,4,1,1,1,1];
appl.bnd = bnd;
clear equ
equ.D = {'D',1,'D'};
equ.init = {0,0,'L0'};
equ.usage = {1,0,1};
equ.ind = [1,2,2,2,2,2,2,2,2,2,2,3,2];
appl.equ = equ;
fem.appl{1} = appl;

% Application mode 2
clear appl
appl.mode.class = 'FlPDEWBoundary';
appl.dim = {'R','R_t'};
appl.sshape = 2;
```

```
appl.assignsuffix = '_wb';
clear prop
clear weakconstr
weakconstr.value = 'off';
weakconstr.dim = {'lm2','lm3'};
prop.weakconstr = weakconstr;
appl.prop = prop;
clear bnd
bnd.dweak = {0,'R_test*R_time'};
bnd.init = {0,{'Rint';0}};
bnd.usage = {0,1};
bnd.weak = {0,'DR*(-RTx_test*RTx-RTy_test*RTy-RTz_test*RTz)+R_test*(surf_recept)'};
bnd.ind = [1,1,1,1,1,1,2,2,1,2,2,1,2,2,1,2,2,2,1,2,1,1,1,1,1,1,1,1,1,1, ...
  1,1,2,1,2,1,2,1,1,2,1,2,1,1,2,1,2,1,1,2,1,2,2,1,1,1,1,1,1,1,1,1,1,1, ...
  1,1,1,1,1,1];
appl.bnd = bnd;
fem.appl{2} = appl;

% Application mode 3
clear appl
appl.mode.class = 'FlPDEWBoundary';
appl.dim = {'C','C_t'};
appl.name = 'wb2';
appl.sshape = 2;
appl.assignsuffix = '_wb2';
clear prop
clear weakconstr
weakconstr.value = 'off';
weakconstr.dim = {'lm4','lm5'};
prop.weakconstr = weakconstr;
appl.prop = prop;
clear bnd
bnd.dweak = {0,'C_test*C_time'};
bnd.usage = {0,1};
bnd.weak = {0,'DC*(-CTx_test*CTx-CTy_test*CTy-CTz_test*CTz)+C_test*(surf_comp)'};
bnd.ind = [1,1,1,1,1,1,2,2,1,2,2,1,2,2,1,2,2,2,1,2,1,1,1,1,1,1,1,1,1,1, ...
  1,1,2,1,2,1,2,1,1,2,1,2,1,1,2,1,2,1,1,2,1,2,2,1,1,1,1,1,1,1,1,1,1,1, ...
  1,1,1,1,1,1];
appl.bnd = bnd;
fem.appl{3} = appl;
fem.frame = {'ref'};
fem.border = 1;
fem.outform = 'general';
clear units;
units.basesystem = 'SI';
fem.units = units;

% Boundary settings
clear bnd
bnd.ind = [1,1,1,1,1,1,2,2,1,2,2,1,2,2,1,2,2,2,1,2,1,1,1,1,1,1,1,1,1,1, ...
  1,1,2,1,2,1,2,1,1,2,1,2,1,1,2,1,2,1,1,2,1,2,2,1,1,1,1,1,1,1,1,1,1,1, ...
  1,1,1,1,1,1];
bnd.dim = {'L','R','C'};

% Boundary expressions
bnd.expr = {'surf_recept',{'','-kf*R*L'}, ...
```

```
  'surf_comp',{'','kf*R*L'}};
fem.bnd = bnd;

% ODE Settings
clear ode
clear units;
units.basesystem = 'SI';
ode.units = units;
fem.ode=ode;

% Multiphysics
fem=multiphysics(fem);

% Extend mesh
fem.xmesh=meshextend(fem);

if Conc == 1
% Solve problem
fem.sol=femtime(fem,'symmetric','off', 'solcomp',{'R','C','L'},...
              'outcomp',{'C','R','L'}, 'blocksize','auto', ...
              'tlist',[colon(0,1,Time)], 'rtol',RTol, 'tout','tlist', ...
              'atol',ATol,'linsolver','gmres','prefun','amg');

else
fem.sol=femtime(fem,'init',fem0.sol,'symmetric','off','solcomp',{'R','C','L'}, ...
              'outcomp',{'C','R','L'},'blocksize','auto', ...
              'tlist',[colon(0,1,Time)],'rtol',RTol,'tout','tlist', ...
              'atol',ATol,'linsolver','gmres','prefun','amg');
end

% Save current fem structure for restart purposes
fem0=fem;
```

Modelgap3.m

```
function fem = modelgap3(Time,Conc,fem0)

global kf RDensity C ATol RTol D

if Conc == 1
   Var = 'L0';
else
   Var = 0;
end

% Geometry
g9=block3('0.00050','0.00050','0.00050','base','corner','pos',{'0','0','0'},'axis',{'0','0','1'},'rot','0');
g11=cylinder3('1.0E-5','1.0E-5','pos',{'0.00025','0.00025','0'},'axis',{'0','0','1'},'rot','0');
g15=cylinder3('1e-5','1e-5','pos',{'2.5e-4','2.6e-4','0'},'axis',{'0','0','1'},'rot','0');
g18=cylinder3('1e-5','1e-5','pos',{'2.5e-4','2.4e-4','0'},'axis',{'0','0','1'},'rot','0');
g19=geomcomp({g11,g15,g18},'ns',{'g11','g15','g18'},'sf','g11+g15+g18','face','none','edge','all');

% Constants
fem.const = {'kf',kf, ...
```

```
 'D',D, ...
 'DC','1e-14', ...
 'DR','1e-14', ...
 'L0',C, ...
 'Rint',RDensity};

% Geometry
g3=block3('1.0E-4','4.0E-5','1.0E-5','base','center','pos',{'2.5E-4','2.5E-4','1.5E-5'},'axis',{'0','0','1'},'rot','90');
g10=cylinder3('3.0E-6','1.0E-5','pos',{'2.8E-4','2.5E-4','0.5E-5'},'axis',{'1','0','0'},'rot','0');
g11=cylinder3('3.0E-6','1.0E-5','pos',{'2.7E-4','2.5E-4','0.5e-5'},'axis',{'1','0','0'},'rot','0');
g13=cylinder3('2.5E-6','1.0E-5','pos',{'2.7E-4','2.5E-4','0.5e-5'},'axis',{'1','0','0'},'rot','0');

% Analyzed geometry
clear s
s.objs={g19,g9,g3,g10,g11,g13};
s.name={'BLK3','CO1','BLK2','CYL3','CYL2','CYL1'};
s.tags={'g19','g9','g3','g10','g11','g13'};

fem.draw=struct('s',s);
fem.geom=geomcsg(fem);

% Initialize mesh
fem.mesh=meshinit(fem, ...
                  'hauto',5);

% (Default values are not included)

% Application mode 1
clear appl
appl.mode.class = 'ConvDiff';
appl.dim = {'L'};
appl.module = 'CHEM';
appl.sshape = 2;
appl.border = 'on';
appl.assignsuffix = '_chcd';
clear bnd
bnd.c0 = {0,0,0,Var};
bnd.N = {0,'-kf*L*R',0,0};
bnd.type = {'N0','N','cont','C'};
bnd.ind = [1,1,1,1,1,1,1,1,1,1,2,2,3,3,2,2,3,3,2,2,3,3,3,3,3,3,3,3,3, ...
  2,3,3,3,3,3,3,2,2,2,2,2,1,1,1,1,3,1,1,1,1,1,1,3,1,1,4,1,1,1,1];
appl.bnd = bnd;
clear equ
equ.D = {'D',1,'D'};
equ.init = {0,0,'L0'};
equ.usage = {1,0,1};
equ.ind = [1,2,2,2,2,2,2,2,2,3,2];
appl.equ = equ;
fem.appl{1} = appl;

% Application mode 2
clear appl
appl.mode.class = 'FlPDEWBoundary';
appl.dim = {'R','R_t'};
appl.sshape = 2;
appl.assignsuffix = '_wb';
```

```
clear prop
clear weakconstr
weakconstr.value = 'off';
weakconstr.dim = {'lm2','lm3'};
prop.weakconstr = weakconstr;
appl.prop = prop;
clear bnd
bnd.dweak = {0,'R_test*R_time'};
bnd.init = {0,{'Rint';0}};
bnd.usage = {0,1};
bnd.weak = {0,'DR*(-RTx_test*RTx-RTy_test*RTy-RTz_test*RTz)+R_test*(surf_recept)'};
bnd.ind = [1,1,1,1,1,1,1,1,1,1,2,2,1,1,2,2,1,1,2,2,1,1,1,1,1,1,1,1,1, ...
  2,1,1,1,1,1,1,2,2,2,2,2,1,1,1,1,1,1,1,1,1,1,1,1,1,1,1,1,1,1,1,1,1];
appl.bnd = bnd;
fem.appl{2} = appl;

% Application mode 3
clear appl
appl.mode.class = 'FlPDEWBoundary';
appl.dim = {'C','C_t'};
appl.name = 'wb2';
appl.sshape = 2;
appl.assignsuffix = '_wb2';
clear prop
clear weakconstr
weakconstr.value = 'off';
weakconstr.dim = {'lm4','lm5'};
prop.weakconstr = weakconstr;
appl.prop = prop;
clear bnd
bnd.dweak = {0,'C_test*C_time'};
bnd.usage = {0,1};
bnd.weak = {0,'DC*(-CTx_test*CTx-CTy_test*CTy-CTz_test*CTz)+C_test*(surf_comp)'};
bnd.ind = [1,1,1,1,1,1,1,1,1,1,2,2,1,1,2,2,1,1,2,2,1,1,1,1,1,1,1,1,1, ...
  2,1,1,1,1,1,1,2,2,2,2,2,1,1,1,1,1,1,1,1,1,1,1,1,1,1,1,1,1,1,1,1,1];
appl.bnd = bnd;
fem.appl{3} = appl;
fem.frame = {'ref'};
fem.border = 1;
fem.outform = 'general';
clear units;
units.basesystem = 'SI';
fem.units = units;

% Boundary settings
clear bnd
bnd.ind = [1,1,1,1,1,1,1,1,1,1,2,2,1,1,2,2,1,1,2,2,1,1,1,1,1,1,1,1,1, ...
  2,1,1,1,1,1,1,2,2,2,2,2,1,1,1,1,1,1,1,1,1,1,1,1,1,1,1,1,1,1,1,1,1];
bnd.dim = {'L','R','C'};

% Boundary expressions
bnd.expr = {'surf_recept',{'','-kf*R*L'}, ...
  'surf_comp',{'','kf*R*L'}};
fem.bnd = bnd;

% ODE Settings
```

```
clear ode
clear units;
units.basesystem = 'SI';
ode.units = units;
fem.ode=ode;

% Multiphysics
fem=multiphysics(fem);

% Extend mesh
fem.xmesh=meshextend(fem);

if Conc == 1
% Solve problem
fem.sol=femtime(fem,'symmetric','off', 'solcomp',{'R','C','L'},...
            'outcomp',{'C','R','L'}, 'blocksize','auto', ...
            'tlist',[colon(0,1,Time)], 'rtol',RTol, 'tout','tlist', ...
            'atol',ATol,'linsolver','gmres','prefun','amg');

else
fem.sol=femtime(fem,'init',fem0.sol,'symmetric','off','solcomp',{'R','C','L'}, ...
            'outcomp',{'C','R','L'},'blocksize','auto', ...
            'tlist',[colon(0,1,Time)],'rtol',RTol,'tout','tlist', ...
            'atol',ATol,'linsolver','gmres','prefun','amg');
end

% Save current fem structure for restart purposes
fem0=fem;
```

Modelgap5.m

```
function fem = modelgap5(Time,Conc,fem0)

global kf RDensity C ATol RTol D

if Conc == 1
   Var = 'L0';
else
   Var = 0;
end

% Constants
fem.const = {'kf',kf, ...
 'D',D, ...
 'DC','1e-14', ...
 'DR','1e-14', ...
 'L0',C, ...
 'Rint',RDensity};

% Geometry
g9=block3('0.00050','0.00050','0.00050','base','corner','pos',{'0','0','0'},'axis',{'0','0','1'},'rot','0');
g10=block3('0.00010','5.0E-5','1.0E-5','base','center','pos',{'0.00025','0.00025','2.0E-5'},'axis',{'0','0','1'},'rot','90');
g11=cylinder3('1.0E-5','1.0E-5','pos',{'0.00025','0.00025','0'},'axis',{'0','0','1'},'rot','0');
g15=cylinder3('1e-5','1e-5','pos',{'2.5e-4','2.6e-4','0'},'axis',{'0','0','1'},'rot','0');
```

```
g18=cylinder3('1e-5','1e-5','pos',{'2.5e-4','2.4e-4','0'},'axis',{'0','0','1'},'rot','0');
g19=geomcomp({g11,g15,g18},'ns',{'g11','g15','g18'},'sf','g11+g15+g18','face','none','edge','all');
g3=block3('1.0E-4','4.0E-5','1.0E-5','base','center','pos',{'2.5E-4','2.5E-4','1.5E-5'},'axis',{'0','0','1'},'rot','90');
g10=cylinder3('3.0E-6','1.0E-5','pos',{'2.8E-4','2.5E-4','0.5E-5'},'axis',{'1','0','0'},'rot','0');
g11=cylinder3('3.0E-6','1.0E-5','pos',{'2.7E-4','2.5E-4','0.5e-5'},'axis',{'1','0','0'},'rot','0');
g13=cylinder3('2.5E-6','1.0E-5','pos',{'2.7E-4','2.5E-4','0.5e-5'},'axis',{'1','0','0'},'rot','0');
g14=cylinder3('1e-5','1e-5','pos',{'2.5e-4','2.7e-4','0'},'axis',{'0','0','1'},'rot','0');
g16=cylinder3('1e-5','1e-5','pos',{'2.5e-4','2.3e-4','0'},'axis',{'0','0','1'},'rot','0');
g17=geomcomp({g19,g14,g16},'ns',{'g19','g14','g16'},'sf','g19+g14+g16','face','none','edge','all');

% Analyzed geometry
clear s
s.objs={g9,g3,g10,g11,g13,g17};
s.name={'CO1','BLK2','CYL3','CYL2','CYL1','CO2'};
s.tags={'g9','g3','g10','g11','g13','g17'};

fem.draw=struct('s',s);
fem.geom=geomcsg(fem);

% Initialize mesh
fem.mesh=meshinit(fem, ...
                  'hauto',5);

% (Default values are not included)

% Application mode 1
clear appl
appl.mode.class = 'ConvDiff';
appl.dim = {'L'};
appl.module = 'CHEM';
appl.border = 'on';
appl.assignsuffix = '_chcd';
clear bnd
bnd.c0 = {0,0,0,0,Var};
bnd.N = {0,0,'-kf*L*R','-kf*L*R',0};
bnd.type = {'N0','cont','N','cont','C'};
bnd.ind = [1,1,1,1,1,1,1,1,1,1,1,1,2,2,3,3,2,2,3,3,2,2,3,3,2,2,1,1,2,2, ...
  4,2,2,2,2,2,2,2,2,2,2,2,2,4,2,2,1,4,2,2,2,2,2,2,2,2,2,2,2,2,4,1,1,3,3, ...
  3,3,3,3,1,1,1,1,1,2,1,1,1,1,1,1,2,1,1,5,1,1,1,1];
appl.bnd = bnd;
clear equ
equ.D = {'D',1,'D'};
equ.init = {0,0,'L0'};
equ.usage = {1,0,1};
equ.ind = [1,2,2,2,2,2,2,2,2,2,2,2,2,2,2,3,2];
appl.equ = equ;
fem.appl{1} = appl;

% Application mode 2
clear appl
appl.mode.class = 'FlPDEWBoundary';
appl.dim = {'R','R_t'};
appl.sshape = 2;
appl.assignsuffix = '_wb';
clear prop
clear weakconstr
```

```
weakconstr.value = 'off';
weakconstr.dim = {'lm2','lm3'};
prop.weakconstr = weakconstr;
appl.prop = prop;
clear bnd
bnd.dweak = {0,'R_test*R_time','R_test*R_time'};
bnd.init = {0,{'Rint';0},{'Rint';0}};
bnd.usage = {0,1,0};
bnd.weak = {0,'DR*(-RTx_test*RTx-RTy_test*RTy-RTz_test*RTz)+R_test*(surf_recept)', ...
 'DR*(-RTx_test*RTx-RTy_test*RTy-RTz_test*RTz)+R_test*(surf_recept)'};
bnd.ind = [1,1,1,1,1,1,1,1,1,1,2,2,1,1,2,2,1,1,2,2,1,1,2,2,1,1,2,2,1,1, ...
  3,1,1,1,1,1,1,1,1,1,1,1,1,3,1,1,2,3,1,1,1,1,1,1,1,1,1,1,1,3,2,2,2,2, ...
  2,2,2,2,2,1,1,1,1,1,1,1,1,1,1,1,1,1,1,1,1,1,1,1,1,1,1,1,1,1];
appl.bnd = bnd;
fem.appl{2} = appl;

% Application mode 3
clear appl
appl.mode.class = 'FlPDEWBoundary';
appl.dim = {'C','C_t'};
appl.name = 'wb2';
appl.sshape = 2;
appl.assignsuffix = '_wb2';
clear prop
clear weakconstr
weakconstr.value = 'off';
weakconstr.dim = {'lm4','lm5'};
prop.weakconstr = weakconstr;
appl.prop = prop;
clear bnd
bnd.dweak = {0,'C_test*C_time','C_test*C_time'};
bnd.usage = {0,1,0};
bnd.weak = {0,'DC*(-CTx_test*CTx-CTy_test*CTy-CTz_test*CTz)+C_test*(surf_comp)', ...
 'DC*(-CTx_test*CTx-CTy_test*CTy-CTz_test*CTz)+C_test*(surf_comp)'};
bnd.ind = [1,1,1,1,1,1,1,1,1,1,2,2,1,1,2,2,1,1,2,2,1,1,2,2,1,1,2,2,1,1, ...
  3,1,1,1,1,1,1,1,1,1,1,1,1,3,1,1,2,3,1,1,1,1,1,1,1,1,1,1,1,3,2,2,2,2, ...
  2,2,2,2,2,1,1,1,1,1,1,1,1,1,1,1,1,1,1,1,1,1,1,1,1,1,1,1,1,1];
appl.bnd = bnd;
fem.appl{3} = appl;
fem.frame = {'ref'};
fem.border = 1;
fem.outform = 'general';
clear units;
units.basesystem = 'SI';
fem.units = units;

% Boundary settings
clear bnd
bnd.ind = [1,1,1,1,1,1,1,1,1,1,2,2,1,1,2,2,1,1,2,2,1,1,2,2,1,1,2,2,1,1, ...
  1,1,1,1,1,1,1,1,1,1,1,1,1,1,1,1,1,1,2,1,1,1,1,1,1,1,1,1,1,1,2,2,2,2, ...
  2,2,2,2,2,1,1,1,1,1,1,1,1,1,1,1,1,1,1,1,1,1,1,1,1,1,1,1,1,1];
bnd.dim = {'L','R','C'};

% Boundary expressions
bnd.expr = {'surf_recept',{'','-kf*R*L'}, ...
 'surf_comp',{'','kf*R*L'}};
```

```
fem.bnd = bnd;

% ODE Settings
clear ode
clear units;
units.basesystem = 'SI';
ode.units = units;
fem.ode=ode;

% Multiphysics
fem=multiphysics(fem);

% Extend mesh
fem.xmesh=meshextend(fem);

if Conc == 1
% Solve problem
fem.sol=femtime(fem,'symmetric','off', 'solcomp',{'R','C','L'},...
            'outcomp',{'C','R','L'}, 'blocksize','auto', ...
            'tlist',[colon(0,1,Time)], 'rtol',RTol, 'tout','tlist', ...
            'atol',ATol,'linsolver','gmres','prefun','amg');

else
fem.sol=femtime(fem,'init',fem0.sol,'symmetric','off','solcomp',{'R','C','L'}, ...
            'outcomp',{'C','R','L'},'blocksize','auto', ...
            'tlist',[colon(0,1,Time)],'rtol',RTol,'tout','tlist', ...
            'atol',ATol,'linsolver','gmres','prefun','amg');
end

% Save current fem structure for restart purposes
fem0=fem;
```

Adhe3cellstart.m

```
clear global
clear
clc

global D kf RDensity C ATol RTol Rreal AvangadroNumber

CellSurfaceArea = 4*1.23903e-10;
ReceptorN = 47362; %Receptors
kf = 1.3627e5; %Forward Constant - m^3/mol*s
AvangadroNumber = 6.02e23;
EGFMolarMass = 6045; %g/mol
D = 1.89e-10;
Concentration = 100;

RDensity = ReceptorN/(2*pi*12.599e-6^2*6.02e23);
Rreal = 47362/(2*pi*12.599e-6^2)*4*1.23903e-10;
C = Concentration/EGFMolarMass/1e3;

%Solution Parameters
Time = 1200;
```

```
RTol = 1e-12;
ATol = 1e-12;

fem = modeladh3(120,1,0);
fem0=fem;

for k = 1:120
  Result = adhint3(k,fem);
  PIResult(k) = Result(1);
  POFront(k) = Result(2);
  POBack(k) = Result(3);
end

fem = modeladh3(1200-120,2,fem0);

for k = 1:1200-120
  Result = adhint3(k,fem);
  PIResult(k+120) = Result(1);
  POFront(k+120) = Result(2);
  POBack(k+120) = Result(3);
end

xlswrite('PIResultAdh3.xls',PIResult')
xlswrite('POFrontAdh3.xls',POFront')
xlswrite('POBackAdh3.xls',POBack')

plot((1:1200)/60,POFront','k-',(1:1200)/60,POBack','b-',(1:1200)/60,POFront'-POBack','g-','LineWidth',2)
grid on
set(gca,'FontSize',18,'LineWidth',2)
xlabel('Time [min]','FontSize',18)
ylabel('Percent Occupancy','FontSize',18)
title('PO_F_r_o_n_t and PO_B_a_c_k for Adherent 3 cell system','FontSize',18)
axis([0 20 0 100])
%legend('PO_F_r_o_n_t','PO_B_a_c_k','Difference PO_F_r_o_n_t and PO_B_a_c_k','Location','SouthOutside')
print -dtiff -r600 Adh3cellPO.tif
```

Adh5cellstart.m

```
clear
clc
close all

CellSurfaceArea = 2*1.239026e-10;
ReceptorN = 47362; %Receptors
kf = 1.3627e5; %Forward Constant - m^3/mol*s
AvangadroNumber = 6.02e23;
EGFMolarMass = 6045; %g/mol
D = 1.89e-10;
Concentration = 100;

RDensity = ReceptorN/(4*1.239026e-10*6.023e23);
Rreal = 47362/(2*pi*12.599e-6^2)*4*1.23903e-10;
C = Concentration/EGFMolarMass/1e3;

%Solution Parameters
```

```
Time = 1200;
RTol = 1e-12;
ATol = 1e-12;

fem = modeladh5(120,1,0);
fem0=fem;

for k = 1:120
  Result = adhint5(k,fem);
  PIResult(k) = Result(1);
  POFront(k) = Result(2);
  POBack(k) = Result(3);
end

fem = modeladh5(1200-120,2,fem0);

for k = 1:1200-120
  Result = adhint5(k,fem);
  PIResult(k+120) = Result(1);
  POFront(k+120) = Result(2);
  POBack(k+120) = Result(3);
end

xlswrite('PIResultAdh5.xls',PIResult')
xlswrite('POFrontAdh5.xls',POFront')
xlswrite('POBackAdh5.xls',POBack')

plot((1:1200)/60,POFront','k-',(1:1200)/60,POBack','b-',(1:1200)/60,POFront'-POBack','g-','LineWidth',2)
grid on
set(gca,'FontSize',18,'LineWidth',2)
xlabel('Time [min]','FontSize',18)
ylabel('Percent Occupancy','FontSize',18)
title('PO_F_r_o_n_t and PO_B_a_c_k for Adherent 5 cell system','FontSize',18)
axis([0 20 0 100])
%legend('PO_F_r_o_n_t','PO_B_a_c_k','Difference PO_F_r_o_n_t and PO_B_a_c_k','Location','SouthOutside')
print -dtiff -r600 Adh5cellPO.tif
```

Gap3cellstart.m

```
clear global
clear
clc

global D kf RDensity C ATol RTol Rreal AvangadroNumber

CellSurfaceArea = 4*5.221057e-11;
ReceptorN = 47362; %Receptors
kf = 1.3627e5; %Forward Constant - m^3/mol*s
AvangadroNumber = 6.02e23;
EGFMolarMass = 6045; %g/mol
D = 1.89e-10;
Concentration = 100;

RDensity = ReceptorN/(AvangadroNumber*(2*pi*11.547e-6*10e-6));
```

```
Rreal = 47362/(2*pi*11.547e-6*10e-6)*4*5.221057e-11;
C = Concentration/EGFMolarMass/1e3;

%Solution Parameters
Time = 1200;
RTol = 1e-12;
ATol = 1e-12;

fem = modelgap3(120,1,0);
fem0=fem;

for k = 1:120
  Result = gapint3(k,fem);
  PIResult(k) = Result(1);
  POFront(k) = Result(2);
  POBack(k) = Result(3);
end

fem = modelgap3(1200-120,2,fem0);

for k = 1:1200-120
  Result = gapint3(k,fem);
  PIResult(k+120) = Result(1);
  POFront(k+120) = Result(2);
  POBack(k+120) = Result(3);
end

xlswrite('PIResultGap3.xls',PIResult')
xlswrite('POFrontGap3.xls',POFront')
xlswrite('POBackGap3.xls',POBack')

plot((1:1200)/60,POFront','k-',(1:1200)/60,POBack','b-',(1:1200)/60,POFront'-POBack','g-','LineWidth',2)
grid on
set(gca,'FontSize',18,'LineWidth',2)
xlabel('Time [min]','FontSize',18)
ylabel('Percent Occupancy','FontSize',18)
title('PO_F_r_o_n_t and PO_B_a_c_k for Gap 3 cell system','FontSize',18)
axis([0 20 0 100])
%legend('PO_F_r_o_n_t','PO_B_a_c_k','Difference PO_F_r_o_n_t and PO_B_a_c_k','Location','SouthOutside')
print -dtiff -r600 Gap3cellPO.tif
```

Gap5cellstart.m

```
clear global
clear
clc

global D kf RDensity C ATol RTol Rreal AvangadroNumber

CellSurfaceArea = 4*5.221057e-11;
ReceptorN = 47362; %Receptors
kf = 1.3627e5; %Forward Constant - m^3/mol*s
AvangadroNumber = 6.02e23;
EGFMolarMass = 6045; %g/mol
```

```
D = 1.89e-10;
Concentration = 100;

RDensity = ReceptorN/(AvangadroNumber*(2*pi*11.547e-6*10e-6));
Rreal = 47362/(2*pi*11.547e-6*10e-6)*4*5.221057e-11;
C = Concentration/EGFMolarMass/1e3;

%Solution Parameters
Time = 1200;
RTol = 1e-12;
ATol = 1e-12;

fem = modelgap5(120,1,0);
fem0=fem;

for k = 1:120
  Result = gapint5(k,fem);
  PIResult(k) = Result(1);
  POFront(k) = Result(2);
  POBack(k) = Result(3);
end

fem = modelgap5(1200-120,2,fem0);

for k = 1:1200-120
  Result = gapint5(k,fem);
  PIResult(k+120) = Result(1);
  POFront(k+120) = Result(2);
  POBack(k+120) = Result(3);
end

xlswrite('PIResultGap5.xls',PIResult')
xlswrite('POFrontGap5.xls',POFront')
xlswrite('POBackGap5.xls',POBack')

plot((1:1200)/60,POFront','k-',(1:1200)/60,POBack','b-',(1:1200)/60,POFront'-POBack','g-','LineWidth',2)
grid on
set(gca,'FontSize',18,'LineWidth',2)
xlabel('Time [min]','FontSize',18)
ylabel('Percent Occupancy','FontSize',18)
title('PO_F_r_o_n_t and PO_B_a_c_k for Gap 5 cell system','FontSize',18)
axis([0 20 0 100])
%legend('PO_F_r_o_n_t','PO_B_a_c_k','Difference PO_F_r_o_n_t and PO_B_a_c_k','Location','SouthOutside')
print -dtiff -r600 Gap5cellPO.tif
```

Adhint3.m

```
function Result = adhint3(k,fem)

global Rreal AvangadroNumber

TimePoints = linspace(0,1200,1200);
```

```
 try
% Integrate - Back Half
I1=postint(fem,'C', 'unit','', 'recover','off', 'dl',[10,11], ...
        'edim',2, 'solnum',TimePoints(k));

% Integrate
I2=postint(fem,'C', 'unit','', 'recover','off', ...
        'dl',[25,28], 'edim',2, 'solnum',TimePoints(k));

% Integrate
I3=postint(fem,'R', 'unit','', 'recover','off', ...
        'dl',[10,11], 'edim',2, 'solnum',TimePoints(k));

% Integrate
I4=postint(fem,'R', 'unit','', 'recover','off', ...
        'dl',[25,28], 'edim',2, 'solnum',TimePoints(k));

PI = I1/I2;
POFront = (1-I4/(0.5*Rreal/AvangadroNumber))*100;
POBack = (1-I3/(0.5*Rreal/AvangadroNumber))*100;

catch exception
   PI = NaN;
   POFront = NaN;
   POBack = NaN;
end

Result = [PI POFront POBack];
```

Adhint5.m

```
function Result = adhint5(k,fem)

global Rreal AvangadroNumber

TimePoints = linspace(0,1200,1200);

 try
% Integrate - Back Half
I1=postint(fem,'C', 'unit','', 'recover','off', 'dl',[13,14], ...
        'edim',2, 'solnum',TimePoints(k));

% Integrate
I2=postint(fem,'C', 'unit','', 'recover','off', ...
        'dl',[42,45], 'edim',2, 'solnum',TimePoints(k));

% Integrate
I3=postint(fem,'R', 'unit','', 'recover','off', ...
        'dl',[13,14], 'edim',2, 'solnum',TimePoints(k));

% Integrate
I4=postint(fem,'R', 'unit','', 'recover','off', ...
        'dl',[42,45], 'edim',2, 'solnum',TimePoints(k));
```

```
PI = I1/I2;
POFront = (1-I4/(0.5*Rreal/AvangadroNumber))*100;
POBack = (1-I3/(0.5*Rreal/AvangadroNumber))*100;

catch exception
   PI = NaN;
   POFront = NaN;
   POBack = NaN;
end

Result = [PI POFront POBack];
```

Gapint3.m

```
function Result = gapint3(k,fem)

global Rreal AvangadroNumber

TimePoints = linspace(0,1200,1200);

 try
% Integrate - Back Half
I1=postint(fem,'C', 'unit','', 'recover','off', 'dl',[15,16], ...
        'edim',2, 'solnum',TimePoints(k));

% Integrate
I2=postint(fem,'C', 'unit','', 'recover','off', ...
        'dl',[40,41], 'edim',2, 'solnum',TimePoints(k));

% Integrate
I3=postint(fem,'R', 'unit','', 'recover','off', ...
        'dl',[15,16], 'edim',2, 'solnum',TimePoints(k));

% Integrate
I4=postint(fem,'R', 'unit','', 'recover','off', ...
        'dl',[40,41], 'edim',2, 'solnum',TimePoints(k));

PI = I1/I2;
POFront = (1-I4/(0.5*Rreal/AvangadroNumber))*100;
POBack = (1-I3/(0.5*Rreal/AvangadroNumber))*100;

catch exception
   PI = NaN;
   POFront = NaN;
   POBack = NaN;
end

Result = [PI POFront POBack];
```

Gapint5.m

```
function Result = gapint5(k,fem)
```

```
global Rreal AvangadroNumber

TimePoints = linspace(0,1200,1200);

 try
% Integrate - Back Half
I1=postint(fem,'C', 'unit','', 'recover','off', 'dl',[19,20], ...
        'edim',2, 'solnum',TimePoints(k));

% Integrate
I2=postint(fem,'C', 'unit','', 'recover','off', ...
        'dl',[66,67], 'edim',2, 'solnum',TimePoints(k));

% Integrate
I3=postint(fem,'R', 'unit','', 'recover','off', ...
        'dl',[19,20], 'edim',2, 'solnum',TimePoints(k));

% Integrate
I4=postint(fem,'R', 'unit','', 'recover','off', ...
        'dl',[66,67], 'edim',2, 'solnum',TimePoints(k));

PI = I1/I2;
POFront = (1-I4/(0.5*Rreal/AvangadroNumber))*100;
POBack = (1-I3/(0.5*Rreal/AvangadroNumber))*100;

catch exception
   PI = NaN;
   POFront = NaN;
   POBack = NaN;
end

Result = [PI POFront POBack];
```

Generateplot.m

```
close all
clear

Adh1 = 1./xlsread('AdhPI.xls','1','A1:A1200');
Adh3 = 1./xlsread('PIResultAdh3.xls','Sheet1','A1:A1200');
Adh5 = 1./xlsread('PIResultAdh5.xls','Sheet1','A1:A1200');
Gap1 = xlsread('GapPI.xls','1','A1:A1200');
Gap3 = 1./xlsread('PIResultGap3.xls','Sheet1','A1:A1200');
Gap5 = 1./xlsread('PIResultGap5.xls','Sheet1','A1:A1200');

Time = 1:1198;
Time = Time/60;

figure
plot(Time,Adh1,'k-','LineWidth',2)
hold on
plot(Time,Adh3,'b-','LineWidth',2)
plot(Time,Adh5,'g-','LineWidth',2)
grid on
```

```
set(gca,'FontSize',18,'LineWidth',2)
axis([0 20 1 10])
xlabel('Time [min]','FontSize',18)
ylabel('Polarization Index','FontSize',18)
title('Multiple Cell Systems for PI - Adherent','FontSize',18)
legend('1 Cell','3 Cells','5 Cells','Location','NorthWest')
print -dtiff -r600 TorAllAdhPI.tif

figure
plot(Time,Gap1,'k-','LineWidth',2)
hold on
plot(Time,Gap3,'b-','LineWidth',2)
plot(Time,Gap5,'g-','LineWidth',2)
grid on
set(gca,'FontSize',18,'LineWidth',2)
axis([0 20 1 10])
xlabel('Time [min]','FontSize',18)
ylabel('Polarization Index','FontSize',18)
title('Multiple Cell Systems for PI - Gap','FontSize',18)
legend('1 Cell','3 Cells','5 Cells','Location','NorthEast')
print -dtiff -r600 TorAllGapPI.tif
```

Model Correlation with Experimental Data

Modelellips.m

```
function fem = modelellips(Time,Conc,fem0)

global kf RDensity C ATol RTol D

if Conc == 1
   Var = 'L0';
else
   Var = 0;
end

% Geometry
g4=block3('5.0E-4','5.0E-4','5.0E-4','base','center','pos',{'0','0','0'},'axis',{'0','0','1'},'rot','0');
g6=block3('2.0E-4','2.0E-4','1.0E-5','base','center','pos',{'0','0','-2.45E-4'},'axis',{'0','0','1'},'rot','0');
g7=ellipsoid3('25e-6','54e-6','50e-6','pos',{'0','0','-2.45e-4'},'axis',{'0','0','1'},'rot','0');
g8=geomcomp({g6,g7},'ns',{'g6','g7'},'sf','g6*g7','face','none','edge','all');
g13=block3('2*1.125E-4','2.0E-4','1.0E-5','base','center','pos',{'0','0','-2.35E-4'},'axis',{'0','0','1'},'rot','0');
g17=cylinder3('5.5E-6','1.0E-5','pos',{'1.15E-4','0','-2.4E-4'},'axis',{'1','0','0'},'rot','0');
g18=cylinder3('4.5E-6','1.0E-5','pos',{'1.15E-4','0','-2.4E-4'},'axis',{'1','0','0'},'rot','0');
g19=cylinder3('5.5e-6','1e-5','pos',{'1.25e-4','0','-2.4e-4'},'axis',{'1','0','0'},'rot','0');

% Constants
fem.const = {'D',D, ...
  'kf',kf, ...
  'DC','1e-14', ...
  'DR','1e-14', ...
  'L0',C', ...
```

```
 'Rint',RDensity};

% Geometry

% Analyzed geometry
clear s
s.objs={g4,g8,g13,g17,g18,g19};
s.name={'Block','CO1','BLK1','CYL2','CYL1','CYL3'};
s.tags={'g4','g8','g13','g17','g18','g19'};

fem.draw=struct('s',s);
fem.geom=geomcsg(fem);

% COMSOL Multiphysics Model M-file
% Generated by COMSOL 3.5a (COMSOL 3.5.0.603, $Date: 2008/12/03 17:02:19 $)

% Initialize mesh
fem.mesh=meshinit(fem, ...
                  'hauto',5);

% (Default values are not included)

% Application mode 1
clear appl
appl.mode.class = 'ConvDiff';
appl.dim = {'L'};
appl.module = 'CHEM';
appl.border = 'on';
appl.assignsuffix = '_chcd';
clear bnd
bnd.c0 = {0,0,0,Var};
bnd.N = {0,0,'-kf*L*R',0};
bnd.type = {'N0','cont','N','C'};
bnd.ind = [1,1,1,1,1,1,1,1,1,1,3,3,3,3,2,2,3,3,3,3,1,1,1,1,2,1,1,1,1,1, ...
  1,2,1,1,4,1,1,1,1];
appl.bnd = bnd;
clear equ
equ.D = {'D',1,'D'};
equ.init = {0,0,'L0'};
equ.usage = {1,0,1};
equ.ind = [1,2,2,2,3,2];
appl.equ = equ;
fem.appl{1} = appl;

% Application mode 2
clear appl
appl.mode.class = 'FlPDEWBoundary';
appl.dim = {'R','R_t'};
appl.assignsuffix = '_wb';
clear prop
clear weakconstr
weakconstr.value = 'off';
weakconstr.dim = {'lm2','lm3'};
prop.weakconstr = weakconstr;
appl.prop = prop;
clear bnd
```

```
bnd.dweak = {0,'R_test*R_time'};
bnd.init = {0,{'Rint';0}};
bnd.usage = {0,1};
bnd.weak = {0,'DR*(-RTx_test*RTx-RTy_test*RTy-RTz_test*RTz)+R_test*(surf_recept)'};
bnd.ind = [1,1,1,1,1,1,1,1,1,1,2,2,2,2,2,1,1,2,2,2,2,2,1,1,1,1,1,1,1,1,1,1,1,1, ...
  1,1,1,1,1,1,1,1,1,1];
appl.bnd = bnd;
fem.appl{2} = appl;

% Application mode 3
clear appl
appl.mode.class = 'FlPDEWBoundary';
appl.dim = {'C','C_t'};
appl.name = 'wb2';
appl.assignsuffix = '_wb2';
clear prop
clear weakconstr
weakconstr.value = 'off';
weakconstr.dim = {'lm4','lm5'};
prop.weakconstr = weakconstr;
appl.prop = prop;
clear bnd
bnd.dweak = {0,'C_test*C_time'};
bnd.usage = {0,1};
bnd.weak = {0,'DC*(-CTx_test*CTx-CTy_test*CTy-CTz_test*CTz)+C_test*(surf_comp)'};
bnd.ind = [1,1,1,1,1,1,1,1,1,1,2,2,2,2,2,1,1,2,2,2,2,2,1,1,1,1,1,1,1,1,1,1,1,1, ...
  1,1,1,1,1,1,1,1,1,1];
appl.bnd = bnd;
fem.appl{3} = appl;
fem.frame = {'ref'};
fem.border = 1;
fem.outform = 'general';
clear units;
units.basesystem = 'SI';
fem.units = units;

% Boundary settings
clear bnd
bnd.ind = [1,1,1,1,1,1,1,1,1,1,2,2,2,2,2,1,1,2,2,2,2,2,1,1,1,1,1,1,1,1,1,1,1,1, ...
  1,1,1,1,1,1,1,1,1,1];
bnd.dim = {'L','R','C'};

% Boundary expressions
bnd.expr = {'surf_recept',{'','-kf*R*L'}, ...
  'surf_comp',{'','kf*R*L'}};
fem.bnd = bnd;

% ODE Settings
clear ode
clear units;
units.basesystem = 'SI';
ode.units = units;
fem.ode=ode;

% Multiphysics
fem=multiphysics(fem);
```

```
% Extend mesh
fem.xmesh=meshextend(fem);

if Conc == 1
% Solve problem
fem.sol=femtime(fem, 'symmetric','off', 'solcomp',{'C','R','L'}, ...
            'outcomp',{'R','C','L'}, 'blocksize','auto', ...
            'tlist',[colon(0,1,Time)], 'rtol',RTol, ...
            'tout','tlist', 'atol',ATol, 'linsolver','gmres', ...
            'prefun','amg');

else
fem.sol=femtime(fem,'init',fem0.sol,'symmetric','off','solcomp',{'R','C','L'}, ...
            'outcomp',{'C','R','L'},'blocksize','auto', ...
            'tlist',[colon(0,1,Time)],'rtol',RTol,'tout','tlist', ...
            'atol',ATol,'linsolver','gmres','prefun','amg');
end

% Save current fem structure for restart purposes
fem0=fem;
```

Modelhellips.m

```
function fem = modelhellips(Time,Conc,fem0)

global kf RDensity C ATol RTol D

if Conc == 1
   Var = 'L0';
else
   Var = 0;
end

% Geometry
g7=ellipsoid3('2.934E-5','6.6E-5','1e-4','pos',{'2.5e-4','2.5e-4','0'},'axis',{'0','0','1'},'rot','0');
g9=block3('5.0E-4','5.0E-4','1e-5','base','corner','pos',{'0','0','0'},'axis',{'0','0','1'},'rot','0');
g10=geomcomp({g7,g9},'ns',{'g7','g9'},'sf','g7*g9','face','none','edge','all');
g12=block3('2.5e-4','5e-4','1e-5','base','corner','pos',{'0','0','0'},'axis',{'0','0','1'},'rot','0');
g15=geomcomp({g10,g12},'ns',{'g10','g12'},'sf','g10*g12','face','none','edge','all');
g17=block3('5e-4','5e-4','5e-4','base','corner','pos',{'0','0','0'},'axis',{'0','0','1'},'rot','0');
g27=cylinder3('3.0E-6','1.0E-5','pos',{'3.1E-4','2.55E-4','5.0E-6'},'axis',{'1','0','0'},'rot','0');
g28=cylinder3('2.5E-6','1.0E-5','pos',{'3.1E-4','2.55E-4','5.0E-6'},'axis',{'1','0','0'},'rot','0');
g30=cylinder3('3e-6','1e-5','pos',{'3.2e-4','2.55e-4','5e-6'},'axis',{'1','0','0'},'rot','0');

% Constants
fem.const = {'Rint',RDensity, ...
  'L0',C, ...
  'kf',kf, ...
  'DC','1e-14', ...
  'DR','1e-14', ...
  'D',D};

% Geometry
```

```
g4=block3('1e-4','2e-4','1e-5','base','center','pos',{'2.5e-4-6e-6','2.5e-4','1.5e-5'},'axis',{'0','0','1'},'rot','0');
g5=geomcomp({g15,g4},'ns',{'g15','g4'},'sf','g15+g4','face','none','edge','all');

% Analyzed geometry
clear s
s.objs={g17,g27,g28,g30,g5};
s.name={'BLK2','CO2','CYL1','CYL2','CO1'};
s.tags={'g17','g27','g28','g30','g5'};

fem.draw=struct('s',s);
fem.geom=geomcsg(fem);

% COMSOL Multiphysics Model M-file
% Generated by COMSOL 3.5a (COMSOL 3.5.0.603, $Date: 2008/12/03 17:02:19 $)

% Initialize mesh
fem.mesh=meshinit(fem, ...
                  'hauto',5);

% (Default values are not included)

% Application mode 1
clear appl
appl.mode.class = 'ConvDiff';
appl.dim = {'L'};
appl.module = 'CHEM';
appl.assignsuffix = '_chcd';
clear bnd
bnd.c0 = {0,0,0,'L0'};
bnd.N = {0,0,'-kf*L*R',0};
bnd.type = {'N0','cont','N','C'};
bnd.ind = [1,1,1,1,1,1,1,1,1,1,3,3,2,2,3,1,1,1,1,2,1,1,1,1,1,1,2,1,1,4, ...
  1,1,1,1];
appl.bnd = bnd;
clear equ
equ.D = {'D',1,'D'};
equ.init = {0,0,'L0'};
equ.usage = {1,0,1};
equ.ind = [1,2,2,2,3,2];
appl.equ = equ;
fem.appl{1} = appl;

% Application mode 2
clear appl
appl.mode.class = 'FlPDEWBoundary';
appl.dim = {'R','R_t'};
appl.assignsuffix = '_wb';
clear prop
clear weakconstr
weakconstr.value = 'off';
weakconstr.dim = {'lm2','lm3'};
prop.weakconstr = weakconstr;
appl.prop = prop;
clear bnd
bnd.dweak = {0,'R_test*R_time'};
bnd.init = {0,{'Rint';0}};
```

```
bnd.usage = {0,1};
bnd.weak = {0,'DR*(-RTx_test*RTx-RTy_test*RTy-RTz_test*RTz)+R_test*(surf_recept)'};
bnd.ind = [1,1,1,1,1,1,1,1,1,1,2,2,1,1,2,1,1,1,1,1,1,1,1,1,1,1,1,1,1,1, ...
  1,1,1,1];
appl.bnd = bnd;
fem.appl{2} = appl;

% Application mode 3
clear appl
appl.mode.class = 'FlPDEWBoundary';
appl.dim = {'C','C_t'};
appl.name = 'wb2';
appl.assignsuffix = '_wb2';
clear prop
clear weakconstr
weakconstr.value = 'off';
weakconstr.dim = {'lm4','lm5'};
prop.weakconstr = weakconstr;
appl.prop = prop;
clear bnd
bnd.dweak = {0,'C_test*C_time'};
bnd.usage = {0,1};
bnd.weak = {0,'DC*(-CTx_test*CTx-CTy_test*CTy-CTz_test*CTz)+C_test*(surf_comp)'};
bnd.ind = [1,1,1,1,1,1,1,1,1,1,2,2,1,1,2,1,1,1,1,1,1,1,1,1,1,1,1,1,1,1, ...
  1,1,1,1];
appl.bnd = bnd;
fem.appl{3} = appl;
fem.frame = {'ref'};
fem.border = 1;
fem.outform = 'general';
clear units;
units.basesystem = 'SI';
fem.units = units;

% Boundary settings
clear bnd
bnd.ind = [1,1,1,1,1,1,1,1,1,1,2,2,1,1,2,1,1,1,1,1,1,1,1,1,1,1,1,1,1,1, ...
  1,1,1,1];
bnd.dim = {'L','R','C'};

% Boundary expressions
bnd.expr = {'surf_recept',{'','-kf*R*L'}, ...
  'surf_comp',{'','kf*R*L'}};
fem.bnd = bnd;

% ODE Settings
clear ode
clear units;
units.basesystem = 'SI';
ode.units = units;
fem.ode=ode;

% Multiphysics
fem=multiphysics(fem);

% Extend mesh
```

```
fem.xmesh=meshextend(fem);

if Conc == 1
% Solve problem
fem.sol=femtime(fem, 'symmetric','off', 'solcomp',{'C','R','L'}, ...
            'outcomp',{'R','C','L'}, 'blocksize','auto', ...
            'tlist',[colon(0,1,Time)], 'rtol',RTol, ...
            'tout','tlist', 'atol',ATol, 'linsolver','gmres', ...
            'prefun','amg');

else
fem.sol=femtime(fem,'init',fem0.sol,'symmetric','off','solcomp',{'R','C','L'}, ...
            'outcomp',{'C','R','L'},'blocksize','auto', ...
            'tlist',[colon(0,1,Time)],'rtol',RTol,'tout','tlist', ...
            'atol',ATol,'linsolver','gmres','prefun','amg');
end

% Save current fem structure for restart purposes
fem0=fem;
```

Ellipsint.m

```
function Result = ellipsint(k,fem)

global RDensity CellSurfaceArea

TimePoints = linspace(0,1200,1200);

 try
% Integrate - Back Half
I1=postint(fem,'C', 'unit','','recover','off', 'dl',[11,12,13,14], ...
        'edim',2, 'solnum',TimePoints(k));

% Integrate - Front Half
I2=postint(fem,'C', 'unit','', 'recover','off', 'dl',[17,18,19,20], ...
        'edim',2, 'solnum',TimePoints(k));

% Integrate - R
I3=postint(fem,'R', 'unit','', 'recover','off', ...
        'dl',[11,12,13,14,17,18,19,20], 'edim',2, 'solnum',k);

PIResult = I1/I2;
POResult = (1-I3/(CellSurfaceArea*RDensity))*100;

catch exception
   PIResult(k) = NaN;
   POResult(k) = NaN;
 end

Result = [PIResult POResult];
```

Hellipsint.m

```
function Result = hellipsint(k,fem)

global RDensity CellSurfaceArea

TimePoints = linspace(0,1200,1200);

 try
% Integrate - Back Half
I1=postint(fem,'C', 'unit','','recover','off', 'dl',[11,12], ...
        'edim',2, 'solnum',TimePoints(k));

% Integrate - Front Half
I2=postint(fem,'C', 'unit','', 'recover','off', 'dl',[15], ...
        'edim',2, 'solnum',TimePoints(k));

% Integrate - R
I3=postint(fem,'R', 'unit','', 'recover','off', ...
        'dl',[11,12,15], 'edim',2, 'solnum',TimePoints(k));

PIResult = I1/I2;
POResult = (1-I3/(CellSurfaceArea*RDensity))*100;

catch exception
   PIResult(k) = NaN;
   POResult(k) = NaN;
end

Result = [PIResult POResult];
```

Ellipsoidfit_start.m

```
EGFMolarMass = 6045; %g/mol
ReceptorN = 47362; %Receptors
kf = 1.3627e5; %Forward Constant - m^3/mol*s

%Input of Ranges
TimePoints = linspace(0,1200,1200);

%Solution Parameters
Time = 1200;
RTol = 1e-12;
ATol = 1e-12;

%Calculation of Specific Values
RDensity = ReceptorN/(AvangadroNumber*4*pi*10e-6*10e-6);
C = Concentration/EGFMolarMass/1e3;
D = 1.89e-10;

fem = modelellips(120,1,0);
fem0=fem;

for k = 1:120
  Result = ellipsint(k,fem);
  PIResult(k) = Result(1);
```

```
  POResult(k) = Result(2);
end

fem = modelellips(1200-120,2,fem0);

for k = 1:1200-120
  Result = ellipsint(k,fem);
  PIResult(k+120) = Result(1);
  POResult(k+120) = Result(2);
end

xlswrite('PIResultEllipse.xls',PIResult')
xlswrite('POResultEllipse.xls',POResult')

TimePoints = linspace(1,1200,1200);
Time = [0,2,5,8,11,14,20]*60;
PIExp = [3.442785033, 4.15, 2.78, 2.54, 2.61, 2.77, 2.90];
STDEV = [0.193576522, 0.979198528, 0.230039059, 0.18080547, 0.165642449, ...
    0.207771094, 0.202797271];
ErrorL = PIExp - 2*STDEV;
ErrorU = PIExp + 2*STDEV;

errorbar((Time+60)/60,PIExp',2*STDEV,'kx','LineWidth',2)
hold on
plot(TimePoints/60,1./PIResult,'k-','LineWidth',2)
axis([0 20 1 15])
grid on
set(gca,'FontSize',18,'LineWidth',2)
xlabel('Time [min]','FontSize',18)
ylabel('Polarization Index','FontSize',18)
title('Model Fit to a Single Cell System','FontSize',18)
legend('Experimental Data','Model Prediction','Location','NorthEast')
print -dtiff -r600 DataFit.tif
```

Halfellipsoidfit_start.m

```
close all
clear global
clear
clc

global kf RDensity C ATol RTol D

%Input of Constants
CellRadius = 1.1547e-005; %m
AvangadroNumber = 6.02e23;
Concentration = 100; %ng/mL
CellSurfaceArea = 2.236455e-9; %m^2
EGFMolarMass = 6045; %g/mol
ReceptorN = 47362; %Receptors
kf = 1.3627e5; %Forward Constant - m^3/mol*s

%Input of Ranges
TimePoints = linspace(0,1200,1200);
```

```
%Solution Parameters
Time = 1200;
RTol = 1e-12;
ATol = 1e-12;

%Calculation of Specific Values
RDensity = ReceptorN/(AvangadroNumber*2*pi*12.599e-6^2*6.02e23);
C = Concentration/EGFMolarMass/1e3;
D = 1.89e-10;

fem = modelhellips(120,1,0);
fem0=fem;

for k = 1:120
  Result = hellipsint(k,fem);
  PIResult(k) = Result(1);
  POResult(k) = Result(2);
end

fem = modelhellips(1200-120,2,fem0);

for k = 1:1200-120
  Result = hellipsint(k,fem);
  PIResult(k+120) = Result(1);
  POResult(k+120) = Result(2);
end

xlswrite('PIResultHalfEllipse.xls',PIResult')
xlswrite('POResultHalfEllipse.xls',POResult')

TimePoints = linspace(1,1200,1200);
Time = [0,2,5,8,11,14,17,20]*60;
PIExp = [2.421840647, 4.236346046, 3.819440962, 3.204899927, 3.319287326, ...
    4.029629247, 4.250384957, 4.184942118];
STDEV = [0.307561107, 0.245454479, 0.185993254, 0.241954444, 0.304055835, ...
    0.729719029, 0.724341442, 0.646903011];
ErrorL = PIExp - 2*STDEV;
ErrorU = PIExp + 2*STDEV;

errorbar((Time+60)/60,PIExp',2*STDEV,'kx','LineWidth',2)
hold on
plot(TimePoints/60,1./PIResult','k-','LineWidth',2)
grid on
set(gca,'FontSize',18,'LineWidth',2)
axis([0 20 1 20])
xlabel('Time [min]','FontSize',18)
ylabel('Polarization Index','FontSize',18)
title('Model Fit to a Single Cell System','FontSize',18)
legend('Experimental Data','Model Prediction','Location','Best')
print -dtiff -r600 DataFit2.tif
```

Appendix C: ImageJ macro

Vertical single cell splitting

```
run("Set Measurements...", "area mean standard modal min centroid center perimeter bounding fit shape feret's integrated median skewness kurtosis area_fraction stack limit display scientific redirect=None decimal=9"); //Ensure that all properties are met in the results table
imgw = getWidth();

org = roiManager("Count");
xCorr = 0;
d = 10; //make sure that it has a number (number has no meaning)

srcDir = File.directory(); //Stores the directory path of the file.
srcNam = File.name(); //Stores the name of the file with the extension.

setFont("Cambria",20," italic antialiased"); //Set font properties for the particle labeler function.
drwCol = 255; //Set font colour of the particle labeler function.

doit();

function doit()
{
 for (i=org;i>0;i--)
 {

n = roiManager("Count") - 1; //this is the number of rois in the list, then -1 accounts for the select list with 0 being the first number

//Left Side

roiManager("Select", n);
roiManager("Rename", "Cell " + n);
run("Measure");

makeRectangle(getResult("X",0)+xCorr, 0, imgw - getResult("X",0), imgw);

//print(getResult("X",0)+xCorr+" "+0+" "+imgw - getResult("X",0)+" "+imgw);

roiManager("Add");
roiManager("Select", n);
run("Make Inverse");
roiManager("Add");

roiManager("Select", n+1);
setKeyDown("shift");
roiManager("Select", n+2);
setKeyDown("none");

run("Make Inverse");
roiManager("Add");

roiManager("Select", n+3);
roiManager("Rename", "Partition Left " + n);
//Right Side
```

```
roiManager("Select", n+1);
run("Make Inverse");
roiManager("Add");

roiManager("Select", n+2);
roiManager("Add");

roiManager("Select", n+4);
setKeyDown("shift");
roiManager("Select", n+5);
setKeyDown("none");

run("Make Inverse");
roiManager("Add");

roiManager("Select", n+6);
roiManager("Rename", "Partition Right " + n);

//Clean up

roiManager("Select", n+1);
roiManager("Delete");
roiManager("Select", n+1);
roiManager("Delete");
roiManager("Select", n+2);
roiManager("Delete");
roiManager("Select", n+2);
roiManager("Delete");

//Save

if (xCorr-d == 1)
{
 roiManager("Save",srcDir+srcNam+i+".zip");
}

//remove the left and right partitions and the cell

roiManager("Select", n+2); //Right
run("Measure");
rA = getResult("Area", 1);
//print("ra: "+rA);
roiManager("Delete");

roiManager("Select", n+1); //Left
run("Measure");
lA = getResult("Area", 2);
//print("la: "+lA);
roiManager("Delete");

roiManager("Select", n); //Cell
run("Measure");
//roiManager("Delete");

saveAs("Measurements",srcDir+i+".xls");
```

```
r = getResult("Mode", 2)/getResult("Mode", 1);

//print("Cell: "+i+" Intensity: "+getResult("Mode", 2)/getResult("Mode", 1));
//drawString(i, getResult("X",0), getResult("Y",0));
run("Clear Results");

 if (xCorr-d == 1)
 {
  print("Cell: "+i+" Intensity: "+r);

 }
 else if (lA>rA)
 {
 d = xCorr;
 xCorr--;
 //print("xCorr: "+xCorr);
 //print("abs(lA-rA): "+abs(lA-rA)+"-");
 doit();
 }
 else if (lA<rA)
 {
 d = xCorr;
 xCorr++;
 //print("xCorr: "+xCorr);
 //print("abs(lA-rA): "+abs(lA-rA)+"+");
 doit();
 }
 }
}
```

Appendix D: Table for the conversion Damkhöler number / Diffusion coefficient

D x10e-10 (m^2/s)	Da - Suspension	Da - Adherent	Da - Gap Chamber
1.0000	0.8531	1.3543	1.7063
0.5995	1.4231	2.2591	2.8463
0.3594	2.3739	3.7684	4.7479
0.2154	3.9600	6.2861	7.9199
0.1292	6.6056	10.4859	13.2112
0.0774	11.0188	17.4916	22.0376
0.0464	18.3805	29.1777	36.7610
0.0278	30.6605	48.6714	61.3210
0.0167	51.1448	81.1887	102.2897
0.0100	85.3147	135.4309	170.6294